

Particle trapping with functionalized hybrid optical fibers

DISSERTATION

zur Erlangung des akademischen Grades
doctor rerum naturalium (Dr. rer. nat.)

vorgelegt dem Rat
der Physikalisch-Astronomischen Fakultät
der



**FRIEDRICH-SCHILLER-
UNIVERSITÄT
JENA**

von M.Sc. Malte Plidschun
geboren am 09.11.1991 in Buchholz i. d. N.

Gutachter:

1. Prof. Dr. Markus Schmidt, Friedrich-Schiller-Universität Jena
2. Prof. Dr. Oliver Benson, Humboldt-Universität zu Berlin
3. Prof. Dr. Tijmen Euser, University of Cambridge

Tag der Disputation: 26. Oktober 2021

“What we know is a drop, what we don’t know is an ocean.”

– Sir Isaac Newton

To my beloved grandparents.

Abstract

Understanding processes on sub-micron scales that are obscured from the observer's naked eye represents a long cherished desire of mankind. Unfortunately, single particle studies are time demanding and suffer from Brownian motion, which thus limits their practicability and range of applications. Optical and electrical trapping, however, both awarded with a Nobel prize, represent two sophisticated and widely applied solutions allowing for controlled access to individual particles via almost the entire room angle.

Particle trapping via optical fibers in principle provides a flexible and low-cost photonic platform enabling remotely operable applications within difficult to reach environments, including *in situ* and *in vivo* scenarios. The microtechnologically functionalized tip of a hybrid optical fiber (HOF), in particular, which in contrast to conventional optical fibers incorporates additional materials, offers a unique platform for implementing electromagnetic, i.e., optical and electrical, fields that are essentially required for the trapping of particles and unavailable by standard fibers alone. Within the scope of this work, three unique implementations of HOF tip-based particle traps, which in detail rely on integrating a liquid channel, a pure silica section and metallic wires for functionalizing the fibers, are demonstrated, discussed, and compared to state-of-the-art concepts.

First, the principles of optical phenomena, the motion of microscopic objects and influences of confinements including different particle trapping mechanisms, as well as required methods for analyzing and characterizing fiber-based particle traps are introduced. Subsequently, three unique concepts, which in detail consist of a dual fiber focus trap, a single meta-fiber trap and a fiber point Paul trap, and effectively represent two optical and one electrical trap, are discussed and compared with respect to current implementations. In particular, careful design studies, detailed simulations, and proof of principle experiments are realized in this work, and several applications are achieved by experimentally trapping freely diffusing microbeads as well as biologically relevant bacteria in water.

Finally, the obtained results are assessed and compared, and a vision on further improvements for their employment within future scenarios is given. Concludingly, the here presented unique concepts highlight the potential of HOF tip-based particle traps while opening up the possibility for applications in a variety of fields, including chemical analysis of trapped cells via fiber-based spectroscopy, *in vivo* endomicroscopy, or micro-manipulation and sensing of physical properties for, e.g., tumorous tissue diagnosis.

Zusammenfassung

Das Verständnis von Prozessen auf Submikrometerskalen, die dem bloßen Auge des Beobachters verborgen bleiben, stellt einen lang gehegten Wunsch der Menschheit dar. Leider sind Einzelteilchenuntersuchungen zeitaufwendig und leiden unter der Brownschen Bewegung, was ihre Praktikabilität und Anwendungsbreite einschränkt. Optisches und elektrisches Fangen hingegen, beide mit einem Nobelpreis ausgezeichnet, stellen zwei ausgereifte und weit verbreitete Lösungen dar, welche einen kontrollierten Zugang zu einzelnen Teilchen über nahezu den gesamten Raumwinkel ermöglichen.

Das Partikelfangen mittels optischer Fasern stellt im Grunde eine flexible und kostengünstige photonische Plattform dar, welche fernbedienbare Anwendungen in schwer zugänglichen Umgebungen ermöglicht, darunter auch *in situ* und *in vivo* Szenarien. Insbesondere die mikrotechnologisch funktionalisierte Spitze einer hybriden optischen Faser (HOF), welche im Gegensatz zu konventionellen optischen Fasern zusätzliche Materialien miteinbezieht, bietet eine einzigartige Plattform zur Implementierung von elektromagnetischen, d.h. optischen und elektrischen, Feldern, die für das Fangen von Partikeln essentiell erforderlich und von Standardfasern allein nicht erreicht werden können. Im Rahmen dieser Arbeit werden drei einzigartige Implementierungen von HOF-Spitzen-basierten Partikelfallen, welche im Kern auf der Integration eines Flüssigkanals, eines reinen Quarzabschnitts sowie metallischer Drähte zur Funktionalisierung der Fasern beruhen, demonstriert, ausführlich diskutiert und mit dem aktuellen Stand der Wissenschaft verglichen.

Zunächst werden jedoch die Grundlagen optischer Phänomene, die Bewegung mikroskopischer Objekte und Einflüsse von Einengungen einschließlich verschiedener Partikelfangmechanismen, sowie benötigte Methoden zur Analyse und Charakterisierung faserbasierter Partikelfallen vorgestellt. Anschließend werden drei einzigartige Konzepte, welche im Detail aus einer Doppelfaserfokusfalle, einer Einzelfasermetafalle sowie einer Faser-Punkt-Paulfalle bestehen und somit de facto zwei optische und eine elektrische Falle darstellen, diskutiert und im Hinblick auf aktuelle Implementierungen verglichen. Insbesondere werden in dieser Arbeit sorgfältige Designstudien, detaillierte Simulationen und Machbarkeitsstudien durchgeführt sowie mehrere Anwendungen des experimentellen Fangens frei diffundierender Mikropartikel und biologisch relevanter Bakterien in Wasser realisiert.

Abschließend werden die erzielten Ergebnisse bewertet und verglichen, und es wird ein Ausblick auf weitere Verbesserungen für ihren Einsatz in zukünftigen Szenarien gegeben. Zusammengefasst zeigen die hier vorgestellten einzigartigen Konzepte das Potenzial von HOF-Spitzen-basierten Partikelfallen auf, welche die Möglichkeit für Anwendungen in einer Vielzahl von Bereichen eröffnen, z.B. zur chemischen Analyse gefangener Zellen mittels faserbasierte Spektroskopie, *in vivo* Endomikroskopie, oder Mikromanipulation und Sensorik physikalischer Eigenschaften z.B. zur Diagnose von Tumorgewebe.

Contents

Abstract	v
1 Introduction	1
1.1 Motivation and state-of-the-art	1
1.2 Scope and structure of this work	3
2 Fundamentals of optics	5
2.1 Optical fibers	5
2.1.1 Modes and propagation	6
2.1.2 Hybrid optical fibers	9
2.2 Diffraction and phase effects	10
2.2.1 Diffractive optics	10
2.2.2 Beam propagation	11
3 Particle dynamics and trapping	15
3.1 Free diffusive motion	15
3.2 Influence of confinement	17
3.2.1 Local distribution	17
3.2.2 Particle displacement	18
3.3 Particle trapping mechanisms	20
3.3.1 Optical trapping	22
3.3.2 Electrical trapping	24
4 Characterization of fiber traps	29
4.1 Retrieving trapped particle motion	30
4.1.1 Experimental setup	30
4.1.2 Particle tracking routines	34
4.2 Analysis of fiber trap performance	36
4.2.1 Purely spatial techniques	36
4.2.2 Tempo-spectral methods	37
5 Dual fiber focus trap	41
5.1 Fiber characterization	42
5.1.1 Spatial analysis	42
5.1.2 Spectral analysis	44
5.2 Tunable optical trapping	45
5.2.1 Qualitative description	45
5.2.2 Semi-analytical model	47
5.2.3 Numerical analysis	51

5.3	Experimental demonstration	52
5.3.1	Tunable optical trapping	52
5.3.2	Comparison of results	56
5.3.3	Application outlook	58
5.4	Chapter discussion	61
6	Meta-fiber trap	63
6.1	Meta-fiber concept	64
6.1.1	Beam expansion	65
6.1.2	Direct laser writing	67
6.1.3	Lens design limits	69
6.2	Focusing performance	73
6.2.1	Wavefront errors	73
6.2.2	Implemented meta-fiber	77
6.3	Meta-fiber optical trapping	79
6.3.1	Experimental demonstration	79
6.3.2	Performance analysis	81
6.3.3	Comparison of results	82
6.4	Chapter discussion	84
7	Fiber point Paul trap	85
7.1	Electrical design	86
7.1.1	Fiber compatibility	86
7.1.2	Structure optimization	88
7.2	Fiber trap implementation	89
7.2.1	Microwire filling	90
7.2.2	Electrode structuring	91
7.3	Experimental demonstration	92
7.4	Chapter discussion	94
8	Conclusion and outlook	95
8.1	Assessment of results	95
8.2	Future perspective	97
A	Appendix	101
A.1	Working principle of a point Paul trap	102
A.2	Optical properties of the microwired Paul fiber	104
	References	105
	Acknowledgements	115
	List of Publications	116
	Ehrenwörtliche Erklärung	118

List of Figures

1.1	Concept of particle trapping with a functionalized hybrid optical fiber.	3
2.1	Scheme of waveguiding and beam propagation with step-index fibers.	8
2.2	Examples of experimentally implemented hybrid optical fibers.	9
2.3	Comparison of refractive and diffractive optics for beam manipulation.	11
2.4	Propagation of arbitrary beams using the beam propagation method.	12
2.5	Characteristics and aberration of a diffraction limited focal spot.	14
3.1	Key motivation for trapping a free particle under Brownian motion.	16
3.2	Different scenarios of free, confined, and trapped particle motion.	19
3.3	Prominent trapping mechanisms modeled by a harmonic oscillator.	20
3.4	Working principle of optical tweezers for trapping a single particle.	23
3.5	Different mechanisms behind electrical trapping of a single particle.	25
3.6	Working principle of a linear Paul trap for electrophoretic trapping.	27
3.7	Geometric transition to surface-electrode traps and a point Paul trap.	28
4.1	Exemplary motion of a particle confined within a fiber trap in water.	29
4.2	Sketch of the experimental setup for fiber-based particle trapping.	31
4.3	Beam path and adjustment of Köhler illumination in the optical setup.	33
4.4	Tracking algorithms for retrieving the motion of a trapped particle.	35
4.5	Techniques for spatially analyzing trapped particle motion.	37
4.6	Tempo-spectral methods for analyzing trapped particle motion.	38
4.7	Influence of systematic and acquisition errors on the reliability of results.	40
5.1	Artistic conceptual illustration of a dual fiber focus trap in water.	41
5.2	Fundamental mode and beam profile of a nanobore fiber in water.	43
5.3	Measured spectral loss and single-mode operation of the nanobore fiber.	44
5.4	Implementation and tuning of a dual beam fiber optical trap in water.	47
5.5	Approximated potentials and tunability of the dual fiber focus trap.	50
5.6	Simulated trap performance for a dual beam fiber optical trap in water.	51
5.7	Experimental implementation of optical trapping with a dual fiber trap.	54
5.8	Experimental comparison of tuning a dual beam fiber trap in water.	55
5.9	Comparison of experimental and simulation results for a dual fiber trap.	57
5.10	Application of the dual fiber focus trap for different trapping scenarios.	59
5.11	Optical trapping of an <i>E. coli</i> bacterium with the dual fiber focus trap.	60
6.1	Schematic visualization of an ultra-high NA meta-fiber optical trap.	64
6.2	Concept and experimental implementation of a hybrid single-mode fiber.	66
6.3	Experimentally implemented example structures using direct laser writing.	68
6.4	Influence of lateral resolution on the effective NA of a diffractive lens.	70
6.5	Influence of spectral bandwidth on the coherent operation of a meta-lens.	72

6.6	Influence of wavefront on the experimental performance of a meta-lens. . .	74
6.7	Calculated aberration and correction for diffraction limited performance. .	76
6.8	Experimental focal scan verifying the high NA of a hybrid meta-fiber. . . .	78
6.9	Optical trapping of silica beads and <i>E. coli</i> bacteria with the meta-fiber. .	80
6.10	Experimental analysis of the optical trapping performance of a meta-fiber.	82
7.1	Conceptual representation of an electrical fiber point Paul trap.	85
7.2	Calculated trap efficiency for a finitely extended point Paul trap.	87
7.3	Optimization of the geometry for a finite fiber point Paul trap.	88
7.4	Scheme of the workflow for implementing a fiber point Paul trap.	89
7.5	Design and implementation of a microwired hybrid Paul trap fiber.	91
7.6	Final experimental implementation of a hybrid fiber point Paul trap. . . .	92
7.7	Demonstration of electrical trapping with a fiber point Paul trap.	93
A.1	Principle of the electrochemical Stern charge double layer.	101
A.2	Working principle and potentials of a surface-electrode point Paul trap. . .	102
A.3	Approximation of the point Paul trap by an ideal hyperbolic quadrupole. .	103
A.4	Capability of tuning the point Paul trap potential via a DC bias voltage. .	103
A.5	Design and measurement of the optical properties of the Paul fiber.	104

1

Introduction

Here, a brief summary of state-of-the-art particle trapping concepts (section 1.1) as well as the principal scope and structure of this work are given (section 1.2).

1.1 Motivation and state-of-the-art

Observing and understanding processes on microscopic^[1,2], nanoscopic^[3,4], molecular^[5,6] or even atomic scales^[7,8] that remain hidden from the observer's naked eye represents a key motivation for studying individual particles. Unfortunately, many investigations are generally time demanding and thus suffer from the random motion of the object of interest, which is commonly known as Brownian motion^[9,10]. As a result, this effectively complicates their practicability and limits their full potential.

Single particle trapping

The trapping or levitation of particles^[11-13], however, which denotes the contact-free and non-destructive immobilization of freely diffusive particles within media, represents a sophisticated solution significantly reducing this motion. In general, particle trapping techniques provide free access via almost the entire room angle^[14], thus enabling investigation and control of individual sub-microscopic objects. Applications include, for example, chemical sensing of molecular compositions via spectroscopy^[15,16], controlled rotation and micro-manipulation^[17,18] of biological specimen, e.g., single DNA^[19] and bacterial cells^[20,21], for their 3D observation and physical analysis, or shuttling single ions for quantum computing^[8,22] as well as measuring atomic transitions^[23].

In principle, particle trapping relies on different physical mechanisms, two of which are given by the most prominent examples of optical^[11,12] and electrical^[13,24] trapping. Highlighting the large relevance of optical trapping, in particular, two Nobel prizes were awarded, i.e., for the invention of single beam gradient force traps commonly known as optical tweezers^[12] (2018), and for the trapping and cooling of single atoms^[7] (1997). Electrical forces, in contrast, are of great importance within biological applications^[16,25,26], while enabling the trapping of particles that are effectively unsuited within optical trapping, e.g., due to exhibiting a rough scattering surface. The invention of a device that allows

electrodynamically trapping charged particles, specifically, a Paul trap^[13], was awarded with the Nobel prize even before optical trapping in 1989.

Functionalized hybrid fiber tips

Optical fibers, in principle, represent a length-invariant, flexible and low-cost photonic platform allowing the transmission of signals over hundreds of kilometers^[27], which was awarded with the Nobel prize in 2009 for enabling optical communication. Due to their unique integrability and remote operability in difficult to reach environments, specifically, this led to various applications, including infrastructural health monitoring via distributed strain, temperature, or electromagnetic field sensors^[28–30], nonlinear light generation^[31–33], and fiber lasers and sensors in medicine^[34–36]. Particularly their small cross-section and large aspect ratio are perfectly suited for *in situ* and *in vivo* applications, such as fiber-based spectroscopy, imaging and endomicroscopy^[37–42] or optical micro-manipulation and trapping of single particles^[43–46], the latter of which is the scope of this work.

Hybrid optical fibers^[47] (HOFs), specifically, represent a special type of fibers that are combined with additional materials to multi-material fibers^[48,49]. Here, the flat cleaved tip of an HOF effectively provides a unique platform for functionalization via micro- and nanotechnology^[50–52], while the additional fiber materials in particular offer a broad range of opportunities to implement electromagnetic, i.e., optical and electrical, fields that are essentially required for trapping freely diffusing particles and difficult to obtain otherwise. For this purpose, different materials such as, e.g., liquids^[32,53], glasses^[31,54] and metals^[55,56] are introduced along the fiber or directly on its tip, which thus explicitly enables fiber beams that differ significantly^[46,57] from traditional ones. Particularly metals, for example, enable the creation of electrical fields^[58,59] in front of the HOF tip, all of which is not possible via using conventional optical fibers.

Fiber-based particle traps

Combining particle traps with optical fibers^[58,60,61], in particular, opens up the possibility for their remote operability as well as transferring unique trapping concepts to within difficult to reach environments. This specifically includes a broad variety of life science scenarios, where fiber-based trapping of individual particles effectively enables *in situ* and *in vivo* applications^[21,44]. For example, this provides direct access to chemical analysis via, e.g., fiber-based Raman spectroscopy of trapped individual bacteria and cells^[37,38,62], while additionally allowing analysis of their physical properties as well via, e.g., investigating bacterial motility within the optical trap^[63].

Scenarios of further applications include, for instance, fiber-based optical manipulation via, e.g., rotating and stretching individual trapped red blood cells (RBCs) and single giant unilamellar vesicle cells^[64–66] for investigating lipid membrane mechanics, thus effectively

providing the basis for tumorous tissue diagnosis. Moreover, specifically the diffraction limited high numerical aperture (NA) focal spot of a fiber-based single beam gradient trap, i.e., optical fiber tweezers^[44,46,61], potentially paves the way towards future *in vivo* imaging applications while acting as a fiber endomicroscope^[40–42].

Figure 1.1 demonstrates the concept of a hybrid fiber-based particle trap, which relies on an HOF whose tip is functionalized for trapping individual particles in front of the facet. This effectively enables controlled and unhindered access to the object of interest.

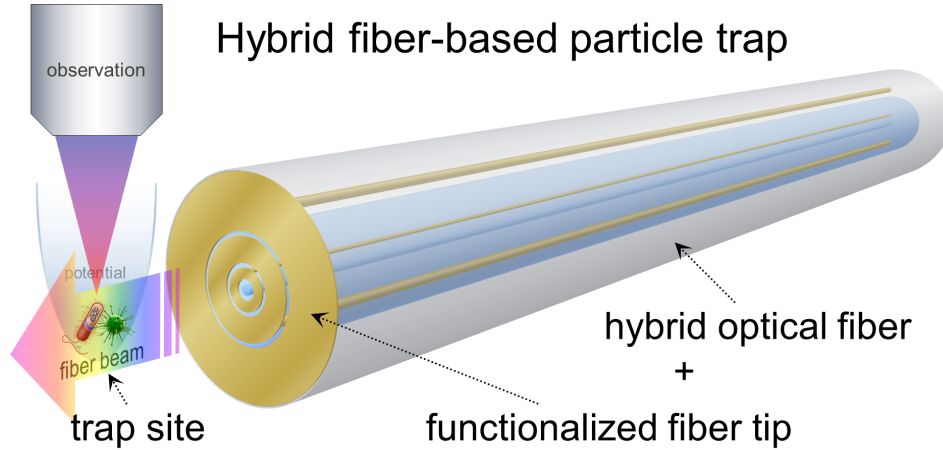


Fig. 1.1. Concept of a hybrid fiber-based particle trap using the functionalized tip of an HOF. The tip of a hybrid optical fiber (HOF), including different materials such as liquids, glasses, or metals, is functionalized via micro- and nanotechnology. This provides optical and electrical fields significantly different from conventional optical fibers in front of the facet, effectively creating a trapping potential for controlled and unhindered access.

1.2 Scope and structure of this work

Within the scope of this work, in particular, three different implementations of hybrid fiber-based particle traps that rely on functionalized HOF tips are realized, discussed, and compared to state-of-the-art concepts. Specifically, these HOFs consist of unique combinations of a water filled channel (chapter 5), a pure silica section (chapter 6) or metallic wires (chapter 7) implemented within the fiber, and represent two optical (chapters 5 and 6) and one electrical trapping concept (chapter 7).

However, for a fundamental understanding of fiber-based particle trapping principles, first, the essential prerequisites are introduced in chapters 2–7. Specifically, in chapter 2, the principles of optical fibers and related phenomena are presented, such as diffraction effects and the propagation of beams. Followed by chapter 3, an insight into the motion of microscopic particles as well as influences of confinements is given, and different trapping concepts including their mechanisms are portrayed. Finally, the prerequisite part is completed with chapter 4, where effectively required techniques for analyzing and characterizing fiber-based traps are elaborated in detail.

The unique HOF trapping concepts, i.e., a dual fiber focus trap, a single meta-fiber trap and a fiber point Paul trap, are presented and discussed in chapters 5–7. Specifically, this includes their design, the simulation and an experimental demonstration of exemplarily trapping single microbeads and biologically relevant bacteria in water.

Dual fiber focus trap

In chapter 5, the concept of a dual fiber focus trap is presented and principally compared to a conventional dual fiber trap^[45,60]. Due to the presence of two foci between the fibers, here, a simple and straight-forward enhancement over a standard solid-core fiber is achieved. In contrast to conventional optical fibers, this unique concept specifically relies on the integration of a water filled central channel that yields a distinct beam profile of the HOF^[45,57]. Here, optical trapping is first predicted within a simulation and is later experimentally demonstrated on the example of freely diffusing microbeads and bacteria in water, followed by a detailed discussion of potential applications.

Meta-fiber trap

The concept of a meta-fiber trap^[46], which in principle relies on a diffractive meta-lens^[67] that is optically three-dimensional (3D) printed onto the tip of a hybrid silica fiber, is presented in chapter 6. In contrast to a dual fiber trap, the meta-fiber trap consists of only one fiber, thus effectively enabling flexible, robust, and remote optical trapping of freely diffusing particles in water using a single beam, which, in particular, is uniquely only achieved via an ultra-high numerical aperture of the meta-lens. Here, its detailed design, implementation, and the performance of the meta-fiber, including an exemplary demonstration of its application for optically trapping microbeads and relevant bacteria, as well as further potentials are discussed within detail.

Fiber point Paul trap

In contrast to the two fiber-based optical trapping concepts, in chapter 7, the alternative of implementing a point Paul trap^[68] onto the facet of a microwired HOF for electrical trapping of particles^[58] is discussed as an outlook. Here, the realized concept uniquely relies on contacting an electrical trapping structure via the microwired fiber itself, thus representing a key feature and major advantage over common traps. Specifically, the design, its implementation, and an experimental application of trapping charged beads are achieved and subsequently discussed for potential employment within future scenarios.

Ultimately, in chapter 8, all obtained results are assessed, and compared to state-of-the-art concepts, and the work is concluded with an outlook on envisioned applications.

2

Fundamentals of optics

This chapter introduces the essentially required principles for a solid understanding of optical phenomena. A starting point for deriving a solution to most problems, such as, e.g., waveguiding within optical fibers, represent the microscopic Maxwell's equations that relate the electrical field \vec{E} and the magnetic flux density \vec{B} :

$$\vec{\nabla} \cdot \vec{E} = \frac{\rho}{\varepsilon_0} \quad (2.0a) \quad \vec{\nabla} \times \vec{E} = -\frac{\partial \vec{B}}{\partial t} \quad (2.0b)$$

$$\vec{\nabla} \cdot \vec{B} = 0 \quad (2.0c) \quad \vec{\nabla} \times \vec{B} = \mu_0 \vec{j} + \frac{1}{c^2} \frac{\partial \vec{E}}{\partial t}. \quad (2.0d)$$

Here, ρ denotes the electrical charge density, \vec{j} the current density, ε_0 and μ_0 the vacuum permittivity and permeability, respectively, and $c = \sqrt{\frac{1}{\varepsilon_0 \mu_0}} = 2.99792458 \cdot 10^8$ m/s the vacuum speed of light. For optics in a linear, homogeneous, and isotropic dielectric matter, it is convenient to introduce the magnetic field \vec{H} and the electric displacement field \vec{D} :

$$\vec{H} = \frac{1}{\mu_0} \vec{B} \quad (2.1a) \quad \vec{D} = \varepsilon_0 \varepsilon_r \vec{E}. \quad (2.1b)$$

The relative permittivity of a medium ε_r , in particular, exhibits a dispersion $\varepsilon_r = n_m^2(\lambda)$ that depends on the vacuum wavelength λ and corresponds to the refractive index n_m .

In this chapter, first, the principles of waveguiding and beam propagation within optical fibers are introduced (section 2.1), which is followed by a detailed consideration of diffraction and phase effects (section 2.2).

2.1 Optical fibers

Optical fibers are waveguides that, generally, exhibit a cylindrical geometry and are made from ultra-pure glass, effectively allowing the transmission of signals over hundreds of kilometers for which the Nobel prize was awarded in 2009 [27]. Here, light is principally guided along the optical axis z within a central core that is surrounded via a cladding (Figure 2.1A). Commonly, optical fibers are covered with a thin layer of acrylate coating that makes the fiber bendable and protects it against environmental influences such as, e.g., humidity. Various types of fibers that differ by their mechanism of optical waveguiding

are widely used and commercially available, including, e.g., step-index and graded-index fibers^[27,69], photonic crystal fibers^[70,71], and anti-resonant hollow core fibers^[72,73].

The simplest type of fiber to describe waveguiding within an optical fiber is based on a step-index fiber, which exhibits a rotational and axial symmetry along its azimuthal angle φ and the propagation direction z . Here, optical waveguiding relies on the total internal reflection between a higher refractive index n_{core} of the core and a lower refractive index n_{clad} of the cladding (Figure 2.1, A and B). In the following, discrete solutions to waveguiding within step-index fibers are derived (subsection 2.1.1), and, specifically, the propagation of the emitted fiber beam in free space is described. Finally, the concept of hybrid optical fibers used within the scope of this work is briefly introduced (subsection 2.1.2).

2.1.1 Guided modes and free space propagation

Due to the geometry of optical fibers, it is particularly convenient to make an ansatz within cylindrical coordinates (r, φ, z) , using $\vec{E}, \vec{H} = \vec{A}(\vec{r}, t) = \vec{A}(r, \varphi) \exp[ik_0(n_{\text{eff}}z - ct)]$. Here, $k_0 = 2\pi/\lambda$ is the wavenumber and n_{eff} the eigenvalue to solve for. For non-magnetic media in the absence of free charges ($\rho = \vec{j} = 0$), the combination of Equations 2.0b and 2.0d yields the wave equation, which transforms into the latter Helmholtz equation:

$$\left(\vec{\nabla}^2 - \frac{n^2}{c^2} \frac{\partial^2}{\partial t^2}\right) \vec{A} = (\vec{\nabla}^2 + k^2) \vec{A} = 0. \quad (2.2)$$

The above relation describes the propagation of waves with wavenumber $k = k_0 n_m$ in a medium of refractive index n_m . Solutions to Equation 2.2 for a core of radius $r = a$, however, are given via a transcendental equation that can only be solved numerically^[69]:

$$\left(\frac{J'_\nu(U)}{U J_\nu(U)} + \frac{K'_\nu(W)}{W K_\nu(W)}\right) \left(\frac{J'_\nu(U)}{U J_\nu(U)} + \frac{n_{\text{clad}}^2}{n_{\text{core}}^2} \frac{K'_\nu(W)}{W K_\nu(W)}\right) = \left(\nu \frac{n_{\text{eff}}}{n_{\text{core}}}\right)^2 \left(\frac{1}{U^2} + \frac{1}{W^2}\right) \quad (2.3a)$$

$$U = ak_0 \sqrt{n_{\text{core}}^2 - n_{\text{eff}}^2} \quad (2.3b) \quad W = ak_0 \sqrt{n_{\text{eff}}^2 - n_{\text{clad}}^2}. \quad (2.3c)$$

Here, J_ν and K_ν represent the Bessel functions of first- and modified second-kind of order ν , J'_ν and K'_ν their derivatives with respect to the argument, and U and W are auxiliary modal parameters. Solutions to Equation 2.3a are principally given via discrete modes of eigenvalues $n_{\text{clad}} < n_{\text{eff}} < n_{\text{core}}$, where the fundamental mode is always represented by the highest effective refractive index n_{eff} closest to the index of the core n_{core} (Figure 2.1B). For the special case of $\nu = 0$ and a low refractive index contrast, in particular, Equation 2.3a yields the linear polarized (LP_{0m}) modes, where m denotes the mode order. In case of higher contrast, these consist of transversal electric TE_{0m} and transversal magnetic TM_{0m} modes, and, as in general, if a higher azimuthal order of $\nu \geq 1$ is present, this effectively leads to the coupling of TE_{0m} and TM_{0m} modes into hybrid HE _{ν m} modes.

An optical waveguide that supports only a few modes can often be described by the normalized frequency or V parameter, which is related to the numerical aperture (NA) and the maximum acceptance angle θ for incident rays (see Figure 2.1A):

$$V = \sqrt{U^2 + W^2} = ak_0 \sqrt{n_{\text{core}}^2 - n_{\text{clad}}^2} \quad (2.4)$$

$$\text{NA} = n \sin(\theta) = \sqrt{n_{\text{core}}^2 - n_{\text{clad}}^2}. \quad (2.5)$$

The V parameter represents the contrast of the refractive index n between the core and the cladding of the optical waveguide and thus the confinement and the quality of guidance of a mode. While fibers with small V , in particular, are more susceptible to bending loss, multi-mode fibers (MMFs) with large V robustly support many modes. Here, the number M of modes can generally be approximated via $M \approx V^2/2$. A single-mode optical fiber (SMF), in contrast, only supports one, namely the fundamental HE_{11} mode, whose intensity profile is best approximated via a Gaussian profile (Figure 2.1C), which is thus most efficient for its excitation.

Generally, optical fibers are single-mode up to a normalized frequency of approximately $V > 2.405$, where the fundamental mode cuts off and higher order modes arise. Inversely proportional to the V parameter of the fundamental mode, however, is the mode field diameter (MFD), which is defined as where the intensity at the radial coordinate r drops to $I(r) = I_0/e^2$, with $I_0 = I(r = 0, z = 0)$. The NA of a fiber, in contrast, is linked via the bandwidth product and the conservation of the etendue. It is thus as well obtained via a Fourier transformation of the mode, followed by retrieving the radial $1/e^2$ value of the resulting angular spectrum (Figures 2.1F and 2.4, B and E).

Gaussian beams

Since the fundamental mode of an optical fiber exhibits a near Gaussian intensity profile, it is convenient to describe its propagation in free space via the analytical model of a Gaussian beam. This type of beam is defined entirely via its opening angle (numerical aperture) θ and the initial beam width (mode field diameter) $2w_0 = \text{MFD}$. In equivalence to the MFD, it is convenient to introduce the Rayleigh length (full width half maximum) $2z_R = \text{FWHM}_z$ as where the intensity along the axial direction z drops to $I(z) = I_0/2$ and the beam yields $\sqrt{2}$ times its initial width. This allows describing the beam diameter $2w(z)$ and the curvature radius $R(z)$ of wavefronts along the propagation direction z :

$$w(z) = w_0 \sqrt{1 + (z/z_R)^2} \quad (2.6a) \quad R(z) = z \left[1 + (z_R/z)^2 \right] \quad (2.6b)$$

$$z_R = \frac{n\pi w_0^2}{\lambda M^2} \quad (2.6c) \quad M^2 = \frac{n\pi w_0}{\lambda} \tan(\theta). \quad (2.6d)$$

Here, M^2 denotes the beam quality factor, which yields unity for a perfect Gaussian beam

and $M^2 \lesssim 1$ for near diffraction limited SMF beams (Figure 2.4). Generally, these exhibit Rayleigh lengths of $z_R \sim 10 \dots 20 \mu\text{m}$ for visible wavelengths in air. The intensity $I(r, z)$ along the radial and axial directions is finally given via:

$$I(r, z) = \left| \underbrace{\frac{w_0}{w(z)} \cdot \exp\left(-\frac{r^2}{w(z)^2}\right)}_{A(r,z)} \cdot \exp\left(i \underbrace{\left[kz - \arctan\left(\frac{z}{z_R}\right) + \frac{kr^2}{2R(z)}\right]}_{\Phi(r,z)}\right) \right|^2 \quad (2.7)$$

$$= \frac{w_0^2}{w(z)^2} \cdot \exp\left(-\frac{2r^2}{w(z)^2}\right).$$

The above relation consists of a real valued amplitude $A(r, z)$ and a complex term including the phase $\Phi(r, z)$, which is important later when considering diffraction effects (details see Figure 6.7). Figure 2.1D exemplarily illustrates the calculated beam profile that is emitted by a typical single-mode fiber for a wavelength of $\lambda = 660 \text{ nm}$ in air.

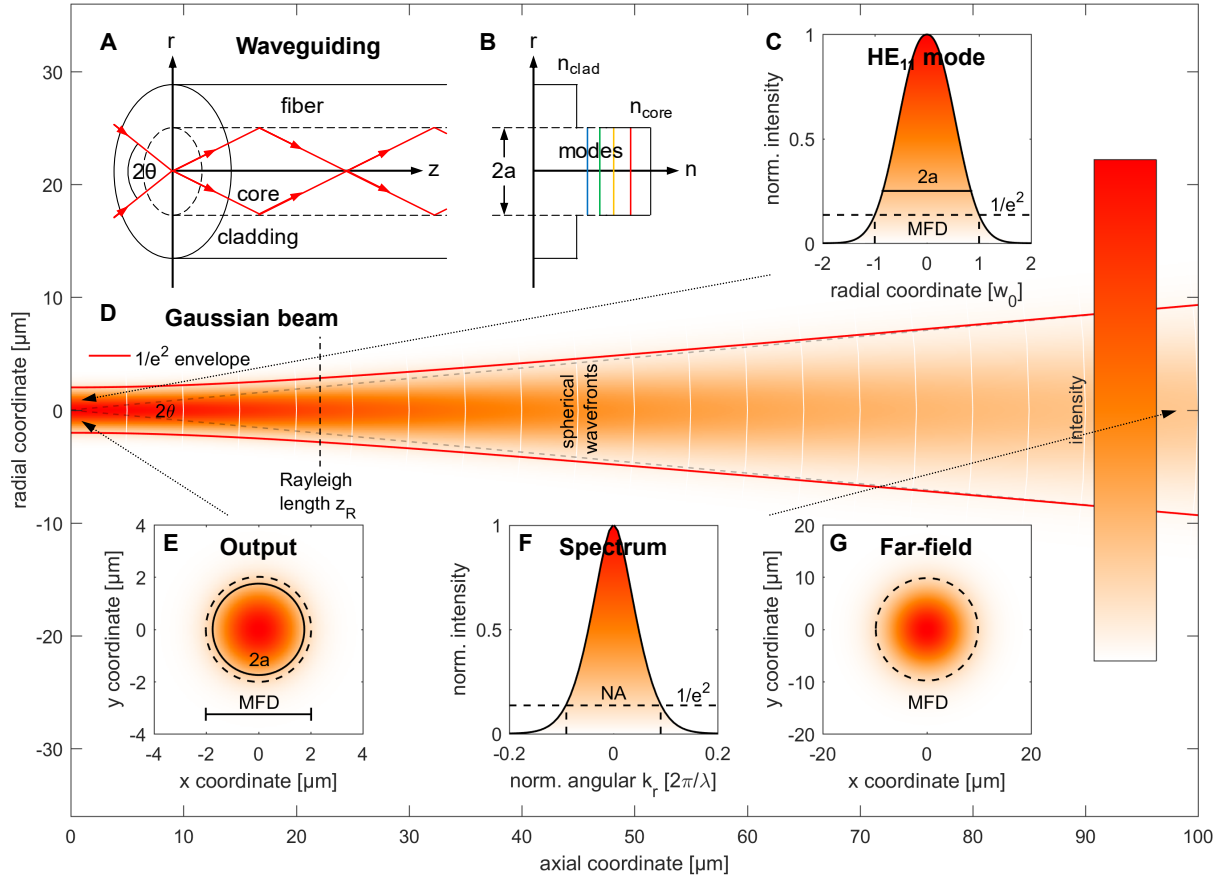


Fig. 2.1. Schematic illustration of waveguiding and beam propagation with a step-index optical fiber. (A) The principle of waveguiding relies on total internal reflection, where incident rays up to a maximum acceptance angle of 2θ are guided along the fiber. (B) A refractive step-index profile yields the formation of discrete modes, where the highest effective index lies closest to the index of the core and represents the fundamental mode of the fiber. (C) Calculated 1D and (E) 2D profiles of the fundamental HE_{11} mode for a wavelength of 660 nm . Here, $2a$ represents the diameter of the core and MFD denotes the mode field diameter of the fiber where the intensity drops to $1/e^2$. (D) Calculated propagation of the near Gaussian shaped fiber beam in air. (F) Conserved angular spectrum of the fiber mode, where NA denotes the numerical aperture taken at the $1/e^2$ value. (G) Propagated 2D profile of the mode in the far-field at a distance of $100 \mu\text{m}$.

2.1.2 Hybrid optical fibers

Hybrid optical fibers^[47] (HOFs), in particular, represent a special type of fibers based on microstructured fibers^[74] that include longitudinal holes parallel to their optical axis z . In this work, the concept specifically relies on combining a single-mode fiber (SMF) with additional materials to a hybrid-material fiber^[48,49]. Generally, these materials are implemented inside or close to the core via filling the holes of a microstructured fiber^[58,75,76] and range from active, nonlinear dopants and different glasses^[31,34] over liquids and gases^[32,33] to metals and semiconductors^[55,77]. Specific applications include, e.g., the generation of supercontinuum within nonlinear HOFs^[31–33], biological, chemical, and pharmaceutical sensing^[53,78,79], the detection of nanoparticles^[4,80,81], and beam shaping and particle trapping (compare refs. [45, 46, 57]) being the scope of this work.

Figure 2.2 illustrates several examples of experimentally implemented hybrid optical SMFs. A water filled central channel (bore) inside the core of a nanobore fiber^[4,45,57] (Figure 2.2, A and B), for example, yields a beam profile that differs significantly from the usual Gaussian shape, while being specifically useful within optical trapping (compare chapter 5 and ref. [45]). Combining an SMF and an MMF^[46,82,83] (Figure 2.2, C and D), in particular, serves to deliver an enlarged HE_{11} mode to a diffractive lens that is implemented on its tip for ultra-high NA focusing (compare chapter 6 and ref. [46]). Metallic wires inside a microwired hybrid fiber^[58,75,76] (Figure 2.2E), in contrast, enable contacting a structure on its facet for electrical trapping of particles (details see chapter 7).

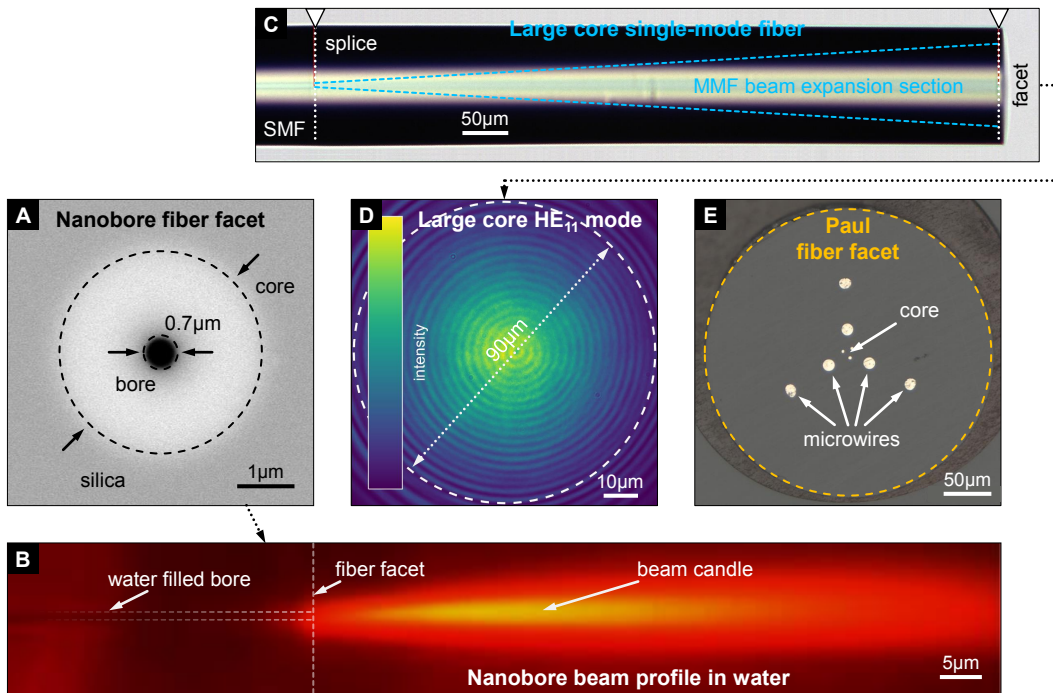


Fig. 2.2. Examples of experimentally implemented hybrid optical fibers. (A) The water filled central bore of a nanobore fiber (NBF) yields (B) a beam profile that is particularly useful within optical trapping. (C) The combination with a multi-mode fiber (MMF) provides (D) an enlarged HE_{11} mode for beam shaping. (E) Metallic wires inside a microstructured fiber allow contacting an electrical trapping structure on its facet.

2.2 Diffraction and phase effects

Since typical fiber beam diameters range within just a few microns, any kind of optical manipulation requires the consideration of diffraction, i.e., the bending of rays around objects due to a retardation of their phase. This effect is most pronounced for feature sizes comparable to the dimension of the wavelength and also occurs in media with varying refractive index. While subsection 2.1.1 described the propagation of fiber beams in free space via the approximation of an analytical Gaussian model, this section treats the employment of optical elements with dimensions close to those of fiber beams.

2.2.1 Diffractive optics

Traditionally, bulk lenses rely on the principle of refraction, where the direction of incident light changes upon passing from one medium to another. A thin diffractive optical element (DOE) or diffractive lens (also termed meta-lens later, compare refs. [46, 67, 84]), in contrast, manipulates the propagation of an incident beam via the modulation of its phase. An ideal lens, which focuses a spherical wave at a propagation distance and focal length of $z = f$, exhibits a radially varying phase that is described via a hyperbolic profile as accordingly achieved with an asphere (Figure 2.3C)^[46,67,84]:

$$\phi_{\text{ideal}}(r, f) = -k \left(\sqrt{r^2 + f^2} - f \right). \quad (2.8)$$

For convenience, a parabolic approximation is often used, which is specifically obtained via a Taylor series expansion of the hyperbolic phase function:

$$\begin{aligned} \phi_{\text{par}}(r, f) &= \phi_{\text{ideal}}(0, f) + \left. \frac{\partial}{\partial r} \phi_{\text{ideal}}(r, f) \right|_{r=0} \cdot r + \left. \frac{\partial^2}{\partial r^2} \phi_{\text{ideal}}(r, f) \right|_{r=0} \cdot r^2 + \dots \\ &\approx -\frac{kr^2}{2f} + \mathcal{O}(r^4). \end{aligned} \quad (2.9)$$

In contrast to Equation 2.8C, this is achieved via a spherical lens and is also visible in the phase $\Phi(r, z)$ of a Gaussian beam (Equation 2.7). The stronger curvature of the parabolic phase, however, inevitably leads to a positive spherical aberration where marginal rays focus early (Figure 2.3B). Figure 2.3D compares the phase profiles of both refractive lenses (spherical lens and bulk asphere) with the one of a diffractive lens^[46,85,86]:

$$\Phi_{\text{diff}}(r, f) = \text{mod}(\phi(r, f), 2\pi). \quad (2.10)$$

The above equation represents a kinoform (Figure 2.3E), dividing a diffractive lens into a number of $N_{\text{Fres}} = \phi(r_{\text{max}}, z)/2\pi$ so-called Fresnel zones^[46]. A key advantage of a diffractive lens over a refractive lens, which is N_{Fres} times thicker, particularly relies on

its thickness of just a few wavelengths. However, the experimental implementation of the continuous kinoform profile is practically limited, generally leading to a quantization into a number of N_h discrete phase levels (Figure 2.3F). The diffractive focusing efficiency η of a discretized kinoform, specifically, is proportional to the number of levels and is defined via $\eta \propto \text{sinc}^2(1/N_h)$, which for an amplitude grating (Figure 2.3G) is as low as $\eta = 10.1\%$ [85, 87]. One example of an experimentally implemented discretized kinoform (see chapter 6), i.e., a diffractive phase-type meta-lens, is effectively demonstrated in Figure 6.3.

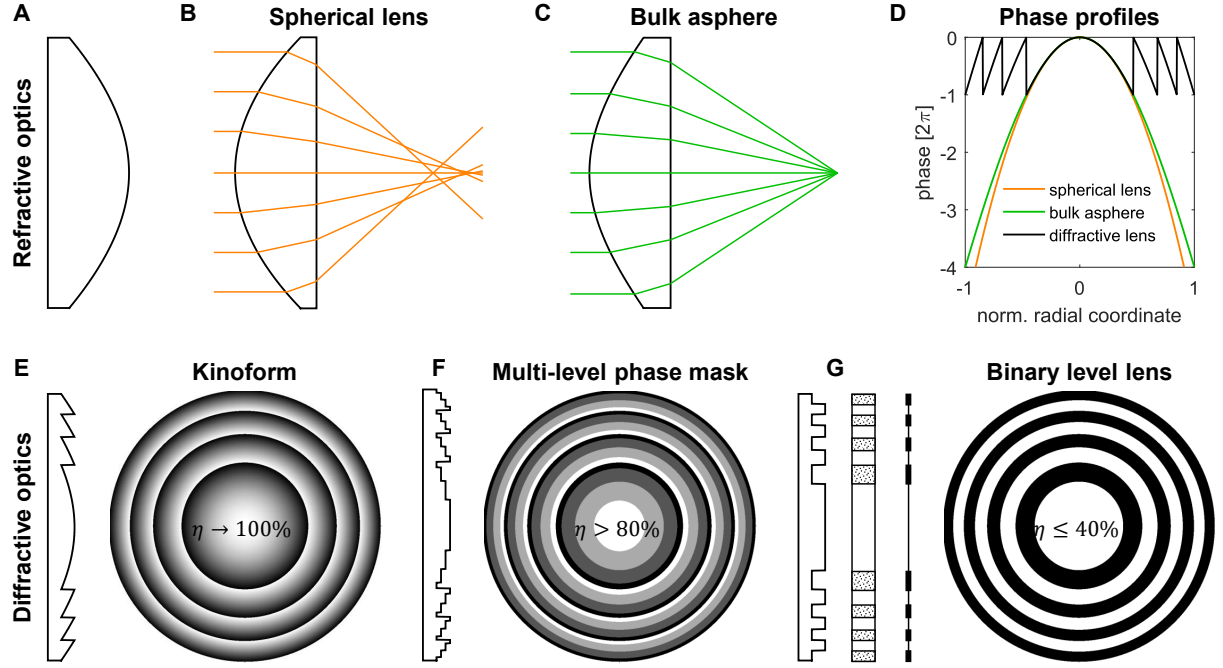


Fig. 2.3. Comparison of refractive and diffractive optics for manipulating a beam. (A–D) Refractive optics for the example of (B) a spherical lens with a positive spherical aberration resulting from the marginal rays, and (C) an ideal aberration free asphere. (D) Comparison of the phase profiles of the two refractive lenses with the one of an ideal diffractive lens. (E–G) Diffractive optics for the example of (E) the ideal continuous profile in D, (F) the quantized profile with discrete phase levels and (G) a binary level lens. This can either be (from left to right) a phase mask, a refractive index element or an amplitude grating (adapted from [87]).

2.2.2 Beam propagation

Often, the profile of an incident plane wave that propagates along z exhibits an arbitrary amplitude $u(\vec{r}_0)$ in the aperture plane at the position $\vec{r}_0 = (x, y, 0)$. The Huygens-Fresnel principle, in particular, describes a wavefront $\exp(i\vec{k} \cdot \vec{r})$ as the superposition of individual spherical wavelets, each solving the Helmholtz equation (Equation 2.2). The amplitude $u(\vec{r})$ of the diffracted pattern at the position $\vec{r} = (x, y, z)$ is thus given as the sum of all rays emerging from the aperture plane at \vec{r}_0 under all angles of the wave vector \vec{k} :

$$\begin{aligned} u(\vec{r}) &= \iint_{-\infty}^{\infty} u(\vec{r}_0) \exp(i\vec{k} \cdot [\vec{r} - \vec{r}_0]) d\vec{r}_0 d\vec{k} \\ &= \iiint_{-\infty}^{\infty} u(\vec{r}_0) \exp(-i[k_x x + k_y y]) dx dy \exp(ik_z z) d\vec{k} \end{aligned} \quad (2.11)$$

$$\begin{aligned}
 &= \iint_{-\infty}^{\infty} \mathcal{F}\{u(x, y)\} \exp\left(i\sqrt{k^2 - k_x^2 - k_y^2}z\right) dk_x dk_y \\
 &= \mathcal{F}^{-1}\{\mathcal{F}\{u(x, y)\} \exp(ik_z z)\}.
 \end{aligned} \tag{2.12}$$

The above equation effectively reduces to a simple three step routine for numerically calculating the diffracted pattern $u(\vec{r})$ of an arbitrary input profile $u(\vec{r}_0)$:

1. Fourier transformation of the input amplitude $u(\vec{r}_0)$ to obtain the angular spectrum.
2. Multiplication with a plane wave propagation term, where the component of the \vec{k} vector along the propagation direction z is given via $k_z = \sqrt{k^2 - k_x^2 - k_y^2}$.
3. Back transformation to obtain the final diffracted amplitude $u(\vec{r})$.

In the following, this is referred to as the beam propagation method (BPM) and is exemplarily shown in Figure 2.4 for the beam of (i) an MMF (Figure 2.4, A to C), (ii) an SMF (Figure 2.4, D to F) and (iii) a plane wave (Figure 2.4, G and I). Specifically, the propagation is fixed via the initial phase predetermining the beam divergence or focusing.

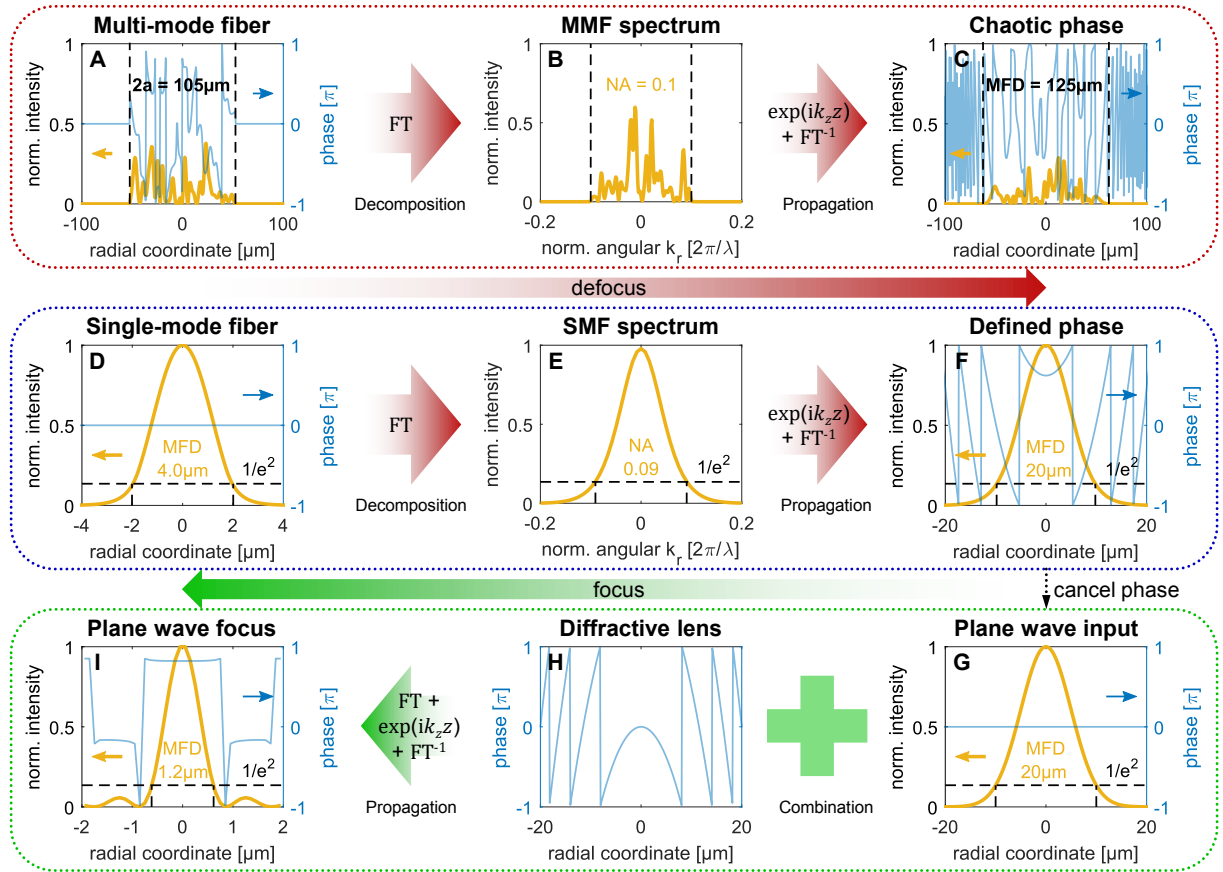


Fig. 2.4. Propagation of arbitrary beams calculated using the beam propagation method (BPM) for a distance of 100 μm in air at a wavelength of 660 nm. (A–C) Propagation of the divergent beam emitted by a multi-mode fiber (MMF) of (A) 105 μm core diameter and (B) 0.1 NA in the angular spectrum. (C) The chaotic phase of the MMF beam limits reversing its propagation (focusing) via a phase structure. (D–F) Same for a single-mode fiber (SMF) of (D) 4 μm MFD, corresponding to (E) 0.09 NA in the spectrum. (F) The phase of the SMF beam is well-defined and can thus be canceled via a phase lens for refocusing the beam. (G–I) A beam with a flat phase (plane wave) can be focused via a diffractive lens to close to wavelength dimensions.

However, several approximations of Equation 2.12 allow for an analytical expression of the diffracted field, including the Fresnel near field and the Fraunhofer far field approximation. Specifically, both variants rely on a paraxial approximation of $k_z = \sqrt{k^2 - k_x^2 - k_y^2}$ via a Taylor series expansion, followed by neglecting higher order terms.

Figure 2.4 effectively reveals that a well-defined phase of a beam can be altered via a diffractive element in order to change the direction of its propagation, e.g., to focus or defocus the beam. For multi-mode fibers (Figure 2.4, A to C), in particular, this task remains a challenge due to their chaotic phase at the output that changes upon bending the fiber. In case of single-mode fibers (Figure 2.4, C to F), however, this is relatively straight-forward to achieve, since their beam exhibits a flat phase upon emission while behaving like a spherical wave (Figure 2.4, I to G). A well-defined phase thus represents a key requirement for near diffraction limited beams, while principally allowing for features sizes on the order of the wavelength (Figure 2.4I).

Experimental examples of the cases (i)–(iii) discussed in Figure 2.4 are demonstrated in chapter 6: (i) focusing an MMF beam (Figure 6.6, B and G), (ii) expanding and focusing an SMF beam (Figure 6.6, C and I), and (iii) focusing a plane wave (Figure 6.6, A and F).

Diffraction limits

The diffraction pattern that is obtained from focusing an infinitely extended plane wave of wavelength λ through an ideal circular lens of phase profile $\phi_{\text{ideal}}(r, z)$, numerical aperture NA and focal length f is principally given via^[46,88]:

$$I(r, z = 0) \propto \text{jinc}^2 \left(\text{NA} \cdot \frac{r}{\lambda} \right) \quad \text{with} \quad \text{jinc}(r) = \frac{2J_1(2\pi r)}{2\pi r} \quad (2.13a)$$

$$I(z, r = 0) \propto \text{sinc}^2 \left(\left(n - \sqrt{n^2 - \text{NA}^2} \right) \cdot \frac{(z - f)}{\lambda} \right) \quad \text{with} \quad \text{sinc}(z) = \frac{\sin(\pi z)}{\pi z}. \quad (2.13b)$$

Equation 2.13a describes the two-dimensional diffraction pattern in the focal plane and is commonly referred to as the Airy function. Here, the finest resolvable feature size is principally limited by the distance $d(\lambda)$ between the maxima of two neighboring Airy discs, which is defined via the first root of the Airy function. This specifically yields the Abbe formula for the diffraction limit and the resolution of an optical system:

$$\text{jinc}^2 \left(\text{NA} \cdot \frac{d}{\lambda} \right) = 0 \quad \text{with} \quad d(\lambda) = \frac{1.22\lambda}{2 \text{NA}}. \quad (2.14)$$

However, it is important to note that the formalism to analytically describe the propagation of Gaussian beams (Equation 2.7) does not comply with Equations 2.13a and 2.13b and is thus not suitable within the following. Depending on the dimensions of a finitely extended beam compared to the size of a lens aperture, effectively, the above equations

require the convolution with the incident beam profile. Figure 2.5 exemplarily displays the obtained foci of the two different types of diffractive lenses (Equations 2.8 and 2.9) calculated for a numerical aperture of $NA = 0.89$ in air. Specifically, here, the profile of the incident beam is given via a plane wave of wavelength $\lambda = 660$ nm.

Due to the infinite extension of the input plane wave, in particular, the asphere produces a well-defined diffraction limited focal spot (Figure 2.5, A and B). The spherical lens, in contrast, principally suffers from strong positive spherical aberration in the focal spot as a result of the increased marginal curvature and the related early focusing of rays (see Figure 2.3B). This is effectively observed in both the one-dimensional (Figure 2.5, C and D) and the two-dimensional (Figure 2.5, E and F) cross-section profiles of the intensity within the focal planes. When introducing the lens into a different immersion medium, however, such as, e.g., water, the aspect ratio of the full width half maximum (FWHM) of the focal spot changes due to a resulting change in the NA (Figure 2.5G).

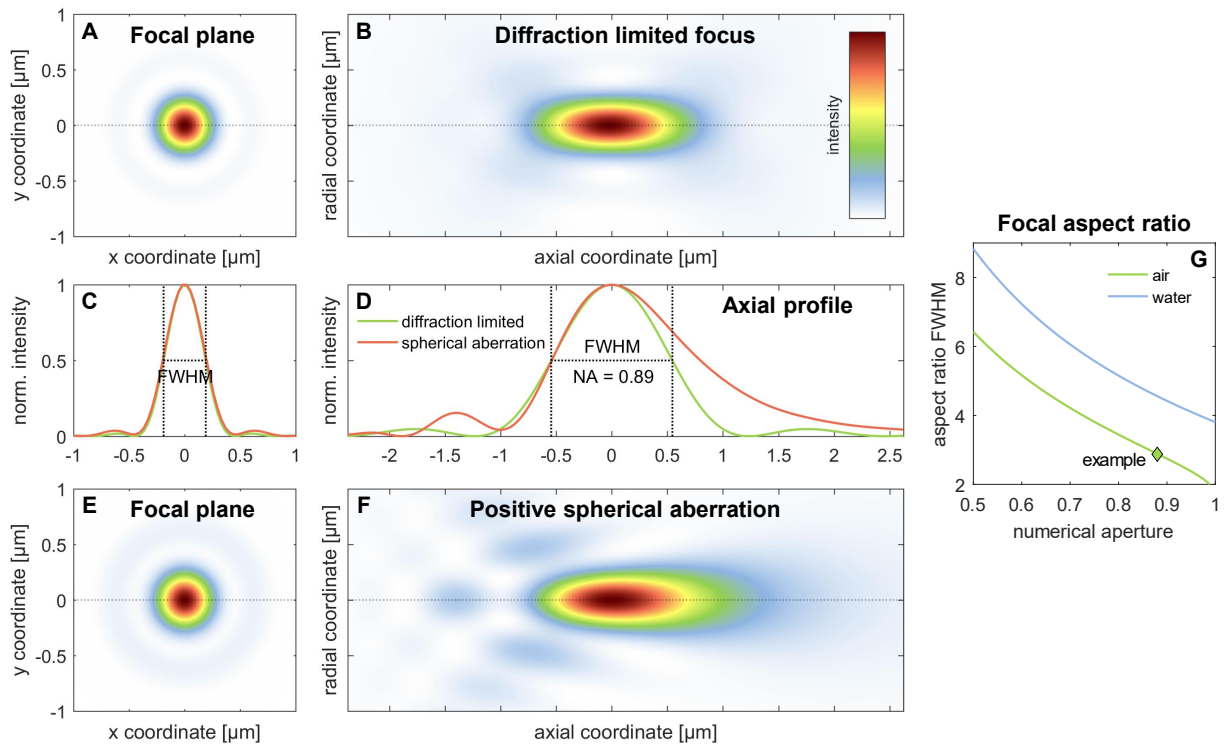


Fig. 2.5. Characteristics and aberration of a focused plane wave calculated for a wavelength of 660 nm in air. (A) Radial and (B) axial 2D intensity profiles of a diffraction limited spot in the focal plane obtained from an ideal lens with a hyperbolic phase profile and a numerical aperture of $NA = 0.89$. (C) Radial and (D) axial 1D profiles along the dotted lines of the diffraction limited focus (A and B) compared to an aberrated focal spot (E and F) obtained from a spherical lens with a parabolic phase profile and the same NA. (E) Radial and (F) axial 2D intensity profiles of the aberrated focal spot, which exhibits a positive spherical aberration due to early focusing of marginal rays. (G) Aspect ratio of the full width half maximum (FWHM) of the focal spot for different NAs in air compared to water. The ratio decreases significantly for higher NAs and changes with the immersion medium, however, it shows no dependence on the incident wavelength.

3

Particle dynamics and trapping

Key motivation for studying single particles is the general desire to observe and understand processes that happen on microscopic^[64–66], nanoscopic^[3,20,80], molecular^[5,6,89] or even atomic scales^[7,8,22]. Unfortunately, applications of sub-micron precision are generally time demanding, while ranging from the observation and analysis of physical properties via microscopy^[64,66,80], the chemical detection and sensing via spectroscopy^[15,37,62] to the sorting and manipulation of mesoscopic objects with respect to a certain property^[25,90,91]. A main limiting factor of all prior scenarios, however, represents the issue of particle movement, which is commonly known as Brownian motion^[9,10,92].

In this chapter, an insight into free particle dynamics is given (section 3.1), followed by a description of mechanisms to suppress Brownian motion. Specifically, these include a physical (section 3.2) and a virtual, non-contact confinement (section 3.3), while particularly the latter is discussed for the examples of optical and electrical trapping. Figure 3.1A provides an overview of applications that are enabled via a non-contact confinement.

3.1 Free diffusive motion

Brownian motion in principle describes the effect of self-propelled random motion within a medium due to its internal energy resulting from collisions with the molecules of the medium. This yields a transfer into kinetic energy as described via the kinetic gas theory. A Wiener process is a mathematical model that describes this stochastic process exhibiting a normally distributed and independent time-continuous increase^[92]. Throughout this work, only single particles are considered, specifically assumed to be independent yet representing the entire batch. The random walk $x(t)$ of a particle of mass m over the time t can thus be calculated via the Brownian dynamics as an approximation of the stochastic differential Langevin equation^[10,92]:

$$m\ddot{x} + \gamma\dot{x} + \nabla U(x) = \sqrt{2\gamma k_B T}\xi(t) \quad \text{with} \quad \langle \xi(t)\xi(t') \rangle = \delta(t - t'). \quad (3.1)$$

The above equation effectively describes a damped harmonic oscillator in the diffusive regime without ballistic inertia (generally $t > 1 \mu\text{s}$), where $\gamma = 6\pi\eta R$ is the Stokes friction coefficient for a particle of diameter $2R$ within a medium of viscosity η and a potential U .

Specifically, the product of the Boltzmann constant k_B and the absolute temperature T represents the internal energy of the system, and $\xi(t)$ denotes a stochastic thermal noise, i.e., white noise, that is modeled via the random Gaussian process with zero mean and unity variance^[92]. The diffusion coefficient D describes the thermal mobility of balancing inhomogeneities within a medium of concentration gradient and is related to the variance of the covered distance $\langle x^2 \rangle$ of the particle along one dimension within a given time t ^[9,92]:

$$\frac{\langle x^2 \rangle}{2t} \stackrel{\text{ESR}}{=} D \stackrel{\text{SEQ}}{=} \frac{k_B T}{6\pi\eta R}. \quad (3.2)$$

Here, ESR denotes the Einstein-Smoluchowski relation and SEQ the Stokes-Einstein equation. Equation 3.2 effectively reveals that the diffusion D of a particle scales inversely with its size, which thus particularly complicates the observation and analysis of small beads due to their rapid diffusion. A lack of buoyancy within the medium, however, additionally results in the effect of sedimentation, thus leading to a slow and steady downwards drift with velocity v_{drift} . In addition to diffusion, this generally limits a long-time observation that suffers from motion blur, thus excluding applications such as spectroscopy due to the rapid vanishment of the object of interest. Commonly, a particle moves more than its own diameter within seconds and escapes the field of view (Figure 3.1B) within minutes.

Figure 3.1B displays calculated trajectories for two different kinds of beads (polystyrene and silica, $2R = 2 \mu\text{m}$ each) in water (chosen for all following scenarios) using Equation 3.1. Here, the two beads of same size but different material particularly emphasize the influence of sedimentation due to their masses that differ by a factor of two.

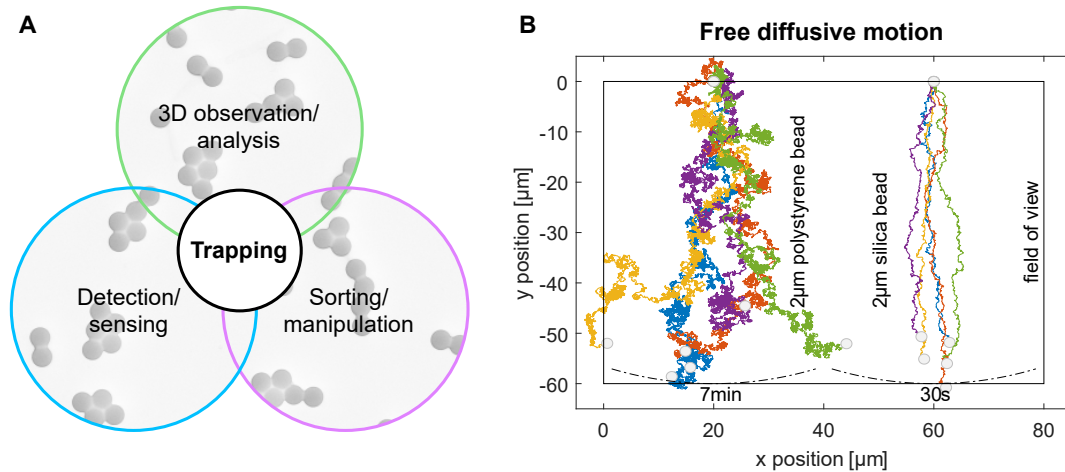


Fig. 3.1. Key aspects and motivation behind trapping a diffusing particle under Brownian motion. (A) Time demanding applications that benefit from a non-contact confinement. These include, e.g., three-dimensional (3D) observation and analysis of physical properties via microscopy, detection and sensing via spectroscopy, and sorting and manipulation with respect to a certain property. The background shows a scanning electron microscope (SEM) image of silica beads. (B) Exemplary trajectories for two different beads in water of masses that differ by a factor of two. The frame shows the field of view (FOV) for a $4.7 \text{ mm} \times 3.5 \text{ mm}$ camera sensor at a magnification of $55\times$ as in later experiments. The beads exceed their own diameter within seconds and escape the FOV (dashed circle segment) within minutes, excluding them from applications in A.

3.2 Influence of confinement

The main limiting cause for time demanding applications presented in Figure 3.1A is the random movement of a freely diffusive particle. One solution to suppress the diffusion represents confining the particle of interest within a potential U (see Equation 3.1 and Figure 3.2A). This effectively allows for studying the particle via limiting its degrees of freedom, yielding its macroscopically confined motion as well as an effect commonly referred to as hindered diffusion^[93,94]. While the prior is simply observed and identified within the statistics of its motion, the latter, in contrast, is of microscopic origin and results from interactions with the boundaries of the confinement^[93,94].

In principle, various origins of confinement within a potential U exist, being either of physical or of non-contact nature. Confinement within a slit, a box, or a pore (Figure 3.2B) represent examples of physical confinement, specifically differing by their appearance within the statistics of the motion. A non-contact mechanism to suppress the free diffusive motion, in contrast, is generally referred to as the trapping within a parabolic potential U_{trap} with a linear restoring force $\vec{F}_{\text{trap}} = -\nabla U_{\text{trap}}$ (Figure 3.2C).

3.2.1 Local distribution

A simple statistical method for investigating and characterizing particle motion represents the analysis within a histogram. Here, a first indication of confinement is obtained via examining the particle's local distribution. The probability $\rho(x)$ of finding a particle within a confining potential $U(x)$ along one dimension results from the kinetic gas theory and is given via the Boltzmann distribution^[95]:

$$\rho(x) \propto \exp\left(-\frac{U(x)}{k_{\text{B}}T}\right). \quad (3.3)$$

The particle's local distribution strongly depends on the shape and the strength of the confinement, which thus directly allows for its identification. While the local probability of a free particle under no influence of a confining potential U is equally distributed along the entire dimension x (Figure 3.2A, corresponding to a flat histogram), the confinement within a slit is described via a box potential (Figure 3.2B, visible as a linear boundary within the local distribution). A box, moreover, limits one more dimension of freedom than a slit and is effectively revealed when examining the full 3D trajectory in Cartesian coordinates. A confining pore, in contrast, is straight-forwardly identified when a coordinate transformation into cylindrical coordinates is performed. Otherwise, it appears as a half disc within the localization histogram. In case of confinement within a harmonic trap potential $U_{\text{trap}}(x) \propto x^2$ (Figure 3.2C), however, the distribution exhibits a Gaussian shape, as illustrated alongside the previous scenarios in Figure 3.2D.

3.2.2 Particle displacement

The local distribution of a particle, however, only yields information about the type and the degree of macroscopic confinement but not about the microscopic diffusion itself. To obtain this information, it is useful to analyze the displacement $\Delta x_i = x(t + t_i) - x(t)$ of a particle, which is defined as the change of the trajectory $x(t)$ with respect to the time increment t_i . Its probability density function $\rho(\Delta x_i, t_i)$ along one dimension is given via^[9]:

$$\rho(\Delta x_i, t_i) = \frac{1}{\sqrt{4\pi Dt_i}} \exp\left(-\frac{(\Delta x_i)^2}{4Dt_i}\right). \quad (3.4)$$

In principle, the above equation defines a normal Gaussian distribution with zero mean and variance $2Dt_i$ dependent on the diffusion D and the incremental time t_i , as resulting from the stochastic process described in Equation 3.1. Note that for particle sizes 15 times smaller compared to the dimensions of physical confinement (as present within a slit in later experiments, see chapter 5) the effect of hindered diffusion only denotes a few percent^[93,94] and is thus neglected throughout this work.

Temporal evolution

Generally, only a limited part of the motion is analyzed, which is namely referred to as the finite trajectory $x(t)$ in the following. The probability density $\rho(\Delta x_i, t_i)$ of Equation 3.4 can thus be extended to describe the displacement of a particle for an arbitrary interval of time Δt commonly referred to as the lag time. Analyzing the temporal evolution of the displacement $\Delta x(\Delta t)$ via its variance for all lag times Δt of the same length, however, represents a powerful method for investigating the characteristics of the motion. Compared to the description of the entire distribution for only a single lag time Δt , in particular, this reveals even more detailed information about the dynamics of a particle and is commonly referred to as the mean square displacement (MSD)^[81,96,97]:

$$\langle (\Delta x(\Delta t))^2 \rangle = \frac{2k_B T}{\nabla^2 U} \left(1 - \exp\left[-D\Delta t \frac{\nabla^2 U}{k_B T}\right] \right) + \varepsilon^2 \quad (3.5)$$

$$= \begin{cases} 2D\Delta t & + \varepsilon^2 & \text{for } \Delta t \rightarrow 0 \text{ or } \nabla^2 U = 0 \\ 2k_B T / \nabla^2 U + \varepsilon^2 & & \text{for } \Delta t \rightarrow \infty \text{ and } \nabla^2 U \neq 0. \end{cases} \quad (3.6)$$

Here, ε^2 denotes an experimental error resulting from the computer-based analysis, i.e., the finite precision in retrieving the particle trajectory $x(t)$ (see section 4.1.2). In principle, the diffusion D can be attributed as free with a linear time-dependent slope for short lag times $\Delta t \sim 0$, yielding information about the particle itself such as, e.g., its size^[80,81], as well as properties of the surrounding medium. For long lag times $\Delta t \gg 0$, however, the effect of confinement plays a major role, and the slope decreases while approaching an asymptotic

limit that describes the degree of confinement. A steady drift such as, e.g., sedimentation of velocity v_{sed} , in particular, yields an additional term $(v_{\text{sed}}\Delta t)^2$ in Equation 3.5. Figure 3.2E displays a temporal analysis of the previously introduced scenarios.

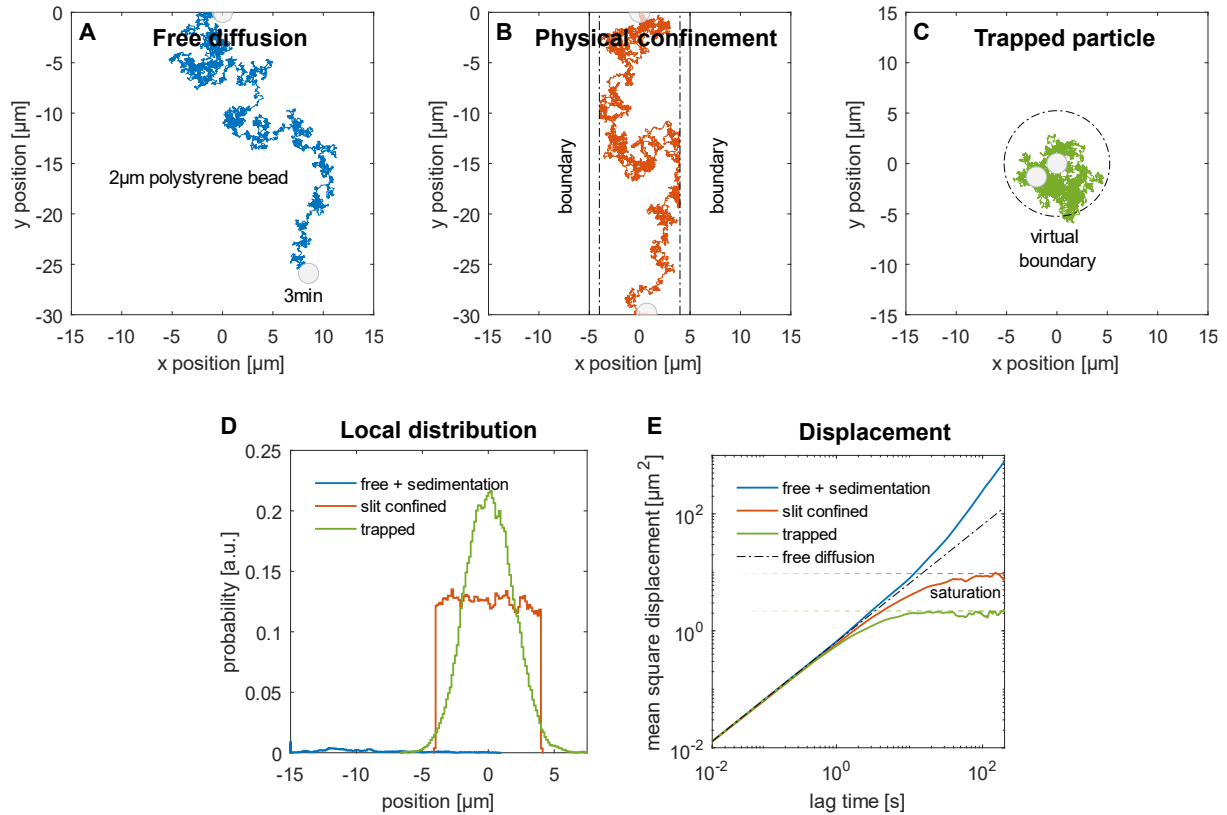


Fig. 3.2. Different simulated scenarios of free, confined, and trapped motion for a 2 μm diameter polystyrene bead in water and identification via statistics. (A) Free diffusive motion calculated for a time of three minutes. The gray circle marks the start and end position of the bead after 3 min. (B) The same bead as in A is let to freely diffuse but is confined within a slit between two physical boundaries. (C) The bead is confined within a non-contact harmonic trapping potential. (D) Local distribution along the x dimension of the bead in A–C. The type of confining potential is directly revealed via the shape of the distribution. (E) Time-dependent mean square displacement (MSD) analysis of the scenarios in D. The bead diffuses freely on short timescales but deviates from the linear slope of the MSD under external influences for long times.

Both methods, i.e., analyzing the local distribution or the MSD (Figure 3.2, D and E), allow for differentiating between free and confined motion of a particle as well as for identifying external influences. Potential origins of these represent, e.g., the influence of drift due to sedimentation, a continuous flow of the liquid, or external trapping forces. Particularly, even detailed information about the microscopic hindered diffusion resulting in a different free diffusive slope can be identified when analyzing the displacement of a particle via the MSD (Figure 3.2E). Hence, its use represents an extremely powerful and versatile method for characterizing finite particle trajectories $x(t)$. However, in contrast to a histogram of only a single lag time Δt , unfortunately, this generally requires significant computation capacities due to considering all possible lag times Δt .

In the following, specific principles of virtual non-contact particle confinement for suppressing free diffusive Brownian motion are elaborated in further detail.

3.3 Particle trapping mechanisms

The trapping or levitation of particles^[11–13] in principle represents a sophisticated solution for providing control as well as unhindered access via almost the entire room angle^[14]. This allows for investigating individual microscopic to atomic objects within applications previously introduced in Figure 3.1A, enabling, e.g., the controlled rotation^[17,18] of microscopic specimen for their 3D observation and physical analysis via microscopy^[20,66], chemical detection and sensing of molecular compositions via spectroscopy^[15,37,62], and even cooling and measuring atomic transitions within single ions^[7,68,98]. Further applications include, e.g., the controlled micro-manipulation of biological cells^[64–66] and single DNA^[19,89] through membranes *in vivo*^[21], sorting mesoscopic objects with respect to a certain property^[25,90,91] as well as shuttling single ions for quantum computing^[8,22].

However, the mechanisms behind particle trapping uniquely rely on different physical principles, some of which are given by the most prominent examples of optical tweezers^[12], plasmonic trapping^[3], dielectrophoretic trapping^[90] and electrophoretic trapping^[13], while representing the principles of optical and electrical trapping as summarized in Figure 3.3A. A qualitative model for describing a trapped particle is based on the damped harmonic oscillator of Equation 3.1 with a parabolic trap potential $U_{\text{trap}}(x) = \kappa x^2$ and a linear restoring force $\vec{F}_{\text{trap}} = -\nabla U = -\kappa \vec{x}$. This is shown for one dimension in Figure 3.3B, where κ is the restoring spring constant that completely describes the properties and the performance of a trap and specifically represents the key quantity for comparing its degree of confinement.

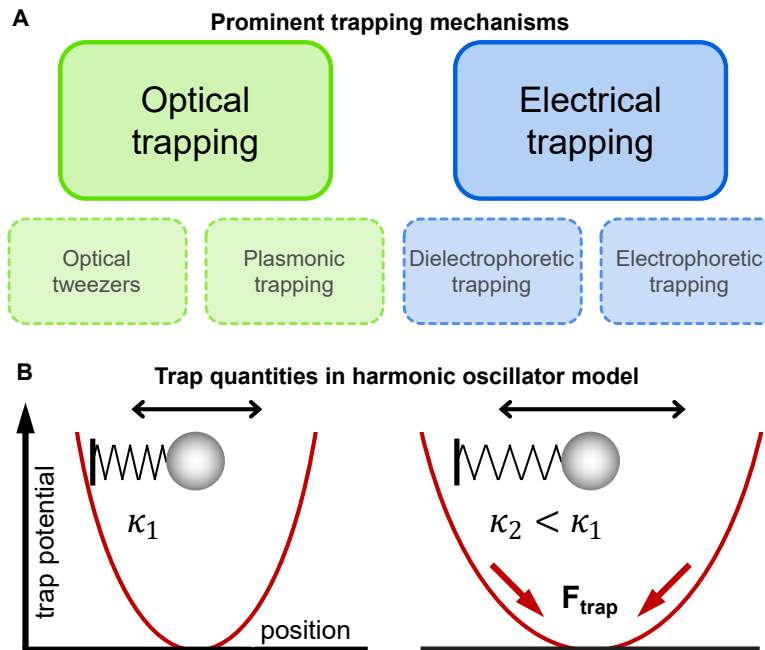


Fig. 3.3. Overview of prominent particle trapping mechanisms modeled by a harmonic oscillator. (A) Examples of prominent trapping mechanisms that rely on the principle of optical trapping (left) or electrical trapping (right). (B) A harmonic oscillator allows for modeling the trap and characterizing its quantities. The restoring spring constant κ completely describes the degree of confinement and is thus used for comparison.

Table 3.1 provides a detailed overview of most prominent particle trapping mechanisms introduced in Figure 3.3A and gives a comparison of several important quantities for characterizing a trap. In principle, the mechanisms behind trapping can be grouped into two categories, namely representing optical and electrical trapping. While optical tweezers and plasmonic trapping rely on the principle of optical trapping, dielectrophoresis and electrophoresis, in contrast, represent examples of electrical trapping.

Tab. 3.1. Overview of prominent particle trapping mechanisms and comparison of their most relevant quantities for characterizing a trap. Additionally, key advantages and limitations of each method are summarized. The plasmonic trapping force is not explicitly reported in the cited literature.

	<i>Optical tweezers</i>	<i>Plasmonic trapping</i>	<i>Dielectrophoresis</i>	<i>Electrophoresis</i>
Particle size [μm]	$10^{-4} \dots 10^2$	$10^{-2} \dots 0.5$	$0.01 \dots 15$	$10^{-4} \dots 10$
Displacement [μm]	$10^{-4} \dots 10^2$	$10^{-3} \dots 0.5$	$0.01 \dots 0.1$	$10^{-4} \dots 1$
Trapping force [pN]	$0.003 \dots 10^2$		$0.1 \dots 15$	$10^{-2} \dots 0.1$
Trap stiffness [pN/ μm]	$0.002 \dots 10^3$	$10^{-4} \dots 1$	$0.1 \dots 100$	$10^{-2} \dots 15$
Key advantages	large particles, long range	metallic particles	arbitrary particles	selective sorting
Limitations	transparency, scattering	nanostructures, short range	immersion medium	particle charge
Reference	[7, 45, 62, 99]	[3, 100, 101]	[90, 102, 103]	[68, 102–105]

A key advantage of optical over electrical trapping, in particular, represents its low dependence on the immersion medium, which effectively even allows operating through translucent barriers. While its demand for transparency, for example, limits the application of optical tweezers, plasmonic trapping, in contrast, requires particle sizes well below the operating wavelength, which thus excludes it from many applications. The unknown plasmonic trapping force \vec{F}_{trap} is assumed to range within $10^{-4} \dots 0.1$ pN, which is one to three orders of magnitude lower than within optical tweezers.

Electrical traps, in contrast, generally benefit from their functionality with arbitrary particles exhibiting, e.g., a rough scattering surface, which thus complicates their use within optical tweezers. The main drawback of electrophoresis, however, represents its demand for charged particles, while dielectrophoresis, in contrast, is limited to operating within an immersion medium, thus excluding atomic particle sizes.

Nevertheless, the trapping force \vec{F}_{trap} and stiffness κ of all mechanisms are effectively limited on the lower end due to losing a trapped particle under the influence of thermal fluctuations or additional external forces such as, e.g., particle drift. However, they principally scale with the incident power and are thus often normalized. In the following, the principles of optical (subsection 3.3.1) and electrical trapping (subsection 3.3.2) are elaborated in further detail for their application within later experiments.

3.3.1 Optical trapping

Due to its large scalability and range of applications, here, optical trapping is discussed for the example of optical tweezers. In this context, plasmonic trapping is neglected since it requires subwavelength dimensions that are not observable via conventional light microscopy. The first observation of photonic forces, which are sometimes referred to as the effect of photophoresis, was made by Arthur Ashkin in 1970^[11]. Here, the working principle effectively relies on the relative refractive index contrast $m = n_p/n_m$ between a particle of refractive index n_p and the surrounding medium of index n_m .

In particular, a photon that strikes a particle generates a momentum, which yields an acceleration of the particle into the opposite direction in order to compensate this momentum (Figure 3.4A). This is principally known as the gradient force \vec{F}_{grad} , which is always directed towards the maximum of the intensity profile I_0 along the radial direction r and along the axial direction z for a focused beam (Figure 3.4B). For a dielectric sphere of radius R in the approximation of a point dipole \vec{p} within the Rayleigh regime well below the dimensions of the wavelength λ , this force reads^[12,61,95]:

$$\vec{F}_{\text{grad}}(\vec{r}) = \underbrace{(\vec{p} \cdot \vec{\nabla})}_{\sim \text{sphere polarizability}} \vec{E} = 2\pi R^3 \left(\frac{m^2 - 1}{m^2 + 2} \right) \frac{n_m}{c} \cdot \vec{\nabla} I_0(\vec{r}). \quad (3.7)$$

A scattering force \vec{F}_{scat} , in contrast, results from the radiation pressure being only experienced along the propagation direction \hat{z} of the incident beam. In early experiments, this had to be compensated via two counter-propagating beams^[12,61,95]:

$$\vec{F}_{\text{scat}}(\vec{r}) = \underbrace{\frac{8\pi k_0^4 R^6}{3} \left(\frac{m^2 - 1}{m^2 + 2} \right)^2}_{\text{scattering cross-section}} \frac{n_m}{c} \cdot I_0(\vec{r}) \hat{z} \quad \text{with} \quad |\hat{z}| = |\vec{z}/z| = 1. \quad (3.8)$$

Both optical forces principally scale with the incident intensity I_0 and the diameter $2R$ of a trapped particle, which thus complicates the trapping of small particles and hence requires the exploitation of the axial gradient force $\vec{F}_{\text{grad}}(z)$. This effectively led to the establishment of single beam gradient force traps (Figure 3.4C) commonly known as optical tweezers^[12], for which the Nobel prize was awarded in 2018. However, generally no limitations on the size of the trapped object exist, which was demonstrated via, e.g., trapping individual bacteria and viruses on the micro- and nanoscopic level^[1,2] or single atoms on the Ångström scale^[7,98], awarded with the Nobel prize in 1997. This enabled the development of a broad range of applications particularly in life sciences, including, e.g., the Raman spectroscopy of trapped cells^[15,37,62], their rotation and stretching to study lipid membrane mechanics^[64–66], optical manipulation inside a living zebrafish^[21] as well as the investigation of single DNA and proteins for molecular motors^[5,19].

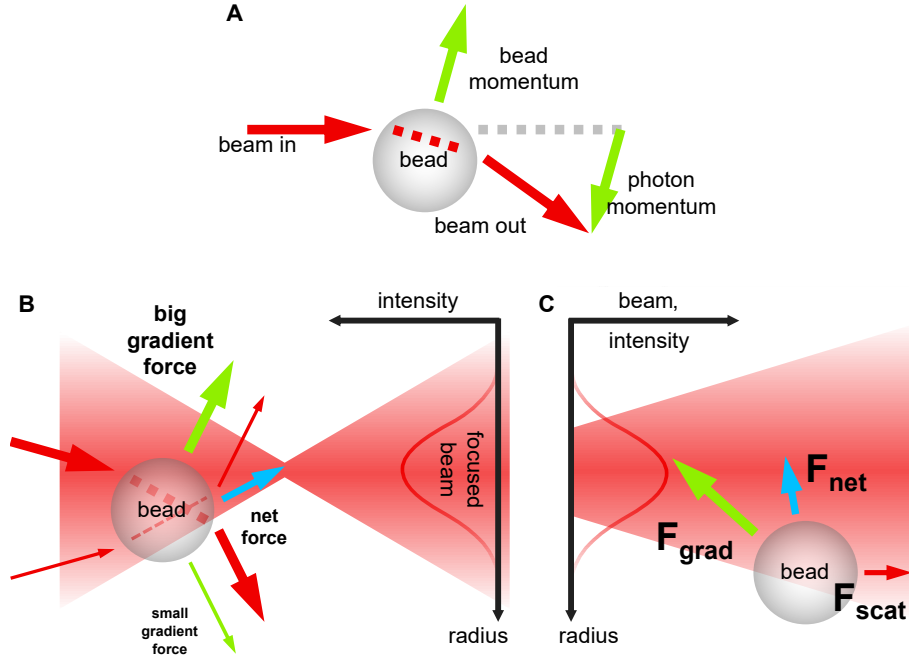


Fig. 3.4. Working principle of optical tweezers for trapping a particle (adapted from [106, 107]). (A) A photon is incident onto a bead, which generates a momentum that yields its acceleration into the opposite direction in order to compensate this. (B) The resulting gradient force is always directed towards the maximum of a focused beam along the radial and the axial direction. (C) The scattering force, in contrast, is always directed towards the propagation direction of the incident beam. This particularly requires a tight focus for optical trapping with a single beam and compensating the scattering force via the axial gradient force.

Of particular rapid progress is the field of optical manipulation driven by the invention of holographic optical traps^[18,44,108]. In contrast to conventional optical tweezers, which solely rely on the intensity of an incident beam, this concept also exploits its polarization and phase, thus enabling, e.g., the generation of conveyor and tractor beams^[108–110] or the creation of multiple time varying trapping sites^[18,44,108]. Further applications include, e.g., the controlled rotation of objects via optical vortices^[17,18] or full 3D specimen observation^[20], the sorting via periodic optical potentials^[111,112] as well as the transport and delivery of particles^[108,110] and even single qubits for quantum computing^[22].

Limitations

The analytical description of optical forces (Equations 3.7 and 3.8), however, is only valid for a single spherical particle in the Rayleigh regime well below the dimensions of the wavelength^[12,95]. Determining the optical potential U and the resulting trap stiffness κ for larger microscopic particles within the Mie scattering regime, in contrast, particularly requires a rigorous numerical calculation via the time averaged Maxwell stress tensor $\langle \hat{T}(\vec{r}) \rangle$. Here, the optical force \vec{F}_{opt} that acts upon a particle of arbitrary shape is given via the integration over its surface S with respect to the surface normal $\vec{n}(\vec{r})$ ^[61,113]:

$$\vec{F}_{\text{opt}}(\vec{r}) = \oint_S \langle \hat{T}(\vec{r}) \rangle \cdot \vec{n}(\vec{r}) dS. \quad (3.9)$$

Often, the obtained trap stiffness κ is normalized to the optical power P of an incident beam^[43,45,86], which thus allows quantitatively comparing the trap performance. Typical values of κ/P range within $(10^{-3} \dots 10^{-1})$ pN/ μm /mW depending on the size and the material of the particle (compare refs. [43, 45, 114] and Table 8.1). However, if more than one particle is confined within the optical trap, generally a coupling between individual particles occurs. This is commonly referred to as optical binding^[115–117] (see Figure 5.10, B and D) and specifically complicates the description of the optical trap and its stiffness κ via the simplified model of a single damped harmonic oscillator (Figure 3.3B).

Since the principle of optical tweezers particularly relies on the gradient force \vec{F}_{grad} for optical trapping, which is generally ensured via a tightly focused laser beam to compensate the axial scattering force $\vec{F}_{\text{scat}}(z)$, microscope objectives of high numerical aperture, i.e., $\text{NA} > 0.8$, are conventionally used. The previously mentioned application of two counter-propagating beams^[11,45,117], however, represents a simple technique for compensating axial scattering forces $\vec{F}_{\text{scat}}(z)$, effectively allowing for the application of arbitrary beams. These specifically include the divergent beams emitted by conventional single-mode fibers of generally low NAs ~ 0.1 (see section 2.1) being insufficient for optical trapping with a single beam alone and thus excluding them from certain applications. The counter-propagating beam concept thus enables applications such as, e.g., the prior mentioned rotation and stretching of single red blood^[64,66,118] and giant unilamellar vesicle cells^[65] as well as Raman spectroscopy of trapped cells^[62].

One implementation of two identical fibers as a dual beam fiber trap (compare refs. [45, 60, 64]) is thoroughly discussed in chapter 5. However, several different approaches to circumvent the demand for high NAs have been exploited in the past. For example, these represent the trapping against a surface^[82,119,120], in reflection via a standing wave^[117,121] as well as the combination of an optical fiber with a focusing element^[42,52,122]. Particularly the latter represents a sophisticated concept enabling high numerical apertures of $\text{NA} > 0.8$ as required within single beam optical trapping (compare refs. [44, 46, 83]), being presented in detail in chapter 6.

3.3.2 Electrical trapping

Electrical trapping of individual particles effectively represents an alternative to the previously discussed concept of optical tweezers in case the exhibited properties are incompatible, e.g., due to limited transparency. Particularly, electrical forces are of importance within biological applications^[16,25,26] due to the electrochemical charge double layer that surrounds a freely diffusing object, i.e., the Stern layer^[123] (details see Figure A.1 in the appendix). For example, this influences the behavior of biological macro-molecules including proteins and nucleic acids in electrolytes, representing the essential requirement for analytical methods in bio-medicine, such as DNA sequencing^[24,26].

The mechanisms behind electrical trapping can principally be grouped into electrophoretic (EP) and dielectrophoretic (DEP) forces, which rely on two fundamentally different principles^[24,102]. While the EP force \vec{F}_{ep} , in particular, requires a fixed net charge Q , the DEP force \vec{F}_{dep} , in contrast, relies on the induced dipole moment \vec{p} of a particle. Equivalent to the gradient force \vec{F}_{grad} in optical trapping via photophoresis, this effectively requires the gradient $\nabla\vec{E}$ of an inhomogeneous electric field \vec{E} :

$$\vec{F}_{\text{ep}}(\vec{r}) = Q\vec{E}(\vec{r}) \quad (3.10a)$$

$$\vec{F}_{\text{dep}}(\vec{r}) = \vec{p} \cdot \nabla\vec{E}(\vec{r}). \quad (3.10b)$$

Applications of electrical forces include, e.g., charge selective^[13] trapping of single DNA^[89] and ions^[8,68] (EP), bacteria^[16] and protein molecules^[6] (DEP) as well as sorting biological cells via flow cytometry^[25] (EP) or DEP^[90,124]. Due to its versatility and independence on immersion media^[89,105] and particularly with respect to life sciences, where most biological cells exhibit negatively charged functional groups^[24,26], here, the principles of EP trapping are briefly discussed in the following. Figure 3.5 exemplarily compares the mechanisms behind EP and DEP trapping of a single particle.

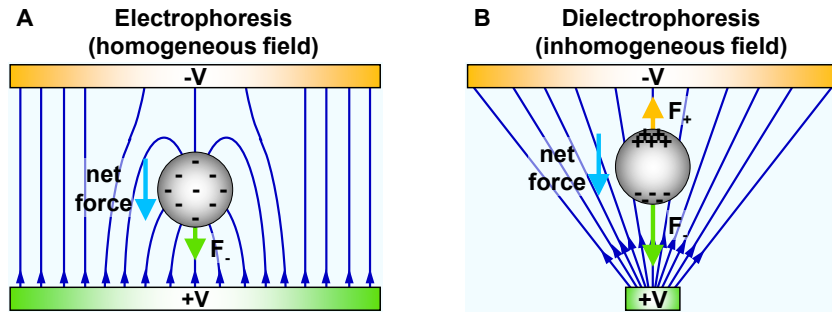


Fig. 3.5. Different mechanisms behind electrical trapping of a single particle (adapted from [24]). (A) The electrophoretic (EP) force acts upon a particle that exhibits a net charge and is thus observed in homogeneous electric fields. (B) The dielectrophoretic (DEP) force, in contrast, does not rely on net charges but on the polarizability of the particle. Hence, this requires the gradient of an inhomogeneous electric field.

In the following, the working principle of a device for the electrophoretic trapping of charged particles, i.e., a Paul trap^[13], is introduced. Subsequently, the concept is extended to a circular geometry particularly complying better with the one of optical fibers^[58,68].

Linear quadrupole trap

A linear quadrupole Paul trap^[13], for whose invention the Nobel prize was awarded in 1989, allows for electrodynamic trapping of charged particles. Ideally, it consists of four hyperbolic rods separated by a distance $2r_0$, while an alternating (AC) voltage V_{ac} of radio frequency (RF) ω is applied to two opposite rods and the remaining two are kept on ground (GND) or on a direct (DC) potential U_{dc} (Figure 3.6, A and B). This creates a time-dependent electric potential Φ ^[13,105] between the rods (Figure 3.6, B and C):

$$\Phi(x, y, t) = \frac{\Phi_0(t)}{2r_0^2} (x^2 - y^2) \quad \text{with} \quad \Phi_0(t) = U_{\text{dc}} + V_{\text{ac}} \cos(\omega t). \quad (3.11)$$

EP trapping in particular relies on the ponderomotive principle^[13], which demands the Laplace equation $\nabla^2\Phi = 0$ to be satisfied at all times and here is specifically ensured via the rapidly alternating saddle point of the electric potential Φ . A particle of mass m and charge Q is thus confined within the time-independent trap potential $\langle\Psi_{\text{ep}}\rangle \propto |\nabla\Phi|^2$ (Figure 3.6C), and equivalent to Equation 3.1, the equation of motion reads:

$$m\ddot{x} + \gamma\dot{x} + Q\nabla\Phi(t) = F_t(t) \quad \text{with} \quad \langle F_t(t)F_t(t') \rangle = 2\gamma k_{\text{B}}T\delta(t - t'). \quad (3.12)$$

Here, $\gamma = 6\pi\eta R$ is the Stokes friction coefficient for a particle of diameter $2R$ within a medium of viscosity η and $F_t(t)$ represents the stochastic thermal force. The introduction of a dimensionless time $\tau = \omega t/2$ effectively yields the Mathieu differential equation^[13,105]:

$$\frac{d^2u}{d\tau^2} + b\frac{du}{d\tau} \pm [a + 2q \cos(2\tau)]u = \frac{4F_t}{m\omega^2} \quad \text{with} \quad u = x, y. \quad (3.13)$$

In particular, b , a and q are dimensionless parameters defining the motion of the particle within the electrophoretic Paul trap, where b describes the damping influence of the immersion medium, and a , q denote the respective DC and AC stability of the trapping:

$$a = \frac{4QU_{\text{dc}}}{mr_0^2\omega^2}\Lambda \quad (3.14a) \quad q = \frac{2QV_{\text{ac}}}{mr_0^2\omega^2}\Lambda \quad (3.14b) \quad b = \frac{2\gamma}{m\omega}. \quad (3.14c)$$

However, a particle is only confined stably along two spatial dimensions (e.g., x and y for a linear trap, where the displacement along z is invariant) for $a < 0.24$ and $q < 0.91$ (Figure 3.6D), while the overlap of both regions generally increases for $b > 0$ ^[125,126]. Here, $\Lambda \leq 1$ describes the geometry of the trap, yielding unity for an ideal quadrupole^[68]. For the AC-only case ($a = 0$, $q \ll 1$), in particular, the ponderomotive potential $\langle\Psi_{\text{ep}}\rangle$ and the resulting electrophoretic trapping force $\langle\vec{F}_{\text{ep}}\rangle$ can be approximated^[68,102]:

$$\langle\Psi_{\text{ep}}(x, y)\rangle \approx \frac{Q^2 |\Lambda\nabla\Phi_{\text{ac}}|^2}{m\omega^2 [4 + b^2]} = \frac{q\Lambda}{4 + b^2} \frac{QV_{\text{ac}}}{2r_0^2} (x^2 + y^2) \quad (3.15)$$

$$\langle\vec{F}_{\text{ep}}(x, y)\rangle = -\nabla\langle\Psi_{\text{ep}}\rangle = -\kappa(x + y) \quad \text{with} \quad \kappa = \frac{q^2}{4 + b^2} \frac{m\omega^2}{2}. \quad (3.16)$$

This effectively yields a harmonic trap potential $\langle\Psi_{\text{ep}}\rangle \propto u^2$ for a linear quadrupole (Figure 3.6E). For an adiabatic process ($b \gg q$), in particular, the oscillatory motion $u(t)$ of a confined particle within the ponderomotive potential $\langle\Psi_{\text{ep}}(u)\rangle$ is given via^[68,102]:

$$u(t) \approx u_0 \left[1 - \frac{2q}{4 + b^2} \left(\cos(\omega t) - \frac{b}{2} \sin(\omega t) \right) \right] \exp\left(-\frac{4q^2}{4b^2 + b^4} \omega t \right). \quad (3.17)$$

The trapped particle's motion principally consists of a slow secular part of frequency $\Omega \approx \omega\sqrt{q^2/8}$ and a fast micro motion of frequency ω . However, as the equations hold only for a point charge, the trapping of a macroscopic particle cannot be described analytically. Equivalent to optical trapping, nevertheless, the trap stiffness κ (Equation 3.16) scales with the particle size and is thus often normalized to units of Volt^{-2} . Moreover, κ strongly depends on the specific EP trap geometry, which thus requires a careful design.

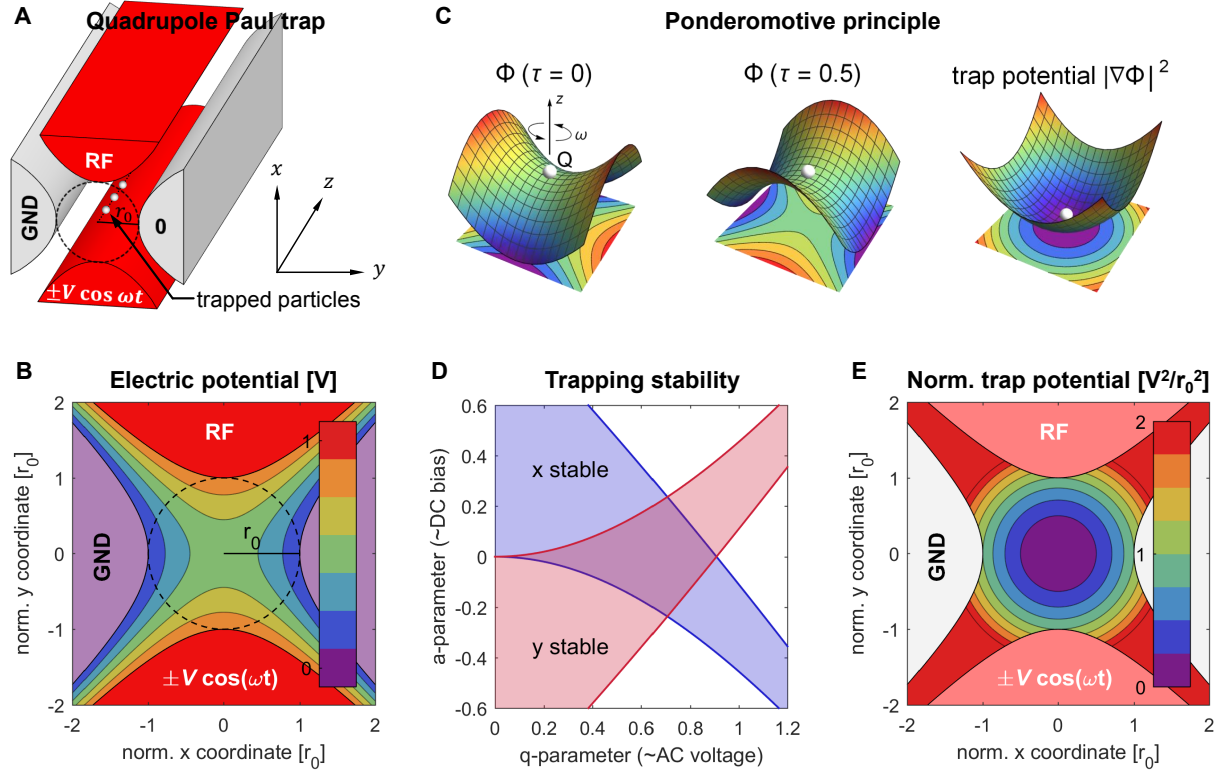


Fig. 3.6. Working principle of a linear Paul trap for electrophoretic trapping of charged particles. (A) An ideal quadrupole trap consists of four hyperbolic rods, where a radio frequency (RF) electric potential is applied to two opposite rods while the remaining two are kept on ground (GND). (B) The resulting electric potential exhibits a saddle point between the four rods. (C) Ponderomotive principle of electrophoretic trapping. The rapidly alternating electric saddle point creates a time-independent ponderomotive trap potential for the charged particle (see main text, adapted from [127]). (D) Stable trapping along two spatial dimensions is provided where both regions overlap. (E) Resulting harmonic ponderomotive potential around the trap center.

In the following, the concept of a surface-electrode point Paul trap is briefly presented, which particularly complies better with the geometry of an optical fiber.

Surface-electrode point Paul trap

Conventionally, the only theoretical geometry of an ideal hyperbolic quadrupole is adapted to a four-rod linear Paul trap^[68,128,129] as exemplarily demonstrated in Figure 3.7A. However, the confinement within linear traps is principally only provided along two spatial dimensions, e.g., x and y , while particles are chained along z in the center of the trap and thus exhibit one degree of freedom. Since the EP trapping between longitudinal wires inside an optical fiber is generally complicated, a deformation of three-dimensional (3D) rods into a

2D surface-electrode trap^[68,128,129] is particularly convenient, where particles are trapped at a height z_0 above the surface as illustrated within Figure 3.7B.¹ This specifically allows for a periodic repetition of the electrodes, including the rearrangement of wires into a surface geometry of five electrodes^[128] as visualized in Figure 3.7C.

A surface-electrode point Paul trap^[68] specifically represents the transformation and circular continuation of an odd number of periodic surface-electrodes into a concentric symmetry^[58,68,130]. In particular, this ensures a better compatibility with the geometry of an optical fiber, while being rotationally invariant within the azimuthal angle φ as presented within Figure 3.7D. This effectively allows simultaneously confining a particle along all three spatial dimensions in the center of the trap at a height z_0 .¹ Figure 3.7, E to G, exemplarily displays the ponderomotive potentials $\langle \Psi_{ep} \rangle$ of the configurations depicted in Figure 3.7, A to D, respectively, where a larger number of electrodes generally leads to a stronger confinement of a charged particle within the EP trap.

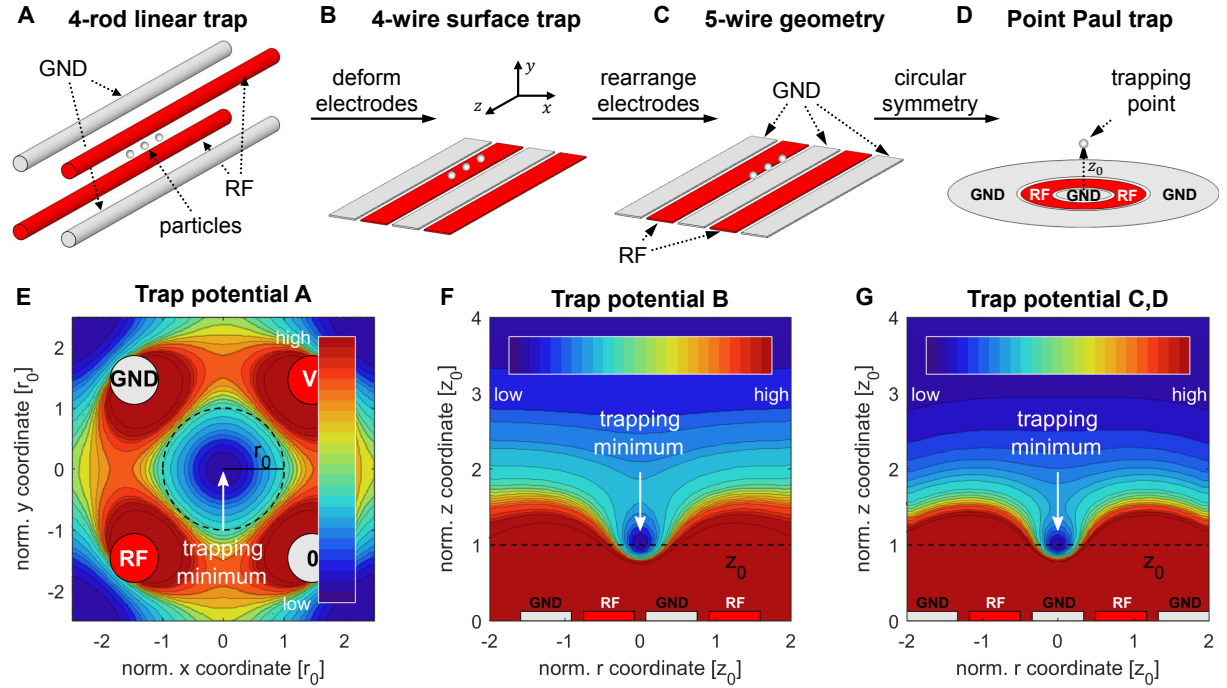


Fig. 3.7. Geometric transition to surface-electrodes and a point Paul trap (adapted from [128, 129]). (A) Conventionally, a four-rod linear trap is used instead of an only theoretical ideal hyperbolic quadrupole, confining charged particles along a line in the center of the trap. (B) Deforming the wires yields a two-dimensional (2D) surface-electrode trap, where the particles are trapped above the surface.¹ (C) In principle, a periodic repetition is allowed, including the rearrangement of electrodes into a five-wire geometry. (D) The circular transformation yields a concentric symmetric point Paul trap, where a particle is confined above the center of the trap. (E–G) Resulting ponderomotive potentials for the configurations in A–D, respectively. A larger number of electrodes effectively yields a stronger confinement of charged particles within the trap.

The working principle of a concentric three ring electrode point Paul trap is demonstrated in further detail in Figure A.2 in the appendix. In addition, Figure A.3 exemplarily illustrates the approximation of its potential via an ideal hyperbolic quadrupole.

Characterization of fiber traps

The previous chapter in principle focused on the free diffusive dynamics of a single particle and highlighted some of the key motivations for its trapping. In this context, an introduction to particle trapping mechanisms was given, and applications were presented and discussed. This chapter, however, is dedicated to the experimental implementation and methodology of fiber-based particle trapping, which in all experiments was carried out within aqueous solutions.

Here, a key motivation arises from the importance of retrieving the motion of a trapped particle for analyzing and comparing the performance of the fiber trap, which specifically requires a subsequent detailed investigation of the trapped particle dynamics. Figure 4.1 exemplarily illustrates the motion of a trapped silica bead of $2R = 2\ \mu\text{m}$ diameter that was experimentally confined within a fiber-based optical trap in water.

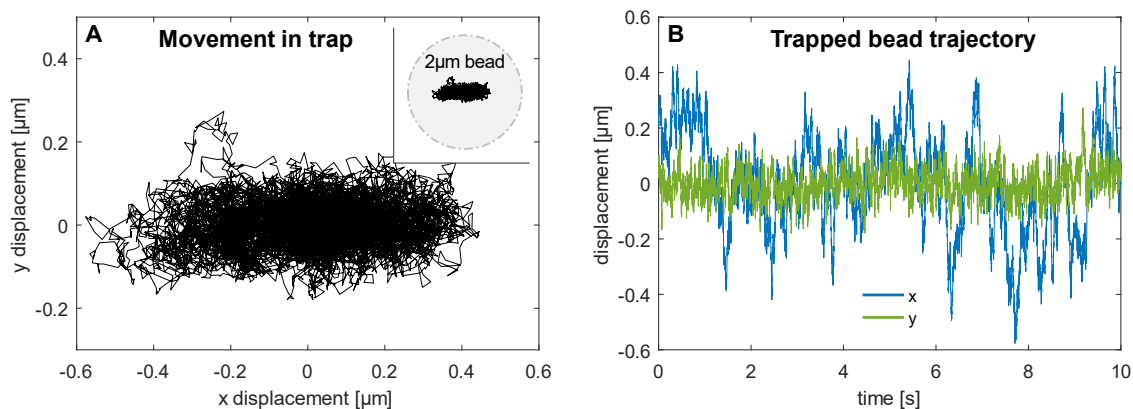


Fig. 4.1. Motion of an example of a $2\ \mu\text{m}$ diameter silica bead confined within a fiber trap in water. (A) The bead oscillates rapidly within the trap; however, its displacement is below its own diameter as displayed by the inset. (B) The bead covers the entire effective trapping region in approximately under 10 s, which specifically demands a fast acquisition of its movement in order to properly analyze and characterize the trap.

Figure 4.1 shows the rapid oscillatory movement of the bead within the fiber trap, which specifically covers the entire effective trapping region in under 10 s. This particularly requires a fast acquisition of the motion in order to entirely understand its behavior and thoroughly characterize the fiber-based trap. In the following, the experimental retrieval of trapped particle dynamics is discussed in detail (section 4.1), and subsequently, an introduction into the analysis for the examples of spatial as well as time and frequency domain techniques is given (section 4.2).

4.1 Retrieving trapped particle motion

Within this section, first, an overview of the experimental setup for the example of fiber-based optical trapping of single particles in water is given (subsection 4.1.1). In principle, this allows a straight-forward transfer to the application of fiber-based electrical trapping while requiring only little adjustment. Subsequently, established examples of techniques for retrieving trapped particle motion are discussed in detail (subsection 4.1.2).

4.1.1 Experimental setup

The implemented optical path for fiber-based optical trapping of individual particles is schematically illustrated in Figure 4.2A. In detail, it consists of a laser source in combination with variable optical density (OD) filters for reducing the optical power P_0 of the beam. A continuous wave (CW) laser diode of power $P_0 = 120$ mW at a wavelength of $\lambda = 660$ nm (Thorlabs L660P120) in combination with a collimating lens of focal length $f = 4.5$ mm (Thorlabs C230TMD-A) were used within the single meta-fiber optical trapping (chapter 6, compare ref. [46]). For dual beam fiber trapping experiments (chapter 5, compare ref. [45]), however, a CW laser of power $P_0 = 100$ mW at a wavelength of $\lambda = 635$ nm was used, and the optical path was split into two arms via a beam splitter (BS). In both cases, this resulted in final beam diameters of $\varnothing \sim 2 \dots 3$ mm.

Each arm of the optical path was steered via mirrors (M) to correct for angle and offset errors of the beam. A $20\times$ dry objective (Olympus MPLN, NA = 0.4) was used for exciting the fundamental HE_{11} mode of an optical fiber (see section 2.1), while the fibers (presented in chapters 5 and 6 in further detail) were mounted with their input sides on three-axis micro-precision stages (Elliot Martock MDE122). In combination with the beam steering mirrors, this effectively allows optimizing the fiber coupling in order to approximately match the profile of the fundamental fiber mode. Here, optical powers of $P_{1,2} \approx 30$ mW were generally reached at the output of each fiber.

Observation

A custom-built optical microscope forms the essential part within the observation of trapped particle motion, consisting of an imaging (Figure 4.2B) and an illumination section (Figure 4.2D, presented in further detail in Figure 4.3). Here, both were built along the horizontal plane in order to minimize vibrations.

The imaging section specifically consists of a dry objective (OBJ) in combination with a tube lens (L), followed by a high-speed camera (CAM) as depicted in Figure 4.2B. A $40\times$ dry objective (Olympus MPLN, NA = 0.65) in combination with a tube lens of focal length $f_t = 250$ mm were used for the observation of a particle within the dual beam fiber trap^[45]. For the single meta-fiber trap^[46], in contrast, a $50\times$ dry objective (Olympus MPLFLN,

NA = 0.8) was used, followed by an achromatic tube lens of focal length $f_t = 200$ mm (Thorlabs AC254-200-A-ML). In both cases, this yields final magnifications of $M = 55\times$ for all experiments as a direct result of the fact that Olympus objectives are referenced to a tube length of $f_t = 180$ mm.

Moreover, scattered trapping laser light was blocked using a notch filter in the collimated infinity space between the objective and the tube lens (Figure 4.3A), and high-speed videos of a trapped particle were recorded via a camera (640 px \times 480 px sensor and 7.4 μm pixel size, Basler pilot piA640-210gm) at a high frame rate of $1/\Delta t = 1000$ fps in all experiments. For all recordings, the minimum duration was $t > 30$ s and the exposure time $\tau < 1$ ms.

Sample chamber

In this work, all experiments were carried out in aqueous solutions, for which stock solutions of particles were diluted within ultra-pure water to final particle concentrations of $c \sim 5 \cdot 10^6 \text{ cm}^{-3}$. Specifically, either silica beads of diameters $2R = 2 \mu\text{m}$ (Micromod Inc., Figure 6.9A) or inactivated *Escherichia coli* (*E. coli*) bacteria of approximately $1 \mu\text{m} \times 3 \mu\text{m}$ size (Figure 6.9B) were used within the experiments. A sample chamber (Figure 4.2C) was fabricated via 3D printing (Ultimaker²), effectively allowing confinement of the suspended particle solution as well as up to two optical fibers for trapping.

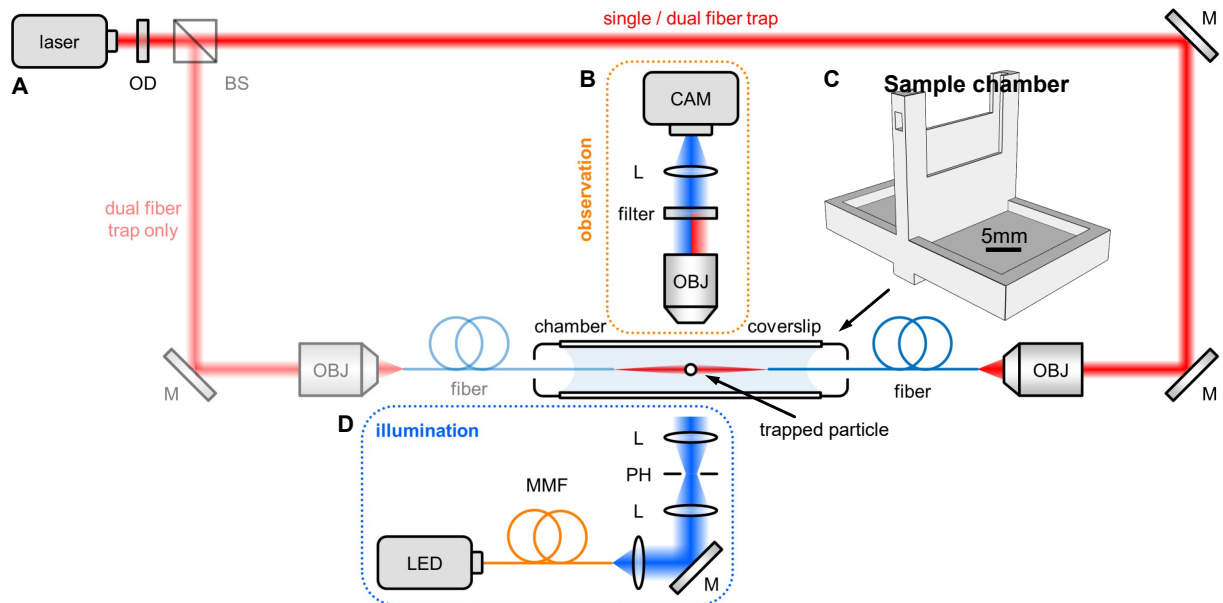


Fig. 4.2. Sketch of the experimental setup for fiber-based optical trapping of single particles in water. (A) A laser beam is split into two arms for a dual beam fiber trap via a beam splitter (BS), which is removed within single meta-fiber optical trapping. The beam is steered via mirrors (M) and focused into an optical fiber via an objective (OBJ). Optical density (OD) filters attenuate the beam. The motion of a trapped particle is recorded via a custom-built optical microscope that consists of (B) an observation and (D) an illumination part. (B) Observation relies on a high-NA objective, a tube lens (L), and a high-speed camera (CAM), while a filter blocks the scattered trapping laser. (C) A sample chamber was 3D printed for confining a thin film of particle solution between two parallel coverslips. Holes on both sides allow inserting optical fibers for trapping a particle inside. (D) Illumination is provided via a fiber-coupled LED in Köhler geometry (discussed later).

In detail, the sample chamber consists of a part for mounting within the optical setup's microscope, while exhibiting two slots for microscope coverslips on both sides as well as two holes for inserting optical fibers on the other ends. The free output end of an optical fiber, in particular, was mounted on a three-axis micro-precision stage as well, which thus allowed for a well-controlled insertion through one of the holes of the chamber as well as for a precise displacement under the custom-built microscope for optical trapping. A few ten microliters of the suspended particle solution were subsequently pipetted between the 170 μm thick coverslips of the chamber that are spaced 0.5 mm apart and confined there during the experiment via adhesion.

Illumination

The illumination within the optical microscope was provided via a fiber-coupled light emitting diode (LED) at a wavelength of $\lambda = 455 \text{ nm}$ (Thorlabs M455F3), which was connected to a multi-mode fiber (MMF) of core diameter $2a = 105 \mu\text{m}$ and NA of 0.22 (Thorlabs M18L). Here, the principle of Köhler illumination was applied for ensuring a homogeneously illuminated sample as well as avoiding an image of the source (commonly referred to as lamp filament) within the sample and the final image plane. Generally, this reduces image artifacts and provides a high contrast image of the sample, which is particularly important for minimizing pixelation effects when retrieving trapped particle motion (discussed in further detail within subsection 4.1.2).

As schematically illustrated within Figure 4.3A, the implementation of Köhler illumination in principle demands the following order of components:

1. collector or collimating lens of focal length f_c
2. field stop
3. optional field lens (focal length f_f)
4. aperture stop
5. condenser lens (f_n).

The rays that pass through the different components can principally be categorized into image formation and illumination rays. While orange lines denote the image formation (or marginal) rays in Figure 4.3A, blue lines, in contrast, represent the illumination (or principal) rays. In particular, the two types of rays are conjugate to each other, if one is collimated, the other one exhibits a focus, and their bandwidth product is fixed via the etendue of the optical system. The planes of maximum collimation, however, which are commonly referred to as conjugate image planes, can be grouped into field (collimated illumination rays) and aperture planes (collimated image formation rays).

Specifically, principal rays determine the size of the image, while marginal rays, on the other hand, define the resolution of the optical system via the effective numerical aperture

$NA \propto \sin \theta$. Adjusting the field stop thus changes the amount of light that is incident onto the sample plane, while adjusting the aperture stop, however, changes the contrast of the sample and the depth of field via the effective NA. As previously mentioned, this is of particular importance when retrieving trapped particle motion and generally allows reducing the influence of pixelation.

A lens, in principle, performs a Fourier transformation after twice its focal length f_i , converting previously collimated rays into a focal spot. The actual size of the spot, however, specifically depends on the prior beam divergence θ_{i-1} , yielding $\varnothing_i = 2f_i \tan \theta_{i-1}$ in air. After a further propagation distance of $2f_{i+1}$, this effect is reversed via a second lens (commonly referred to as a $2f_i + 2f_{i+1} \hat{=} 4f$ -system), which finally results in an inversed, scaled image of magnification $M = f_2/f_1$. Here, a combination of aspheric lenses with $f_c = 6.24$ mm, $f_f = 150$ mm and $f_n = 8$ mm was used, effectively yielding an illuminated focal spot of diameter $\varnothing = 150$ μ m and $NA = 0.16$ within the sample plane.

Instead of changing the aperture stop, however, it is particularly useful to adjust the NA via a combination of lenses for maximum illumination efficiency. This effectively allows reducing the exposure time, thus minimizing image blur. Figure 4.3, B to D, shows several example images of dual beam fiber traps in water using different illumination NAs.

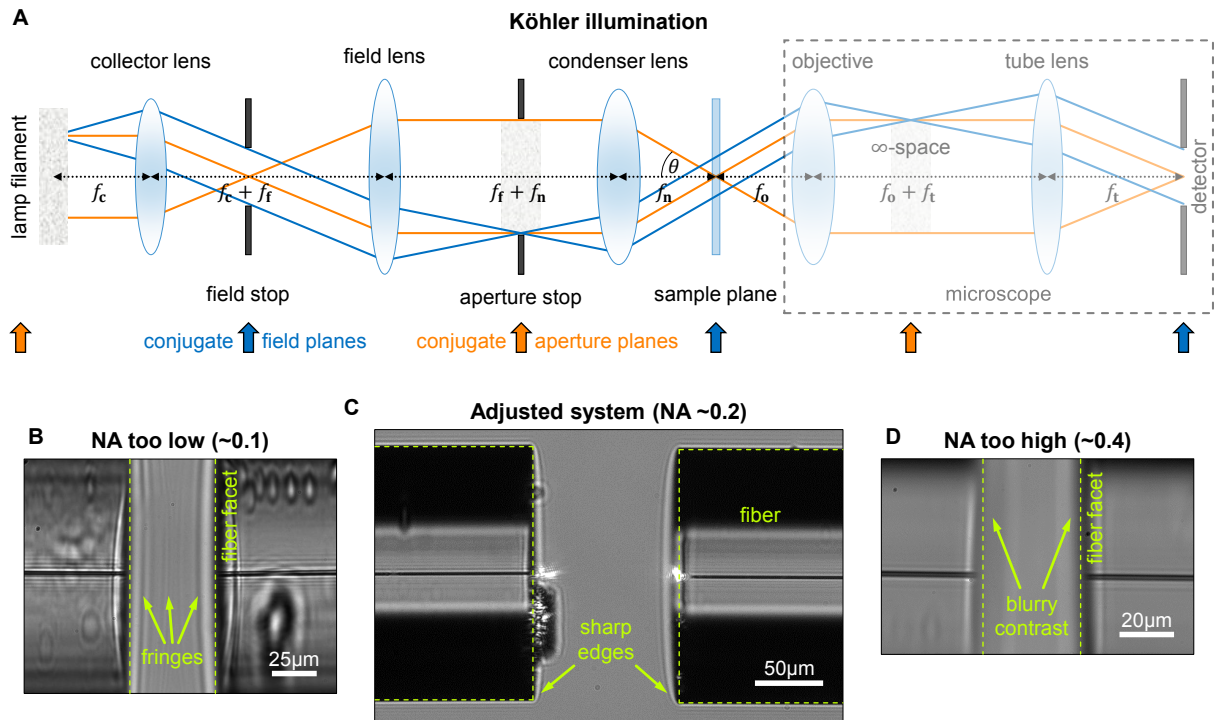


Fig. 4.3. Schematic beam path and adjustment of Köhler illumination within the optical setup for observing trapped particles. (A) The principle of Köhler illumination relies on an odd number of lenses that image the source into an intermediate plane to avoid overlapping with the sample plane. Image resolution and contrast, i.e., numerical aperture (NA), are changed via the marginal rays (orange), while principal rays (blue) adjust the size of the illumination spot (details see main text). (B–D) Adjustment of the illumination NA for the example of a dual beam fiber trap, where (B) a very low NA leads to the formation of fringes, (C) the system is perfectly adjusted, and (D) the NA is too high, which results in poor image contrast.

4.1.2 Particle tracking routines

In the following, an overview of implemented techniques for the retrieval of trapped particle motion is given. Within this context, the recorded high-speed videos were first cropped to an area of interest (AOI) containing relevant information about the motion of a particle (Figure 4.4A). Subsequently, the intensity of the recordings was linearized in order to cover the entire dynamic range. Finally, every video was analyzed frame-by-frame while tracking the displacement of the particle in every image.

However, no comparison between individual images was made, yet each frame was effectively treated independently of its preceding one. Here, two techniques for extracting the displacement of a particle in individual frames are presented, both finally yielding its time-dependent trajectory. Specifically, these represent a fitting routine (Figure 4.4B) and an image shift algorithm (Figure 4.4C) as discussed in detail in the following.

Fit method

A simple method for tracking the displacement of a trapped particle is principally given via a fitting routine (Figure 4.4B). Here, the specific aim is to approximate the particle's intensity distribution in every frame via a jinc-function (see Equation 2.13a) added on top of a non-zero static background. In general, this approach is very fast and yields decent results in case the intensity profile allows for a simple description. One advantage, in particular, is given by the possibility to describe non-rotational symmetric profiles. A main drawback, on the other hand, represents the inaccuracy or even failure to retrieve the displacement if the particle is located close to the border or partially leaves the frame. Compared to other routines, however, the final trajectories are more prone to noise.

Shift algorithm

One alternative to retrieving trapped particle motion via the fit method represents the implementation of an image shift algorithm (Figure 4.4C). This technique principally relies on the application of a sub-pixel shift Δx to each frame $I(x)$ in real space via the multiplication of a linear phase in the Fourier domain. The displacement $x + \Delta x$ of the particle is then varied while minimizing the deviation to the mirrored image $I(-x)$ ^[44,45,131]:

$$I(x + \Delta x) = \mathcal{F}^{-1} \left\{ \mathcal{F} \{I(x)\} e^{-2\pi i k \Delta x} \right\} \quad (4.1a)$$

$$\Delta x = \min_{\Delta x} \left\{ [I(x + \Delta x) - I(-x - \Delta x)]^2 \right\}. \quad (4.1b)$$

Here, \mathcal{F} denotes the Fourier transformation and k the grid of the transformed image in the Fourier space. This method principally benefits from its robustness and yields a very high accuracy with sub-pixel precision, which effectively allows for combining the centered image stack into one high resolution image of the particle that represents the entire video.

For example, this allows for analyzing the size of a particle (Figure 4.4F) in comparison to reference images taken via scanning electron microscopy (SEM). A main drawback, however, results from the comparison of a frame to its inverse, which specifically requires a high degree of symmetry of the particle in every frame.

Pixelation

If the images are poorly adjusted in contrast, e.g., due to excessively high NA illumination (Figure 4.3D), the effect of pixelation occurs (Figure 4.4D). Here, the information contained within the relevant pixels is not sufficient and the retrieved particle displacement tends to integer values (Figure 4.4E). In particular, this also occurs if the static background within each image is subtracted via the minimum of every pixel across all frames. Nevertheless, since the previous fitting routine is more prone to pixelation, the image shift algorithm was applied within all experiments. Once adjusted, the tracking algorithm then reliably yields the final trajectory of a trapped particle (Figure 4.4G).

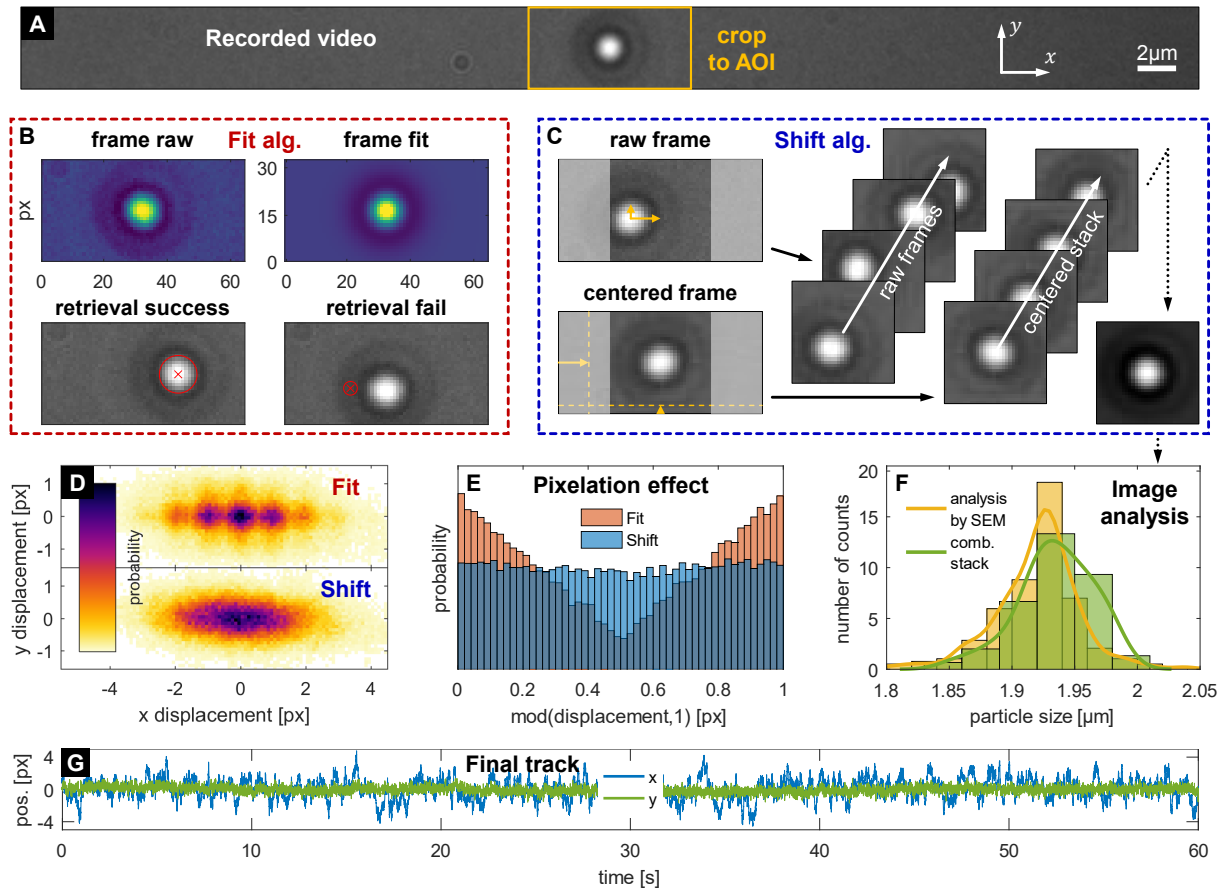


Fig. 4.4. Tracking algorithms for retrieving trapped particle motion. (A) Recorded videos are cut to an area of interest (AOI) that contains relevant information about the particle. (B) A fit of its intensity profile represents a simple and fast method, however, it yields inaccurate results. (C) A trapped $2\ \mu\text{m}$ silica bead is tracked via shifting each frame until maximum symmetry is reached (see main text). (D–E) In contrast to pixelized fitting results, this yields sub-pixel accuracy. (F) Example of combining the centered stack into one high resolution image representing the entire video (bottom right in C) for subsequently analyzing particle size, which is in perfect agreement with scanning electron microscopy (SEM). (G) Final trajectory of a trapped bead.

4.2 Analysis of fiber trap performance

Determining its stiffness κ , which represents a key quantity for a comparison (details see section 3.3), essentially plays an important role when analyzing the performance of a particle trap. Various different techniques exist for verifying the trapping of a particle from its previously obtained time-dependent trajectory $x(t)$ principally exist. In general, these can be categorized into purely spatial (subsection 4.2.1) and tempo-spectral techniques (subsection 4.2.2), as presented and discussed within detail in the following.

4.2.1 Purely spatial techniques

One straight-forward approach for determining the stiffness κ of a trap effectively relies on directly observing the trapping force F_{trap} or the displacement Δx of a trapped particle via, e.g., the Stokes drag force method or a quadrant photo diode (QPD)^[95,99,117]. The prior, in particular, relies on applying an external force F_{ext} to the particle via, e.g., a viscous flow that displaces the sample. A large displacement $\Delta x = x - x_0$ of the particle from its equilibrium x_0 in response to the applied external force F_{ext} can thus directly be measured, which hence determines the stiffness κ of the trap. However, this procedure easily suffers from external influences that distort the sensitive motion of the particle and also does not allow for detailed investigation of neither particle nor medium^[99].

A QPD, on the other hand, represents a reliable and accurate alternative to the previously discussed concept of image-based particle tracking. Here, the displacement of a particle (commonly in the order of a few ten nanometers) is effectively measured via the interference of a laser beam that is incident onto its surface. Subsequently, the beam is scattered into one of the four quadrants of the QPD, which effectively allows for immediately determining the displacement of the particle within the trap.

Equipartition

Analyzing the retrieved displacement $\Delta x = x - x_0$ of a trapped particle from its equilibrium (Figure 4.5A) via a histogram, in particular, yields its local distribution (Figure 4.5B). This principally allows directly obtaining the underlying trap potential $U(\Delta x)$ (Figure 4.5C) by a Boltzmann distribution (Equation 3.3). Here, the variance $\langle(\Delta x)^2\rangle$ of displacement inside a harmonic potential $U(x) = \kappa x^2/2$ is related via the equipartition theorem^[95,99,117]:

$$\frac{1}{2}\kappa\langle\Delta x^2\rangle = \frac{1}{2}k_{\text{B}}T. \quad (4.2)$$

Determining the stiffness κ of the trap via this technique, however, only yields reliable and accurate results if its potential $U(\Delta x)$ is nearly harmonic and the particle is trapped long enough to satisfy statistics via covering the entire effective region of the trap.

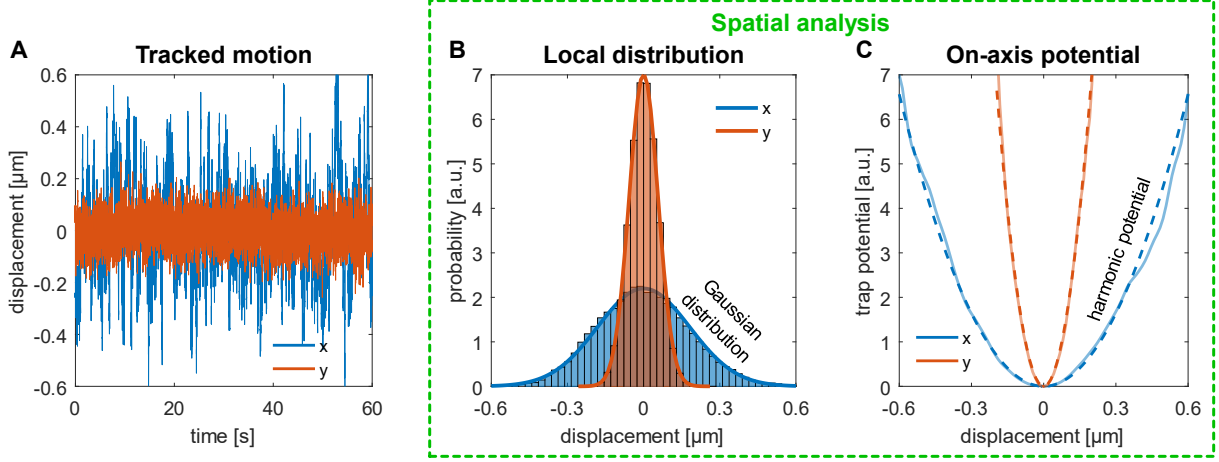


Fig. 4.5. Spatial analysis of tracked motion of a trapped particle. (A) Tracked motion of a particle inside a fiber-based optical trap in water. (B) Local distribution of A, where the variance of the displacement yields the stiffness κ of the trap. (C) On-axis trap potential of B obtained via a Boltzmann distribution. The trap potential is nearly perfectly harmonic due to the Gaussian distribution of the particle displacement.

4.2.2 Tempo-spectral methods

In general, the previously presented spatial techniques are limited to information that is directly accessible. A time (for details see section 3.2) or frequency domain-based analysis of the particle trajectory $x(t)$, however, effectively represents a sophisticated approach usually revealing more details about its motion and behavior within the trap.

Autocorrelation

A correlation of the time-dependent displacement $\Delta x(t)$ of a particle with itself for later times $t + \Delta t$ represents a simple technique for analyzing its behavior within the trap^[132]:

$$\langle \Delta x(t + \Delta t) \Delta x(t) \rangle = \frac{k_B T}{\kappa} e^{-|\Delta t|/\tau_c} \quad \text{with} \quad \tau_c = \frac{k_B T}{\kappa D}. \quad (4.3)$$

In principle, this directly yields the trap stiffness κ , where τ_c denotes the mean lifetime of confinement (or trap relaxation time) that is related to the diffusion D of the particle. Figure 4.6A exemplarily demonstrates this for the previously tracked trajectory $x(t)$ of a trapped particle (Figure 4.5A). In particular, the motion is correlated for large delays Δt , which is represented via the exponential decay of the autocorrelation.

Mean square displacement

The mean square displacement (MSD) of a trapped particle (see section 3.2), however, yields information about temporal processes. This specifically allows identifying external forces^[81,96,97] and is displayed in Figure 4.6B (log.-log. plot) for the previous example:

$$\langle (\Delta x(\Delta t))^2 \rangle = 2D\tau_c (1 - e^{-\Delta t/\tau_c}) + \varepsilon^2. \quad (4.4)$$

Here, ε^2 denotes experimental noise that results from the computer-based recording and the finite precision in retrieving the trapped particle motion. Specifically, the MSD exhibits a linear slope $\sim 2D\Delta t$ for short lag times Δt that is proportional to the displacement of the particle via the free diffusion D . On long timescales, however, this behavior saturates into a plateau $\sim 2D\tau_c = 2k_B T/\kappa$, which effectively describes the confinement inside the trap and thus directly yields its stiffness κ .

Power spectrum

In contrast to the previously discussed MSD of a trapped particle, however, the power spectrum (PS) of a trajectory is obtained via its Fourier transformation \mathcal{F} . In principle, this yields information about the spectral repetition of occurrences^[132–134]:

$$P_{\text{Lorentz}}(f) = |\mathcal{F}\{x(t)\}|^2 = \frac{2D/(2\pi)^2}{f_c^2 + f^2} + \varepsilon^2 \quad \text{with} \quad \frac{1}{2\pi f_c} = \tau_c. \quad (4.5)$$

Theoretically, a power spectrum is described via an ideal Lorentzian profile with f , the frequency, and $f_c = \kappa D/(2\pi k_B T)$, the corner frequency at which a PS drops to $P(f) = 1/2$. This is visualized in Figure 4.6C for the previously retrieved displacement of a trapped particle (Figure 4.5A) and allows determining the stiffness κ . Specifically, the PS exhibits a $1/f^2$ spectral dependence, which equivalently to the MSD represents the random Brownian noise of the particle that is proportional to its free diffusion D . Here, the confinement within the trap is represented by a plateau $\sim 2D/(2\pi f_c)^2$ on the low frequency side of the spectrum. Again, ε^2 denotes an experimental noise error.

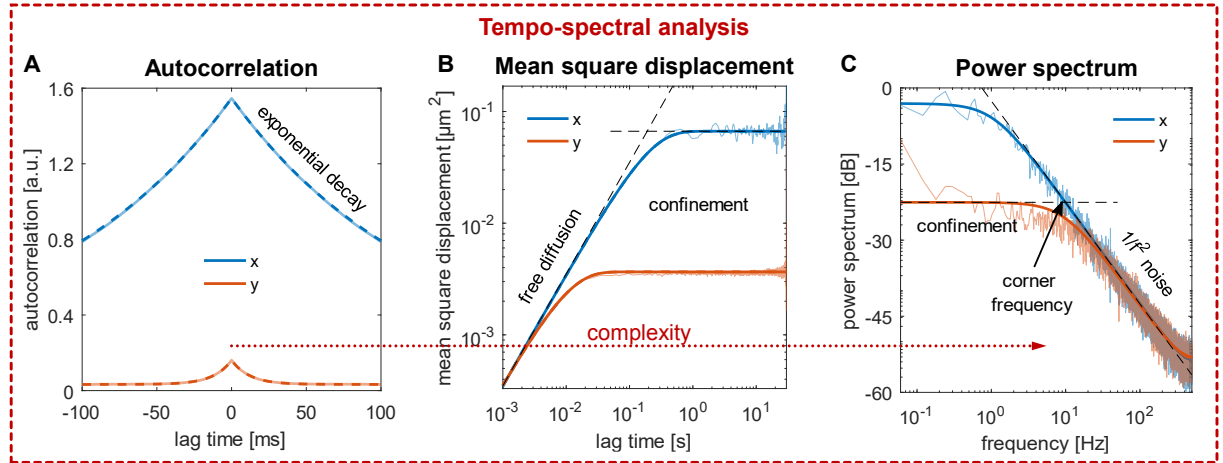


Fig. 4.6. Tempo-spectral analysis of trapped particle motion. (A) Autocorrelation of the previously tracked motion of a trapped particle. The exponential decay describes the correlated motion for large temporal delays, which yields the stiffness κ of the trap. (B) Log.-log. plot of the mean square displacement (MSD) for the same trajectory. The particle displacement is freely diffusive for short lag times and saturates into a plateau on long timescales. This describes the confinement within the trap and yields the stiffness κ . (C) Log.-log. plot of the power spectrum (PS) of the trajectory, where the motion is confined within the trap for low frequencies and freely diffusive otherwise. The PS drops to $1/2$ at the corner frequency, which yields the trap stiffness κ .

Influence of errors

In principle, the previously introduced tempo-spectral methods for analyzing the trap stiffness κ increase within their complexity in Figure 4.6, A to C. While the autocorrelation, in particular, represents a simple and robust technique, frequency domain methods, on the other hand, such as, e.g., the power spectrum (PS), specifically, are more prone to errors. Here, noise in general, systematic errors (bias) as well as acquisition errors (alias and motion blur) distort the signal^[134,135] and are discussed in detail in the following.

Systematic errors

Applying least sum of squares (LSQ) fitting to experimental data in principle only yields correct results if errors are normally distributed^[134–136]. However, since experimental data is usually correlated, this yields a biased fit (Figure 4.7A). The correlation of MSD data, in particular, results from the fact that each data point within a certain lag time Δt_i is counted multiple times for different lag times Δt_j . Nevertheless, this is directly to account for via including fit weights $w_i = 1/i$, since the i^{th} lag time consists of i_{max}/i correlated data points^[81]. Describing correlated PS data, however, is more complicated.

One solution to correct for normally distributed errors, in particular, represents compressing the data prior to fitting. Therefore, in principle different methods exist, however, all rely on grouping the data into separate bins or blocks. While for binning, a number of N subsequent points is averaged into one bin, for blocking, in contrast, the entire data is first split into a number of N blocks, followed by averaging into one compressed block. Nevertheless, this results in compressed data of length $L = i_{\text{max}}/N$ in both cases.

A particular advantage of blocking over binning is that, e.g., subsequent blocks are allowed to overlap to prevent spectral leakage at their intersects (Welch’s method)^[134,137]. Here, this is applied to all experimental data first, and the compressed data is subsequently fitted via minimizing a bias-free maximum likelihood estimate (MLE)^[134–136]:

$$\chi^2 = \min_f \sum \left(\frac{P_{\text{exp}}(f)}{P_{\text{fit}}(f)} + \log P_{\text{fit}}(f) \right), \quad (4.6)$$

where χ^2 denotes the fit residuals, $P_{\text{exp}}(f)$ a measured PS, and $P_{\text{fit}}(f)$ its desired fit.

Acquisition errors

Since a PS generally deviates from its ideal Lorentzian shape (Figure 4.7B), further correction terms need to be included within the fit. Finite sampling, e.g., leads to aliasing, where thermal noise $f > f_{\text{Nyq}} = 1/(2\Delta t)$ (the Nyquist frequency) is perceived as lower frequencies that contribute to the PS^[132–134]. Moreover, motion artifacts arise from the finite camera exposure, averaging the displacement of a trapped particle over the exposure

time τ_e and thus blurring the obtained image. Within the MSD, in particular, this is straight-forwardly to accounted for via an additional error ε^2 visible in the bottom left corner. The influence of image acquisition and blur on a PS, however, is given via^[132–134]:

$$P_{\text{alias}}(f) = \sum_{n=-\infty}^{\infty} P(f + 2nf_{\text{Nyq}}) \quad (4.7a)$$

$$P_{\text{blur}}(f) = P(f) \text{sinc}^2(\pi f \tau_e). \quad (4.7b)$$

Figure 4.7C reveals motion blur as the main error source particularly at high frequencies.

Overall reliability

Infinite compression, however, asymptotically yields a perfect fit for only two data points. Figure 4.7D shows the behavior of the fit parameters f_c , D , the resulting stiffness κ , and the error χ^2 for fitting single power spectra. Here, a compression of eight blocks represents the best trade-off between a minimum χ^2 while keeping the entire power-dependent data set^[45,138] in agreement (Figure 4.7E), thus being applied to all following data.

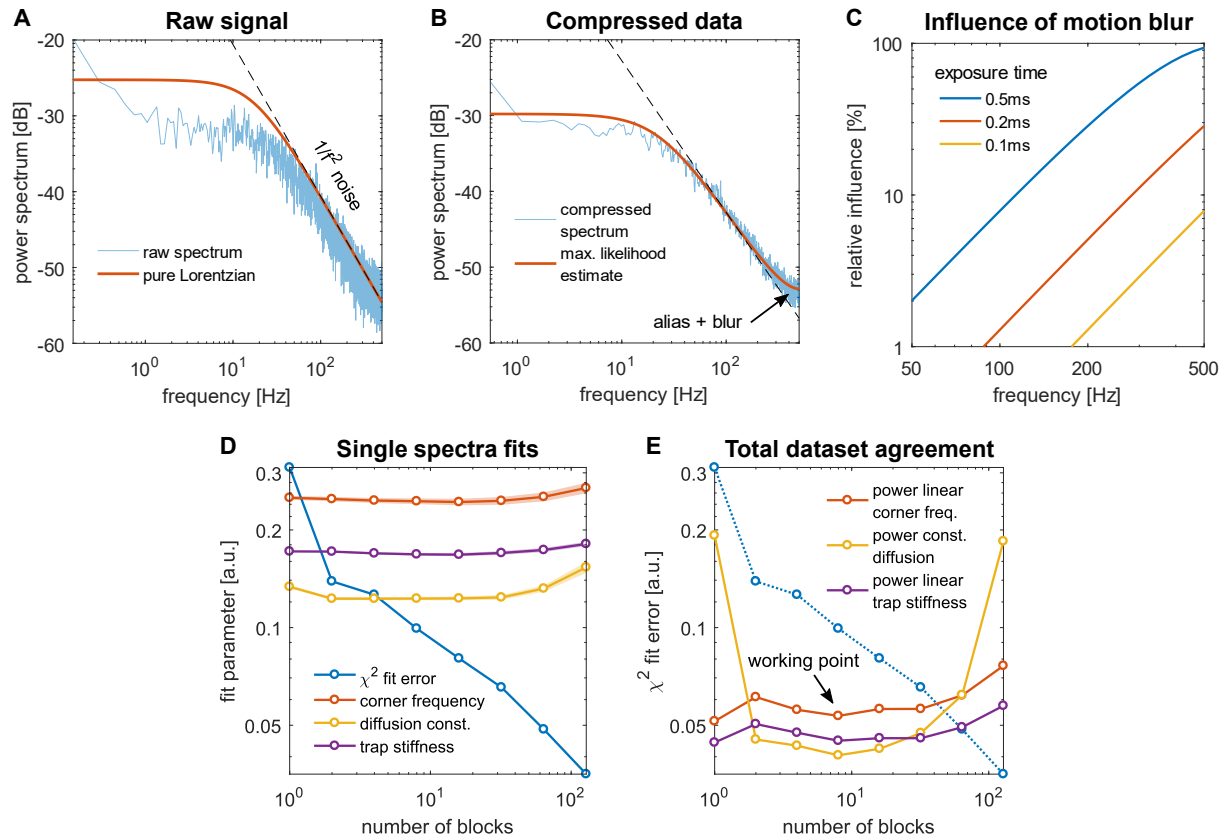


Fig. 4.7. Influence of systematic and acquisition errors on the reliability of spectral analysis results. (A) Fitting a power spectrum (PS) using a least-squares routine yields inaccurate results due to correlated experimental data. (B) To obtain reliable results, the data is compressed and fitted using a maximum likelihood estimate (MLE, for details see main text). (C) Motion blur is the main error influence particularly at high frequencies. (D) Data compression reduces the error of the fit without significantly affecting its parameters. (E) Here, compression via eight blocks yields the best agreement within the entire power-dependent data set.

Dual fiber focus trap

After the necessary prerequisites for analyzing trapped particles and fiber-based traps were introduced before, this chapter focuses on the concept of a dual fiber optical trap. In contrast to a single fiber solution, which in principle exhibits the highest flexibility but bears only few options for adjustment, the simplest approach, from a fabrication point of view as well, relies on using two optical fibers^[60,61,64]. This allows the compensation of axial scattering forces, while effectively enabling applications such as optical micro-manipulation of trapped cells^[64–66] as well as fiber-based Raman spectroscopy^[62].

The dual fiber focus trap presented in this chapter represents a special type of dual fiber trap based on two nanobore fibers (NBFs). Specifically, these exhibit a central channel (bore) inside their core, yielding a focal spot in front of each facet (Figure 5.1, compare refs. [45, 57]). Ideally, both foci are brought to overlap within the optical trap, which effectively represents the key advantage of this hybrid fiber-based (see subsection 2.1.2) particle trap over the diverging beams found within regular dual fiber traps.

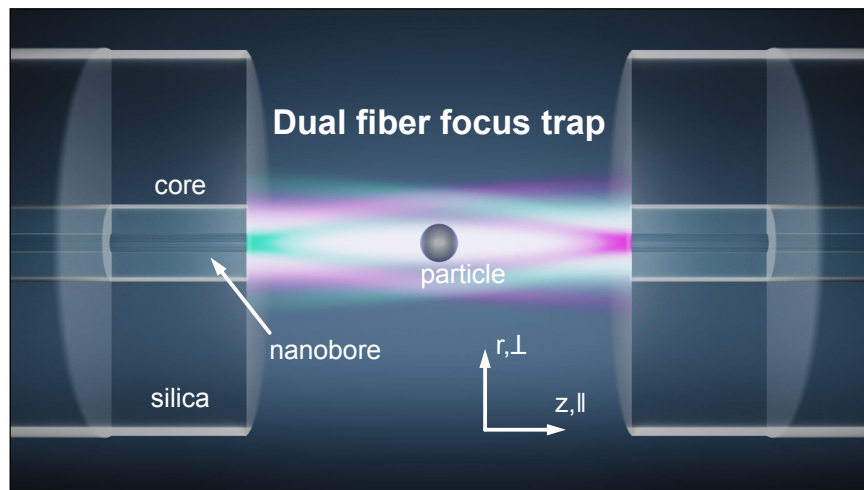


Fig. 5.1. Artistic illustration of a dual fiber focus trap in water (compare ref. [45]). The concept relies on two identical nanobore fibers with counter-propagating beams. Each beam exhibits a focus due to a central bore inside the fiber core. Optical trapping of a particle in the center is greatly enhanced if both foci overlap.

Within this chapter, first, an individual nanobore fiber is characterized (section 5.1), followed by estimating the dual fiber focus trap performance compared to a regular dual beam fiber trap (section 5.2). Finally, optical trapping of individual objects is experimentally demonstrated, analyzed, and compared (section 5.3).

5.1 Fiber characterization

For a detailed characterization of the dual fiber focus trap, first, the beam emitted by an individual fiber is analyzed. Here, its profile is spatially recorded via a fluorescence measurement, followed by estimating its numerical aperture (NA) being of particular importance within optical trapping. Finally, the emitted light is spectrally analyzed in order to determine the optimum operating wavelength of the dual fiber focus trap.

5.1.1 Spatial analysis

The key difference between the previously introduced nanobore fiber (NBF) and a conventional step-index single-mode fiber (SMF) is the presence of a central channel (bore) inside the core of the NBF that runs along its entire length^[4,53,55]. Figure 5.2A presents a scanning electron microscope (SEM) image of the cross-section of an NBF used throughout all experiments (compare ref. [45]). Here, the diameter of the core approximately yields $2a = 3.4 \mu\text{m}$, the outer diameter of the fiber is $180 \mu\text{m}$, the inner diameter of the central channel yields $2b = 0.7 \mu\text{m}$, and the fiber exhibits a refractive index contrast of $\Delta n = 8 \cdot 10^{-3}$ between the core and the cladding.

Fundamental mode diffraction

The unique geometry of the NBF effectively results in a fundamental mode that is notably different from the one obtained from a conventional SMF. In contrast to an HE_{11} mode (see Figure 2.1), in particular, the fundamental NBF mode exhibits a central minimum as a result of the evanescent field that leaks into its channel. Figure 5.2B exemplarily illustrates the calculated fundamental mode profile for a wavelength of $\lambda = 635 \text{ nm}$. The donut-shaped mode of the NBF, specifically, enables certain applications such as the detection of nanoparticles^[4], excitation of surface plasmons within metallic wires^[55], absorption spectroscopy of liquids^[53] as well as trapping of individual particles (compare ref. [45]), which is within the scope of this work.

Here, its application effectively relies on the diffraction (see subsection 2.2.2) of the donut-shaped fundamental mode. Upon freely propagating along the optical axis z , the central minimum vanishes, and the mode diffracts into a focal spot after approximately $z_f \approx 7 \mu\text{m}$ in water. After a total distance of $z \approx 16 \mu\text{m}$, however, the beam focus completely transforms into a Gaussian profile with a subsequent divergence equivalent to the beam of a conventional SMF (compare refs. [45, 57]). Figure 5.2C exemplarily shows the diffracted donut-shaped NBF mode in water, which was calculated using the beam propagation method (BPM, see section 2.2.2). A qualitative explanation, for example, relies on two laterally separated (by the channel diameter $2b$) parallel Gaussian beams that interfere after a certain distance z of propagation [57].

Experimental verification

In order to experimentally verify the calculated beam profile displayed in Figure 5.2D, the beam of the NBF was recorded via the emission of a fluorescent dye^[57]. Specifically, a continuous wave (CW) laser at a wavelength of $\lambda_{\text{ex}} = 532 \text{ nm}$ was used for exciting its fundamental mode, effectively reaching an optical power of $P_1 = 50 \text{ mW}$ at the output of the NBF. For the recording, an amount of 2 mg of the fluorescent dye Rhodamine 6G (R6G, Sigma Aldrich R4127) was dissolved in 10 ml of ultra-pure water, resulting in a final concentration of 200 ppm while ensuring unsaturated fluorescence.¹

For confining the dye solution, a reservoir was created via two parallel strips of double sided tape on a microscope slide and subsequently sealed with a coverslip. This effectively left a small channel into which the NBF was inserted, while ensuring a flat interface for observation. A few hundred microliters of the fluorescent solution were pipetted onto the sample slide and retracted into the channel via capillary forces. Here, scattered laser light was blocked using a notch filter (Thorlabs NF533-17), and the unsaturated fluorescent emission at a wavelength of $\lambda_{\text{em}} = 590 \text{ nm}$ was finally recorded with a custom-built optical microscope (see Figure 4.2) as illustrated in Figure 5.2E.

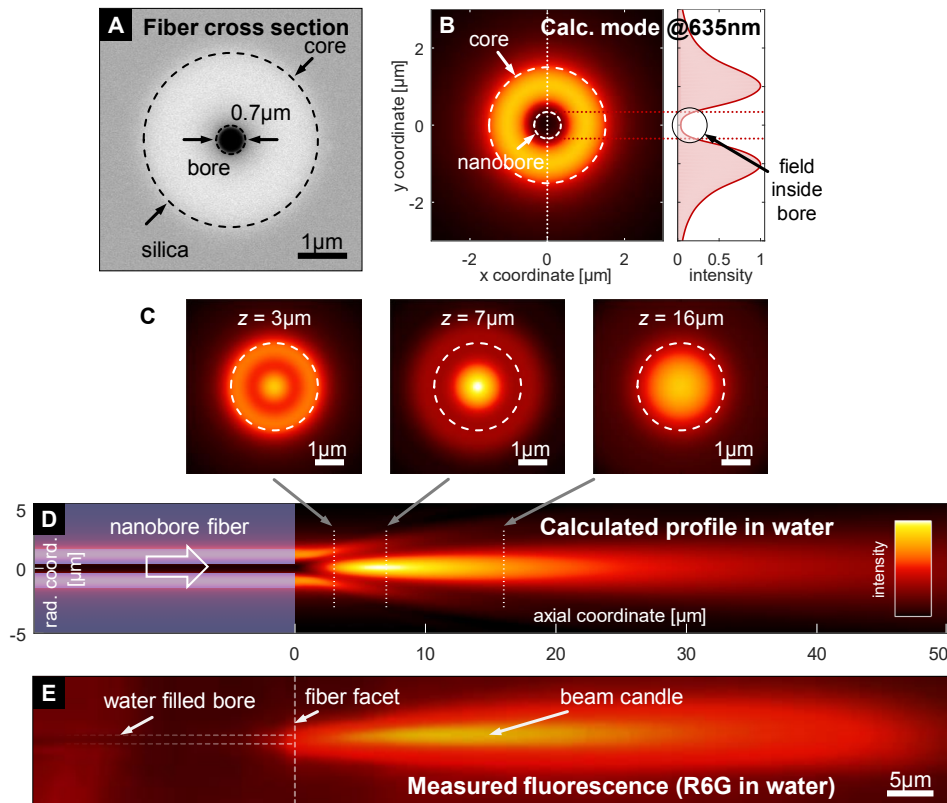


Fig. 5.2. Fundamental mode and beam profile of a nanobore fiber (NBF) in water at a wavelength of 635 nm. (A) Scanning electron microscope (SEM) image of the cross-section of an NBF exhibiting a central bore inside its core. (B) Calculated profile of the fundamental mode. An evanescent field leaks into the bore, yielding the central minimum. (C–D) Propagation of the calculated fundamental mode. The minimum vanishes after 3 μm, diffracts into a focal spot (7 μm), and the beam diverges similar to a Gaussian beam 16 μm behind the facet of the NBF. (E) Recorded beam via the unsaturated fluorescence¹ of the dye Rhodamine 6G (R6G).

¹Ensures that fluorescent emission scales linearly with excitation intensity.

The measured beam of the NBF (Figure 5.2E) effectively exhibits a profile very similar to the one of a candle^[57], while being qualitatively in line with the calculation. In order to estimate its NA, here, the calculated profile (Figure 5.2D) was fitted to the equations describing a diffraction limited focal spot (see Equations 2.13a and 2.13b). For water at a wavelength of $\lambda = 635$ nm, this specifically yields $NA = 0.25$. This procedure is in principle justified, since the NBF represents a hybrid SMF (see subsection 2.1.2) that emits a diffraction limited beam (see subsection 2.2.2).

5.1.2 Spectral analysis

To determine the cut-off wavelength of the fundamental mode of the NBF (see subsection 2.1.1), its spectral response was measured under the influence of bending^[139] (Figure 5.3A). In principle, this procedure relies on the fact that weakly guided fiber modes (normalized frequency of $V < 2.405$) are associated with a low refractive index contrast between the core and the cladding and are thus more susceptible to bending loss. This specifically yields a rapid decrease of the loss within the regime of multi-mode guidance ($V > 2.405$) that appears in the recorded optical spectrum^[139] (Figure 5.3B).

For measuring the spectral response of the NBF, the fiber was excited using a broadband super continuum laser (NKT Photonics SuperK Compact) that emits a wavelength range of $\lambda = 440 \dots 2150$ nm. Here, an optical power of $P_1 = 7.75$ mW at a wavelength of $\lambda = 532$ nm was reached at the fiber output. An optical post of 1" diameter was used to loop the NBF around, and its response to bending was subsequently measured using a spectrometer (Ando AQ-6315). Figure 5.3 illustrates the obtained bending spectra, revealing that a wavelength of $\lambda = 635$ nm lies well within the regime of single-mode guidance for ensuring a fundamental mode operation of the dual fiber focus trap.

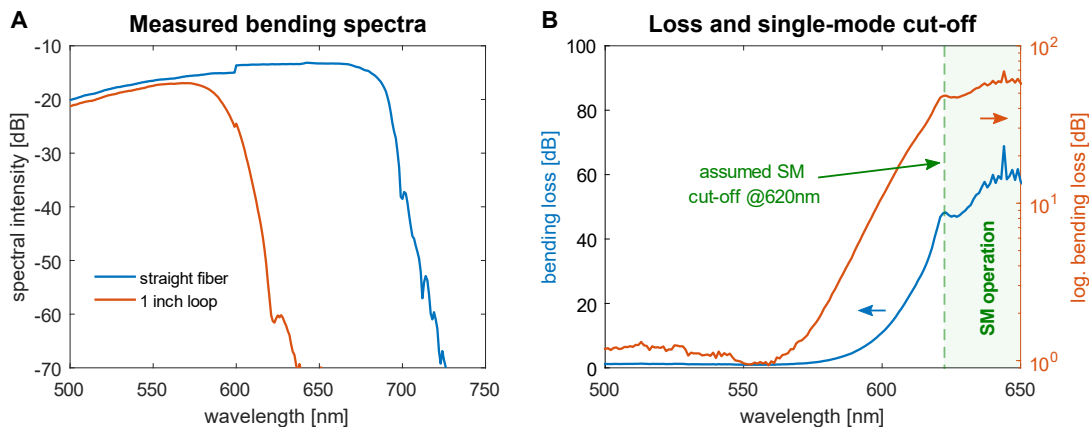


Fig. 5.3. Measured loss as a function of wavelength, obtained from bending the nanobore fiber (NBF) to determine its single-mode (SM) cut-off. (A) Spectral response to bending the NBF around an optical post of one inch diameter. (B) Resulting loss in linear (left) and logarithmic scale (right). The exponential slope denotes the transition to multi-mode guidance within the NBF, yielding its SM cut-off. This effectively ensures a fundamental mode operation of the dual fiber focus trap at a wavelength of 635 nm.

5.2 Tunable optical trapping

A common motivation for a dual fiber optical trap in general results from the fact that the individual fiber beams exhibit NAs that are insufficient for optical trapping on their own (see subsection 3.3.1). Figure 5.4A exemplarily demonstrates a dual fiber trap with counter-propagating beams^[60,61,64], which effectively represents the basis for the previously introduced dual fiber focus trap (compare ref. [45]). Here, a polystyrene bead of diameter $2R = 1.75 \mu\text{m}$ was optically trapped in the center between two nanobore fibers (NBFs) within an aqueous solution (see subsection 4.1.1) at a low power of $P_{1,2} = 7.5 \text{ mW}$ measured at their respective outputs. The NBFs individually exhibit numerical apertures of 0.25 (see previous section) that are insufficient for optical trapping with a single fiber alone, however, in combination effectively allow the compensation of optical forces $\vec{F}_{\text{opt}}(r, z)$ along the radial (r) and particularly the axial direction z .

Using two optical fibers, in addition, opens up the possibility of tuning the trap, which effectively represents a key advantage over an optical trap that is based on only a single fiber. Here, a straight-forward adjustment relies on varying the distance d between both fibers (as well as controlling their individual powers $P_{1,2}$), being also achievable with conventional single-mode fibers (SMFs)^[45,60,140]. Another option for tuning the dual fiber trap involves changing their inclination^[43,60,138], however, this requires their displacement as well in order to maintain a stable equilibrium in the center between both fibers and is (as well as individually adjusting their powers $P_{1,2}$) thus not considered here.

In the following, two different implementations of dual beam fiber traps that are specifically based on (i) two identical commercial SMFs and (ii) the previously introduced NBFs are compared in detail. First, a qualitative description of the trap tunability is given (subsection 5.2.1), followed by approximating their performance via a semi-analytical model (subsection 5.2.2). Finally, a rigorous full numerical simulation of the trap performance using finite element methods (FEMs) is presented (subsection 5.2.3).

5.2.1 Qualitative description

Figure 5.4, B and D, illustrates the calculated intensity $I_0(r, z)$ of the beam that is emitted by a commercial SMF (Thorlabs SM450, core diameter $2a = 3 \mu\text{m}$) and its profile $I_0(z)$ along the optical axis z ($r = 0$). Here, the monotonous near Gaussian intensity distribution stands in direct contrast to the beam of the NBF (core diameter $2a = 3.4 \mu\text{m}$, bore diameter $2b = 0.7 \mu\text{m}$), which exhibits a non-monotonous profile $I_0(z)$ along z . This is visualized in Figure 5.4, C and E, and results from the previously discussed diffraction of the fundamental mode that yields the focal spot. Specifically, both profiles were calculated for water at a wavelength of $\lambda = 635 \text{ nm}$ and normalized to the maximum intensity of their respective outputs (Figure 5.4, B and C).

A key advantage of the dual fiber focus trap concept over using two conventional SMFs, in particular, represents the possibility to overlap both NBF foci. Specifically, this allows adjusting the performance of the dual fiber trap via their interplay and thus to address different independent combinations of radial and axial confinement (compare ref. [45]) for controlling the behavior of a trapped particle inside. However, generally not the sum $I_+ = I_1 + I_2$ of the individual counter-propagating beam intensities $I_{1,2}$ but rather their difference $I_- = I_1 - I_2$ is of importance. A particle is effectively trapped where the difference $I_-(r, z)$ between both fiber beams vanishes and the resulting optical forces $\vec{F}_{\text{opt}}(r, z)$, i.e., the axial scattering force $\vec{F}_{\text{scat}}(z)$ (see Equation 3.8) along z , are balanced (Figure 5.4A). For example, this allows the creation of multiple variable trapping sites using, e.g., a standing wave or sophisticated beam profiles^[108,110,121].

Within a dual fiber trap of two identical optical fibers that are axially separated by the distance d , while both exhibit monotonous profiles of their individual beam intensities $I_0(r, z)$, in general only one stable trapping site in the center between both fibers at $z_0 = d/2$ exists (given they emit the same powers $P_{1,2}$). Figure 5.4, F and G, displays the intensity difference $I_-(r, z)$ for two counter-propagating beams (gray arrows) emitted by the fibers within a dual fiber trap for the example of (i) two commercial SMFs (Figure 5.4F) and (ii) two NBFs (Figure 5.4G) separated at different inter-fiber distances d . Here, the intensity $I_1(r, z - z_0)$ of the beam emitted by the left fiber ranges linearly from white (zero) to cyan (maximum) and the intensity of the right fiber beam $I_2(r, z_0 - z)$ from white to magenta. This results in a blue tone where the intensities $I_{1,2}(r, z)$ of both beams and hence the resulting optical forces $\vec{F}_{\text{opt}}(r, z)$ are balanced, thus indicating the region of stable confinement within the trap.

Controlling the separation distance d between both fibers in principle represents a simple concept to dynamically adjust the optical potential of the dual fiber trap, while the final performance mainly depends on a steep gradient of the dual beam intensity profile. Decreasing the distance d in a dual SMF trap (Figure 5.4F), in particular, yields a monotonous increase of the optical trap performance, although a single SMF effectively exhibits a negative NA due to its diverging Gaussian beam (Figure 5.4D). The calculated beam profile of a single NBF, in contrast, previously revealed $\text{NA} = 0.25$ for the focal spot located approximately $z_f \approx 7 \mu\text{m}$ in front of the fiber facet (Figure 5.4E).

Overlapping both NBF foci (Figure 5.4G) increases the NA of the dual fiber trap significantly, which effectively represents a key advantage of the dual fiber focus trap over a dual SMF trap especially at short inter-fiber distances d . Here, the optimum separating distance d between two NBFs in principle lies at $d_{\text{opt}} = 2z_f$. Fitting the resulting intensity distribution of the two counter-propagating NBF beams to Equations 2.13a and 2.13b for an inter-fiber distance of $d_{\text{opt}} = 14 \mu\text{m}$ yields a maximum effective NA of 0.36 for the dual fiber focus trap. Again, the calculation assumes water as the immersion medium and an operating wavelength of $\lambda = 635 \text{ nm}$.

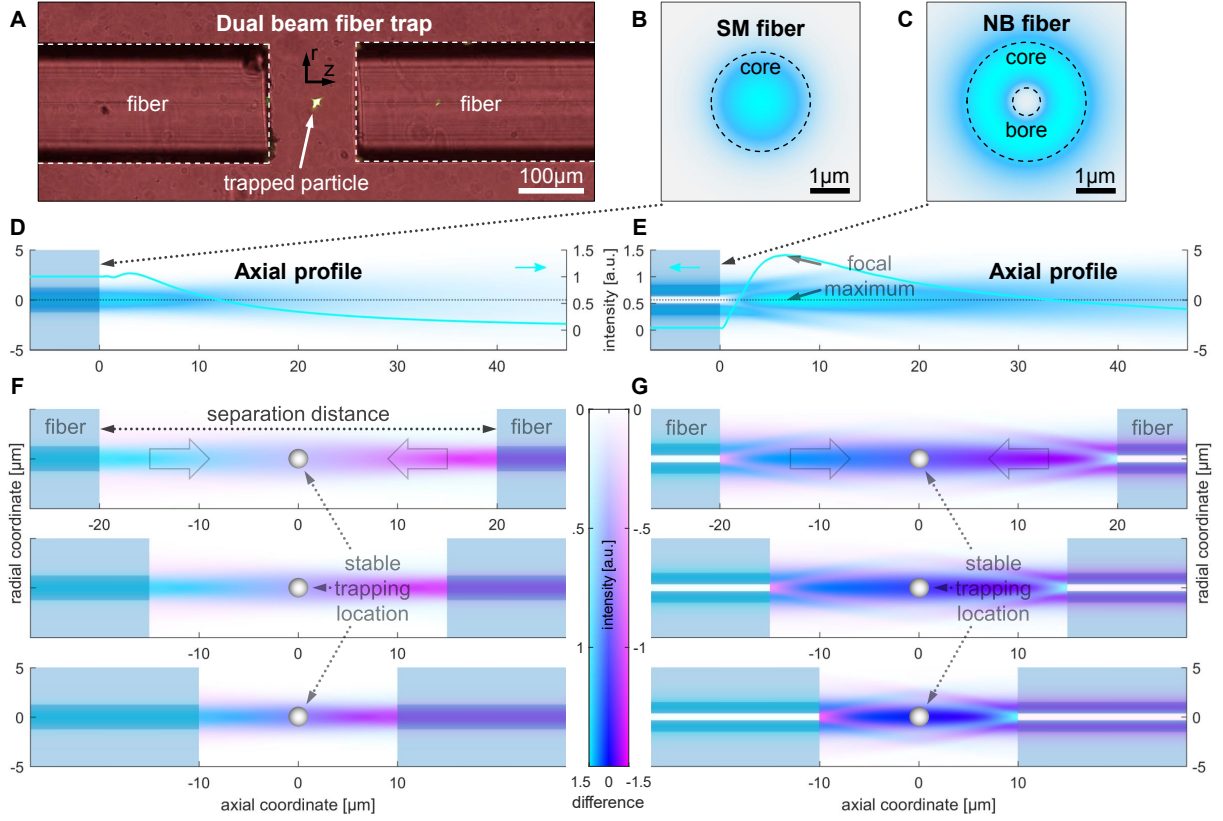


Fig. 5.4. Implementation and tuning of a dual beam fiber trap in water at a wavelength of 635 nm. (A) Micrograph of a dual fiber trap with counter-propagating beams. A polystyrene bead of $1.75\ \mu\text{m}$ diameter is optically trapped in the center between both fibers. (B) Calculated intensity of the fundamental mode and (D) of the beam emitted by a commercial SMF, exhibiting a monotonous near Gaussian profile. (C,E) Same for the NBF exhibiting a non-monotonous beam intensity profile due to the diffraction of its fundamental mode, yielding a focal spot $7\ \mu\text{m}$ in front of the fiber. (F–G) Intensity difference of two counter-propagating beams (gray arrows) based on D and E for different fiber separations. The left beam intensity ranges from white to cyan and the right one from white to magenta. Optical trapping is stable where the difference vanishes (blue).

5.2.2 Semi-analytical model

In the previous subsection, only a qualitative analysis of the performance and tunability of a dual fiber trap was carried out. As this procedure is principally limited in its amount of detail, the key quantity for comparison, the stiffness κ , still remains unknown. In the following, a model for computing the tuning capability of the optical trap and its stiffness κ is thus presented, which, however, still relies on an approximation.

A key advantage of a semi-analytical model over a rigorous full numerical analysis via, e.g., a finite element method (FEM) simulation is apparent in its reduced computational effort. In particular, this is achieved via considering only specific on-axis scenarios in the Rayleigh approximation^[12,95] and, subsequently, extending them to the macroscopic case via one-dimensional integration (similar to Equation 3.9), thus significantly minimizing computational duration. Here, specifically the scenarios of inter-fiber distances $d = 50, 40, 30, 20, 10\ \mu\text{m}$ for a dual fiber trap were treated, while the results for two NBFs of the dual fiber focus trap are exemplified by graphs in Figure 5.5, A to D.²

²Beam intensities $I_0(r, z)$ again calculated for water immersion at a wavelength of $\lambda = 635\ \text{nm}$.

Model limits

Describing the performance of an optical trap for a confined particle requires considering optical gradient (\vec{F}_{grad}) and scattering (\vec{F}_{scat}) forces (see Equations 3.7 and 3.8). Their analytical validity, however, is only given within the Rayleigh regime for nanoscopic particles much smaller than the wavelength of operation^[12,95]. Treating macroscopic particles much larger than the operating wavelength, such as the $2R = 2\ \mu\text{m}$ silica beads used within the experiments (see subsection 4.1.1 and section 5.3), in the Mie regime, on the other hand, effectively requires a rigorous numerical calculation that is based on, e.g., an FEM simulation (subsection 5.2.3). Nevertheless, the forces retain their proportionality and directly scale with the incident intensity $I_0(r, z)$.

Radial confinement

The only contributing optical force \vec{F}_{opt} for stable confinement within a dual fiber trap along the radial direction r in the center between both fibers at $z_0 = d/2$ in principle represents the radial gradient force $\vec{F}_{\text{grad}}(r, z_0)$. For a point dipole^[95,117], this force is proportional to the gradient ∇_r of the total intensity $I_+(r, z_0) = I_1(r, z_0) + I_2(r, z_0)$ that results from the sum of the two individual counter-propagating beam profiles. The on-axis optical potential $U_{\text{opt}}(r, z_0)$ is thus proportional to the integral over the gradient force $\vec{F}_{\text{grad}}(r, z_0)$ in the center of the trap at z_0 and hence directly proportional to twice the intensity $2I_0(r, d/2)$ of the beam emitted by a single fiber:

$$U_{\text{opt}}(r, z_0) = - \int \vec{F}_{\text{grad}}(r, z_0) dr \quad \propto \quad - \int \nabla_r I_+(r, z_0) dr = -2I_0(r, d/2). \quad (5.1)$$

Often, the on-axis optical potential $U_{\text{opt}}(r, z_0)$ is approximated via a harmonic trap potential $U_{\text{trap}}(r, z_0) = \frac{1}{2}\kappa_{\perp}r^2$ for small displacements $r \approx 0$ around the center of the trap along the transverse (\perp) direction of both fibers. Figure 5.5A exemplarily demonstrates this for two counter-facing NBFs that are separated by the distance $d = 20\ \mu\text{m}$.

Axial confinement

Stable optical confinement of a particle along the axial direction z at $r = 0$ within a dual fiber trap, in contrast, mainly relies on compensating the axial scattering forces $\vec{F}_{\text{scat}}(0, z)$ along the optical axis z . For weakly focused beams, in particular, such as the ones emitted by the NBFs and the monotonous profile of a conventional SMF, the axial gradient force $\vec{F}_{\text{grad}}(0, z)$ can generally be neglected. In the dipole approximation^[95,117], specifically, the total scattering force $\vec{F}_{\text{scat}}(0, z)$ that has to be compensated along z is directly proportional to the intensity difference $I_-(0, z) = I_1(0, z - z_0) - I_2(0, z_0 - z)$ between the individual profiles of the two counter-propagating beams. Equivalent to the previously discussed gradient force \vec{F}_{grad} , the on-axis optical potential $U_{\text{opt}}(0, z)$ is thus

proportional to the integral over the scattering force $\vec{F}_{\text{scat}}(0, z)$:

$$U_{\text{opt}}(0, z) = - \int \vec{F}_{\text{scat}}(0, z) dz \propto - \int I_{-}(0, z) dr = \int \{I_0(0, d - z) - I_0(0, z)\} dz. \quad (5.2)$$

Again, the on-axis potential $U_{\text{opt}}(0, z)$ is approximated via a harmonic trap potential $U_{\text{trap}}(0, z) = \frac{1}{2}\kappa_{\parallel}(z - z_0)^2$ for small displacements $z \approx z_0$ around the center of the trap along the axial (\parallel) direction parallel to the optical axis z . Figure 5.5B presents this for the dual fiber focus trap at an inter-fiber distance of $d = 20 \mu\text{m}$.

Macroscopic approximation

To describe the behavior of a macroscopic particle within the optical trap, here, an approximation was made. This specifically consisted of integrating the optical forces $\vec{F}_{\text{opt}}(r, z)$ over the particle size along the respective axes r, z in one dimension in order to obtain the on-axis optical potentials $U_{\text{opt}}(r, z)$ (Figure 5.5, C and D). Here, only trapping in the center of the dual fiber trap at $z_0 = d/2$ was considered, which effectively represents the only stable trapping site for the monotonous beams emitted by two conventional SMFs (see Figure 5.4F). Figure 5.5, C and D, exemplarily presents the on-axis optical potentials $U_{\text{opt}}(r, z)$ for a dual fiber focus trap that is axially separated by different inter-fiber distances d for the radial direction r and the axial direction z , respectively.

Figure 5.5D effectively reveals that a minimum fiber separation d_{min} for stable optical trapping along the axial direction z between both NBFs exists, which is specifically given via twice the focal length $2z_f \approx 14 \mu\text{m}$ of the beam that is emitted by a single NBF ($d_{\text{min}} = 2z_f$). For $d > d_{\text{min}}$, in particular, the axial scattering forces $\vec{F}_{\text{scat}}(z)$ of both fiber beams are balanced, and stable optical trapping is possible in the center of the dual fiber trap at z_0 . However, if both focal maxima cross, i.e., for $d < 14 \mu\text{m}$, a central compensation is no longer possible as visible in Figure 5.5D for an inter-fiber distance of $d = 10 \mu\text{m}$. In this case the description of optical trapping principally requires considering the axial gradient force $\vec{F}_{\text{grad}}(z)$ or off-center trapping sites (compare ref. [45] and subsection 5.2.3), which, nevertheless, is beyond the scope of this model.

Optical trap stiffness

The stiffness $\kappa_{\perp, \parallel}$ of the harmonic trap potentials $U_{\text{trap}}(r, z)$ (harmonic approximation of the curves in Figure 5.5, C and D) for small displacements around the center of the trap effectively denotes the key quantity for analyzing and comparing the performance of the individual implementations of fiber-based optical trapping (see section 3.3). Figure 5.5E shows the trap stiffness $\kappa_{\perp, \parallel}(d)$ in the transverse (\perp , top: linear scale) and the axial (\parallel , bottom: logarithmic scale) fiber direction of the dual fiber trap as a function of the inter-fiber distance d for both dual NBF and dual SMF traps.

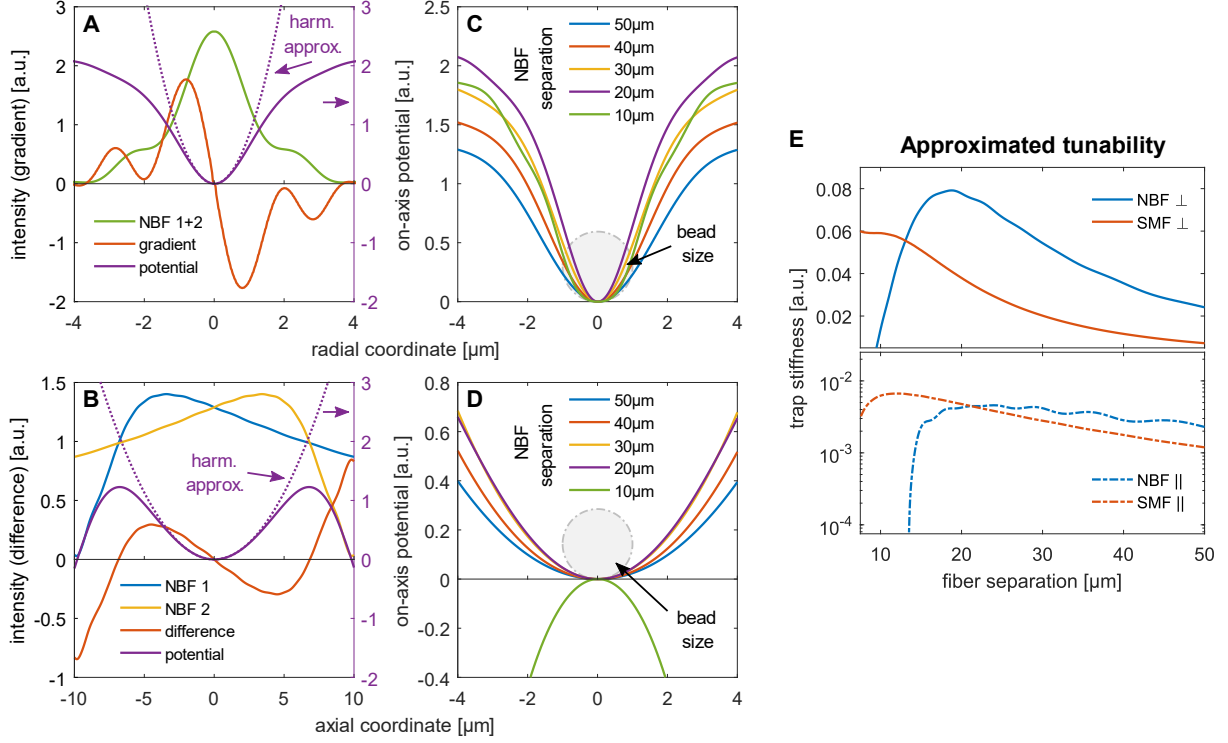


Fig. 5.5. Approximated on-axis optical potentials and tunability of the dual fiber focus trap in water calculated for a wavelength of 635 nm. (A) Sum of the intensity profiles of two NBFs (20 μm separation) and resulting gradient along the radial direction in the center of the trap as basis for the on-axis optical potential. (B) Difference of the two NBF profiles and proportional on-axis optical potential along the axial direction. (C) Approximated on-axis potentials for a dual fiber focus trap of different separations along the radial and (D) the axial direction in the center of the trap. To obtain the harmonic on-axis trap potentials (dotted curves in A and B), the optical potentials are averaged over a moving frame of the particle size prior to integration. (E) Tunability of the approximated stiffness for a dual NBF compared to a dual SMF trap as a function of fiber separation along the transverse (\perp , top in lin. scale) and the axial (\parallel , bottom in log. scale) direction of the dual fiber trap. The curves reveal a general dependence similar to the profile of the beam that is emitted by a single fiber, which results in axially unstable trapping for two NBFs separated by less than 14 μm .

Since the optical potential $U_{\text{opt}}(P) \propto P$ scales linearly with the power P within the trap^[45,114,138], this effectively allows simultaneously adjusting the value $\kappa_{\perp,\parallel}(P)$ and the ratio $\kappa_{\perp}(d)/\kappa_{\parallel}(d)$ between the transverse and the axial component of the stiffness $\kappa_{\perp,\parallel}(P, d)$. In particular, this enables access to explicit combinations as well as a high degree of control over the behavior of the trap. Here, the contrast between stable trapping and unstable anti-trapping behavior within the dual NBF trap specifically allows for tuning the ratio of the stiffness $\kappa_{\perp,\parallel}(d)$ via the fiber separation d , thus granting access to unique combinations that are practically inaccessible to dual SMF traps (compare ref. [45]).

The axial instability of optical trapping within the dual fiber focus trap for inter-fiber distances $d < d_{\text{min}}$, however, yields a significantly reduced performance in the transverse and the axial component of the stiffness $\kappa_{\perp,\parallel}(d)$ below $d_{\text{min}} \approx 14 \mu\text{m}$ as seen in Figure 5.5E. Interestingly, the overall dependence of the stiffness $\kappa_{\perp,\parallel}(d)$ for both dual fiber trap implementations behaves similar to the intensity profile $I_0(2z)$ of the beam emitted by a single fiber, thus allowing a rough estimate for a qualitative comparison.

5.2.3 Numerical analysis

In the previous subsection, the tunability of dual fiber traps was approximated for specific scenarios of on-axis trapping, yielding discrete curves for the stiffness $\kappa_{\perp,||}(d)$ (Figure 5.5). Here, a rigorous FEM simulation was carried out³ via the Barton formalism for macroscopic particles (compare refs. [45, 61, 113] and Equation 3.9), which additionally allows for variations of the size $2R$ (y -axis) and off-center trapping at different fiber distances d (x -axis of Figure 5.6). Specifically, the color represents the normalized stiffness $\kappa_{\perp,||}(d, 2R)/P_{1,2}$ in water at a wavelength of $\lambda = 635$ nm ($P_{1,2}$ denotes the fiber output power).

Overall, the dual NBF trap exhibits a greater stiffness $\kappa_{\perp}(d)$ (Figure 5.6A) than the dual SMF trap (Figure 5.6B) with a peak at $d = 14$ μm , in both cases matching Figure 5.5E very well. For small NBF separations $d < 10$ μm , however, the increase of $\kappa_{||}(d)$ (Figure 5.6C) differs notably from the flat dependence of $\kappa_{||}(d)$ within the dual SMF trap (Figure 5.6D) and from the axial instability in Figure 5.5E. This results from the focus of the NBF beam and its axial gradient force $\vec{F}_{\text{grad}}(z)$, which here was included in the simulation and hence contributes to stable trapping sites outside the trap center once all optical forces $\vec{F}_{\text{opt}}(r, z)$ are balanced. Nevertheless, the results depend only little on the particle size $2R$.

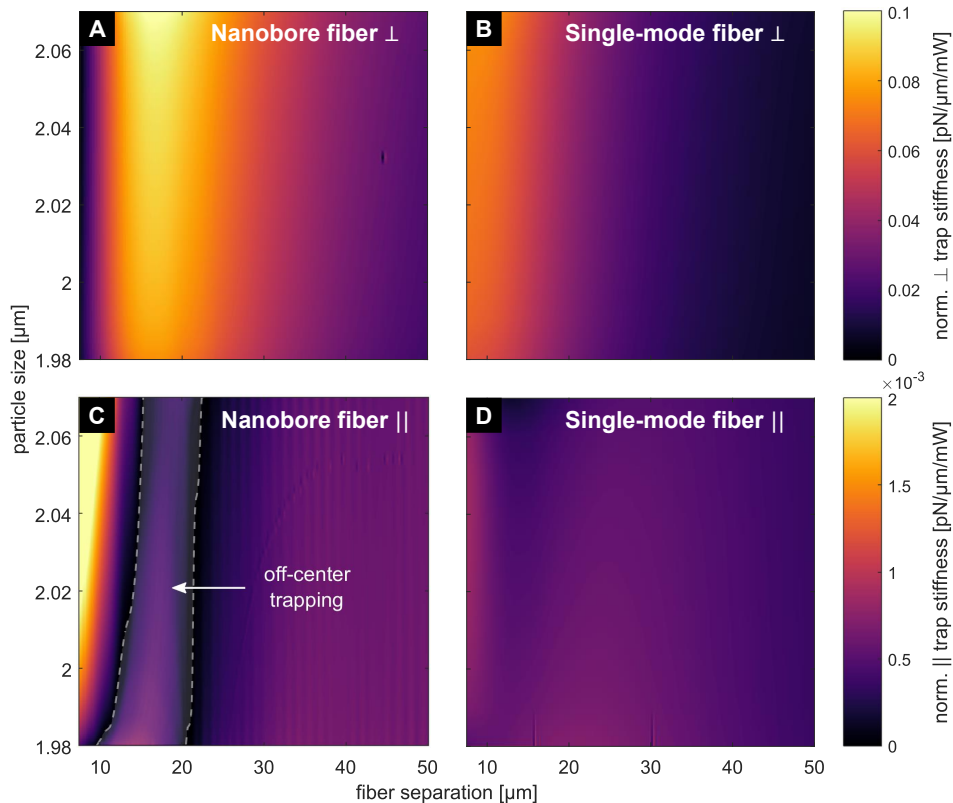


Fig. 5.6. Simulated power normalized stiffness for a dual fiber trap in water at a wavelength of 635 nm as function of particle size and fiber separation. (A) Stiffness in the transverse (\perp) direction for a dual NBF and (B) a dual SMF trap. The NBF overall exhibits a greater stiffness than the SMF with a maximum at 14 μm separation. (C) Stiffness in the axial ($||$) direction for dual NBF and (D) dual SMF trap. In contrast to the constant stiffness of the SMF, the one of the NBF increases significantly below 10 μm separation due to its focus and the resulting gradient force. All plots show only weak dependence on the particle size.

³Simulation by Martin Šiler, Institute of Scientific Instruments of the CAS, Brno (CZ), in ref. [45].

5.3 Experimental demonstration

For an experimental verification of the performance enhancement of the dual fiber focus trap over a regular dual beam fiber trap, tuning its trap stiffness $\kappa(P, d)$ via the optical power P and the fiber separation d is discussed first (subsection 5.3.1). This is followed by comparing the results of different techniques for analyzing the performance (subsection 5.3.2). Finally, an outlook is given on its application within different trapping scenarios, including *Escherichia coli* bacteria as a more sensitive probe for measuring the trap performance (subsection 5.3.3).

5.3.1 Tunable optical trapping

As previously discussed in section 5.2, a dual fiber trap principally enables simultaneously adjusting the optical powers $P_{1,2}$ and the distance d between both fibers^[45,60,114]. Effectively, this grants access to unique combinations of the trap stiffness $\kappa_{\perp,||}(P_{1,2}, d)$ while allowing the control of the individual components along the transverse (\perp) and the axial ($||$) direction of the fiber optical trap independently (see Figures 5.5E and 5.6).

To experimentally verify the tunability of a dual fiber trap and to compare the performances of dual nanobore fiber (NBF) and dual single-mode fiber (SMF) trap, a continuous wave (CW) laser that emits a power of $P_0 = 100$ mW at a wavelength of $\lambda = 635$ nm was used for exciting the fundamental modes of the two different fibers (see Figure 5.4, B and C). Here, the same NBF (core diameter of $2a = 3.4$ μm , channel diameter of $2b = 0.7$ μm) and SMF (core diameter of $2a = 3$ μm) as already introduced in section 5.1 and subsection 5.2.1 were used, while both fibers were independently excited to optical powers of $P_{1,2} = 30$ mW measured at their respective outputs. Specifically, the experiment was carried out in ultra-pure water with a 1:2500-fold dilution of silica beads (Micromod Inc., diameters $2R = 2$ μm), resulting in a final particle concentration of $c \sim 5 \cdot 10^6$ cm^{-3} . Approximately 50 μl of the particle solution were pipetted into the sample chamber (Figure 4.2C, details of the setup see subsection 4.1.1), and the experiment was started as soon as a single bead was stably confined in the center of the trap.

Figure 5.7A illustrates an experimental implementation of a dual fiber focus trap of two identical NBFs with counter-propagating beams (green arrows) that are axially separated by an inter-fiber distance d . Here, the dashed green lines indicate the boundaries of the respective fiber facets inside the sample chamber, while the water filled central channel (bore) of both NBFs is clearly identified as a black bar due to its good refractive index contrast to silica. A custom-built optical microscope was used for observing the motion $x = (r, z)$ of a trapped bead, which here was imaged via a 40 \times dry objective (Olympus MPLN, NA = 0.65) in combination with a tube lens of focal length $f_t = 250$ mm. Moreover, the illumination was provided via a fiber-coupled light emitting diode (LED) at

a wavelength of $\lambda = 617$ nm (Thorlabs M617F2), while scattered laser light was blocked using a notch filter of central wavelength $\lambda_0 = 633$ nm (Thorlabs NF633-25).

In order to properly analyze the motion $x_{\perp,\parallel}(t)$ of an individual trapped bead, high-speed videos were recorded for all measurements as a small area strip containing only the relevant information about its motion (dashed yellow rectangle in Figures 5.7A and 5.7B indicating the recording area). Here, the videos were recorded at a high frame rate of $1/\Delta t = 1000$ fps for a duration of $t_{\max} = 30$ s, while the exposure time was $\tau = 0.7$ ms. After recording, the videos were cropped to an area of interest (AOI) around the bead (dashed black square in Figure 5.7B) and subsequently passed to a tracking algorithm for retrieving its motion $x_{\perp,\parallel}(t)$ (details of the tracking routine see subsection 4.1.2).

Power tuning

Figure 5.7C exemplarily displays the trajectory $x_{\perp,\parallel}(t)$ of a bead that was optically trapped in the center at $z_0 = d/2$ between the two NBFs of a dual fiber focus trap (Figure 5.7, A and B) for two different powers P (power 2 < power 1). Here, its trajectory $x_{\perp,\parallel}(t)$ was obtained using the image shift algorithm, i.e., the independent retrieval of its displacement $\Delta x(t_i)$ (relative shift) in every frame t_i via centering the cropped AOI of the recorded video (compare refs. [44, 45]). However, since the total optical power P (sum of the individual fiber powers $P_{1,2}$) linearly scales the stiffness $\kappa_{\perp,\parallel}(P) \propto P$ of the optical trap^[45,114,138], this effectively yields an increased standard deviation σ of the trajectory $x_{\perp,\parallel}(t)$ (Figure 5.7C) as well as a broader local distribution $\rho(x_{\perp,\parallel})$ for lower powers P . This is visualized in Figure 5.7D via the 2σ boundary (including 95% of the data) for the near Gaussian shaped distribution, being principally in line with the predicted behavior of a trapped particle^[95] (see Figures 3.2D and 4.5B).

To obtain the power normalized stiffness $\kappa_{\perp,\parallel}/P_{1,2}$ of the dual fiber trap (see Figure 5.6), the laser beam was attenuated using optical density (OD) filters. Within all measurements, filters of OD 0.1, 0.3, 0.6 and 1.0 were used, which effectively results in a near linear reduction of the power $P_{1,2}$ at each fiber output. At every power $P_{1,2}$, the trajectory $x_{\perp,\parallel}(t)$ of a trapped particle was obtained from a recorded video and afterwards analyzed via its mean square displacement^[81,96,97] (MSD, see Equation 4.4) for determining the stiffness $\kappa_{\perp,\parallel}(P_{1,2}) \propto P_{1,2}$ and finally the slope. In order to account for potential variations of the diameters $2R$ within the batch of particles, the experiment was restarted once a trapped bead was lost or a second one diffused into the trap throughout the measurement, hence specifically ensuring a general validity for a quantitative comparison.

Figure 5.7E exemplarily compares the recorded power slope of the optical trap stiffness $\kappa_{\perp,\parallel}(P_{1,2})$ for the two different fiber traps, i.e., dual NBF and dual SMF trap, both being separated at an inter-fiber distance of $d = 10$ μm . Here, the results reveal that optical trapping with the dual fiber focus trap is principally possible at this short fiber

separation d , and that the dual NBF trap performs better than the dual SMF trap overall. Specifically, it exhibits a greater trap stiffness $\kappa_{\perp,\parallel}(P_{1,2})$ along both (\perp and \parallel) directions, which is in good agreement with the approximate calculation presented in Figure 5.5E as well as with the numerical FEM simulation of Figure 5.6.

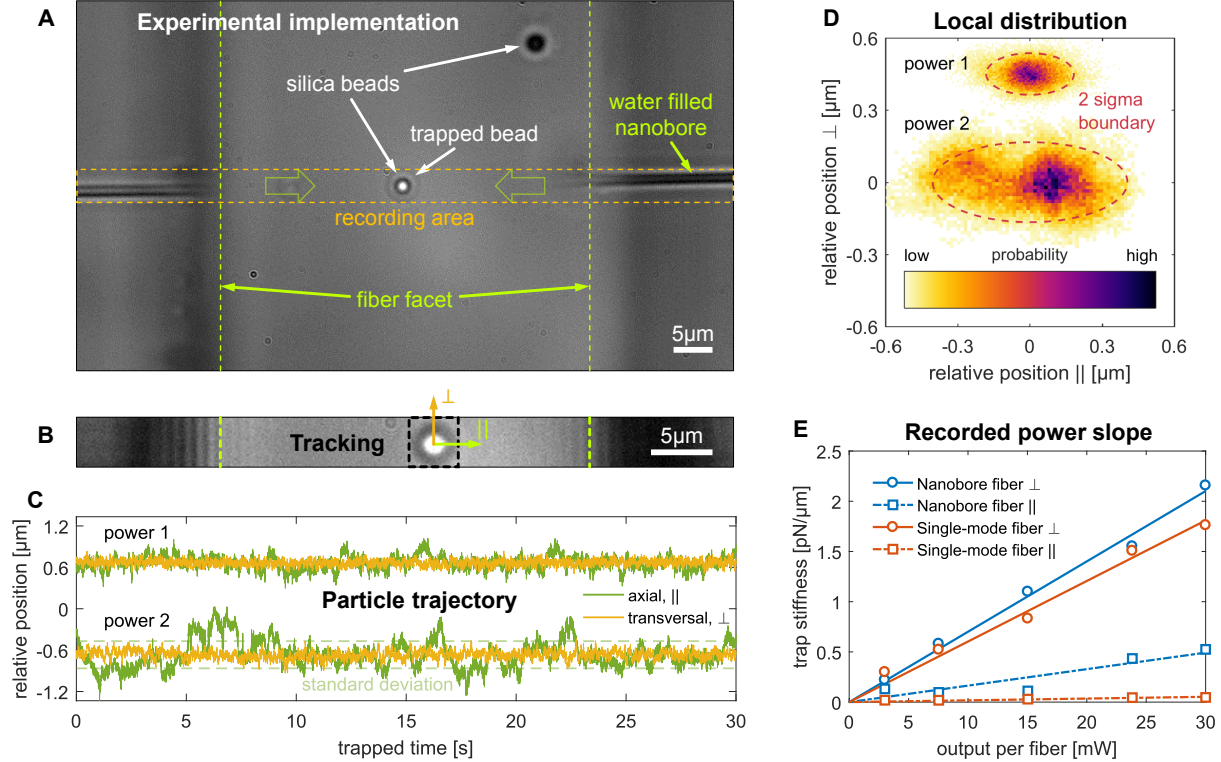


Fig. 5.7. Optical trapping of a 2 μm diameter silica bead and experimental demonstration of power tuning with a dual fiber trap in water. (A) Experimental implementation of a dual fiber focus trap consisting of two identical nanobore fibers with counter-propagating beams (green arrows). The dashed green lines indicate the respective fiber facets, and the horizontal black bar represents the water filled central bore. (B) Videos of a single trapped bead were recorded at 1000 fps only of the area containing relevant information about its motion (dashed yellow rectangle in A). After recording, the videos were cropped to an area of interest (AOI) around the bead (dashed black square) for tracking its motion. (C) Tracked trajectory and (D) local distribution of a bead for two different optical powers. Due to the power dependent stiffness of the trap, a lower power (power 2 $<$ power 1) yields a broader standard deviation σ of the bead position, as indicated by the 2σ boundary including 95% of the data. (E) Recorded power dependent stiffness of the trap at a wavelength of 635 nm, yielding the power normalized slope for the example of 10 μm fiber separation. The dual NBF trap performs better than the dual SMF trap, i.e., reveals a greater stiffness for a trapped 2 μm diameter silica bead.

Distance tuning

In order to experimentally demonstrate tuning the normalized stiffness $\kappa_{\perp,\parallel}(d)/P_{1,2}$ via adjusting the inter-fiber distance d of the dual fiber trap, the separation between both fibers was decreased from $d = 50 \dots 10 \mu\text{m}$ in steps of $\Delta d = 10 \mu\text{m}$, as previously presented in Figure 5.5, C and D. Specifically, Figure 5.8A illustrates the optical trapping of a $2R = 2 \mu\text{m}$ silica bead in water between two NBFs with counter-propagating beams (green arrows), i.e., the dual fiber focus trap, for different inter-fiber distances d (top: $d = 50 \mu\text{m}$, bottom: $d = 10 \mu\text{m}$). For every separation d , an individual set of videos was

recorded for five different powers $P_{1,2}$ as shown in Figure 5.7E, thus effectively yielding a total of 5×5 values for the stiffness $\kappa_{\perp,\parallel}(P_{1,2}, d)$. To account for potential variations of the diameters within the batch of particles, the experiment was restarted once if a trapped bead was lost or a second one diffused into the trap during the measurement. Essentially, this was repeated for the dual SMF trap as visualized in Figure 5.8B.

Figure 5.8C exemplarily displays the one-dimensional (\perp or \parallel to the fiber orientation) local distribution $\rho(x_{\perp,\parallel})$ and underlying potential $U_{\text{opt}}(x_{\perp,\parallel})$ for an optically trapped bead between the two fibers of a dual fiber trap being separated by different inter-fiber distances d (distance $d_2 >$ distance d_1). According to the theory of trapping^[95], the underlying potential $U_{\text{opt}}(x_{\perp,\parallel})$ effectively allows approximation via a harmonic potential $U_{\text{trap}}(x_{\perp,\parallel}) = \frac{1}{2}\kappa_{\perp,\parallel}x_{\perp,\parallel}^2$ if the resulting local distribution $\rho(x_{\perp,\parallel})$ exhibits a near Gaussian shape (details see Figure 4.5, B and C). Here, the opening factor of the trap potential $U_{\text{trap}}(d)$ reveals a greater stiffness $\kappa_{\perp,\parallel}(d)$ for the dual fiber trap at smaller separations d , i.e., $d_1 < d_2$, which is principally in line with Figure 5.5, C and D.

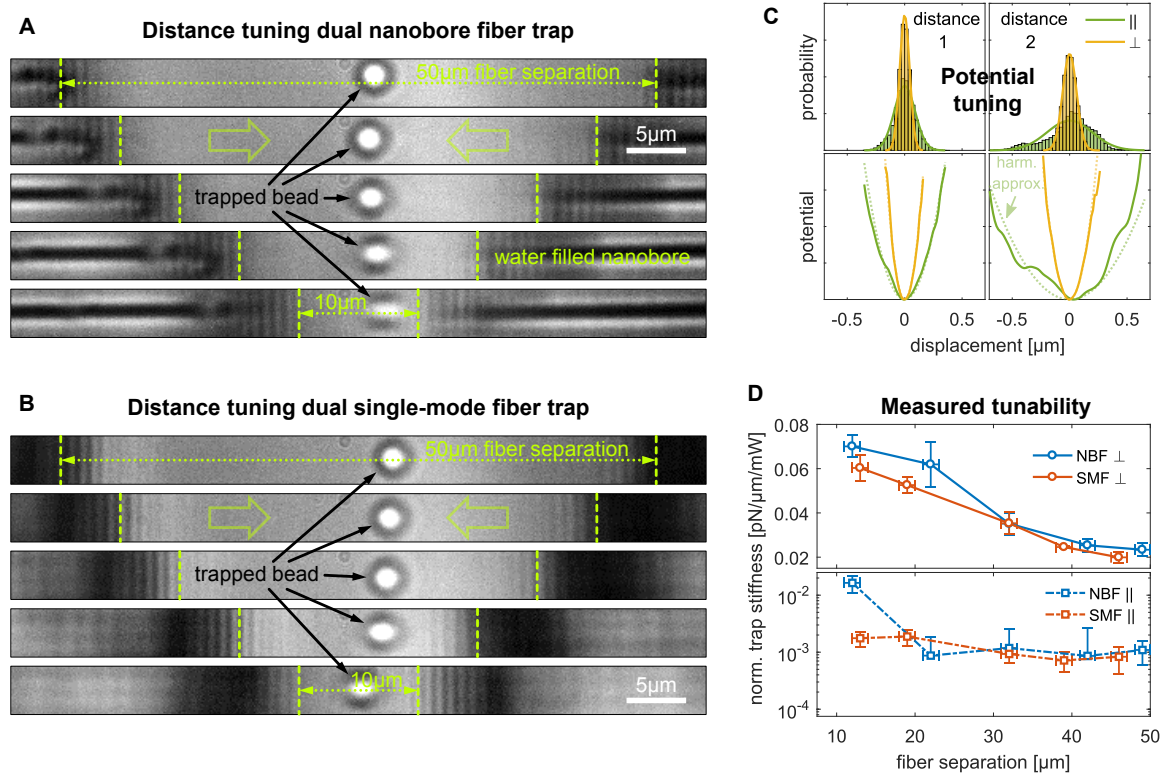


Fig. 5.8. Experimental comparison of distance tuning with a dual nanobore fiber (NBF) and a dual single-mode fiber (SMF) trap for a 2 μm diameter silica bead in water. (A) The distance between two NBFs and **(B)** two SMFs with counter-propagating beams (green arrows) is varied from 50 μm (top) to 10 μm (bottom) in steps of 10 μm , while the dashed green lines indicate the respective fiber facets. For every separation, videos of a single trapped bead were recorded at 1000 fps for five different powers using optical density (OD) filters to attenuate the laser. **(C)** The local distribution and underlying potential for a trapped bead broaden significantly with increased fiber distance (distance 2 $>$ distance 1), while a harmonic approximation yields the trap stiffness. **(D)** Obtained power normalized stiffness at a wavelength of 635 nm for the \perp (top: lin. scale) and \parallel direction (bottom: log. scale). The results reveal that the dual NBF overall performs better than the dual SMF trap particularly at short distances due to its focus, which is perfectly in line with previous findings.

Figure 5.8D depicts the obtained normalized stiffness $\kappa_{\perp,\parallel}(d)/P_{1,2}$ (recorded for all inter-fiber distances d as in Figure 5.7E) for the \perp (top: lin. scale) and the \parallel direction (bottom: log. scale, compare ref. [45]). Based on a total of $2 \times 5 \times 5$ recorded videos, the obtained results are perfectly in line with previous findings (detailed comparison see Figure 5.9, E and F), confirming an increasing stiffness $\kappa_{\perp,\parallel}(d)/P_{1,2}$ for decreasing fiber separations d within both dual fiber traps. Specifically, the dual NBF trap performs better than its dual SMF counter-part overall, yet particularly for small inter-fiber distances d as clearly visible within the \parallel component of the stiffness $\kappa_{\parallel}(d)/P_{1,2}$ for $d = 10 \mu\text{m}$ separation. As already predicted, this results from the focus of the NBF beam and its strong axial gradient force $\vec{F}_{\text{grad}}(z)$ along the propagation direction z , thus effectively ensuring stable optical trapping and providing enhanced performance at smallest inter-fiber distances d .

5.3.2 Comparison of results

As mentioned earlier, the trap stiffness $\kappa_{\perp,\parallel}$ presented in Figures 5.7E and 5.8D was specifically determined via a mean square displacement (MSD) analysis of the previously tracked trajectory $x_{\perp,\parallel}(t)$ of a trapped bead. For examining its motion, however, in principle a broad range of different techniques exist, which specifically allow verifying the trapping as well as effectively comparing the trap performance (see section 4.2).

Figure 5.9 illustrates the experimental results obtained from using different techniques, which in principle can be grouped into spatial (Figure 5.9A) and tempo-spectral methods (Figure 5.9, B to D). Overall, the results exhibit an extraordinarily high degree of similarity and are perfectly in line with the previously discussed models for the tunability of a dual fiber trap (Figure 5.9, E and F, see section 5.2), thus emphasizing their reliability. In particular, spatially analyzing a trapped particle via the equipartition theorem^[95,99,117] (Figure 5.9A, see Equation 4.2) and the autocorrelation^[132] of its tracked motion (Figure 5.9B, see Equation 4.3) yield almost indistinguishable results. As a matter of fact, both techniques effectively consider the entire length of a particle trajectory $x_{\perp,\parallel}(t)$ while no specific temporal analysis of occurring events is performed, which thus justifies considering the autocorrelation as a semi-spatio-temporal method as well.

A time domain-based MSD analysis^[81,96,97] of trapped particle motion (Figure 5.9C, see Equation 4.4), on the other hand, yields small differences specifically in the reduced error margins of the normalized axial stiffness $\kappa_{\parallel}(d)/P_{1,2}$. In principle, this results from distortions, such as tracking errors in the fit as well as particle oscillations and drift, which are effectively revealed via this more accurate technique. A spectral domain analysis via the power spectrum^[132–134] (PS) of the particle trajectory $x_{\perp,\parallel}(t)$ (Figure 5.9D, see Equation 4.5), however, comes closest to accurately representing the simulated performance within its error margins. Nevertheless, at the cost of precision particularly within the transverse component of the stiffness $\kappa_{\perp}(d)/P_{1,2}$ due to the required compression of

correlated experimental data (for details see subsection 4.2.2), this represents the most demanding technique in terms of complexity and adjustment.

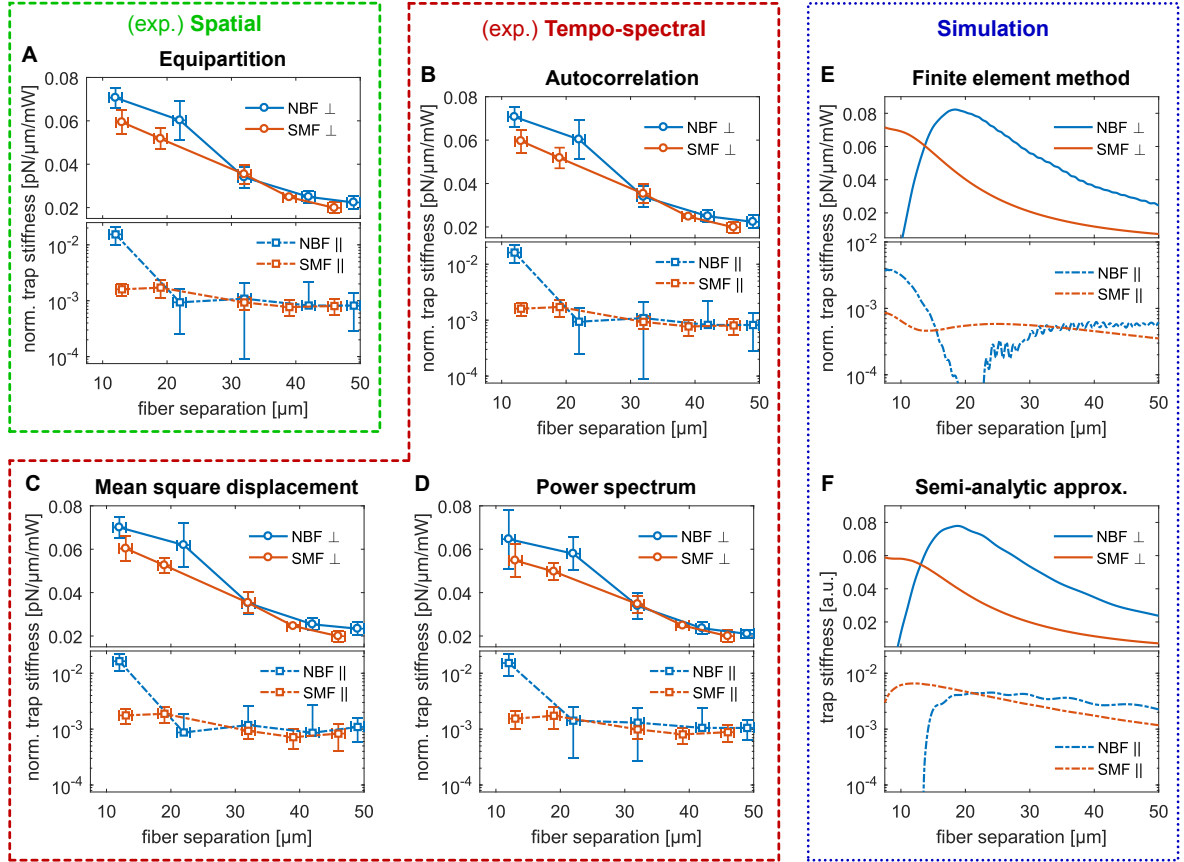


Fig. 5.9. Comparison of experimental and predicted results for a 2 μm diameter silica bead within a dual fiber trap at a wavelength of 635 nm. (A) Spatial and (B–D) tempo-spectral analysis of experimental results via (A) the equipartition theorem, (B) the autocorrelation, (C) the mean square displacement (MSD), and (D) the power spectrum (PS) of previously obtained particle trajectories. The results agree very well and exhibit only minor differences within their error margins due to using differently complex techniques (see main text). (E) Rigorous finite element method (FEM) simulation and (F) semi-analytical approximation of the optical trap stiffness. Both models accurately represent the experimental observations, specifically along the \perp direction, and (E) even match observed details along the \parallel direction due to included axial gradient force.

The simulated results (Figure 5.9, E and F) represent the experimental observations with good accuracy, where the dual NBF trap also performs better than the regular dual SMF trap. For the rigorous FEM simulation (Figure 5.9E), in particular, stable optical trapping along the \parallel direction within the dual fiber focus trap below a fiber separation of $d = 14 \mu\text{m}$ can be attributed to the included axial gradient force $\vec{F}_{\text{grad}}(z)$ resulting from the focus of the NBF beam. In addition to considering stable off-center trapping, being responsible for the significantly reduced axial performance around $d \approx 20 \mu\text{m}$, this, however, is not included within the semi-analytical approximation for the stiffness $\kappa_{\parallel}(d)$ (Figure 5.9F), which explains the significant deviation of the curves. Nevertheless, the approximation model effectively yields a fast, accurate and reliable prediction of the stiffness $\kappa_{\perp, \parallel}$ for the dual fiber trap in terms of agreement with the experiment, principally representing a good approximation for weakly focused beams along the \perp direction.

In the following, the temporal MSD analysis of a trapped particle trajectory is thus effectively referred to as the method of choice when comparing the performance of fiber traps. Specifically with respect to matching the simulations as well as reliably yielding the smallest errors throughout all presented techniques, it reveals the largest amount of detail and most accurately represents the pronounced dip within the axial stiffness $\kappa_{\parallel}(d)/P_{1,2}$ around $d = 20 \mu\text{m}$ inter-fiber distance. In conclusion, the results for $\kappa_{\perp,\parallel}/P_{1,2}$ differ by one order of magnitude between the transverse and the axial performance of the dual fiber trap, particularly being in line with literature reported values^[43,86,114] (see Table 5.1).

5.3.3 Application outlook

In the previous subsection, a quantitative comparison with a regular dual beam fiber trap was made in order to demonstrate the enhanced tunability and performance of the dual fiber focus trap. This subsection, however, is dedicated to giving a qualitative outlook on potential applications of optical trapping with the dual fiber focus trap. Specifically, the trap is based on the same NBF as in previous experiments (core diameter of $2a = 3.4 \mu\text{m}$, channel diameter of $2b = 0.7 \mu\text{m}$), while here, the conditions such as particle type and operating wavelength are altered for the case of the dual NBF focus trap. The experiments were individually carried out within ultra-pure water, while all particle solutions were diluted to final concentrations of $c \sim 5 \cdot 10^6 \text{ cm}^{-3}$ each (details see subsection 4.1.1).

Trapping scenarios

Due to its generally low selectivity to a specific kind of trapped particle, a dual fiber trap in principle allows for confining a broad range of different quantities, sizes, shapes, and materials of particles aside from the previously demonstrated individual $2R = 2 \mu\text{m}$ silica beads. Confining multiple particles simultaneously within an optical trap, however, yields the earlier introduced effect of optical binding^[115–117] (see subsection 3.3.1 and Figure 5.10, B and D). Therefore, no quantitative analysis of the trap performance is effectively carried out here, but rather potential extensions of optical trapping scenarios with the dual fiber focus trap are qualitatively demonstrated.

Figure 5.10, A and B, for example, illustrates the optical trapping of one (A) and two (B) silica beads of $2R = 2 \mu\text{m}$ diameters being confined between two NBFs in the center of a dual fiber focus trap at optical powers of $P_{1,2} = 50 \text{ mW}$ and a wavelength of $\lambda = 532 \text{ nm}$. In Figure 5.10, C and D, in contrast, this is respectively visualized for a single (C) and multiple (D) polystyrene spheres of $2R = 5 \mu\text{m}$ diameters. Figure 5.10, E and F, on the other hand, demonstrates the optical trapping of different individual (E) and two separated (F) inactivated *Escherichia coli* bacteria of approximately $1 \mu\text{m} \times 3 \mu\text{m}$ size, which were confined via powers of $P_{1,2} = 20 \text{ mW}$ at a wavelength of $\lambda = 638 \text{ nm}$.

In contrast to both types of spherical particles (Figure 5.10, B and D), coupling between the rod shaped bacteria due to optical binding^[115–117] is not observed here.

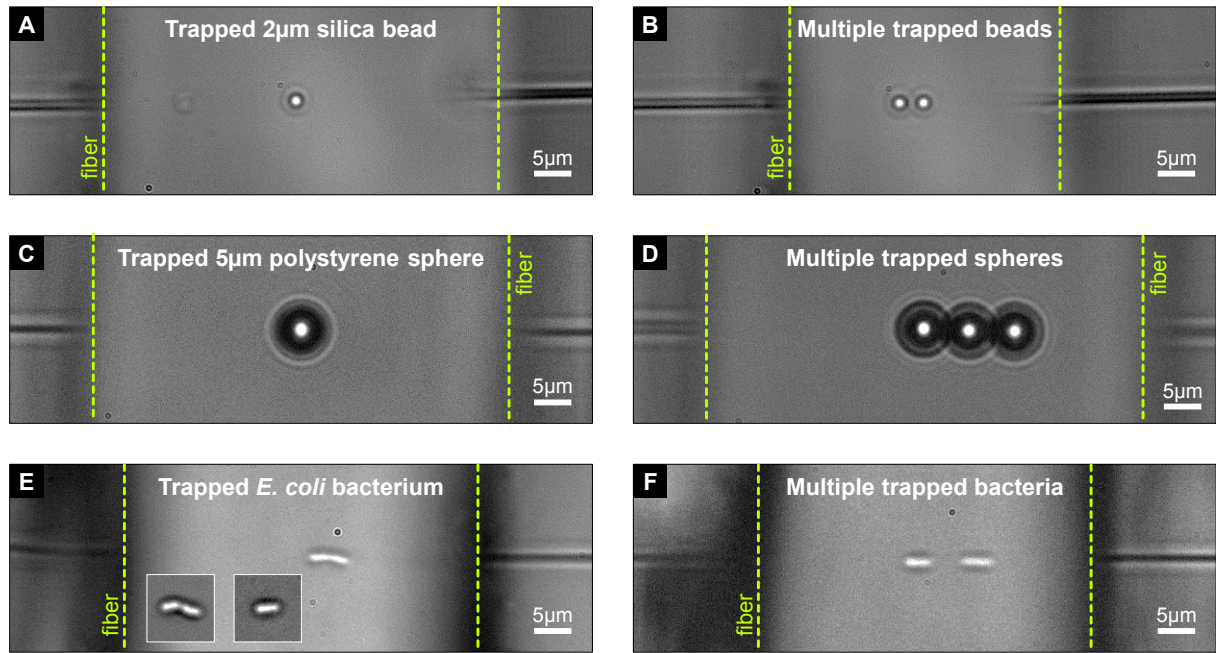


Fig. 5.10. Demonstrated optical trapping for different quantities, sizes, materials, and shapes of particles with the dual fiber focus trap in water. (A) Single and (B) multiple silica beads of 2 μm diameter trapped between two nanobore fibers (NBFs) at optical powers of 50 mW and a wavelength of 532 nm. (C) Same for one and (D) three polystyrene spheres of 5 μm diameter confined in the center of the trap. The coupling between individual particles (B and D) reveals the effect of optical binding (see main text). (E) Single and (F) two individual inactivated *Escherichia coli* (*E. coli*) bacteria trapped at powers of 20 mW and a wavelength of 638 nm. The insets in E display different *E. coli* bacteria being individually trapped between the two NBFs.

In principle, particles of larger diameters $2R$ facilitate optical trapping at lower powers P via increasing the normalized stiffness $\kappa(2R)/P$ [12, 95]. This effectively allows for certain dual beam fiber applications^[61] specifically in life sciences, such as, e.g., the fiber-based Raman spectroscopy of large cells^[62]. However, as generally found within optical traps, controlling the quantity of trapped particles remains challenging, since optical binding yields the formation of long chains^[116,140,141]. In return, this attracts even more objects to the center of the trap, which thus increases the range of optical forces \vec{F}_{opt} and the effective trapping area – an undesired consequence for precise local operation.

***Escherichia coli* probe**

Contrasting previous experiments, in particular, where the rotational symmetry of trapped particles was effectively ensured via spherical beads, here, the influence of elliptical objects on their behavior within the dual fiber focus trap is investigated. *Escherichia coli* (*E. coli*) bacteria of rod-like shapes (see Figure 5.10E) in principle provide ideal probes for measuring their response within the optical trap, while here, specifically, they were inactivated and thus exhibit no self-propelled motion as of flagellar rotation^[2]. Here, the tracking of

their motion was thus performed via the same routine as previously shown in Figure 5.7, B and C (details see subsection 4.1.2), however in this instance, no rotational diffusion^[142] was considered. Nevertheless, it was demonstrated in the past that *E. coli* bacteria are attracted to similar focal beam profiles^[63], while their orientation with respect to the optical trap, especially, is strongly influenced by the trap itself^[2,20,63].

Here, the trapping experiment was carried out with bacteria of approximately $1\ \mu\text{m} \times 3\ \mu\text{m}$ in size, which were diluted at a ratio of 1:100 from their stock solution to a final concentration of $c \sim 5 \cdot 10^6\ \text{cm}^{-3}$. A fiber-pigtailed laser diode emitting an optical power of $P_0 = 70\ \text{mW}$ at a wavelength of $\lambda = 638\ \text{nm}$ (Thorlabs LP637-SF70) was used for exciting both nanobore fibers of the dual fiber focus trap individually, resulting in optical powers of $P_{1,2} = 20\ \text{mW}$ measured at their respective outputs. In accordance with previous experiments, in particular, the same NBF and a similar trapping procedure (Figure 5.8A) were applied via varying the inter-fiber distance d from $d = 35 \dots 10\ \mu\text{m}$ in steps of a few microns as presented in Figure 5.11A. The imaging, however, was changed to a $60\times$ dry objective (NA = 0.85) in combination with a tube lens of focal length $f_t = 200\ \text{mm}$ (details see Figure 4.2), while the illumination was provided via a fiber-coupled LED of wavelength $\lambda = 455\ \text{nm}$ (Thorlabs M455F3). Here, the exposure time for high-speed recording (frame rate $1/\Delta t = 1000\ \text{fps}$) the trapped motion was $\tau = .97\ \text{ms}$.

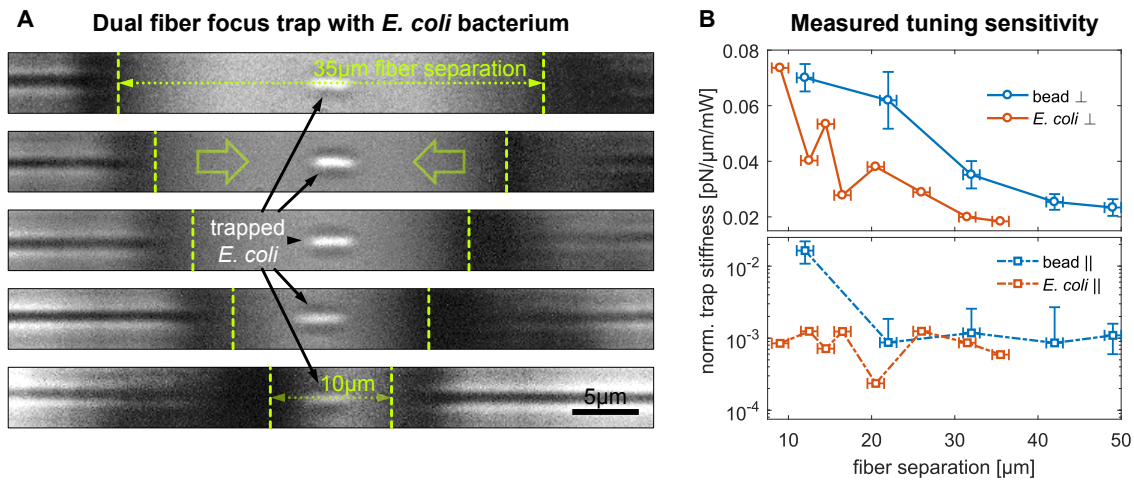


Fig. 5.11. Optical trapping of an *Escherichia coli* (*E. coli*) bacterium and measured sensitivity to tuning the dual fiber focus trap in water. (A) The separation between two nanobore fibers (NBFs) with counter-propagating beams (green arrows) was reduced from $35\ \mu\text{m}$ (top) to $10\ \mu\text{m}$ (bottom) in steps of a few microns while a single *E. coli* bacterium was trapped in the center. The dashed green lines indicate the respective fiber facets. **(B)** Measured power normalized trap stiffness at a wavelength of $638\ \text{nm}$ as a function of fiber separation for the \perp (top: lin. scale) and the \parallel direction (bottom: log. scale) compared to a $2\ \mu\text{m}$ diameter silica bead. Presumably due to its orientation with respect to both NBFs within the optical trap **(A)**, the bacterium reacts as a very sensitive probe particularly to the perfectly overlapping foci of both beams at $14\ \mu\text{m}$ (\perp direction) and to the theoretically predicted performance drop around $20\ \mu\text{m}$ separation (\parallel direction).

Figure 5.11B displays the analyzed results of the normalized stiffness $\kappa_{\perp,\parallel}(d)/P_{1,2}$ for a single trapped *E. coli* bacterium along the transverse (\perp , top: lin. scale) and the axial direction (\parallel , bottom: log. scale) for different fiber separations d . Compared to

the behavior of a trapped spherical bead of $2R = 2\ \mu\text{m}$ diameter from the previous measurement (Figure 5.8D), the elliptical bacterium experiences a completely different response to tuning the dual fiber focus trap. In general, it acts as a more sensitive probe for measuring the optical trap performance and specifically exhibits a more pronounced reaction within the transverse component of the stiffness $\kappa_{\perp}(d)$ at exactly $d = 2z_f = 14\ \mu\text{m}$. This presumably results from its particular shape that yields its orientation with respect to both fibers within the optical trap as clearly visible in Figure 5.11A. Along the axial direction, however, no enhancement of the trap stiffness $\kappa_{\parallel}(d)$ due to the axial gradient force $\vec{F}_{\text{grad}}(z)$ for small d is visible. Nevertheless, a more accurate representation of the significant performance drop at $d \approx 20\ \mu\text{m}$ is revealed, which raises the question about the influence of the trapped object length.

5.4 Chapter discussion

Due to the unique beam profile of the nanobore fiber with its focal spot, the dual fiber focus trap discussed in this chapter represents a cost-efficient and straight-forward enhancement over a regular dual fiber trap. Experimentally tuning the separation distance d between the two fibers of a dual beam fiber trap in principle revealed that the dual fiber focus trap performs better than a regular dual single-mode fiber trap at short inter-fiber distances $d < 20\ \mu\text{m}$, particular along the \parallel direction, while the experimentally obtained results exhibit a good agreement with simulated predictions. Moreover, the performance of optical trapping with a dual fiber trap is about one order of magnitude higher within the transverse than the axial direction and increases significantly for smaller fiber separations d . This allows individually adjusting the optical trap performance along the transverse and axial directions independently, which effectively enables combinations of the trap stiffness $\kappa_{\perp,\parallel}(d)$ that are inaccessible to regular dual single-mode fiber traps.

Table 5.1 provides an overview of similar literature reported dual fiber trapping concepts. Compared to the different listed dual fiber traps, the here obtained results for $\kappa_{\perp,\parallel}$ are in particularly good agreement. Specifically, they benefit from the unique tunability and simplicity of the dual fiber focus trap that is currently unavailable to other implementations. Via a high degree of freedom and the flexibility of inclination, an inclined dual fiber trap^[43,138] comes closest to the tunability of the dual fiber focus trap, nevertheless, it requires additional handling in return. When compared to a dedicated yet more difficult to implement 3D printed, lensed dual fiber trap^[86], however, the dual fiber focus trap concept demonstrated in this work is effectively limited in its performance.

Further improvements of the dual fiber focus trap can be achieved through, e.g., the actual geometry of the nanobore fiber, since changing the core (2a) and the central bore (2b) diameter has a significant impact on the evolution of the fundamental mode.

Tab. 5.1. Overview of literature reported similar dual beam fiber-based optical trapping concepts. The results presented in this chapter are highlighted in gray and are in good agreement with similar concepts. The dual fiber focus trap particularly benefits from unique tunability and simplicity over comparable approaches.

<i>Type of fiber trap</i>	<i>Particle size & material</i>	<i>Stiffness $\kappa_{\perp}, \kappa_{\parallel}$ [pN/μm/mW]</i>	<i>Key features</i>	<i>Reference</i>
Inclined dual fiber trap	3 μ m silica	$6.4 \cdot 10^{-2}$ $1.8 \cdot 10^{-2}$	+ flexibility - handling	[43]
Dual fiber nano tips	1 μ m polyst.	$(5.0 \dots 6.0) \cdot 10^{-2}$ $(0.2 \dots 2.2) \cdot 10^{-2}$	- fabrication	[114, 143]
Dual fiber focus trap (2 \times 0.25 NA)	2 μ m silica	$(2.3 \dots 7.0) \cdot 10^{-2}$ $(0.1 \dots 1.6) \cdot 10^{-2}$	+ tunability + simplicity	this work, [45]
Lensed dual fiber trap (2 \times 0.3 NA)	1 μ m polyst.	$(1.3 \dots 2.7) \cdot 10^{-1}$ $(0.3 \dots 1.4) \cdot 10^{-2}$	+ performance - fabrication	[86]

This specifically yields a greater slope of the fiber-adjacent side of the focal spot^[57] and thus effectively a higher NA for the intensity profile $I(r, z)$ of two counter-propagating beams. Moreover, independently adjusting the individual optical powers $P_{1,2}$ emitted by each of the two fibers as well as changing their inclination^[43,60,138] in principle represent additional improvements of the dual fiber focus trap.

Potential future applications include, e.g., the rotation of individual trapped objects via adjusting the optical fiber mode^[66] as well as subsequently analyzing rotational diffusion^[142]. In principle, this allows extending the scope of applications to more complex shaped living objects aside from the trapped *E. coli* bacteria, e.g., for investigating their motility within the optical trap^[2,63]. Specifically combining the dual fiber focus trap with well-established techniques in life sciences opens up the possibility for applications such as, e.g., fiber-based Raman spectroscopy of individual trapped cells^[62] as well as their optical micro-manipulation^[64,65] for, e.g., tumorous tissue diagnosis.

Meta-fiber trap

For optical trapping of freely diffusing micro-objects in water, the previous chapter introduced the concept of a dual fiber trap (compare ref. [45]), which additionally allows for quantitatively distinguishing between different types of optically trapped particles via accessing their physical properties such as, e.g., size and shape. While noteworthy results were obtained, however, this concept bears several disadvantages, namely the lack of flexibility, integrability and usability in difficult to reach remote environments. Therefore, using an optical trap that is based on only a single flexible fiber beam, which is the scope of this chapter (compare ref. [46]), represents a sophisticated solution to increase flexibility, ease of use as well as enabling remote operability. This effectively enables applications such as, e.g., fiber-based *in vivo* endomicroscopy, imaging and Raman spectroscopy^[37–42] as well as optical sensing^[2,63] and precise micro-manipulation^[21,44].

The divergence of a fiber beam, however, particularly remains a key issue in reaching earlier mentioned high numerical apertures of $NA > 0.8$ as required within single beam fiber optical trapping^[44,61,83]. An often reported solution, for example, relies on increasing the NA via implementing a focusing optic on the tip of a hybrid optical fiber^[52,86,144] (HOF, see subsection 2.1.2 and Table 6.1 for a detailed overview). Here, the fundamental concept for creating a high NA focal spot in front of the fiber principally relies on fusion splicing a length-invariant piece of a single-mode fiber (SMF) to a sub-millimeter short section of a multi-mode fiber (MMF, compare refs. [46, 145, 146]). This allows expanding the SMF beam in order to accommodate the full NA of a focusing lens, here specifically being implemented directly onto the facet of the HOF.

The unique combination of a diffractive lens structure, i.e., a meta-lens^[67], that is interfaced with an HOF is namely referred to as a meta-fiber in the following (compare refs. [42, 46, 84]). Here, this is specifically implemented onto the fiber tip using three-dimensional (3D) optical printing, i.e., direct laser writing (DLW). On the basis of a careful design, this effectively enables diffraction limited focusing of the meta-fiber beam as schematically visualized within Figure 6.1, while reaching an ultra-high NA of 0.88. Illustrated in the inset of Figure 6.1, the measured focal spot in particular forms the necessary requirement for flexible fiber-based remote optical trapping of individual freely diffusing particles in water using only a single SMF.

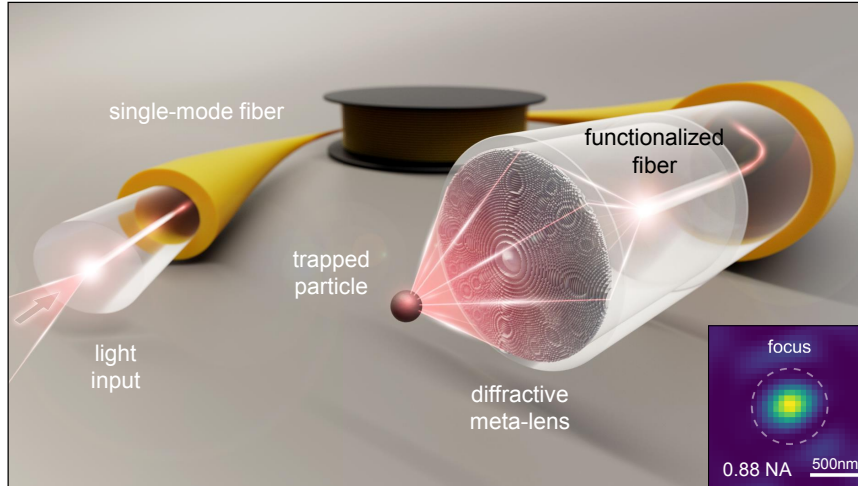


Fig. 6.1. Schematic visualization of an ultra-high NA meta-fiber optical trap (compare ref. [46]). A single-mode fiber is used as the input and functionalized at its output side for enlarging the usable fundamental mode cross-section, yielding a hybrid optical fiber (HOF). Its facet is structured with a diffractive meta-lens, creating a diffraction limited focal spot for optical trapping of single particles in water. The inset illustrates the measured spot at a wavelength of 660 nm, revealing an ultra-high numerical aperture of $NA = 0.88$.

In the following, first, the fundamental concept of a meta-fiber is introduced in detail (section 6.1), including the implementation of a functionalized hybrid fiber, 3D optical printing of a diffractive lens structure as well as a discussion about the limits of the meta-lens design. This is succeeded by characterizing the diffraction limited performance of the hybrid meta-fiber device, including a detailed analysis of potential aberrations (section 6.2). Finally, the chapter is concluded with an experimental demonstration of single meta-fiber-based optical trapping of individual silica microbeads as well as biologically relevant *Escherichia coli* (*E. coli*) bacteria, and the obtained results are compared to similar implementations and discussed in detail (section 6.3).

6.1 Meta-fiber concept

One solution to implement a beam shaping element on the tip of an optical fiber^[50,52,122], e.g., is to reduce the thickness of a bulk refractive optic^[37,122,146] into a thin diffractive optical element^[82,86,147] (DOE, details see Figure 2.3). In the following, a diffractive focusing lens is termed as meta-lens (compare refs. [46, 67, 84] and Table 6.1 for a detailed overview of similar concepts). Since a meta-lens represents a special type of phase element, it requires a well-defined phase of the incident beam (see Figure 2.4). Therefore, two possible options for its implementation exist:

1. To make use of the well-defined wavefront of a single-mode fiber (SMF), exhibiting a flat phase upon its emission from the facet, the meta-lens is implemented directly onto the core of the SMF^[147,148]. In principle, this is achieved via traditional (deep-UV or electron-beam) lithography (EBL) or focused ion beam (FIB) milling, while requiring large-scale machinery and clean room facilities for high resolution.

2. Femtosecond (fs)-direct laser writing (DLW), in contrast, commonly also referred to as three-dimensional (3D) optical printing^[52,122,149], represents a fast, cost-efficient, and reliable alternative relying only on conventional laser laboratory equipment. Due to its lower resolution, however, this requires a prior expansion of the well-defined SMF beam to accommodate a sufficiently large number of phase elements^[52,86].

In this section, first, expanding the SMF beam with its predictable phase resulting from the well-defined wavefront is demonstrated (subsection 6.1.1). Subsequently, a lithography-based fabrication technique for micro-structuring the meta-lens, i.e., DLW, is presented in detail (subsection 6.1.2). Finally, the section is concluded with a discussion about limiting factors in the meta-lens design with respect to applying DLW and interfacing with optical fibers (subsection 6.1.3).

6.1.1 Beam expansion

A key requirement for proper operation of a DOE, such as the previously introduced meta-lens, represents a well-defined phase of the incident beam. Here, this is effectively ensured via using an approximately 50 cm long piece of a conventional SMF with a core of diameter $2a = 3.5 \mu\text{m}$ (Thorlabs 630HP). In order for the SMF to comply with the design and implementation of the diffractive lens, however, the usable cross-section of its fundamental HE_{11} mode (see Figure 2.1) needs to be enlarged. Specifically, the SMF is thus functionalized via fusion splicing a short section of a multi-mode fiber (MMF) of larger core ($2a = 105 \mu\text{m}$, Thorlabs FG105LVA) to its end (compare refs. [46, 145, 146]), thus resulting in a functionalized single-mode fiber (see subsection 2.1.2).

Figure 6.2A demonstrates the concept of a large core functionalized hybrid SMF, while Figure 6.2B illustrates an implemented example of a fusion spliced short beam expansion section of length L . Here, various different samples of lengths ranging from $L = 400 \dots 800 \mu\text{m}$ were in principle fabricated (visualized in Figure 6.2C), while only fibers of $L \geq 720 \mu\text{m}$ effectively provide sufficiently enlarged beams for reaching fundamental mode diameters of about $\varnothing \approx 90 \mu\text{m}$ complying with the design of the meta-lens. In particular, this agrees with the estimated numerical aperture of $\text{NA}_{\text{fiber}} = n_{\text{SiO}_2} \sin\left(\arctan\left(\frac{\varnothing}{2L}\right)\right) \approx 0.09$ for the SMF, as resulting from a Fourier transformation and its obtained angular spectrum of the calculated fundamental mode (details see Figure 2.4, D and E). In the following, two samples are specifically referred to as (i) sample 1: $L_1 \approx 720 \mu\text{m}$ and (ii) sample 2: $L_2 \approx 750 \mu\text{m}$ (compare ref. [46]).

For all fabricated samples, images of the fiber mode were recorded, as exemplarily presented for sample 1 ($L_1 \approx 720 \mu\text{m}$ length) in Figure 6.2D. Here, a continuous wave (CW) laser diode emitting an optical power of $P_0 = 120 \text{ mW}$ at a wavelength of $\lambda = 660 \text{ nm}$ (Thorlabs L660P120) was used for exciting the fundamental mode (details of the setup and the optical microscope for recording the mode images see subsection 4.1.1). Specifically,

coupling efficiencies of $\eta > 60\%$ were reached to verify the excitation and guidance of only the fundamental hybrid SMF mode. Towards the end of the fiber, where the guided mode spreads out to the boundary of the silica cladding in air, total internal reflection (TIR) occurs, i.e., guiding in air. This effectively yields an interference pattern with the guided mode in the core, which is visible as the rings in Figure 6.2D. To obtain the mode field diameter (MFD, see subsection 2.1.1) of the guided mode, the azimuthal average of the intensity $I(r, \varphi)$ for the coordinate φ was calculated in order to preserve radial symmetry, and its $1/e^2$ value was subsequently determined, as displayed for sample 1 in Figure 6.2E.

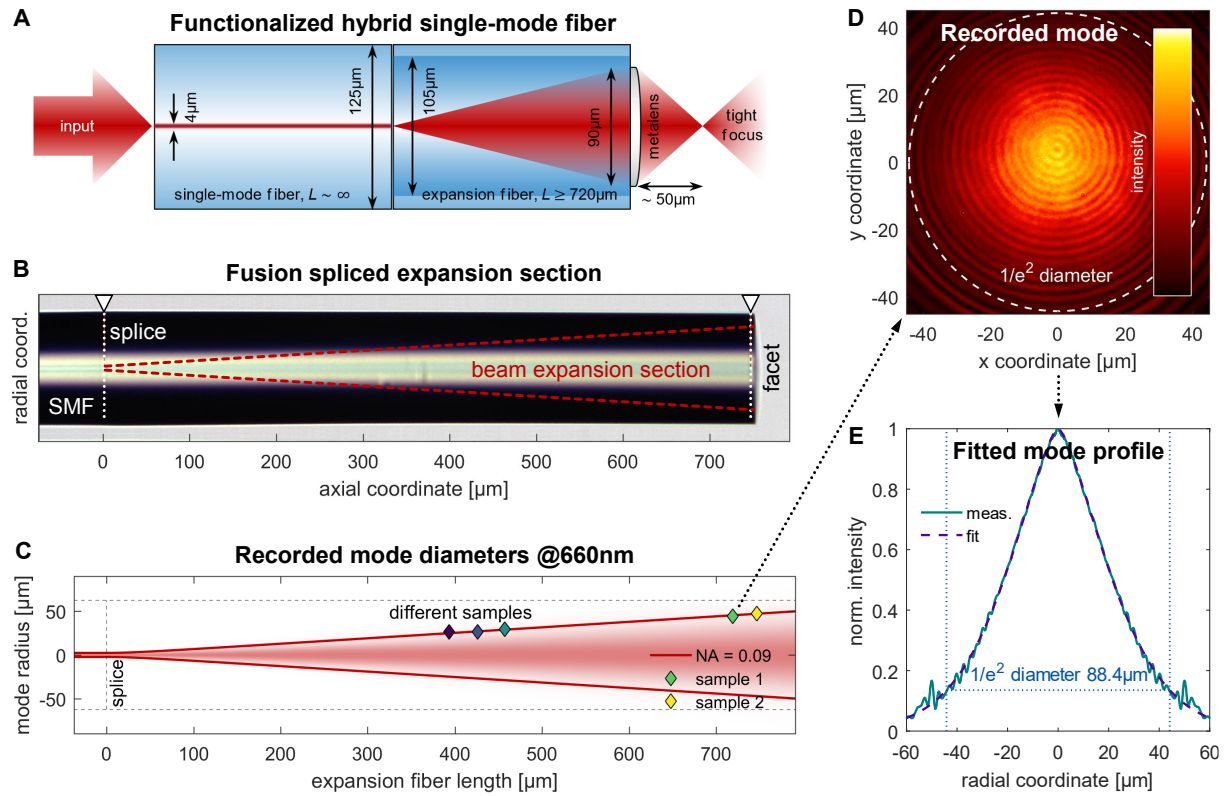


Fig. 6.2. Concept and experimental implementation of a functionalized hybrid single-mode fiber operating at a wavelength of 660 nm. (A) Concept of a large core hybrid optical fiber, consisting of a single-mode fiber (SMF) of small core ($4 \mu\text{m}$ diameter) combined with a multi-mode fiber (MMF) of larger $105 \mu\text{m}$ diameter core. (B) Example of an experimental implementation via fusion splicing the MMF section to the SMF. The dashed red line represents the expanded beam inside. (C) Recorded mode diameters of samples with lengths between $400 \mu\text{m}$ and $800 \mu\text{m}$. Here, sample 1 has a length of $720 \mu\text{m}$, and sample 2 one of $750 \mu\text{m}$. All samples exhibit numerical apertures of 0.09. (D) Recorded mode of sample 1 ($720 \mu\text{m}$), and (E) azimuthal average of the intensity profile with fit for the mode diameter. The ring pattern results from total internal reflection at the silica-air boundary of the MMF and interference with the guided mode inside the core.

Instead of fusion splicing a short beam expansion section onto the tip of the SMF, optical printing of a transparent spacer via 3D direct laser writing^[86,150] effectively represent another solution to homogeneously illuminate an attached optic. Within the following, the technique of DLW for 3D optical printing of a diffractive meta-lens directly onto the facet of the large core hybrid SMF is presented in detail.

6.1.2 Direct laser writing

When comparing reports on interfacing beam shaping elements with optical fibers^[42,52,122] (for a detailed overview see Table 6.1), it stands out that a majority of these concepts rely on lithography-based implementations. In general, these can be categorized into conventional molding and lift-off procedures^[51,147,148] and mask-less direct writing techniques^[52,59,149]. Femtosecond (fs)-direct laser writing (DLW), in particular, commonly also referred to as direct laser lithography or three-dimensional (3D) optical printing^[86,122], represents a mask-less technique relying on two-photon absorption-based polymerization^[52,59,149] via the formation of so-called voxel cells (as for volume pixels, Figure 6.3B). Not only do these principally allow for transparent micro-optical elements on the order of the wavelength^[52,59,149], but effectively represent the building blocks enabling the creation of arbitrary 3D structures^[52,86,122] (Figure 6.3A).

In contrast to structuring dielectrics such as, e.g., Si or TiO₂ via traditional (deep-) UV or electron-beam lithography (EBL)^[42,151], the 3D-capability of DLW provides a key advantage over EBL, which in principle only allows patterning in 2D, and effectively led to its application here. Alongside not requiring large-scale machinery and clean room facilities to achieve high resolution, DLW particularly stands out by its ease of use via relying only on conventional laser laboratory equipment, thus providing a straight-forward, small-scale, cost-efficient, fast and reliable technique in terms of reproducibility.

For optical printing, here, a commercial system (Photonic Professional GT, Nanoscribe GmbH) was used, consisting of a fs-pulsed laser at a wavelength of $\lambda = 780$ nm that is tightly focused via a $63\times$ oil immersion objective (Zeiss Plan-Apochromat, NA = 1.4) into a viscous drop of polymeric negative photoresist. Figure 6.3 demonstrates various examples of experimentally implemented structures using DLW, while here, specifically, the IP-Dip photoresist (Nanoscribe GmbH) was used. However, in principle a broad range of different resists exist^[152,153], such as IP-L 780, e.g., which effectively increases mechanical stability, thus allowing for 3D structures of high aspect ratios^[154] as exemplarily illustrated in Figure 6.3A for the printed sample of total height ≈ 675 μm .

Here, all samples were developed in a PGMEA bath (Sigma-Aldrich 484431) for 20 min, followed by a 2 min NovecTM (Sigma-Aldrich SHH0002) rinse after printing. Figure 6.3B displays an example of polymerized voxel cells, representing a zoomed-in region of a laser written thin diffractive lens that is visualized in Figure 6.3C. Specifically, the voxel cells are only formed where the local peak intensity I_{max} of the fs-laser pulse exceeds a certain threshold that initiates the polymerization, which thus locally hardens the resist^[52,149]. After washing out non-polymerized residue for revealing the final structure, this generally yields lateral feature sizes of ≈ 100 nm with aspect ratios of 1:3.

For stronger bonding between silica substrates and 3D printed microstructures for optical trapping applications in water, here, the substrates were treated via a silanization process

prior to DLW. Overall, this generally improves chemical and mechanical stability and effectively yields a better adhesion between SiO_2 and the polymer^[155,156]. Here, substrates were first activated via an oxygen plasma for 1 min (150 W power), followed by overnight immersion within 1% 3-(Trimethoxysilyl)propyl methacrylate (Sigma-Aldrich 440159) dissolved in ethanol, and finally dried with nitrogen. Figure 6.3D exemplarily shows the process of laser writing a diffractive meta-lens structure on the facet of an optical fiber, where the white bar represents the writing laser that is scanned via two galvanic mirrors.

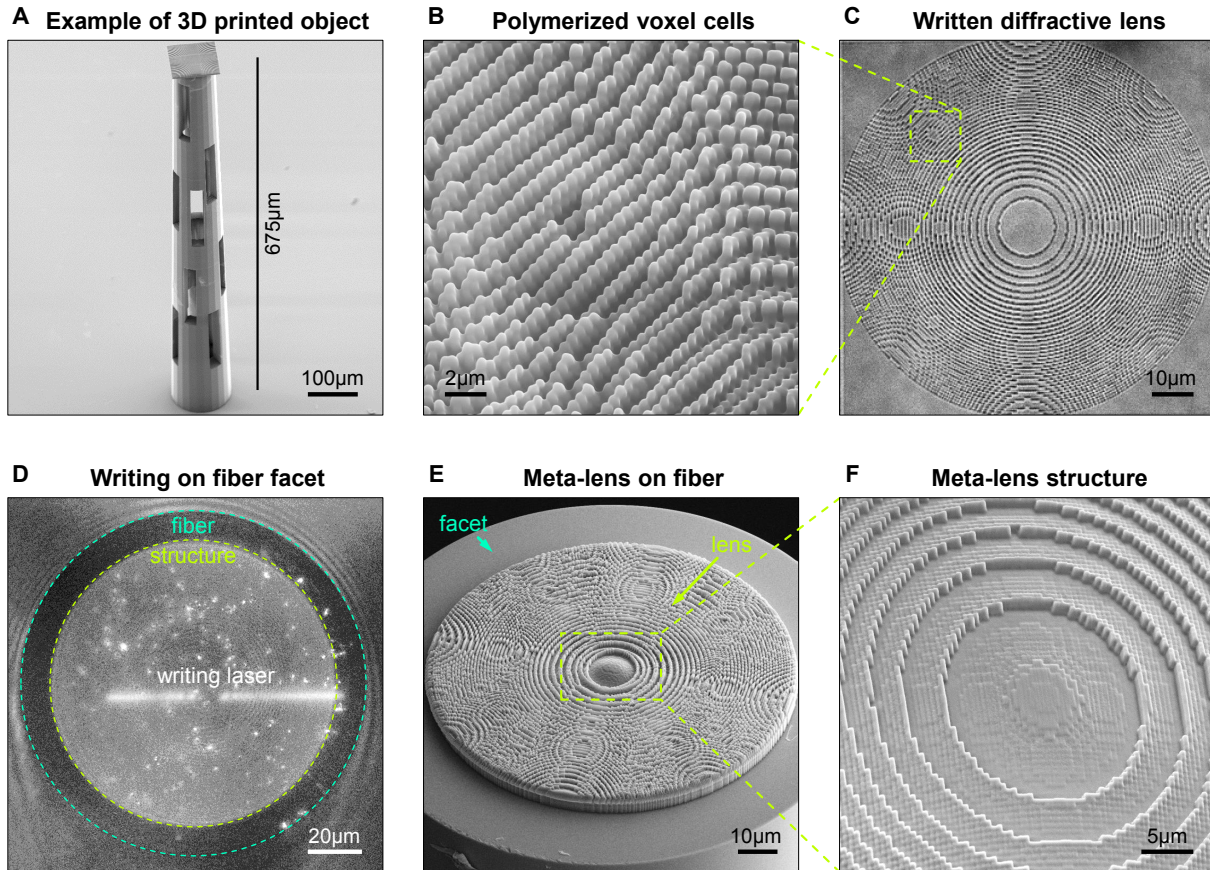


Fig. 6.3. Examples of experimentally implemented structures using 3D direct laser writing (DLW). (A) Example of an optically printed 3D structure reaching a total height of $675\ \mu\text{m}$. (B) Voxel cells resulting from femtosecond (fs)-pulsed laser induced two-photon absorption. The negative photoresist polymerizes only where the peak intensity of the laser pulse exceeds a certain threshold. (C) Laser written example of a diffractive lens on a planar substrate. (D) Process of laser writing a diffractive meta-lens structure (dashed green circle) on the flat-cleaved tip of an optical fiber (dashed cyan circle). The white bar shows the scanned writing laser. (E) Finished result of D, showing an example of an optically 3D printed meta-lens on a fiber tip. (F) Close-up image of the central region of E, effectively revealing the discretized structure of the meta-lens.

Before printing on its facet, however, the optical fiber was flat-cleaved, while no additional polishing or cleaning of its tip was performed. Figure 6.3E depicts a finished example of a meta-fiber, where a base layer of $h = 5\ \mu\text{m}$ height was printed first in order to promote strong mechanical connection. Here, a close-up image of the central region in Figure 6.3F effectively reveals the discretized meta-lens structure, specifically requiring an approximate printing time of $t = 1\ \text{h}$ for a final height of $h = 3\ \mu\text{m}$ (compare ref. [46]).

As generally found within optical techniques, however, a bottleneck lies within the applied wavelength λ , both for imprinting, i.e., encoding a structure, as well as for its later read-out, i.e., the decoding. Here, DLW imposes limits to the meta-lens design via the minimum achievable printing resolution Δx , which is implied by the wavelength λ and is discussed within the following. One solution to decrease the wavelength-dependent resolution $\Delta x(\lambda)$, e.g., represents the principle of stimulated-emission-depletion (STED)-DLW^[157–159].

6.1.3 Lens design limits

In the design of an optically printed meta-lens, principally two main limiting factors arise, both in encoding, i.e., printing, as well as in decoding, i.e., later read-out of the phase structure (compare ref. [46]). Effectively, these are caused by different origins, however, both are implied by wavelength-dependent properties of the respective laser sources:

1. **Aliasing** The spatial discretization of a phase element, in particular, establishes limits to the maximum resolvable phase change between two adjacent pixels via the minimum lateral resolution Δx (implied by the printing process and the wavelength λ of the used writing laser). Defined via the Nyquist-Shannon theorem^[160], in case this limit is violated, this effectively yields the issue of undersampling, i.e., aliasing.
2. **Coherence** A finite spectral bandwidth $\Delta\lambda$ of the used trapping laser during the read-out process, on the other hand, effectively limits the requires coherent interference of wavefronts emerging from all phase elements of the diffractive meta-lens. This mainly affects the geometry and thus the effective NA of the printed lens.

Within the following, these two limits are discussed individually, while here, the design of the meta-lens was specifically calculated for its operation within an aqueous medium.

Aliasing (writing)

Since a meta-lens in principle represents a phase-element, it is effectively prone to aliasing when spatially discretizing its phase profile $\phi(x)$ within the computer-based implementation of DLW (compare refs. [46, 84, 161]). The Nyquist-Shannon theorem^[160], in particular, defines the maximum resolvable phase change $\Delta\phi(x)$ between two adjacent pixels:

$$\left| \frac{\Delta\phi}{\Delta x} \right| \approx \left| \phi'(x) \right| < \frac{\pi}{\Delta x}, \quad (6.1)$$

where $'$ denotes the derivative with respect to the lateral coordinate x .

However, the pixel pitch Δx , generally does not represent the actual width of the finest spatially resolvable feature size d as of the Abbe criterion (see Equation 2.14), since voxel cells are effectively polymerized only above a certain threshold I_{\max} via the

two-photon process (see subsection 6.1.2). Within the optical printing here, a pixel specifically consists of multiple half-overlapping voxels (see Figure 6.3B) set to a lateral resolution, i.e., hatching, of 50 nm and vertical stacking, i.e., slicing, of 200 nm, being well below the Abbe resolution limit. For a diffractive polymer lens of phase profile $\phi(x)$, height $h = \lambda/(n_l - n_m) \approx 3 \mu\text{m}$ and refractive index n_l operating within an aqueous medium of refractive index n_m , this yields ≈ 16 layers including the base layer.

In case Equation 6.1 is violated, however, the imprinted profile of the meta-lens is effectively undersampled, i.e., aliased, and higher diffraction orders emerge. While the focal length f , in principle, remains constant, the constructively contributing fraction of the lens diameter \varnothing and thus the geometric numerical aperture of $\text{NA} = n_m \sin\left(\arctan\left(\frac{\varnothing}{2f}\right)\right)$ particularly are reduced. Figure 6.5A exemplarily illustrates the design of an undersampled diffractive lens (resolution $\Delta x = 500 \text{ nm}$, diameter $\varnothing = 125 \mu\text{m}$, focal length $f = 50 \mu\text{m}$, resulting nominal $\text{NA} \approx 0.8$), whose simulated focusing in air for an incident plane wave is

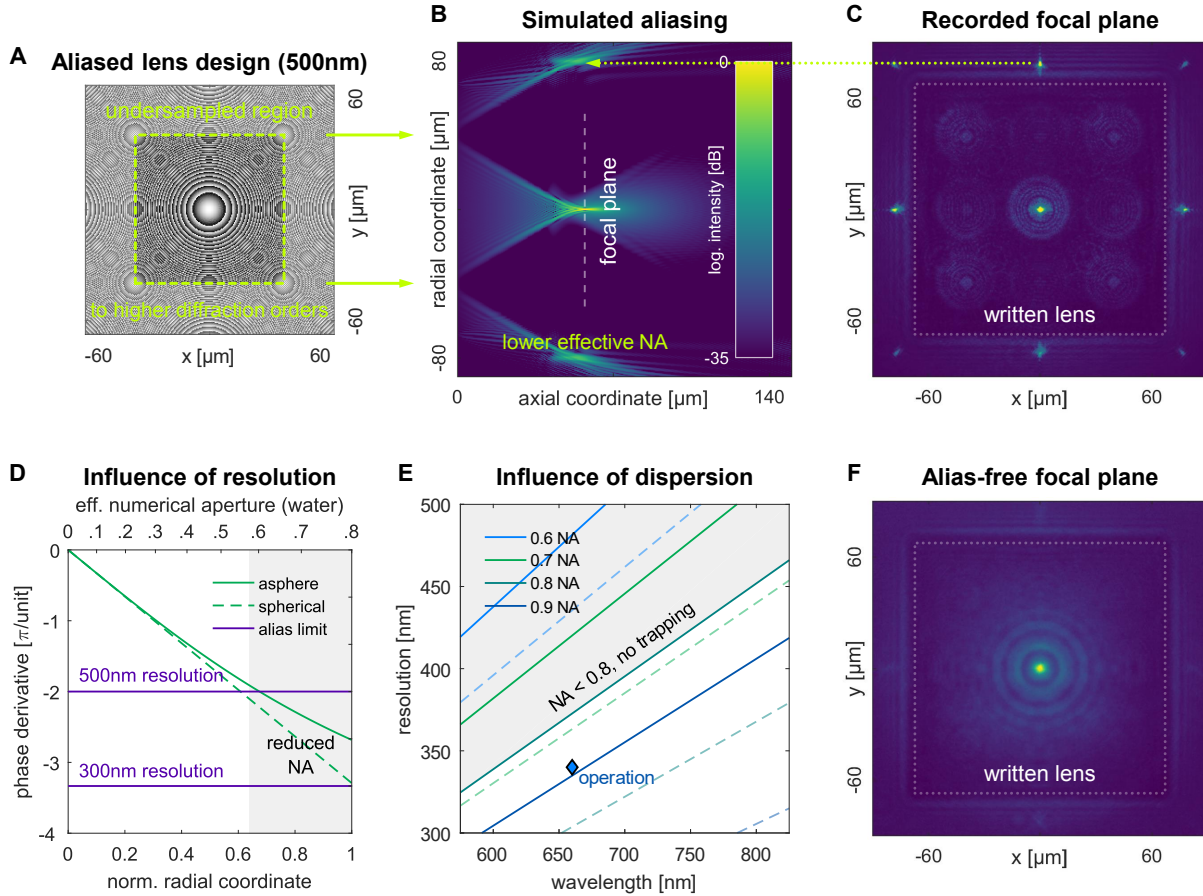


Fig. 6.4. Influence of lateral resolution on the effective numerical aperture (NA) of a diffractive lens. (A) Example design of an aliased lens (nominal 0.8 NA, 500 nm resolution), and (B) simulated focusing in air. The undersampled region in A (dashed green square) lowers the effective NA by contributing to higher diffraction orders while keeping the focal length constant. (C) Experimentally recorded focal plane at a wavelength of 660 nm for a laser written example of A. The bright spots on the edges indicate aliasing. (D) Influence of resolution and (E) dispersion on the effective NA in water for two different phase profiles (see main text). An alias-free operation at $\text{NA} \geq 0.8$ for single beam optical trapping requires at least a resolution of 350 nm at a wavelength of 660 nm. (F) Recorded focal plane of the sample in C, written at an alias-free 300 nm resolution.

demonstrated in Figure 6.4B. Here, an example sample of this lens was optically printed onto a planar substrate, and its focusing was experimentally recorded at a wavelength of $\lambda = 660$ nm as visualized for the focal plane in Figure 6.3C. Specifically, aliasing is revealed via the higher diffraction orders as the bright spots towards the edges of the printed structure, overall being in line with the simulation presented in Figure 6.4B.

In Figure 6.4D, the incremental phase change, i.e., the derivative $\phi'(r)$ with respect to the radial coordinate r , of Equation 6.1 for the ideal profile of a diffractive asphere (see Equation 2.8, $\phi'_{\text{ideal}}(r) = -kr/(f^2 + r^2)^{1/2}$, solid line) is compared to the parabolic approximation of a spherical lens (see Equation 2.9, $\phi'_{\text{par}}(r) = -kr/f$, dashed line, compare ref. [46]). Here, $k = 2\pi n_m/\lambda$ denotes the wavenumber in water, and both functions are normalized to their radial coordinate r reaching unity at the edges of the lens. This specifically reveals how the minimum achievable resolution Δx limits the maximum resolvable inter-pixel phase change $\Delta\phi$ and thus the usable fraction of the diameter \emptyset as well as the effective geometric NA of the lens. Towards the edges ($r \rightarrow 1$), in particular, the ideal profile $\phi_{\text{ideal}}(r)$ exhibits less curvature than the parabolic approximation $\phi_{\text{par}}(r)$, thus being used in the following for achieving a higher NA of the diffractive lens while principally requiring the same printing resolution Δx .

Figure 6.4E depicts the dispersion of the phase profile $\phi(r, \lambda)$ as a function of the trapping laser wavelength λ , which strongly affects the minimum resolution $\Delta x(\lambda)$ required to prevent aliasing. Here, a wavelength of $\lambda = 660$ nm requires a minimum resolution of $\Delta x(\lambda = 660 \text{ nm}) = 350$ nm for alias-free operation of a diffractive lens with an NA of at least 0.8 in water (required within single beam optical trapping, compare refs. [44, 46, 83]). Figure 6.4F experimentally confirms the alias-free operation of an exemplary written sample of the same planar lens structure as previously displayed in Figure 6.4C, which here, in contrast, was printed at a resolution of $\Delta x = 300$ nm.

Coherence (read-out)

Since the concept of a diffractive lens with its discretized phase structure (see Figure 6.3F) effectively relies on the Huygens-Fresnel principle (see subsection 2.2.2), a sufficiently large number of elements is required for imprinting its phase and shaping the wavefront of an incident beam. Here, the focusing efficiency is assumed to increase with the number of elements, i.e., the pixels within a computer-generated phase mask, and highest performance with respect to the NA (at least ≥ 0.8) is thus achieved in case all wavefronts emerging from the phase structure interfere coherently.

However, the spectral bandwidth $\Delta\lambda$ and the resulting coherence length $L_{\text{coh}} = \lambda^2/(n_m\Delta\lambda)$ of a trapping laser effectively limit the contribution of the entire meta-lens diameter \emptyset , which corresponds to a number of $N_{\text{Fres}} = \phi\left(\frac{\emptyset}{2}, \lambda\right)/(2\pi)$ Fresnel zones (see subsection 2.2.1 and Figure 6.5A). For maximum performance and efficiency, the coherent

interference of all radial Fresnel zones thus demands (compare ref. [46]):

$$L_{\text{coh}} > \lambda N_{\text{Fres}}. \quad (6.2)$$

Figure 6.5A demonstrates the influence of spectral properties, i.e., wavelength λ and bandwidth $\Delta\lambda$, of a trapping laser on the number of coherently interfering Fresnel zones F_{Fres} and the resulting effective geometric NA for a diffractive lens in water. For reaching sufficiently high $\text{NA} \geq 0.8$ at a wavelength of $\lambda = 660 \text{ nm}$, a spectral bandwidth of $\Delta\lambda < 15 \text{ nm}$ is effectively required, here specifically being ensured via a CW laser diode (Thorlabs L660P120, $\Delta\lambda = 13 \text{ nm}$) that is consistently used throughout all following considerations. Figure 6.5B illustrates a map of influenced geometric parameters, i.e., diameter \varnothing and focal length f , of the meta-lens, as well containing all previously discussed design limits for a coherent operation in water at a wavelength of $\lambda = 660 \text{ nm}$. While the minimum achievable resolution Δx within 3D printing and the attributed effect of aliasing represent limitations for high NAs, the bandwidth $\Delta\lambda$ and the resulting coherence length L_{coh} of a trapping laser particularly represent key limitations for ultra-high NAs.

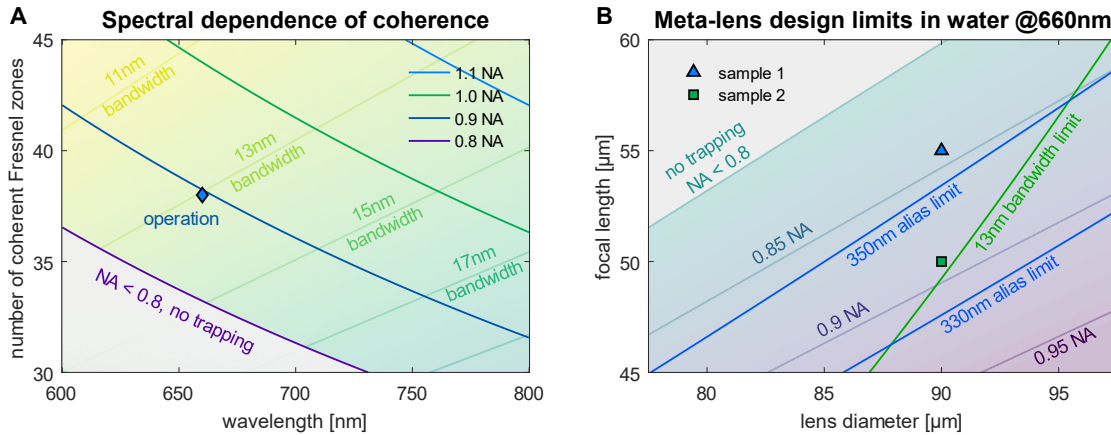


Fig. 6.5. Calculated influence of spectral bandwidth on the coherent operation of a high numerical aperture (NA) meta-lens in water. (A) Number of interfering Fresnel zones and resulting effective geometric NA as a function of wavelength and spectral bandwidth of the trapping laser. A high $\text{NA} \geq 0.8$ for single beam optical trapping demands fewer than 15 nm bandwidth. (B) Resulting geometry, i.e., lens diameter and focal length, for coherent operation of the meta-lens at a wavelength of 660 nm. While resolution and aliasing represent key limitations for high NAs (sample 1: 55 μm focal length at 330 nm resolution), ultra-high NAs (sample 2: 50 μm at 300 nm resolution) are mainly limited by a finite bandwidth and resulting coherence of the trapping laser. Both samples exhibit diameters of 90 μm , corresponding to 0.84 NA and 0.89 NA, respectively.

Here, two samples of the same lens diameter $\varnothing = 90 \mu\text{m}$ (consistently used throughout all following calculations and experiments) but of different remaining parameters (lateral resolution $\Delta x_{1,2}$ and focal length $f_{1,2}$ with corresponding nominal $\text{NA}_{1,2}$) were printed:

- (i) sample 1 ($L_1 \approx 720 \mu\text{m}$): $f_1 = 55 \mu\text{m}$, designed $\text{NA}_1 = 0.84$, $\Delta x_1 = 330 \text{ nm}$, and
- (ii) sample 2 ($L_2 \approx 750 \mu\text{m}$): $f_2 = 50 \mu\text{m}$, designed $\text{NA}_2 = 0.89$, where the minimum resolution within two-photon based optical printing was assumed to be $\Delta x_2 = 300 \text{ nm}$.

In the following, characterizing sample 2, particularly, is discussed based on experimentally recording its focusing performance to verify the ultra-high NA_2 of 0.89.

6.2 Focusing performance

While previously, the concept of a large core functionalized hybrid fiber (see Figure 6.2) and the individual design of a high NA diffractive meta-lens were discussed in detail (Figure 6.5B), this section in particular focuses on their explicit combination. For its proper operation while achieving diffraction limited performance in combination with the hybrid SMF (which requires correctly representing its phase and thus considering the incident wavefront), however, the design of the meta-lens needs to be adapted. Ideally, a Shack-Hartmann wavefront sensor consisting of a microlens array is thus used for characterizing an incident beam, since an incorrectly represented wavefront in the diffractive meta-lens design effectively results in incorrect operation.

Within this section, first, a preliminary analysis of (i) errors due to a general wavefront uncertainty and (ii) specifically a spherical aberration resulting from the wavefront of the hybrid SMF is carried out (subsection 6.2.1). Finally, a detailed experimental investigation via measuring the focusing performance and the NA of the adapted meta-lens design that is implemented on the facet of a large core functionalized hybrid fiber, i.e., the meta-fiber, completes the section (subsection 6.2.2, compare ref. [46]).

6.2.1 Wavefront errors

As previously mentioned, an incorrectly represented wavefront within the design and the implementation of a diffractive meta-lens in combination with an optical fiber effectively leads to an erroneous operation. In principle, these errors are of different origins:

1. wavefront errors resulting from a general uncertainty of the wavefront, and
2. specifically a spherical aberration due to disregarding the fiber wavefront.

In the following, these two errors are discussed individually, while first, the influence of a general wavefront uncertainty on the focusing performance of a diffractive lens is qualitatively investigated within an experimental comparison. Subsequently, the performance of the meta-lens is determined within a simulation in order to quantitatively analyze spherical aberrations and particularly to adapt the specific design of the meta-fiber.

Unknown wavefront

Here, a qualitative experimental comparison between various examples of incident wavefronts (Figure 6.6, A to C, details see Figure 2.4) and their influence on the combination

with optically 3D printed diffractive lenses (Figure 6.6, D and E) is made. Specifically, all experiments were carried out at a wavelength of $\lambda = 660$ nm, while the lenses were designed with respect to operating within their intended media (air or water).

A plane wave of flat phase $\Phi_{\text{plane}}(x, y) = 0$, whose intensity $I(x, y)$ is given in Figure 6.6A, in combination with a planar lens (Figure 6.6D) yields the expected result of an Airy disc in the focal plane as shown within Figure 6.6F. Principally, the focal spot is nearly diffraction limited, but here appears comparably large due to the low NA lens. The mode profile of a multi-mode fiber (MMF), however, as exemplarily visualized in Figure 6.6B, with its not only chaotic but totally incoherent wavefront (see Figure 2.4, A to C), effectively yields a much larger focal spot when interfaced with the same planar lens, which is presented in Figure 6.6G. Due to incoherent emission at its facet, the resulting focal spot exhibits a diameter of $\varnothing_{\text{spot}} = 2f \tan(\arcsin(\text{NA}_{\text{fiber}}))$ as predicted by geometric optics.

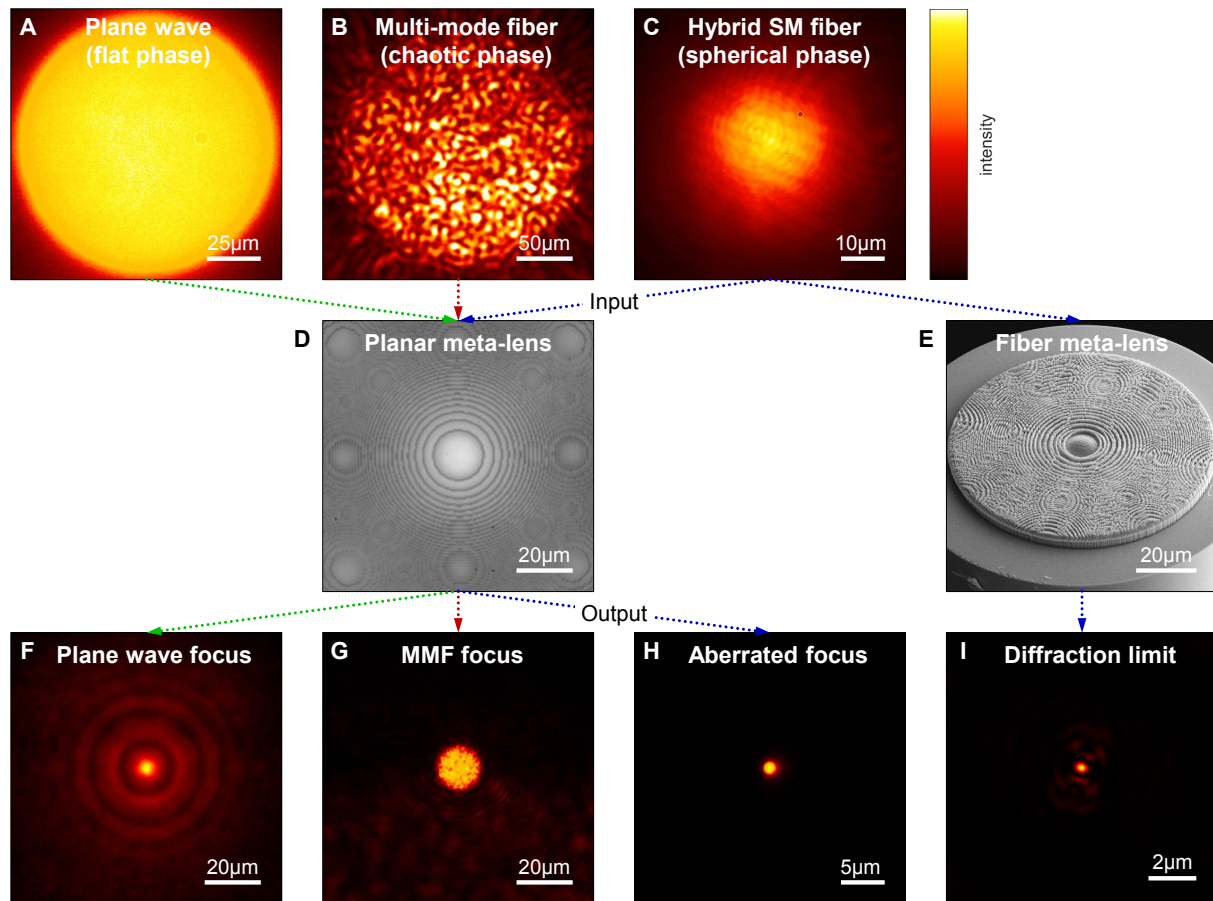


Fig. 6.6. Influence of different experimental wavefronts on the focusing performance of diffractive lenses at a wavelength of 660 nm. Different combinations of (A–C) incident wavefronts with (D) a planar diffractive lens or (E) a fiber corrected meta-lens yield (F–G) different respective patterns in the focal plane. (A) The flat phase of a plane wave combined with the planar lens in D results in (F) a near diffraction limited focal spot. (B) A multi-mode fiber (MMF) of chaotic phase and incoherent wavefront in combination with D yields a larger spot diameter as obtained by geometric optics. (C) The spherical wavefront of a hybrid optical single-mode fiber (SMF) combined with the planar lens in D results in (H) a spherical aberration of the focus. (E) A fiber corrected meta-lens design is required to achieve (I) diffraction limited focusing performance.

Figure 6.6C, in contrast, displays the fundamental HE_{11} mode of a hybrid single-mode fiber (SMF, details see Figure 6.2D), which principally exhibits a well-defined spherical phase $\Phi_{\text{fiber}}(x, y)$ (see Figure 2.4, D to F). Combined with a planar diffractive lens (Figure 6.6D), in particular, this yields a spherical aberration as depicted in Figure 6.6H. For diffraction limited focusing, however, as shown in Figure 6.6I, this specifically demands canceling the spherical fiber wavefront phase $\Phi_{\text{fiber}}(x, y)$ first, using an adapted meta-lens design (Figure 6.6E), followed by shaping the incident beam via imprinting the new phase of the diffractive focusing lens (compare Figure 2.4, G to I, and ref. [46]).

To determine the influence of a spherical wavefront on the focusing performance of the meta-fiber, its interfacing with a diffractive lens was quantitatively analyzed via explicitly simulating the scenarios shown in Figure 6.6, H and I, as discussed in the following.

Spherical aberration

In contrast to Figure 6.6, H and I, where generic wavefront errors were only qualitatively compared, here, the diffraction limited (see subsection 2.2.2) performance of the meta-fiber, as quantitatively analyzed within a simulation, is discussed. Specifically, all calculations assume its operation in water at a wavelength of $\lambda = 660 \text{ nm}$, and the focusing was calculated using the beam propagation method (BPM, details see subsection 2.2.2). After emerging from the aperture of a conventional SMF, wavefronts of the divergent beam are curved with a radius of $R(z) = z \left[1 + (z_{\text{R}}/z)^2 \right]$ and the fiber effectively acts as a negative spherical lens of focal length $-f = R(z) \approx z$ for propagation distances $z \gg z_{\text{R}} \sim 10 \dots 30 \mu\text{m}$ (typical Rayleigh lengths in the visible, see Equations 2.6c and 2.6b). Figure 6.7, A and B, shows the calculated beam profile, i.e., the intensity $I(r, L_{\text{min}})$ and the phase $\Phi(r, L_{\text{min}})$, of a hybrid SMF for a beam expansion section of minimum length $L_{\text{min}} = 720 \mu\text{m}$, where the fiber exhibits the phase (see Equation 2.7 and Figure 2.4F):

$$\Phi_{\text{fiber}}(r, L_{\text{min}}) \approx kL_{\text{min}} - \arctan(L_{\text{min}}) + \frac{kr^2}{2L_{\text{min}}}, \quad (6.3)$$

and $k = 2\pi n_{\text{m}}/\lambda$ is the wavenumber within the aqueous medium of refractive index n_{m} .

The spherical phase $\Phi_{\text{fiber}}(r, L_{\text{min}})$ of the fiber, however, additionally contributes to the overall phase $\Phi_{\text{tot}}(r, f, L) = \Phi_{\text{meta}}(r, f) + \Phi_{\text{fiber}}(r, L)$ of the combined meta-fiber system, i.e., meta-lens of focal length f on expansion section of length L , which effectively yields a spherical aberration due to its curved wavefront. Figure 6.7, C to E, exemplarily illustrates the simulated focusing performance for a diffractive meta-lens of phase $\Phi_{\text{meta}}(\emptyset, f_2) = \text{mod}(\phi_{\text{ideal}}(90 \mu\text{m}, 50 \mu\text{m}), 2\pi)$, i.e., sample 2 of designed $\text{NA}_2 = 0.89$, which is illuminated via the calculated beam of the hybrid fiber (Figure 6.7, A and B, compare ref. [46]). While the inset in Figure 6.7C displays the focal plane, where the dashed line denotes the Airy width, the intensity profiles $I(r, z = 0)$ and $I(r = 0, z)$ along the focal symmetry

axes are given in Figure 6.7, D and E, respectively. For determining the NA, the profiles were fitted along their respective directions according to the diffraction theory (details see Equations 2.13a and 2.13b) as represented by the dashed curves, while the dotted lines indicate the full width half maximum (FWHM) of the focal spot.

Due to the uncorrected fiber wavefront curvature, the focal region suffers from a negative spherical aberration, i.e., the retarded focusing of marginal rays, which is effectively visible as the opposite effect to that obtained from a spherical lens (see Figures 2.3B and 2.5, D and F). This reduces the NA of the meta-fiber by ~ 0.1 to $NA < 0.8$, yielding an axial shift of the focal plane by $\Delta f \sim 5 \mu\text{m}$. To improve the focusing performance of the meta-fiber for reaching ultra-high NAs, however, the concept relies on including a correction term for the spherical aberration of the fiber wavefront. Therefore, the spherical phase $\Phi_{\text{fiber}}(r, L)$ of the hybrid fiber is canceled first, followed by shaping the incident beam and imprinting the new phase $\Phi_{\text{meta}}(r, f)$ of the meta-lens (details see Figure 2.4,

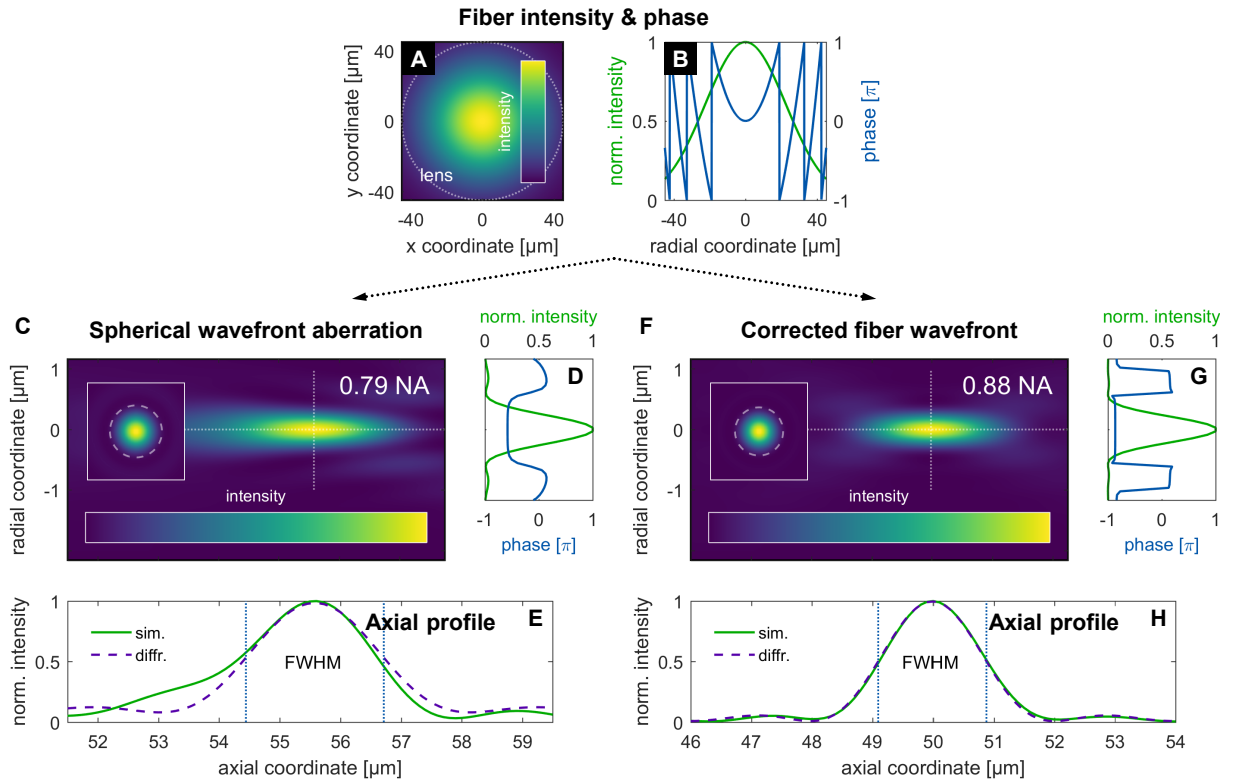


Fig. 6.7. Calculated spherical aberration and correction for diffraction limited performance of a meta-fiber in water at a wavelength of 660 nm. (A) Intensity and (B) phase profile of the beam emitted by a large core functionalized hybrid single-mode fiber (SMF). The fiber exhibits a near Gaussian intensity profile and a well-defined spherical phase. (C) Rotational symmetric, (D) radial and (E) axial profile along the symmetry axes of the focal region indicated by the dotted lines in C when interfacing the hybrid fiber with a planar diffractive meta-lens (inset: focal plane, dashed: width of Airy function). The solid green lines represent the measured curves, the dashed one the fit according to the diffraction theory, and the dotted ones the full width half maximum (FWHM) of the focal spot. A positive spherical aberration due to the curved wavefront of the SMF reduces the designed numerical aperture (NA) by ~ 0.1 to $NA < 0.8$ (see main text). (F–H) Same as in C–E for implemented correction of the curved fiber wavefront within the meta-lens design. The fitted intensity profiles reveal a diffraction limited ultra-high NA of 0.88 for the focal spot of the meta-fiber.

G and H). Here, the spherical aberration as an example of a phase anomaly, in particular, allows for straight-forward correction via a diffractive optic, i.e., the phase-type meta-lens, thus representing a key advantage over traditional refractive optics.

Figure 6.7, F to H, in contrast, shows the simulated focusing performance for a meta-fiber (sample 2, designed $\text{NA}_2 = 0.89$) that particularly includes the wavefront correction, i.e., $\Phi_{\text{tot}}(r, f_2, L_{\text{min}}) - \Phi_{\text{fiber}}(r, L_{\text{min}})$. Here, a minimum length of $L_{\text{min}} = 720 \mu\text{m}$ was assumed to be sufficiently long for a free expansion of the SMF mode across the MMF section and filling the entire lens aperture, effectively yielding a very high numerical aperture of $\text{NA}_{\text{sim}} = 0.88$. Directly compared to the uncorrected design, however, the included wavefront correction exhibits a flat phase $\Phi_{\text{fiber}}(r)$ in the focal plane being only modulated by a value of π , and represents a perfect match of the simulated profile with the design parameters, i.e., $f_2 = 50 \mu\text{m}$ focal length. Specifically, the simulated NA_{sim} of 0.88 deviates only little from the designed value of $\text{NA}_2 = 0.89$ as a result of numerical errors and the illumination with a Gaussian profile instead of a plane wave.

However, due to experimental tolerances within the precision of cleaving a short section of the beam expansion fiber as well as the unavailability of a Shack-Hartmann wavefront sensor for characterizing individual samples, here, a generic meta-lens design was applied to all functionalized fibers. This specifically assumes an underestimated expansion section of length L_{min} , effectively yielding an over-corrected positive spherical aberration (see Figure 2.5, D and F) due to a stronger curvature of the fiber wavefront than an overestimated length of $L > L_{\text{min}}$. Nevertheless, this generally has a smaller impact on the performance than an under-corrected negative spherical aberration (Figure 6.7, C and E) and as well leaves room for possible deviations of the actual from the assumed fiber wavefront within the meta-lens design for the correct length L of the expansion section. To confirm the simulated ultra-high NA_{sim} of 0.88 (designed $\text{NA}_{2,\text{theor}} = 0.89$), the focusing performance of sample 2 was experimentally analyzed as discussed in the following.

6.2.2 Implemented meta-fiber

While previously, only a qualitative comparison (Figure 6.6, E and I) and a simulation (Figure 6.7) revealed the diffraction limited performance of the meta-fiber, here, its experimentally determined focusing for confirming the simulated ultra-high numerical aperture of $\text{NA}_{\text{sim}} = 0.88$ is discussed. Therefore, a continuous wave (CW) laser diode of emission wavelength $\lambda = 660 \text{ nm}$ and bandwidth $\Delta\lambda = 13 \text{ nm}$ (Thorlabs L660P120) was used for coupling light into a final implementation of the meta-fiber. In particular, this included the spherical wavefront corrected design of the diffractive meta-lens being implemented on the facet of a large core functionalized SMF, i.e., sample 2 (MMF length $L_2 \approx 750 \mu\text{m}$, focal length $f_2 = 50 \mu\text{m}$, nominal $\text{NA}_2 = 0.89$, see Figure 6.3, E and F).

Here, the beam profile of the meta-fiber was imaged from the front using an inverted microscope (similar to Figure 4.2), consisting of a $60\times$ water dipping objective (Nikon CFI Apo NIR, NA = 1.0), followed by an achromatic tube lens of focal length $f = 300$ mm and a CMOS camera (Basler acA640-750uc, $4.8\ \mu\text{m}$ pixel size). Specifically, the tip was immersed from the top into a water reservoir created around the objective using paraffin, followed by scanning the focal region along the axial direction z using a piezo-driven objective collar (Mad City Labs Nano-F100) in steps of $\Delta z = 100$ nm. At every step, micrographs for three different exposure times of $\tau = 0.1, 1, 10$ ms were taken and subsequently combined into high-dynamic range (HDR) images noise of floor $< 10^{-5}$. Finally, the resulting HDR images were individually sub-pixel centered using the image shift algorithm (see subsection 4.1.2), averaged over the azimuthal coordinate φ (Figure 6.8, E and F, compare Figure 6.2E and ref. [46]), and axially stacked (Figure 6.8, E and G).

Figure 6.8 demonstrates the experimentally recorded beam profile of a meta-fiber (sample 2) with diffraction limited performance in the focal region. In Figure 6.8, A to D, cross-sections of various different intermediate positions z through the focus are illustrated, where Figure 6.8C visualizes the focal plane and the dashed circle represents the width of

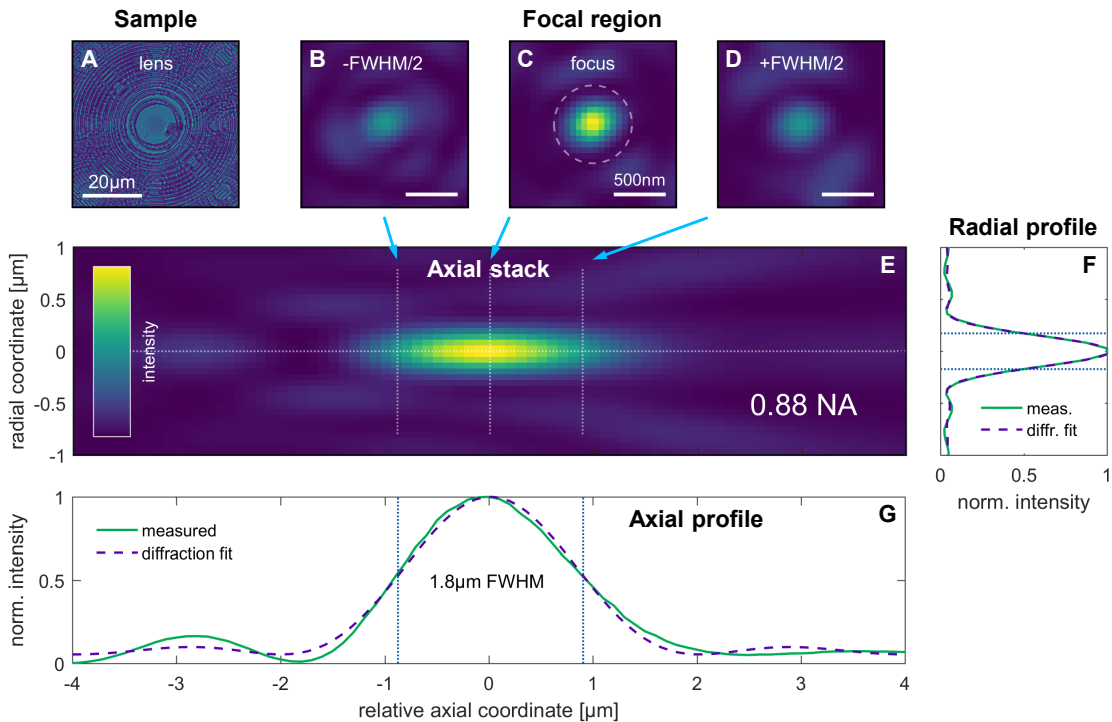


Fig. 6.8. Experimental focal scan verifying the diffraction limited ultra-high numerical aperture (NA) of the meta-fiber in water at a wavelength of 660 nm. (A) Micrograph of the sample plane and (B–D) of different intermediate axial planes in the focal region. (B, D) Negative and positive end of the full width half maximum (FWHM) range, respectively, and (C) focal plane as indicated by the arrows. The dashed circle denotes the width of the Airy function. (E) Rotational symmetric, (F) radial and (G) axial profile relative to the focal plane along the symmetry axes as indicated by the dotted lines in E. The solid curves represent the measured profiles, the dashed ones the respective fits to the diffraction theory, and the dotted ones the FWHMs of the focal spot. The fitted intensity profiles reveal an ultra-high NA of 0.88 for the focal spot, experimentally confirming the diffraction limited operation of the meta-fiber and the prior simulated results.

the Airy function. The radially dependent intensity $I(r, z = 0)$ and the profile $I(r = 0, z)$ on the optical axis z are displayed in Figure 6.8, F and G, respectively, while both profiles were fitted to the corresponding equations describing a diffraction limited focal spot (Equations 2.13a and 2.13b).

Here, the measured value of $\text{NA}_{\text{meas}} = 0.88$ experimentally confirms the diffraction limited ultra-high NA, while being in excellent agreement with the previous simulation and matching the result of $\text{NA}_{\text{sim}} = 0.88$ ($\text{NA}_{2,\text{theor}} = 0.89$). The positive spherical aberration in Figure 6.8, E and G, at a relative position of $z = \pm 3 \mu\text{m}$ (opposite to the simulated scenario in Figure 6.7, C and E), in particular, results from the over-corrected wavefront curvature – an effect of the implemented generic design for an expansion section of length $L_{\text{min}} = 720 \mu\text{m}$ instead of the longer $L_2 \approx 750 \mu\text{m}$ of sample 2 here.

6.3 Meta-fiber optical trapping

The key aim for previously analyzing the meta-fiber focusing performance in such detail particularly represents demanding $\text{NA} > 0.8$ for optical trapping of freely diffusing individual micro-objects in water along all three spatial dimensions simultaneously with only a single beam (compare refs. [44, 46, 83]). In this context, first, the trapping of individual silica microbeads and *Escherichia coli* bacteria (both identical to as in chapter 5) with a single meta-fiber was experimentally demonstrated (subsection 6.3.1). Subsequently, its performance with respect to trapping the silica beads was analyzed (subsection 6.3.2). Finally, the obtained results are assessed in terms of trapping performance, and a comparison to similar literature reported concepts is drawn (subsection 6.3.3).

6.3.1 Experimental demonstration

Here, all trapping experiments were carried out within aqueous solutions at a wavelength of $\lambda = 660 \text{ nm}$, while a continuous wave (CW) laser diode emitting an optical power of $P_0 = 120 \text{ mW}$ (Thorlabs L660P120) was used for coupling light into a functionalized meta-fiber (sample 1: focal length of $f_1 = 55 \mu\text{m}$, designed $\text{NA}_{1,\text{theor}} = 0.84$, and sample 2: $f_2 = 50 \mu\text{m}$, measured $\text{NA}_{2,\text{meas}} = 0.88$). Specifically, both samples reached optical powers of $P > 30 \text{ mW}$ (sample 1: $P_1 = 31 \text{ mW}$, sample 2: $P_2 = 33.5 \text{ mW}$) measured at their respective outputs after the combined system of hybrid fiber with diffractive meta-lens tip. For a consistent particle concentration c throughout all experiments, here, the silica beads of diameters $2R = 2 \mu\text{m}$ (Micromod Inc.) were diluted at a ratio of 1:2000, while the *Escherichia coli* (*E. coli*) bacteria were 1:10-fold diluted from their stock solution within ultra-pure water, both yielding final concentrations of $c \sim 6 \cdot 10^6 \text{ cm}^{-3}$.

For optical trapping, a drop of a few ten microliters of the particle solution was pipetted into the windowed sample chamber (see Figure 4.2C), and the tip of a hybrid meta-fiber

was subsequently immersed into the liquid. Within all measurements, a custom-built microscope consisting of a $50\times$ dry objective (Olympus MPLFLN, $NA = 0.8$), followed by an achromatic tube lens of focal length $f_t = 200$ mm (Thorlabs AC254-200-A-ML), was used for imaging the motion of a trapped particle from the side (details of the setup see Figure 4.2). Meanwhile, scattered trapping laser light was blocked using a notch filter of central wavelength $\lambda_0 = 658$ nm (Thorlabs NF658-26). Here, homogeneous Köhler illumination (see Figure 4.3) was provided via a fiber-coupled light emitting diode (LED) of wavelength $\lambda = 455$ nm (Thorlabs M455F3), which was connected to a multi-mode fiber (Thorlabs M18L, core diameter of $2a = 105$ μm and NA of 0.22).

Figure 6.9A exemplarily demonstrates a $2R = 2$ μm diameter silica bead that was optically trapped along all three spatial dimensions simultaneously using only a single hybrid meta-fiber (sample 1, $f_1 = 55$ μm focal length, designed $NA_{1,\text{theor}} = 0.84$). In Figure 6.9B, in contrast, trapping of a biologically relevant *E. coli* bacterium in front of sample 2 ($f_2 = 50$ μm , $NA_{2,\text{meas}} = 0.88$) is exemplarily illustrated, while the bacterium was effectively trapped on timescales of several minutes. Specifically, no degradation of neither the trapped object (tested damage threshold $P > 50$ mW) nor the functionalized meta-fiber ($I_{\text{max}} \sim 6$ mW/ μm^2) was observed, while the samples have been continuously reused over the course of weeks. The insets in Figure 6.9, A and B, display $5\times$ magnifications of the trapped particles as indicated by the dashed circles, respectively.

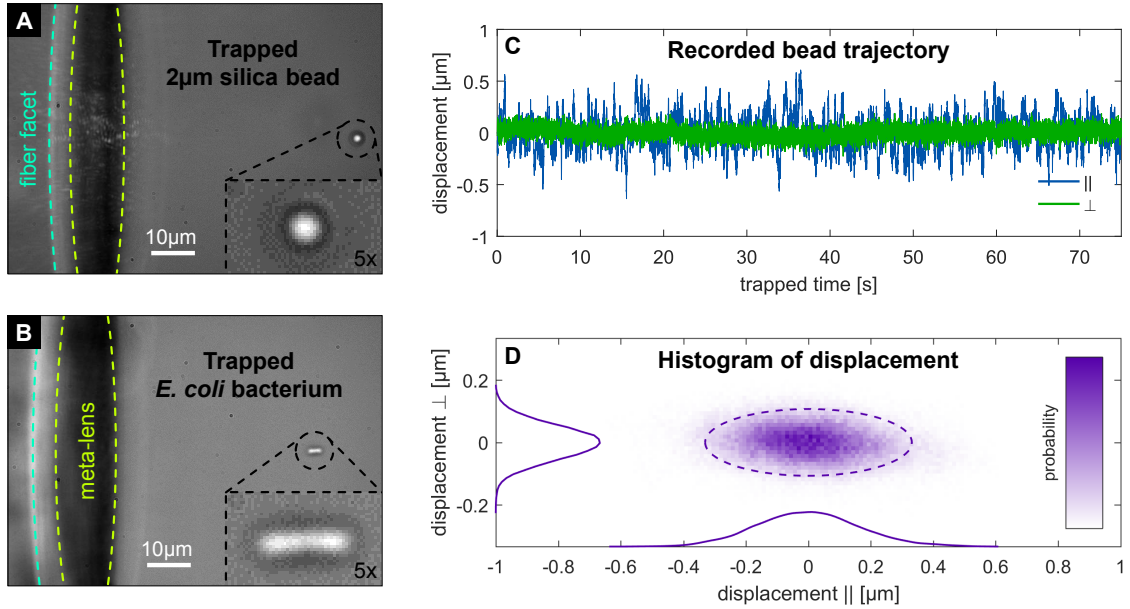


Fig. 6.9. Optical trapping of a silica bead and an *Escherichia coli* (*E. coli*) bacterium in water with a single meta-fiber at a wavelength of 660 nm. (A) Silica bead of 2 μm diameter in front of sample 1 (55 μm focal length, designed numerical aperture $NA_1 = 0.84$), and (B) *E. coli* bacterium in front of sample 2 (50 μm focal length, measured $NA_2 = 0.88$), both optically trapped along all three spatial dimensions using a single meta-fiber. The insets show $5\times$ magnifications of the trapped particles as indicated by the dashed circles. (C) Obtained time-dependent trajectory and (D) histogram of the tracked displacement for the silica bead in A along the transverse (\perp) and the axial (||) direction with respect to the orientation of the meta-fiber trap. The bead was effectively trapped for more than one minute within a volume smaller than the focal region.

For analyzing the performance of a meta-fiber with respect to optical trapping, high-speed videos of a single trapped silica bead were recorded at a high frame rate of $1/\Delta t = 1000$ fps for a minimum duration of $t_{\max} > 60 \dots 75$ s. Here, the exposure time τ was set to as low as $\tau = .01$ ms within all recordings in order to minimize the influence of motion blur, which heavily impacts and distorts the statistical properties (see Figure 4.7C). Subsequently, the trajectory of a trapped bead was retrieved from a recorded video using the image shift algorithm (details of the tracking routine see subsection 4.1.2), effectively yielding its dynamic displacement $\Delta x_{\perp, \parallel}$ along the transverse (\perp) and the axial (\parallel) direction with respect to the orientation of the trap and ultimately its complete time-dependent trajectory $x_{\perp, \parallel}(t)$. Figure 6.9C exemplarily visualizes this for the more than one minute long trajectory $x_{\perp, \parallel}(t)$ of the trapped bead depicted in Figure 6.9A, where specifically a displacement within a volume smaller than the focal region was revealed as presented in Figure 6.9D (compare Figure 6.8E and ref. [46]).

6.3.2 Performance analysis

In order to quantitatively assess the trapping performance of the meta-fiber, subsequently, the dynamics of a trapped bead (diameter $2R = 2 \mu\text{m}$) were analyzed. However, due to additionally required considerations of rotational diffusion^[142] and effectively a more complex tracking routine, the motion of the confined elliptically shaped *E. coli* bacteria was thus not analyzed here. Nevertheless, this principally allows for, e.g., identifying self-driven motion of trapped objects within optical traps^[2,63].

Figure 6.10, A and B, demonstrates the mean square displacement (MSD) and the power spectrum (PS), respectively, of the retrieved trajectory $x_{\perp, \parallel}(t)$ (Figure 6.9C) of a trapped bead (compare subsection 4.2.2 and ref [46]). In principle, both techniques allow for quantitatively analyzing the temporal and spectral properties of its motion as well as filtering potential error influences within the trajectory $x_{\perp, \parallel}(t)$. Here, two important characteristics of its motion are revealed: (i) a linear slope for short lag times $\Delta t \sim 0$ (MSD) and high frequencies $1/\Delta t \gg 0$ (PS), resulting from the free diffusion D of the bead, and (ii) a plateau for long lag times $\Delta t \gg 0$ and low frequencies $1/\Delta t \sim 0$, respectively, denoting its confinement within the meta-fiber-based optical trap.

For the MSD illustrated in Figure 6.10A, in particular, no particle drift on timescales of more than one minute is visible. Furthermore, no superimposed secondary oscillatory motion of the trapped bead appears as a distinct peak within the PS of Figure 6.10B. Moreover, little to no aliasing as of high frequency noise as a result of motion blur is present within the PS, specifically being attributed to the low exposure time of only $\tau = 0.01$ ms. Overall, the results of both PS and MSD are in excellent agreement, while the latter was thus chosen as the method of choice for trap analysis within the following.

To determine the power normalized stiffness $\kappa_{\perp,\parallel}/P_i$ of the meta-fiber trap, in particular, the motion of an optically trapped individual silica bead was tracked at different power levels P_i . Therefore, variable optical density (OD) filters were introduced before the meta-fiber in order to attenuate the laser beam. For all measurements, filters of OD 0.1, 0.2, 0.3, 0.6 and 1.0 were used, effectively resulting in a near linear reduction of the optical power P_i at the meta-fiber output. Here, Figure 6.10C displays the MSD-analyzed power-dependent trap stiffness $\kappa_{\perp,\parallel}(P_i)$ for sample 1 (designed $\text{NA}_{1,\text{theor}} = 0.84$) and sample 2 (measured $\text{NA}_{2,\text{meas}} = 0.88$) along two (\perp and \parallel) spatial dimensions.

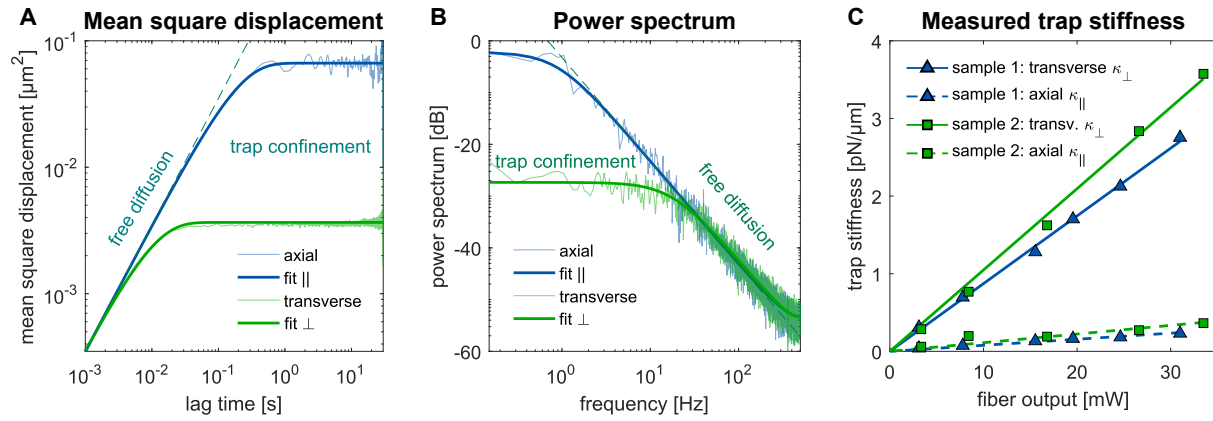


Fig. 6.10. Experimental analysis of optical trapping and performance of two different meta-fiber samples for a 2 μm diameter silica bead in water. (A) Mean square displacement (MSD) and (B) power spectrum (PS) for an exemplary retrieved trapped bead trajectory. The linear slope represents the free diffusion of the bead, and the plateau denotes its confinement within the meta-fiber optical trap. Both techniques reveal a drift- and nearly motion blur-free behavior of the trapped microbead and yield similar results. (C) Analyzed trap stiffness at a wavelength of 660 nm based on the MSD (A) for different optical powers and both meta-fiber samples. Sample 2 ($\text{NA} = 0.88$) overall performs better than sample 1 ($\text{NA} = 0.84$) and exhibits a greater stiffness along the transverse (\perp) than the axial (\parallel) direction due to a smaller aspect ratio of its focal region.

In principle, the transverse stiffness κ_{\perp} of the meta-fiber trap is about one order of magnitude larger than κ_{\parallel} along the axial direction, particularly being attributed to the large focal aspect ratio that impacts the distribution of particle displacement $\Delta x_{\perp,\parallel}$ (compare Figures 6.8E and 6.9D and ref. [46]). Due to its tighter focus, here, the ultra-high $\text{NA}_{2,\text{meas}} = 0.88$ of sample 2 effectively yields a better performance, i.e., stronger trapping with larger stiffness $\kappa_{\perp,\parallel}$, compared to the lower but still high $\text{NA}_{1,\text{theor}} = 0.84$ of sample 1.

6.3.3 Comparison of results

When comparing the normalized stiffness (sample 2: $\kappa_{\perp,\parallel}/P_2 = (10.5, 1.1) \cdot 10^{-2}$ pN/ $\mu\text{m}/\text{mW}$) for the two spatial dimensions, respectively, the single meta-fiber trap performs about a factor of three better than the previously discussed dual fiber focus trap (compare Table 5.1 and ref. [45]). Here, the same trapped beads of $2R = 2 \mu\text{m}$ diameter were used, however, previously a total power of $P = P_1 + P_2 = 60 \text{ mW}$ was applied, which thus demonstrates the importance of the NA within optical trapping. Compared to other diffractive optical traps,

in particular, the single meta-fiber trap ($1 \times 0.88 \text{ NA}_2$) performs almost one order of magnitude better than a diffractive dual fiber trap^[86] ($2 \times 0.7 \text{ NA}$) of similar concept and up to three times better than a planar silicon meta-lens trap^[162] of even higher $\text{NA} = 0.96$, specifically emphasizing the efficiency of this concept here.

In comparison to a holographic optical fiber trap^[44] ($\text{NA} > 0.8$), however, the obtained results exhibit a factor of two lower normalized stiffness $\kappa_{\perp, \parallel}/P$. This presumably results from a higher contribution of axial scattering forces $\vec{F}_{\text{scat}}(z) \propto \lambda^{-1}$ for shorter wavelengths λ (here: $\lambda = 660 \text{ nm}$ compared to $\lambda = 1064 \text{ nm}$ within ref. [44]). A detailed summary of the trapping results, here, including the previously obtained ones of chapter 5, is presented in Table 8.1 within the conclusion of this work.

Table 6.1 summarizes the results of this chapter and gives a comparison to similar literature reports on HOFs interfaced with focusing elements, specifically including demonstrated trapping applications. When comparing the here obtained results to the listed concepts, in particular, it stands out that none of the diffractive optical implementations allow for trapping using only a single fiber beam (compare refs. [46, 82, 86]). Due to their limited NA, however, these approaches often require, e.g., additional surfaces for compensating the axial scattering force $\vec{F}_{\text{scat}}(z)$.

Tab. 6.1. Overview of similar reported concepts of hybrid optical fibers (HOFs) interfaced with focusing optics. The results presented in this chapter are highlighted in gray, while representing the concept of the highest implemented NA based on a diffractive optic (PCF denotes a photonic crystal fiber).

<i>Working principle</i>	<i>Fabrication technique</i>	<i>Lens material</i>	<i>Fiber type</i>	<i>Wave-length</i>	<i>Numerical aperture</i>	<i>Trapping application</i>	<i>Ref.</i>
Refractive micoprism	two-photon lithography	polymer	4 SMF bundle	1070 nm	1.15 water (theor.)	red blood/tumor cells	[37]
Diffractive meta-lens	fs-direct laser writing	polymer	1 SMF + MMF spliced	660 nm	0.88 water	2 μm beads/ <i>E. coli</i>	this work, [46]
Digital holography	spatial light modulator	–	1 MMF	1064 nm	> 0.8 water	1.5 μm beads	[44]
Diffractive meta-lens	fs-direct laser writing	polymer	2 SMFs + spacer print.	808 nm	0.7 water	1 μm / 0.5 μm beads	[86]
Plasmonic nanorods	focused ion beam milling	Au	1 PCF	1550 nm	0.37 air	–	[148]
Refractive GRIN lens	stack & draw + glue	SiO ₂	1 SMF + spacer glued	976 nm	0.16 air	2 μm beads (on surface)	[120]
Refractive microlens	laser exposure	polymer	1 SMF + MMF spliced	980 nm	?	8 μm beads/yeast cells (on surface)	[145]
Diffractive Fresnel plate	focused ion beam milling	SiO ₂	1 SMF + MMF spliced	980 nm	?	8 μm beads/yeast cells (on surface)	[82]

With respect to solely the NA, in particular, it is remarkable that the highest values have been reported when lithography was applied as fabrication^[37,86]. This highlights

the significance of choosing DLW for implementing the design here, which effectively provides full three-dimensional optical trapping along all spatial dimensions simultaneously with only a single hybrid meta-fiber while reaching an ultra-high numerical aperture of $NA = 0.88$. Similar concepts of comparably high NA, in contrast, explicitly require, e.g., non-commercial optical fibers or extensive additional equipment such as, e.g., a spatial light modulator (SLM) or large-scale and cost-intensive clean room facilities^[44,82,148]. The here presented concept, however, solely relies on a low-cost and commercially available SMF and MMF, while the prior specifically benefits from its independence on length and robustness against external influences such as, e.g., bending the fiber.

6.4 Chapter discussion

Based on one single-mode fiber (SMF) that is spliced to a short multi-mode fiber (MMF) section for expanding its beam and accommodating the full NA of a 3D printed diffractive meta-lens on its facet, the hybrid meta-fiber concept presented in this work effectively allows for diffraction limited focusing while reaching an ultra-high $NA = 0.88$ as experimentally confirmed. This specifically enables flexible remote optical trapping of freely diffusing micro-objects using only a single fiber, which was experimentally demonstrated for the example of individual silica microbeads and biologically relevant *E. coli* bacteria in water. Here, the trapped particles were confined along all three spatial dimensions simultaneously to within a volume smaller than the focal region on timescales of several minutes, while no degradation of neither sample nor particle was observed for powers of up to $P = 50$ mW and the samples have been continuously reused over the course of weeks.

Compared to similar reports on concepts of HOFs interfaced with focusing optics, effectively, the here presented concept of a hybrid meta-fiber device benefits from its simple, low-cost, and reliable implementation as well as from its general flexibility, integrability and usability within difficult to reach remote environments. In principle, this allows further extending its scope of applications for including, e.g., high-resolution microscopy^[84,151], fiber-based *in vivo* endomicroscopy, imaging and Raman spectroscopy^[37–42] as well as optical sensing^[2,63] and precise control and micro-manipulation^[21,44].

Potential improvements are given by, e.g., using a narrow band laser for better coherent operation of the meta-lens, i.e., the contribution of all phase-lens elements, thus increasing the usable cross-section and the NA to near-immersion limited values^[151,163]. Ultimately, precisely cleaving the expansion fiber as well as better characterization of each sample via, e.g., using a Shack–Hartmann sensor for individual wavefront analysis, followed by correcting the meta-lens to match the respective expansion length, in principle allows for reducing the over-corrected wavefront error, i.e., positive spherical aberration.

Fiber point Paul trap

Electrical trapping of particles effectively represents an alternative to the previously discussed concepts of optical fiber traps in case particle properties are incompatible, e.g., due to limited transparency. Electrical forces, in particular, are important within biological applications due to the Stern layer^[123] that surrounds freely diffusing objects (see Figure A.1 in the appendix). This enables applications such as the electrical trapping of bacteria^[16], single DNA^[89] and protein molecules^[6], and sorting of biological cells^[25].

Here, the concept uniquely relies on combining an electrophoretic Paul trap with an optical fiber^[23,58,164]. To comply with the circular fiber geometry, in particular, a surface-electrode point Paul trap of three concentric electrode rings^[68] (see Figures 3.7D and A.2 in the appendix for its working principle) was implemented directly onto the facet of a hybrid optical fiber (HOF, see subsection 2.1.2). This specifically allows contacting the electrical trapping structure on its front via microstructured wires inside the HOF^[58,75,76] from the back, effectively representing a key advantage only enabled via the HOF. Figure 7.1 schematically depicts the concept of a fiber point Paul trap, which is based on a microwired HOF and a circular symmetric facet-electrode trapping structure.

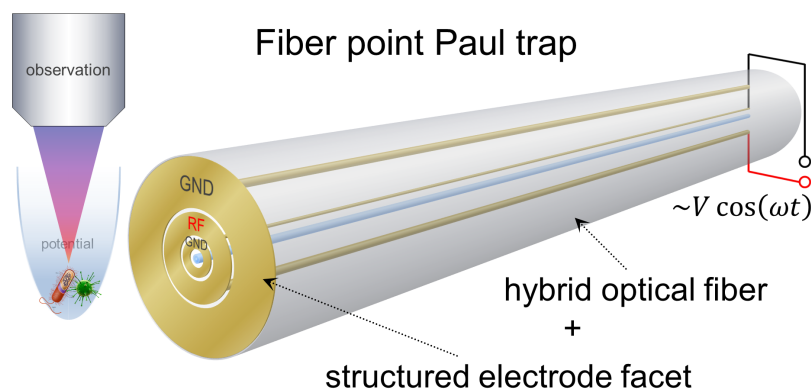


Fig. 7.1. Concept of a fiber point Paul trap for electrically trapping charged particles in water. Wires inside a hybrid optical fiber contact an electrode structure on its facet. An alternating radio frequency (RF) voltage over ground (GND) is applied at its rear, creating an electric potential for charged particles in the front.

In the following, the electrical design of the fiber point Paul trap is presented (section 7.1, for optical properties see Figure A.5 in the appendix), followed by its specific implementation (section 7.2). Finally, an experimental demonstration of electrically trapping charged beads using an implemented trap is discussed as an outlook (section 7.3).¹

¹Due to extensive implementation, here, the level of results is lower than within previous chapters.

7.1 Electrical design

A radial symmetric surface-electrode trap, i.e., a point Paul trap^[68], specifically matches the circular geometry of an optical fiber^[23,58]. In order to maintain its radial symmetry, here, the electrical contacting of the trapping structure is provided from the back using a microwired HOF^[58,75,76] (details see Figure 7.1 and subsection 7.2.1). In the following, its design is particularly limited to the simplest scenario of three concentric planar rings (for details see Figure 3.7, D and G), where a rapidly alternating (AC) voltage V_{ac} of radio frequency (RF) ω is applied to the central electrode of radial coordinate $r_1 < r < r_2$. This effectively creates an electric potential $\Phi(r, z, t)$ for a charged particle that is trapped at a height z_0 above the surface, and can as well be described analytically using the approximation of an infinitely extended gapless plane^[68,130]:

$$\Phi(r, z, t) = V_{ac} \cos(\omega t) \int_0^\infty J_0(kr) [r_2 J_1(kr_2) - r_1 J_1(kr_1)] e^{-kz} dk, \quad (7.1)$$

where J_ν represents the Bessel function of first kind and order ν .

The on-axis ponderomotive potential $\langle \Psi(z) \rangle \propto |\partial_z \Phi(0, z)|^2$ (see Equation 3.15, $\partial_z = \partial/\partial z$ denotes the partial derivative with respect to the axial height z), however, can principally be approximated via a harmonic trap potential $\langle \Psi(z) \rangle \sim \Lambda^2 (z - z_0)^2$ with geometric coefficient Λ . Optimizing $\langle \Psi(z) \rangle$ for a maximum trap depth $\Psi_{max} = \langle \Psi(z_{max}) \rangle$, where $z_{max} \sim 2z_0$ denotes the turning point of the confinement (Figure 7.2B), specifically yields $r_1 \approx 0.65z_0$ and $r_2 \approx 3.58z_0$ [68]. Figure A.2 in the appendix exemplarily demonstrates $\langle \Psi(r, z) \rangle$ for the optimized geometry of a concentric three ring point Paul trap calculated using Equation 7.1, while Figure A.3 illustrates its approximation via an ideal quadrupole of $\Lambda = 1$. The coefficient of this particular geometry here, in contrast, is given via $\Lambda(r_1, r_2) \approx 0.47$, yielding a maximum trap depth of $\Psi_{max} \approx 0.02 \Psi_{4rod}$ with $\Psi_{4rod} = V_{ac}^2 / z_0^2 \cdot \Gamma$, where $\Gamma = Q^2 / (m\omega^2 [4 + b^2])$ is defined as the ponderomotive factor.

For realizing the trap onto the facet of an optical fiber, first, the influence of a finitely extended design of the point Paul trap on the resulting ponderomotive potential $\langle \Psi(r, z) \rangle$ was analyzed within a simulation (subsection 7.1.1). This is followed by optimizing the electrode geometry, while including inter-electrode gaps to prevent electrical shortcuts (subsection 7.1.2). Here, all calculations were carried out using a finite element method (FEM) solver (COMSOL®) for an electrophoretic operation of the fiber trap within any specified medium. This particularly includes de-ionized water^[103,105], which acts as a perfect dielectric insulator and thus does not influence the calculation of the design.

7.1.1 Fiber compatibility

To match the finite diameter \emptyset of an optical fiber, the trap radius $r_2 < r_3 < \infty$ of the outermost ring electrode was varied while keeping the geometry of the remaining

two identical, i.e., at their optimum dimensions $r_1 \approx 0.65z_0$ and $r_2 \approx 3.58z_0$ [68]. Here, a radio frequency (RF) voltage was applied to the central ring, while the innermost ($0 < r < r_1$) and the outermost ($r_2 < r < r_3$) electrodes were kept on ground (GND) and the remaining area of the infinitely extended plane was unassigned as visualized in Figure 7.2A. In Figure 7.2B, the on-axis trap potential $\langle \Psi(0, z) \rangle / \Psi_{4\text{rod}}$ is presented, reaching the maximum value of $\Psi_{\text{max}} / \Psi_{4\text{rod}} \approx 0.02$ for significantly large trap extensions, i.e., $2r_3 = 50z_0$, and decreasing for smaller diameters $\varnothing = 2r_3$.

For a trade-off between a feasible extension of the point Paul trap regarding the cross-section of an optical fiber and a reasonable depth of the trap potential Ψ_{max} , here, a trap diameter of $2r_3 = 20z_0$ was chosen. This yields a trapping height of $z_0 = 15 \mu\text{m}$ for a diameter of $\varnothing = 300 \mu\text{m}$, reaching an efficiency of $\eta = \Psi_{\text{max}} / (0.02\Psi_{4\text{rod}}) = 95\%$ compared to an infinite trap. Subsequently, gaps of $w_g = 3 \mu\text{m}$ width were introduced between the three individual concentric rings to prevent electrical shortcuts up to $V_{\text{ac}} = 10 \text{V}$, and an aperture of $2a = 8 \mu\text{m}$ diameter was included in the center for unperturbed transmission of light from the fiber core for sufficiently large mode diameters. Figure 7.2C displays the resulting geometry with an efficiency of $\eta = 92\%$, and Figure 7.2D summarizes the study.

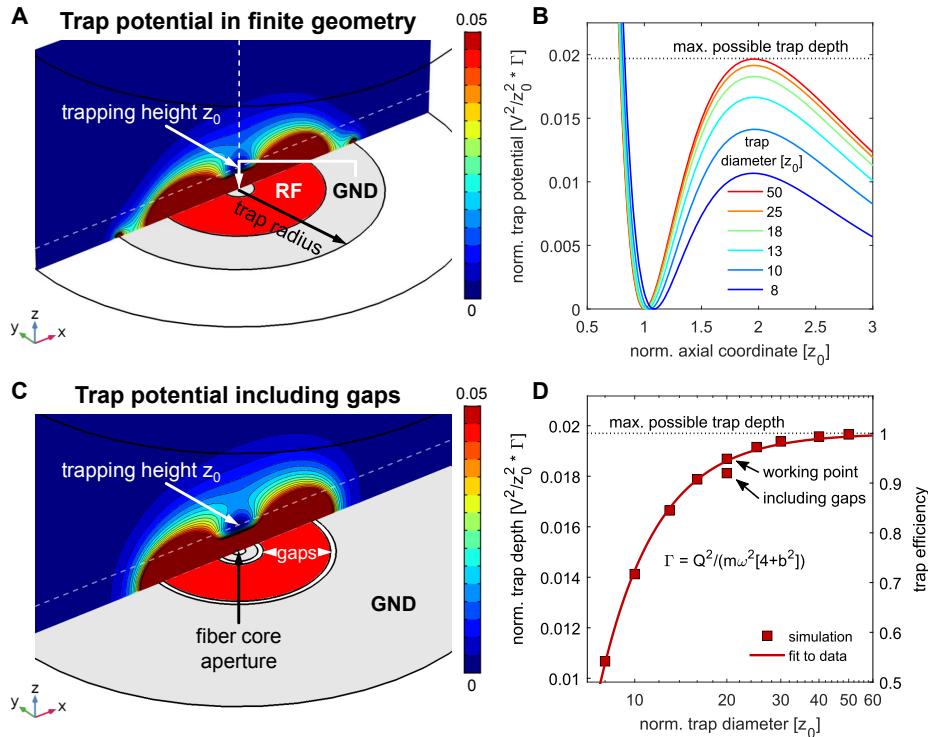


Fig. 7.2. Calculated design efficiency for a finitely extended point Paul trap within arbitrary media. (A) Trap potential for a finite geometry, where $\Gamma = Q^2 / (m\omega^2[4 + b^2])$ denotes the ponderomotive factor. The radius of the outermost ring was varied while on ground (GND), a radio frequency (RF) voltage was applied to the central one, and the white area was unassigned. (B) Resulting on-axis trap potential along the vertical dashed line in A for different trap diameters, reaching the maximum possible trap depth for significantly large extensions and decreasing for smaller ones. (C) $3 \mu\text{m}$ wide gaps were included between the electrodes to prevent electrical shortcuts, and an $8 \mu\text{m}$ diameter aperture for the fiber core was introduced in the center. (D) Summary of the study, yielding an efficiency of 95% for the finite geometry and 92% with electrode gaps.

7.1.2 Structure optimization

Subsequently, a parametric sweep of the widths w_{e1} of the innermost and w_{e2} of the central electrode of a concentric three ring point Paul trap was carried out. Here, a combination of the widths w_{e1} and w_{e2} that yield a particular trapping height of $z_0 = 15 \mu\text{m}$ was targeted, as principally predicted via the analytical gapless plane approximation (details see Equation 7.1). Due to the specific design (see Figure 7.2C), in particular, the width w_{e3} of the outermost electrode for a fiber of diameter $\varnothing = 300 \mu\text{m}$, including inter-electrode gaps of width $w_g = 3 \mu\text{m}$ and a central aperture of $2a = 8 \mu\text{m}$, is effectively given via $w_{e3} = \varnothing/2 - (a + w_{e1} + w_{e2} + 3w_g)$.

Figure 7.3, A and B, compares the analytical results of Equation 7.1 to the ones obtained from the simulated parametric sweep, where the inter-electrode gaps specifically exhibit no significant influence on the trapping height z_0 of the underlying point Paul trap geometry^[128]. Subsequently, the maximum trap depth Ψ_{max} of the on-axis ponderomotive potential $\langle \Psi(z) \rangle$ for the widths w_{e1} and w_{e2} yielding $z_0 = 15 \mu\text{m}$ was calculated, as compared in Figure 7.3, C and D, for Equation 7.1 and the parametric sweep, respectively. Figure 7.3E shows the resulting optimized geometry of the concentric three ring point Paul trap, which is given via $w_{e1} = 5 \mu\text{m}$, $w_{e2} = 36 \mu\text{m}$ and $w_{e3} = 96 \mu\text{m}$, and exhibits an efficiency of $\eta = 92\%$ for the on-axis trap potential $\langle \Psi(z) \rangle$.

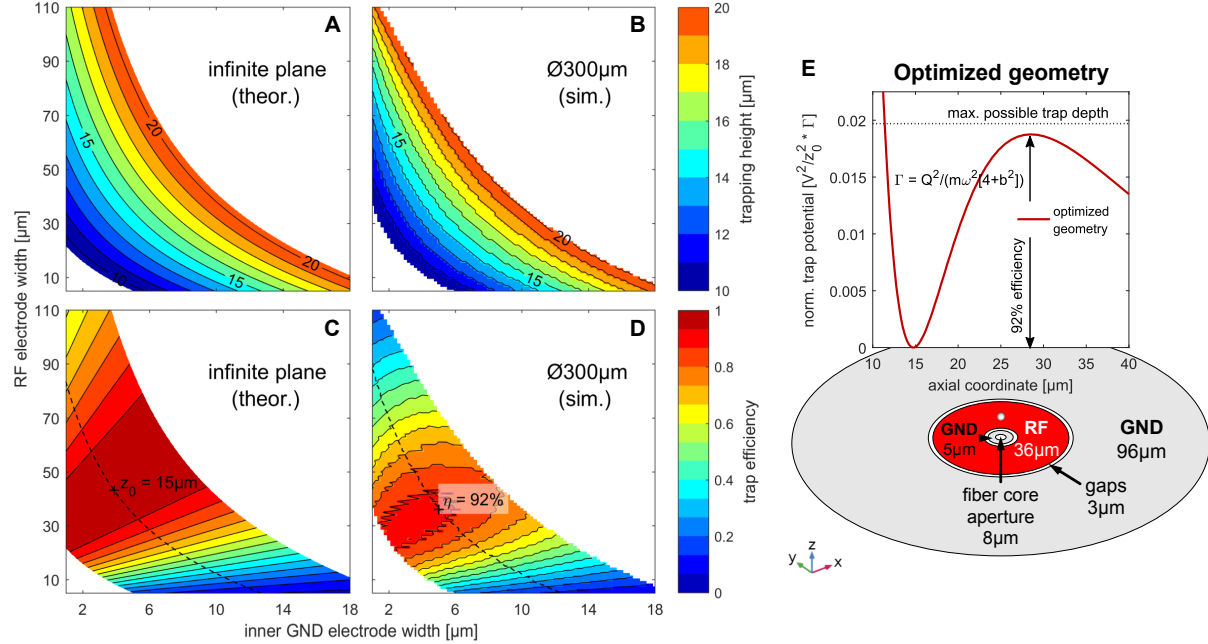


Fig. 7.3. Optimization of the geometry for a three ring electrode point Paul trap of 300 μm diameter. (A) Trapping height above the surface for widths of the innermost ground (GND) electrode and the central radio frequency (RF) electrode, calculated via the approximation of an infinite plane. (B) Simulated trapping height for a finite trap diameter of 300 μm , including inter-electrode gaps of 3 μm width and a central aperture of 8 μm diameter. (C) Theoretical trap efficiency for an infinite plane, defined as unity when reaching the maximum possible on-axis trap depth, and (D) simulation for the 300 μm diameter trap. Only specific combinations for a trapping height of 15 μm were targeted (indicated by the dashed line), yielding a maximum efficiency of 92% for the finite trap. (E) Optimized resulting geometry and on-axis trap potential for the 300 μm diameter trap.

Due to nearly reaching the maximum possible trap depth of $\Psi_{\max} \approx 0.02$, here, the final trapping geometry can effectively be described using Equation 7.1, and a coefficient of $\Lambda(w_{e1}, w_{e2}) \approx 0.47$ was thus assumed in the following when considering stable trapping. Nevertheless, a further improvement and adaptive tuning of the trap potential $\langle \Psi(r, z) \rangle$ can be achieved when applying a static (DC) potential U_{dc} to the innermost ring^[68] (see Figure A.4 in the appendix). The design of the microstructured fiber for contacting the structure, including its optical properties, however, is shown in Figure A.5.

7.2 Fiber trap implementation

The unique concept of the fiber point Paul trap effectively relies on a microwired HOF^[58,75,76] for electrically contacting a trapping microstructure on its facet (see Figure 7.1). Prior to implementing an electrode structure on its tip, however, the concept specifically requires planarizing the hybrid fiber in order to comply with wafer-based microfabrication technology. Here, this is achieved via a multi-step process, which consists of microwire implementation and subsequently polishing its facet, followed by employing state-of-the-art microtechnology including layer deposition, electron-beam lithography (EBL), physical dry etching and resist removal.^[51,165] Figure 7.4 schematically demonstrates the workflow of the experimental implementation procedure.

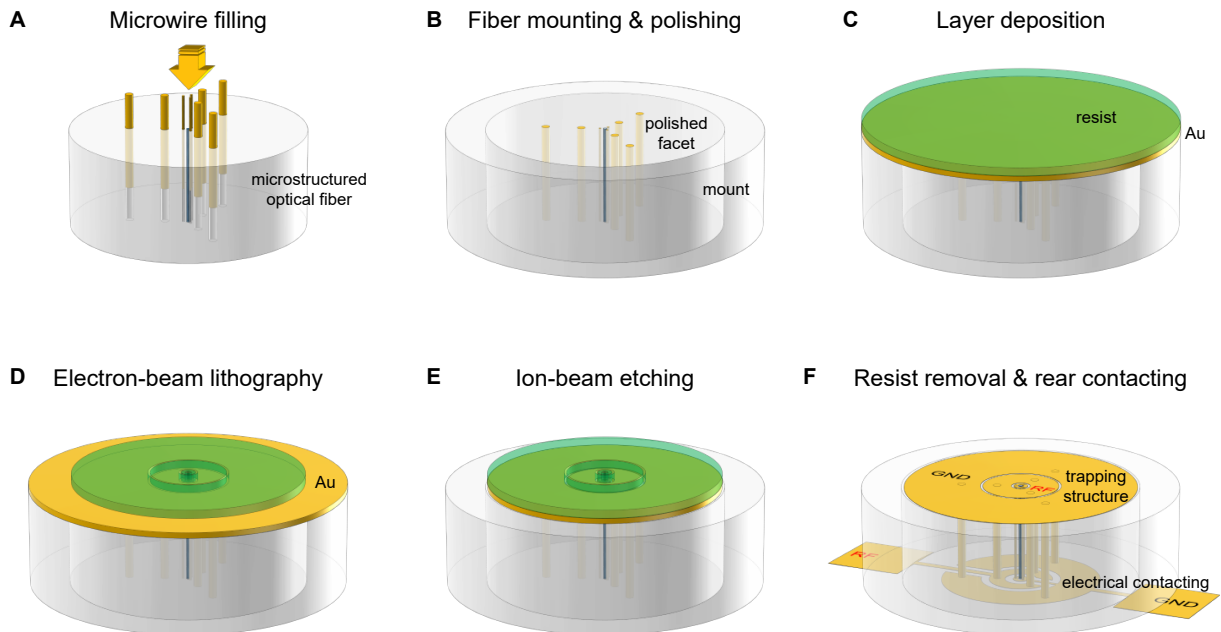


Fig. 7.4. Scheme of the experimental workflow for the implementation of a fiber point Paul trap. (A) Alloy wires are implemented inside a microstructured optical fiber via pressure assisted melt filling^[75]. (B) The microwired fiber is glued into a silica capillary, mounted inside an aluminum disc, and both facets are subsequently polished to obtain smooth surfaces. (C) A 50 nm thin gold film is vapor deposited, followed by spin coating a negative photoresist. (D) The negative resist layer is microstructured via electron-beam lithography (EBL), and (E) the uncovered gold film is dry etched using a reactive ion-beam. (F) Any remaining resist is chemically removed, and steps 3–6 are repeated for implementing the rear contacting structure.

In the following, the experimental implementation of electrically conducting wires inside a microstructured fiber (subsection 7.2.1) and the fabrication of the electrode structures on both fiber ends via EBL (subsection 7.2.2) are presented in detail.

7.2.1 Microwire filling

For electrically contacting a point Paul trap on the facet of an optical fiber, a microstructured fiber was used, which was filled with a low melting alloy via a routine referred to as pressure assisted melt filling^[75]. Here, a three-fold symmetry of the fiber geometry was chosen, effectively providing access to each of the three concentric electrode rings via three contact points as demonstrated within Figure 7.5A. Specifically, the fiber core of diameter $2a = 5 \mu\text{m}$ is surrounded by a ring of three small holes of $3 \mu\text{m}$ diameter at pitches of $6.5 \mu\text{m}$ and by two rings of $10 \mu\text{m}$ diameter holes at pitches of $30 \mu\text{m}$ and $75 \mu\text{m}$, respectively (details of the optical design see Figure A.5 in the appendix). Figure 7.5B illustrates the microstructured design, and Figure 7.5C visualizes an example of the experimental implementation, i.e., the drawn Paul fiber.

Within the pressure assisted melt filling, here, the low melting alloy Au80Sn20 (80% gold, 20% tin) was used, effectively decreasing the high melting temperature $T_{\text{Au}} = 1064 \text{ }^\circ\text{C}$ of pure gold to only $T_{\text{alloy}} = 280 \text{ }^\circ\text{C}$ [166]. This reduces material tension due to thermal contractions when cooling down from the melting temperature T_{alloy} , thus resulting in longer continuous microwires inside the HOF. Specifically, a $125 \mu\text{m}$ diameter Au80Sn20 wire was inserted into a larger capillary with inner diameter of $220 \mu\text{m}$, which was fusion spliced to an $L \sim 20 \text{ cm}$ long piece of the microstructured Paul fiber. This matched its $\varnothing = 300 \mu\text{m}$ outer diameter as exemplarily displayed in Figure 7.5D, while particular care was taken not to collapse the delicate central holes of $3 \mu\text{m}$ diameter.

Subsequently, the fiber was sealed on its other end and evacuated for a duration of $t \sim 1 \dots 2 \text{ h}$, while reaching pressures of $p \sim 10^{-4} \text{ mbar}$. This was followed by heating the fiber to $T \sim 1000 \text{ }^\circ\text{C}$ in order to break potential oxide layers surrounding the alloy wire, and argon gas pressure of $p \sim 50 \text{ bar}$ was ultimately applied for a duration of $t \sim 20 \dots 30 \text{ min}$ to fill the microholes. Afterwards, the fiber was cooled down, effectively yielding centimeter long pieces of continuous microwires inside the hybrid Paul fiber. Figure 7.5E depicts an example of an experimentally implemented microwired Paul trap fiber from the side, and Figure 7.5F shows its facet from the front.

However, heating to $T \sim 1000 \text{ }^\circ\text{C}$ leaves the fiber extremely fragile, which was taken care of via gluing a short piece into a capillary mounted within an aluminum disc (see Figure 7.4B). Figure A.5 in the appendix demonstrates the experimentally determined optical influence of the metallic microwires inside the hybrid Paul fiber. In the following, the implementation of the microstructured trapping and contacting electrodes on the respective facets of the microwired Paul fiber is presented in detail.

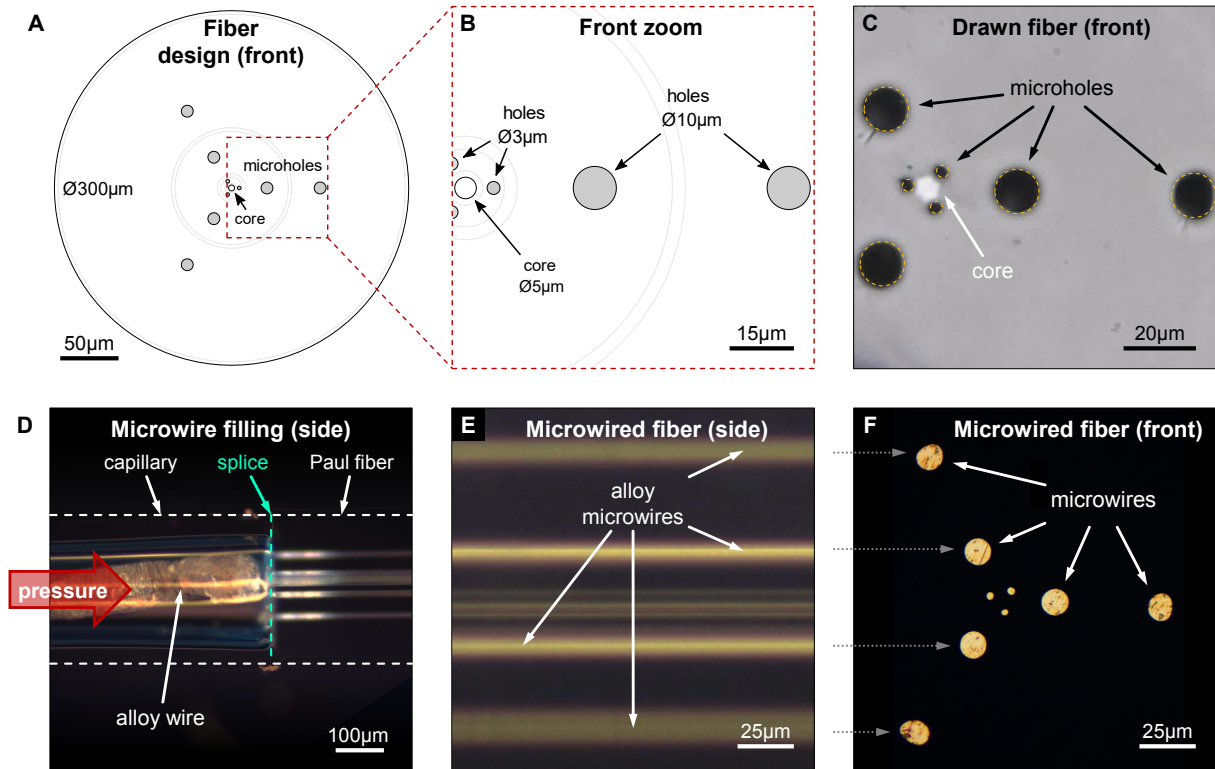


Fig. 7.5. Design and implementation of a microwired Paul trap fiber. (A) Design of the microstructured fiber, exhibiting a three-fold symmetry for contacting each of the concentric electrodes via microholes. (B) The fiber core is surrounded by three small holes of $3\ \mu\text{m}$ diameter for contacting the inner ring and by two rings of $10\ \mu\text{m}$ diameter holes for the central and the outer ring, respectively. (C) Experimental realization of A and B, showing the excellent agreement of the drawn microstructured fiber with the design. (D) Pressure-assisted melt filling of microwires inside the Paul fiber shown in C. A low melting alloy wire (Au80Sn20) was inserted into a larger inner diameter capillary from the left that was spliced to the Paul fiber. (E) The fiber was heated to above the alloy melting point and 50 bar pressure was applied for 20...30 min, yielding centimeter long pieces of continuous microwires inside the hybrid fiber. (F) Resulting cross-section of a microwired Paul fiber.

7.2.2 Electrode structuring

The final implementation of the fiber point Paul trap, which is conceptually illustrated in Figure 7.6A, relies on first, planarizing the fiber in order to comply with wafer-based microtechnology. Therefore, a short piece of the microwired fiber was glued (Norland Adhesives) into a silica capillary, mounted within an aluminum disc, and both sides were polished to obtain smooth surfaces as exemplarily visualized in Figure 7.6B. Subsequently, state-of-the-art microfabrication technology was employed for structuring both fiber facets, including vapor deposition of a $\approx 50\ \text{nm}$ thin gold film, electron-beam lithography (EBL), reactive ion-beam etching and final chemical resist removal.^[51,165]

Figure 7.6C displays an example of an experimentally implemented fiber point Paul trap, which was mounted onto a printed circuit board (PCB) for electrical contacting, and Figure 7.6D depicts its rear side. Here, macroscopic wires were soldered onto the PCB and microscopic wires were bonded to structural contact electrode pads, which are shown enlarged in Figure 7.6E demonstrating the implemented contacting structure on the

rear facet of the microwired HOF with its clearly visible three-fold contacting geometry. The concentric trapping structure on the front fiber facet is illustrated in Figure 7.6F, again showing the implemented in-fiber microwires for electrically contacting the three individual electrode rings from the back via the HOF.

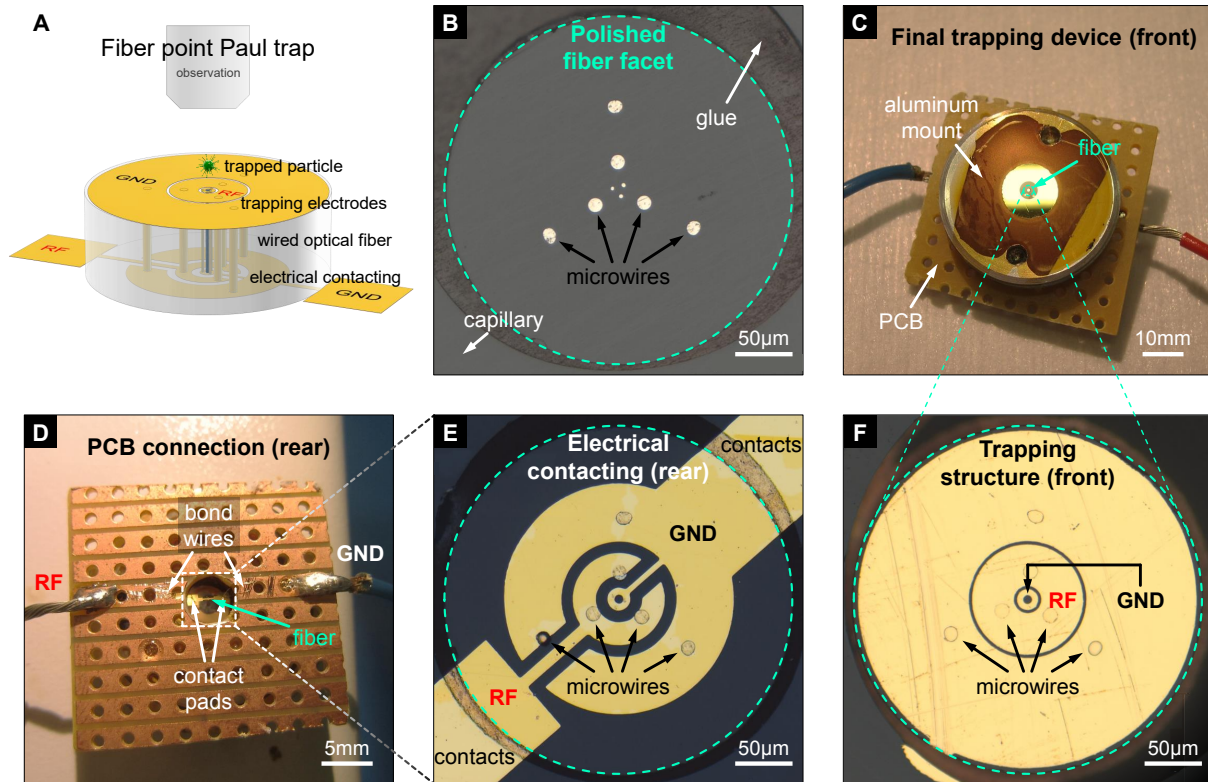


Fig. 7.6. Final experimental implementation of a fiber point Paul trap. (A) Scheme of a fiber point Paul trap, which consists of bottom contact electrodes, a microwired hybrid fiber in between, and microstructured electrodes on its front facet for trapping charged particles. (B) For microstructuring via electrode-beam lithography (EBL), the microwired Paul fiber was first planarized by gluing it into a silica capillary mounted within an aluminum disc, followed by polishing both facets. (C) Final implementation of a fiber point Paul trap mounted on a printed circuit board (PCB) for electrically contacting its bottom. (D) Rear side of the PCB, showing the electrical contacting via macroscopic soldered wires and microscopic bond wires to connect the bottom electrodes. (E) Enlarged center, displaying the contacting via the in-fiber microwires. (F) Enlarged center of C, depicting the implemented on-fiber trapping structure on the front facet of the point Paul fiber.

7.3 Experimental demonstration

For an experimental demonstration of electrical trapping with the implemented fiber point Paul trap, here, carboxyl (COOH^-) functionalized $2R = 3 \mu\text{m}$ diameter polystyrene beads (Polysciences) were 1:1000-fold diluted from their stock solution within de-ionized water to a final concentration of $c \sim 2 \cdot 10^6 \text{ cm}^{-3}$. A few microliters of the aqueous solution were pipetted onto the trap, which is visualized in Figure 7.7, A and B, and sealed with a microscope coverslip and a layer of double sided tape. Specifically, the surface charge Q of the beads was assumed from a comparable stated electron density of $2 \mu\text{mol/g}$ [167],

yielding a charge to mass ratio of $Q/(e_0m) \approx 1.2 \cdot 10^6 \text{ fg}^{-1}$ ($e_0 = 1.602 \cdot 10^{-19} \text{ C}$ denotes the elementary charge) that is in line with literature reports^[102,103,105].

However, since the actual surface charge Q remains an unknown, this particularly complicates the correct adjustment of trap parameters, i.e., AC voltage V_{ac} and frequency ω , thus possibly yielding an incorrect operation of the trap and finally unstable trapping. Nevertheless, since the final fiber trap design can closely be described via the analytical model (details see Equation 7.1), here, the geometric coefficient was assumed as $\Lambda \approx 0.47$, and the trap was operated at a voltage of $V_{ac} = 1 \text{ V}$ and a frequency of $\omega = 2\pi \cdot 500 \text{ kHz}$. For the designed trapping height of $z_0 = 15 \mu\text{m}$, specifically, this results in the dimensionless parameters $a = 0$, $q \sim 0.1$ and $b \sim 1$, effectively yielding an estimated electrophoretic trap stiffness of $\kappa \sim 100 \text{ pN}/\mu\text{m}$ (see Equations 3.14b, 3.14c and 3.16).

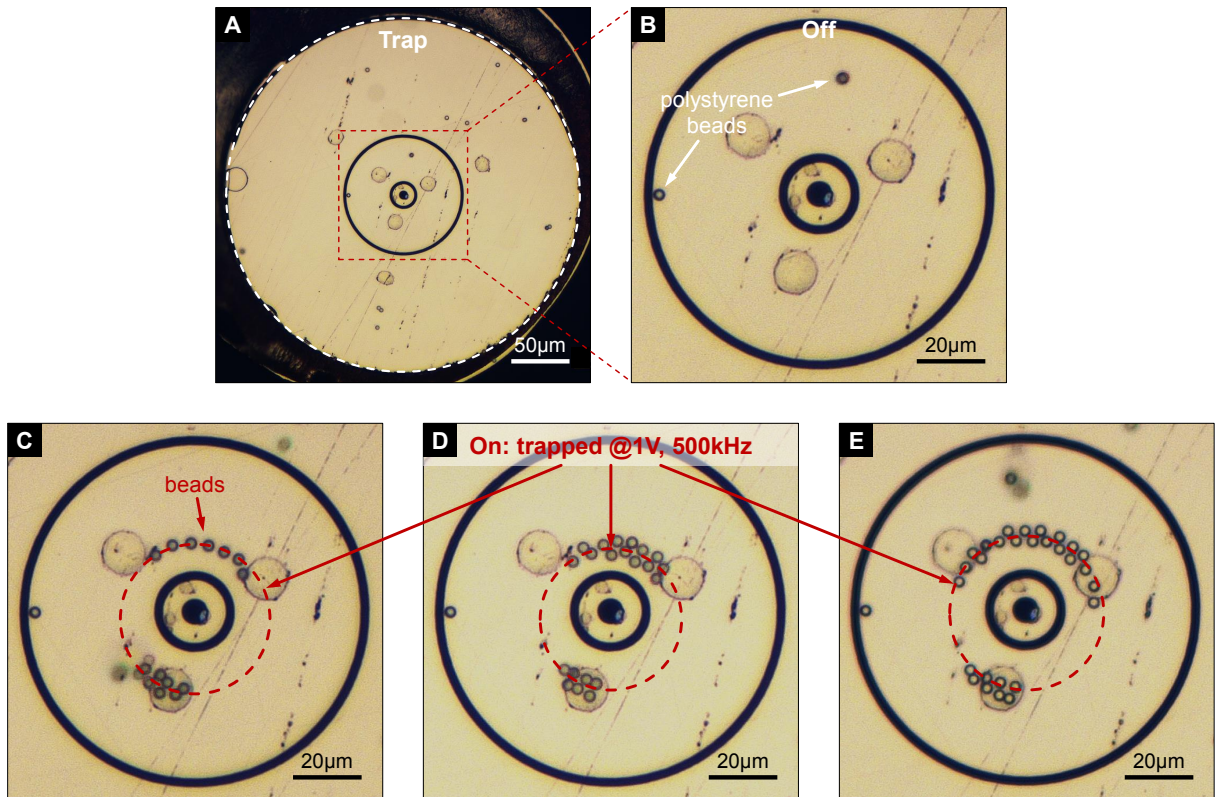


Fig. 7.7. Experimental demonstration of electrical trapping with a fiber point Paul trap. (A,B) The trap was loaded with charged $3 \mu\text{m}$ diameter polystyrene beads suspended in de-ionized water. (C–E) Once turned on and operated at an alternating voltage of 1 V and a frequency of 500 kHz , charged beads were immediately confined along an equipotential ring around the trap center. Avoiding the center presumably results from an excessive number of repulsive charged beads, the effect of dielectrophoresis (DEP) that is always present in addition to electrophoresis (EP) within aqueous media, or an incorrectly operated trap due to unknown surface charges. Nevertheless, the observations clearly reveal the capability of the electrical fiber trap.

As displayed in Figure 7.7, C to E, turning on the trap led to an immediate reaction of the charged beads while confining them on a ring around its center. Since their motion is damped via $u(t) \propto \exp(-t/\tau)$ (see Equation 3.17), they reach an equilibrium $u(t) < 1/e^2$ in water after approximately $\tau \sim 0.2 \text{ ms}$. Here, their confinement along the equipotential ring instead of in the center of the trap presumably results from an excessive number of

charged beads or the effect of dielectrophoresis (DEP), which is principally always present within aqueous media in addition to pure electrophoretic (EP) trapping of charged particles. Leading to the ring-type distribution, this effectively complicates the observation of pure EP trapping due to the electrochemical double layer² and thus a detailed analysis.

Unfortunately, the device quit working after a few seconds and, due to time- and cost-intensive multi-step process fabrication (see Figure 7.4) with low sample yield³, no additional quantitative measurement confirming the operation of the fiber point Paul trap via an improved high-speed recording of the sub-millisecond processes was possible. However, surface coating or undercutting the trapping structure via, e.g., chemical wet etching, potentially improves operation of the trap^[128,168]. This effectively prevents surface charges on the silica between the gold covered electrodes, which otherwise distort the electric potential $\Phi(r, z)$. Moreover, experimentally verifying the actual shape of the potential possibly improves correct adjustment of the fiber point Paul trap.

7.4 Chapter discussion

Within this chapter, the alternative concept of a fiber point Paul trap for electrical trapping of charged particles was presented as an outlook, including its design, implementation, and a qualitative experimental demonstration. An immediate reaction of charged $2R = 3\ \mu\text{m}$ diameter polystyrene beads to operating the trap at $V_{\text{ac}} = 1\ \text{V}$ and $\omega = 2\pi \cdot 500\ \text{kHz}$ was observed, which led to their confinement along an equipotential ring around the center of the trap. This presumably results from an excessive number of charged beads or the effect of DEP, which principally overlays pure EP forces in water due to screened charges. In particular, the stiffness κ of the electrical fiber trap was estimated as $\kappa \sim 100\ \text{pN}/\mu\text{m}$, yet sensitively depends on the specific trap parameters q and b , which potentially enables a broad range of tunability. Unfortunately, the device quit working after a few seconds, which thus prevented the improved high-speed recording of establishing a trapping equilibrium happening within under a millisecond in water.

Specifically the unknown electric potential $\Phi(r, z)$ and any surface charges, both for the trapped beads as for the trap itself, complicate correct EP operation due to providing only an estimated adjustment of parameters, thus possibly resulting in unstable trapping. Potential improvements, for example, include experimentally verifying the actual geometry of $\Phi(r, z)$ or undercutting the electrodes to prevent surface charges as distorting influences. However, since EP trapping effectively relies on net charges Q that are generally present on any surface, switching to DEP potentially provides better control due to reducing this influence. This principally enables applications such as, e.g., DEP combined Raman spectroscopy^[16], which in particular all benefit from a flexible single fiber trap geometry in case the Paul fiber is unmounted from the bulky aluminum disc.

²A diffuse oppositely charged layer screens the bead's surface charge (Fig. A.1 in the appendix).

³Total of one working sample within one year.

8

Conclusion and outlook

Within this chapter, the different concepts of particle trapping using hybrid optical fibers presented throughout this work are summarized. Specifically, the discussed concepts and obtained results are assessed (section 8.1), and the work is concluded with giving a future perspective at the end (section 8.2).

8.1 Assessment of results

In chapters 2–4, the essential prerequisites for understanding optical phenomena and hybrid optical fibers (chapter 2), free diffusive and trapped motion of microscopic objects under confining influences (chapter 3) as well as methods for analyzing fiber-based particle traps (chapter 4) were introduced. Subsequently, three different concepts of HOF traps were presented and discussed in chapters 5–7, including experimental demonstrations of their application for trapping freely diffusing particles in water. Specifically, the concepts represent two optical, i.e., a dual fiber focus trap (chapter 5) and a single meta-fiber trap (chapter 6), as well as one electrical fiber point Paul trap as an outlook (chapter 7), whose obtained results are assessed in the following and concluded in Table 8.1.

Dual fiber focus trap

The concept of a dual nanobore fiber (NBF) focus trap presented in chapter 5 principally represents a simple and straight-forward enhancement over a regular dual single-mode fiber (SMF) optical trap. Specifically, the unique beam profile of the NBF exhibits a focal spot that allows adjustment of the optical trap performance along the transverse and the axial direction independently via tuning the separation distance between both fibers. In particular, this unlocks combinations of the trap stiffness that are currently inaccessible to conventional fiber optical trap, which here was predicted via both a semi-analytical approximation model and a finite element method (FEM) simulation. Finally, the enhancement was experimentally confirmed via optically trapping freely diffusing individual 2 μm diameter silica beads in water using two different dual fiber trap configurations.

Compared to different fiber optical traps, the dual fiber focus trap benefits from its unique tunability and simple implementation while only relying on cleaving a piece of a hundreds

of meters long drawn fiber. Effectively, no time demanding post-processing is required, which in combination with its versatility is currently unavailable to other configurations, thus representing a unique feature and key advantage of the concept presented in this work. However, compared to a more flexible and simpler to integrate single fiber optical trap^[46], the NBF particularly suffers from its low numerical aperture (NA) requiring a dual fiber trap configuration, which thus limits its integrability and trapping performance.

Meta-fiber trap

The hybrid meta-fiber trap that was discussed in chapter 6, in contrast, effectively enables flexible, robust, and remote optical trapping of freely diffusing particles in water using only a single fiber. Specifically, it is based on a length-invariant piece of an SMF being fusion spliced to a sub-millimeter short section of an MMF for expanding the SMF beam and accommodating the full NA of a three-dimensional (3D) optically printed diffractive meta-lens on its facet. Here, the detailed meta-lens design, the implementation of both, the HOF and the 3D printed focusing lens, as well as the diffraction limited performance of an implemented meta-fiber were demonstrated, while particularly the designed ultra-high NA of 0.88 in water was experimentally confirmed.

Subsequently, a single meta-fiber was exemplarily applied for optically trapping individual silica microbeads and biologically relevant *Escherichia coli* (*E. coli*) bacteria in water, specifically confining them to within less than the focal volume for minutes at optical powers of up to 30 mW. However, compared to the dual NBF focus trap and similar HOF traps, in particular, the meta-fiber benefits from its simple, low-cost, reliable, and reproducible implementation. This effectively allows for a stand-alone and simple to integrate single fiber optical trap providing flexible and robust usability within difficult to reach remote scenarios. Nevertheless, the here presented concept principally suffers from its demand for post-processing and general limitation to transparent particles.

Fiber point Paul trap

In contrast to the two concepts of fiber-based optical traps, in chapter 7, the alternative of a fiber point Paul trap for electrically trapping charged particles was discussed as an outlook. Its design, implementation, and a qualitative application of trapping COOH⁻ surface charged 3 μm diameter polystyrene beads was experimentally demonstrated, for which an immediate reaction to operating the fiber trap was observed. This particularly led to their confinement along an equipotential ring around the center instead of in the center of the trap as respectively achieved within both fiber optical traps. Unfortunately, the electrical trap quit working shortly, and, due to extensive fabrication¹, repeated high-speed recording and a quantitative analysis of the established trapping (happening within under 1 ms in water) as respectively carried out for both fiber optical traps was thus not possible.

The discussed possible origins, i.e., a large number of charged beads or dielectrophoresis (DEP) that overlays the targeted pure electrophoretic (EP) trapping in water, represent a fundamental difference to the optical trapping concepts. For those, particle interaction as of optical binding is relatively simple to avoid, since excessive particles are ejected from the comparably small effective trapping volume automatically. This makes the fiber-based electrical trapping of individual particles particularly difficult due to its sensitive stability dependent on applied voltage, frequency, and specifically unknown particle charge, thus limiting reliability and repeatability. Nevertheless, although requiring the most intensive post-processing of all presented concepts, here, the estimated trap stiffness yields the highest value, however, sensitively depends on the parameters q and b .

Summary and comparison

Table 8.1 summarizes the obtained results of the HOF-based particle trapping concepts discussed throughout this work. Specifically, the key features of the different presented concepts are listed and a future perspective on envisioned potential applications is given, as discussed in further detail within the following section.

Tab. 8.1. Summary and comparison of hybrid fiber particle trapping results obtained within this work. The dual fiber focus trap and the meta-fiber trap represent concepts of hybrid optical fiber traps, while the fiber point Paul trap represents a hybrid electrical fiber trap. The listed potential applications were not explicitly demonstrated within the scope of this work but provide an envisioned future perspective.

Type of fiber trap	Demonstrated trapping	Stiffness κ_{\perp} , κ_{\parallel} [pN/ μm]	Key features	Potential applications	Reference
Dual fiber focus trap	2 μm silica, 5 μm polyst. beads, <i>E. coli</i>	0.7...2.1, 0.03...0.5 (2 · 30 mW)	+ tunability + simplicity - integrability	optical sensing & spectroscopy	chapter 5, [45, 62, 64, 65]
Meta-fiber trap	2 μm silica beads, <i>E. coli</i>	3.5, 0.4 (33.5 mW)	+ ultra-high NA + flexibility + reliability	<i>in vivo</i> imaging & manipulation	chapter 6, [21, 42, 44, 46]
Fiber point Paul trap	3 μm polyst. beads (ring)	~ 100 (estimated, 1 V)	+ performance + potentially generic use - complexity	particle sorting	chapter 7, [25, 90, 124]

8.2 Future perspective

In the following, potential further improvements of the hybrid fiber-based particle trapping concepts presented throughout this work and concluded in Table 8.1 are discussed in detail. Ultimately, a vision on future applications is given specifically with respect to optical, electrical and a multi-disciplinary combination of applications.

Optical manipulation and sensing

Optical manipulation, in particular, represents a vastly growing field including applications such as, e.g., the creation of multiple time varying trapping sites^[18,44,108]. Here, the dual fiber focus trap, for example, allows for coherently interfering sophisticated beam profiles, individually adjusting the optical powers emitted by each of the two fibers as well as for changing their inclination^[43,60,138]. In principle, these all represent further improvements, effectively enabling applications such as, e.g., the generation of conveyor and tractor beams for the transport and delivery of trapped particles^[108–110].

Moreover, the counter-propagating beam concept of the dual fiber focus trap in principle enables a full range of optical sensing applications particularly in life sciences. Specifically, these include, e.g., the controlled stretching of individual trapped cells^[64–66,118] for their 3D observation and physical analysis via microscopy as well as studying membrane mechanics, which effectively enables, e.g., tumorous tissue diagnosis. Of further interest, in particular, is the concept of rotating single trapped cells via adjusting the optical fiber mode^[66]. This can potentially be implemented via further improving the specific geometry of the nanobore fiber, since changing the diameter of the core and the central bore has a significant impact on the evolution of the fundamental mode^[45,57].

In situ and *in vivo* operation

Extending the scope of applications of the ultra-high NA single meta-fiber trap, however, to more complex shaped living objects aside from the trapped *E. coli* bacteria, e.g., allows for *in situ* motility sensing within the optical trap^[2,63] as well as subsequently investigating rotational diffusion^[142]. Here, further improvements of the meta-fiber trap in principle include precisely cleaving the expansion fiber as well as characterizing a sample and correcting the meta-lens to match the respective length of the expansion section. Particularly in combination with using a narrow band laser source, this potentially allows increasing the NA to near-immersion limited values^[151,163].

In principle, this enables a broad range of potential future applications specifically in life sciences, including high-resolution microscopy^[84,151] as well as fiber-based imaging^[38,39] and *in vivo* endoscopy^[40,42]. Here, the flexibility of the single meta-fiber device, in particular, is perfectly suited for applications within difficult to reach remote environments, such as high precision *in situ*^[44] or even *in vivo* optical control and manipulation of, e.g., biological cells on sub-micron scales through membranes within living organelles^[21].

Multi-disciplinary combinations

Although not explicitly demonstrated experimentally within the scope of this work due to time- and cost-intensive multi-step process fabrication with low sample yield, the fiber point Paul trap in principle allows for electrical trapping of biologically relevant species^[6,16,89]

as well, including, e.g., individual cells or bacteria. In particular, this is possible via either EP or DEP trapping, thus enabling the trapping of individual neutral and nontransparent particles as well, using DEP. However, as required charges for EP trapping are generally found on any surface, combining the electrical fiber trap with the DEP mechanism effectively provides a broader range of stable control over single trapped specimen. This reduces the dependence on charged particles, while, nevertheless, it was revealed that the charged fiber itself specifically complicates the electrical trapping. Possible solutions are, e.g., experimentally verifying the actual potential geometry, undercutting the electrodes, or removing the fiber from its aluminum mount.

In principle, these potential improvements of the fiber point Paul trap allow extending its scope to a range of multi-disciplinary applications, including, e.g., the sorting of mesoscopic objects such as biological cells with respect to certain properties apart from their charge^[25,90,91,124]. Effectively combining each of the concepts of hybrid fiber-based particle traps presented within this work with well-established techniques in life sciences, for example, opens up the possibility for applications such as, e.g., the chemical detection and sensing of molecular compositions of individual trapped cells via fiber-based^[37,38,62] Raman spectroscopy^[15,16]. This concept particularly stands out by using only one device for trapping, excitation and collection of the spectral signal of the trapped object of interest in front of the facet via the same fiber.

Ultimately, combining the presented concepts of fiber-based optical traps with the electrical fiber point Paul trap, e.g., bears the advantage of having two independent trapping mechanisms within the same fiber. For example, this enables trapping different kinds of particles simultaneously with only one device while observing their interaction. This can be of particular use within applications such as the transport and delivery of single particles^[108–110], e.g., shuttling single ions as qubits for quantum computation and establishing large-scale infrastructure networks^[8,22], or observing sub-molecular processes^[5,19] as well as cooling and measuring atomic transitions^[7,23,98].

Appendix

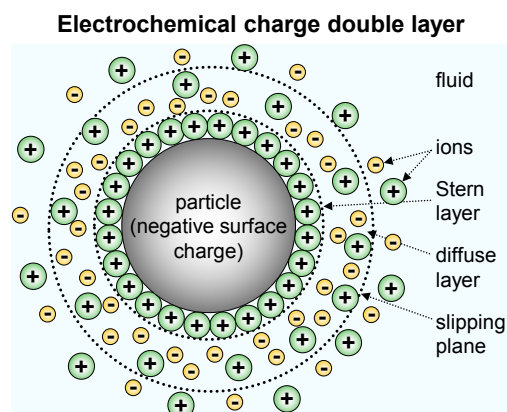


Fig. A.1. Principle of the electrochemical charge double layer (the Stern layer, adapted from [169]). A layer of diffuse oppositely charged ions of a surrounding fluid are attracted to the surface charge of a particle via the Coulomb force, thus screening it electrically. The static first layer represents the Stern layer, while the slipping plane denotes the effectively screened charge, i.e., the ζ potential, of the particle within the fluid.

A.1 Working principle of a point Paul trap

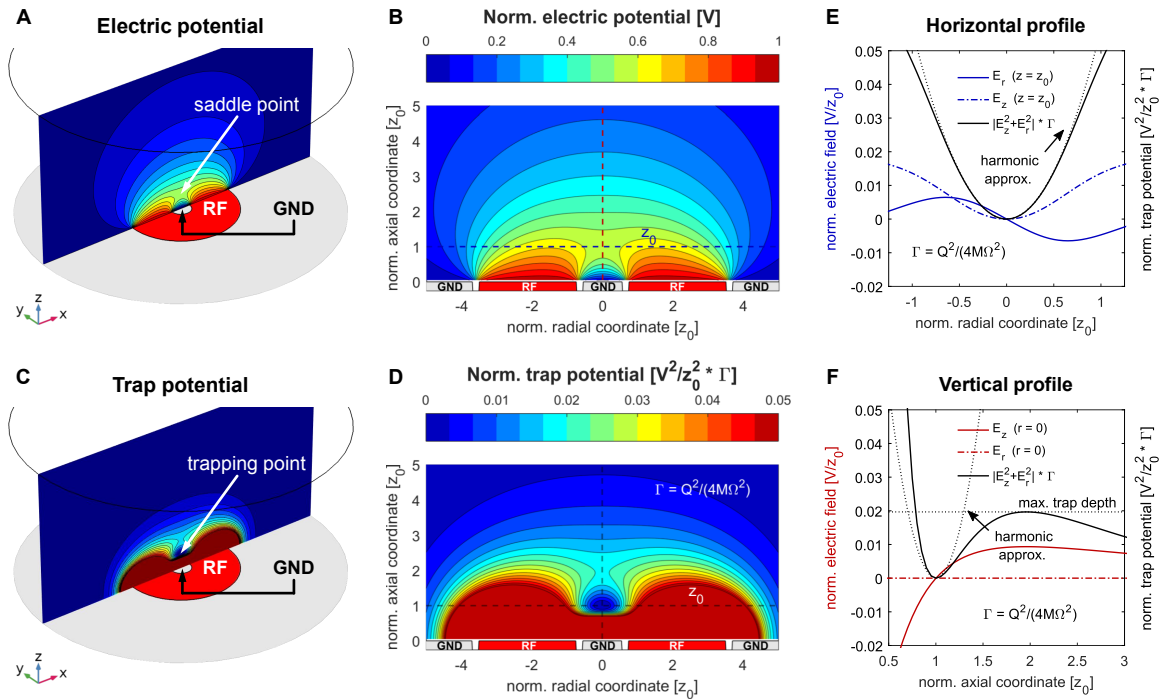


Fig. A.2. Working principle and calculated potentials of a surface-electrode point Paul trap. (A) Electric potential for three concentric rings of alternating polarity, i.e., radio frequency (RF) and ground (GND), inside an arbitrary medium, and (B) planar view of the area in A. The alternating polarity creates a saddle point above the center. (C) Resulting ponderomotive trap potential, and (D) planar view of the area in C as the square of the potential gradient, i.e., the normalized electric field. The vanishing gradient of the saddle point creates the trapping point. (E) Profiles along the horizontal and (F) the vertical dashed lines. Trapping around the center can be approximated via a damped harmonic oscillator (dotted parabolic curve).

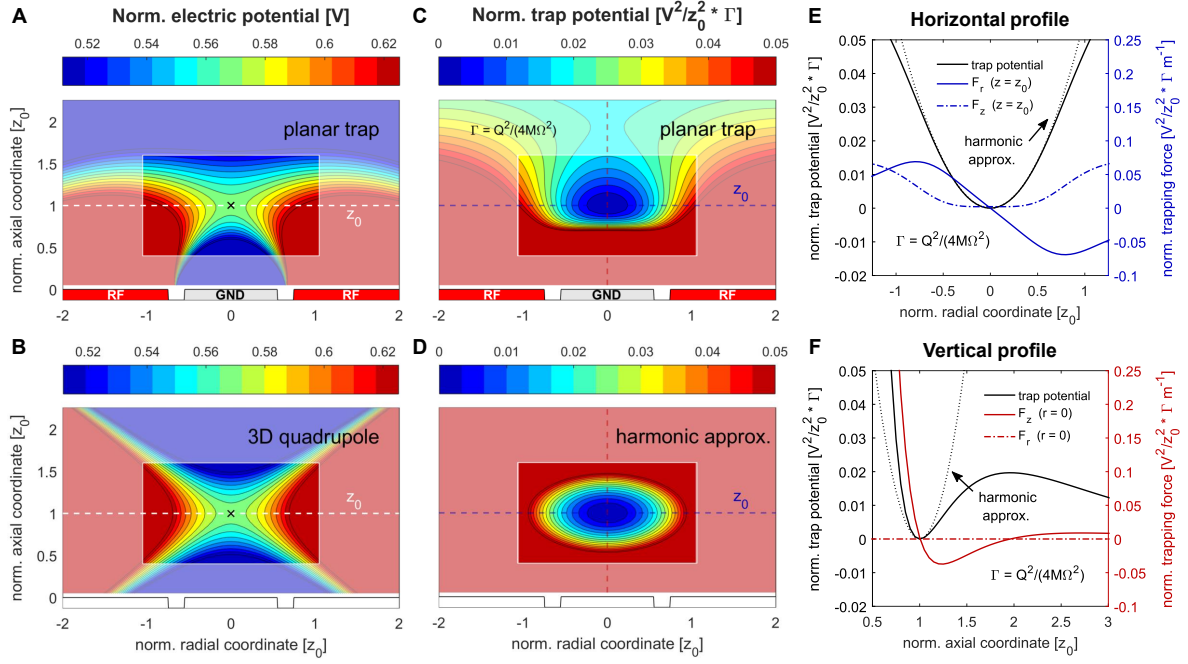


Fig. A.3. Calculated approximation of the point Paul trap via an ideal hyperbolic quadrupole. (A) Normalized electric potential for a planar point Paul trap, and (B) its approximation via a three-dimensional (3D) ideal quadrupole. The plot shows only the central region of the trap, where the innermost disc and the outermost ring are on ground (GND) and a radio frequency (RF) potential is applied to the ring in between. (C,D) Resulting normalized trap potential of A and B, respectively. (E) Profiles along the horizontal and (F) the vertical dashed lines in C and D, and resulting trapping force as the ponderomotive potential gradient.

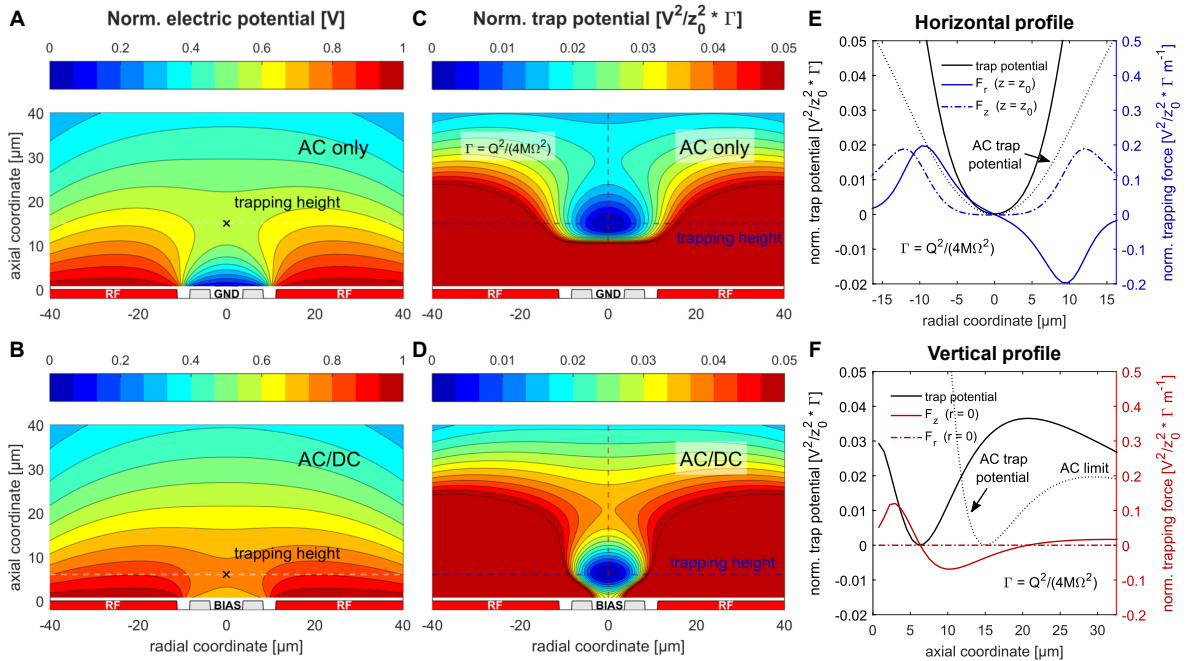


Fig. A.4. Calculated tunability of the point Paul trap potentials via applying a DC bias voltage^[68]. (A) Normalized electric potential for the AC-only case, where the innermost ring is kept on ground (GND) and a radio frequency (RF) voltage is applied to the second ring. (B) A static DC bias voltage is applied to the innermost ring, which lowers the trapping height above the surface. (C,D) Resulting normalized trap potential of A and B, respectively. The DC bias voltage also tightens the ponderomotive potential. (E) Profiles along the horizontal and (F) the vertical dashed lines in C and D, respectively. The DC bias voltage shifts the axial trapping position and increases the potential barrier that is required to escape the electrophoretic Paul trap.

A.2 Optical properties of the microwired Paul fiber

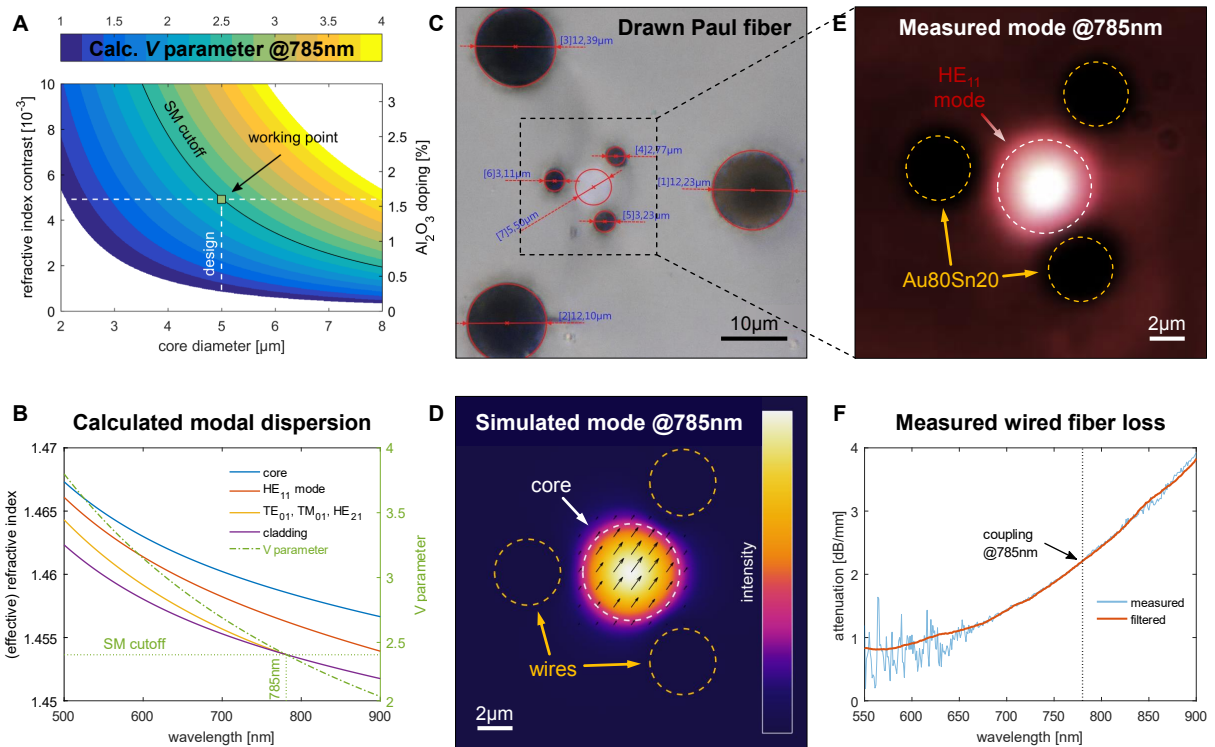


Fig. A.5. Design and measurement of the optical properties of the drawn Paul fiber. (A) Calculated V parameter for a wavelength of 785 nm as function of core diameter and refractive index contrast. A 5 μm diameter core, doped with 1.6% Al_2O_3 , is designed for an operation just below the single-mode (SM) cutoff. (B) Calculated modal dispersion, where the fundamental mode cuts off at 785 nm. (C) Micrograph of the drawn fiber. The result closely matches the design, where a core of 5.5 μm diameter is surrounded by three small holes of 3 μm diameter and by three larger ones of 12 μm diameter. (D) Simulated mode for a wavelength of 785 nm. The small holes (set to metallic wires) close to the core have no influence on the profile of fundamental mode. (E) Measured mode profile at a wavelength of 785 nm, where the holes are filled with the alloy Au80Sn20, forming microwires along the fiber axis. The measurement perfectly agrees with the simulation shown in D. (F) Measured loss of the microwired fiber, where the coupling was optimized for a wavelength of 785 nm. The loss increases significantly for longer wavelengths due to the metallic wires close to the core.

References

- [1] A. Ashkin and J. M. Dziedzic, “Optical trapping and manipulation of viruses and bacteria,” *Science* **235**, 1517–1520 (1987).
- [2] T. L. Min *et al.*, “High-resolution, long-term characterization of bacterial motility using optical tweezers,” *Nat. Methods* **6**, 831–835 (2009).
- [3] K.-Y. Chen *et al.*, “Transport and trapping in two-dimensional nanoscale plasmonic optical lattice,” *Nano Lett.* **13**, 4118–4122 (2013).
- [4] S. Faez *et al.*, “Fast, Label-Free Tracking of Single Viruses and Weakly Scattering Nanoparticles in a Nanofluidic Optical Fiber,” *ACS Nano* **9**, 12349–12357 (2015).
- [5] K. Svoboda *et al.*, “Direct observation of kinesin stepping by optical trapping interferometry,” *Nature* **365**, 721–727 (1993).
- [6] R. Hölzel *et al.*, “Trapping Single Molecules by Dielectrophoresis,” *Phys. Rev. Lett.* **95**, 128102 (2005).
- [7] S. Chu *et al.*, “Experimental Observation of Optically Trapped Atoms,” *Phys. Rev. Lett.* **57**, 314–317 (1986).
- [8] D. Kielpinski, C. Monroe, and D. J. Wineland, “Architecture for a large-scale ion-trap quantum computer,” *Nature* **417**, 709–711 (2002).
- [9] A. Einstein, “Über die von der molekularkinetischen Theorie der Wärme geforderte Bewegung von in ruhenden Flüssigkeiten suspendierten Teilchen,” *Ann. Phys. (Berlin)* **322**, 549–556 (1905).
- [10] P. Langevin, “Sur la théorie du mouvement brownien [On the Theory of Brownian Motion],” *C. R. Acad. Sci. Paris* **146**, 530–553 (1908).
- [11] A. Ashkin, “Acceleration and Trapping of Particles by Radiation Pressure,” *Phys. Rev. Lett.* **24**, 156–159 (1970).
- [12] A. Ashkin *et al.*, “Observation of a single-beam gradient force optical trap for dielectric particles,” *Opt. Lett.* **11**, 288–290 (1986).
- [13] W. Paul, “Electromagnetic traps for charged and neutral particles,” *Rev. Mod. Phys.* **62**, 531–540 (1990).
- [14] R. Maiwald *et al.*, “Stylus ion trap for enhanced access and sensing,” *Nat. Phys.* **5**, 551–554 (2009).
- [15] A. Bankapur *et al.*, “Raman Tweezers Spectroscopy of Live, Single Red and White Blood Cells,” *PLoS One* **5**, e10427 (2010).
- [16] U.-C. Schröder *et al.*, “Combined dielectrophoresis-Raman setup for the classification of pathogens recovered from the urinary tract,” *Anal. Chem.* **85**, 10717–10724 (2013).

- [17] L. Paterson *et al.*, “Controlled rotation of optically trapped microscopic particles,” *Science* **292**, 912–914 (2001).
- [18] D. G. Grier, “A revolution in optical manipulation,” *Nature* **424**, 810–816 (2003).
- [19] M. D. Wang *et al.*, “Stretching DNA with optical tweezers,” *Biophys. J.* **72**, 1335–1346 (1997).
- [20] R. Diekmann *et al.*, “Nanoscopy of bacterial cells immobilized by holographic optical tweezers,” *Nat. Commun.* **7**, 13711 (2016).
- [21] P. L. Johansen *et al.*, “Optical micromanipulation of nanoparticles and cells inside living zebrafish,” *Nat. Commun.* **7**, 10974 (2016).
- [22] J. Beugnon *et al.*, “Two-dimensional transport and transfer of a single atomic qubit in optical tweezers,” *Nat. Phys.* **3**, 696–699 (2007).
- [23] T. H. Kim, P. F. Herskind, and I. L. Chuang, “Surface-electrode ion trap with integrated light source,” *Appl. Phys. Lett.* **98**, 214103 (2011).
- [24] J. Voldman, “Electrical Forces for Microscale Cell Manipulation,” *Annu. Rev. Biomed. Eng.* **8**, 425–454 (2006).
- [25] M. J. Fulwyler, “Electronic Separation of Biological Cells by Volume,” *Science* **150**, 910–911 (1965).
- [26] J. N. Mehrishi and J. Bauer, “Electrophoresis of cells and the biological relevance of surface charge,” *Electrophoresis* **23**, 1984–1994 (2002).
- [27] K. C. Kao and G. A. Hockham, “Dielectric-fibre surface waveguides for optical frequencies,” *Proc. IEE* **113**, 1151–1158 (1966).
- [28] B. Lee, “Review of the present status of optical fiber sensors,” *Opt. Fiber Technol.* **9**, 57–79 (2003).
- [29] T.-H. Yi *et al.*, “Structural Health Monitoring of Civil Infrastructure Using Optical Fiber Sensing Technology: A Comprehensive Review,” *Sci. World J.* **2014**, 652329 (2014).
- [30] P. Lu *et al.*, “Distributed optical fiber sensing: Review and perspective,” *Appl. Phys. Rev.* **6**, 041302 (2019).
- [31] N. Granzow *et al.*, “Supercontinuum generation in chalcogenide-silica step-index fibers,” *Opt. Express* **19**, 21003–21010 (2011).
- [32] M. Chemnitz *et al.*, “Hybrid soliton dynamics in liquid-core fibres,” *Nat. Commun.* **8**, 42 (2017).
- [33] R. Sollapur *et al.*, “Resonance-enhanced multi-octave supercontinuum generation in antiresonant hollow-core fibers,” *Light Sci. Appl.* **6**, e17124 (2017).
- [34] C. Jauregui, J. Limpert, and A. Tünnermann, “High-power fibre lasers,” *Nat. Photonics* **7**, 861–867 (2013).

- [35] V. V. Tuchin, “Lasers and fiber optics in medicine,” in *Optical Methods of Biomedical Diagnostics and Therapy*, Vol. 1981 (Proc. SPIE, 1993).
- [36] P. Roriz *et al.*, “Review of fiber-optic pressure sensors for biomedical and biomechanical applications,” *J. Biomed. Opt.* **18**, 1–19 (2013).
- [37] C. Liberale *et al.*, “Integrated microfluidic device for single-cell trapping and spectroscopy,” *Sci. Rep.* **3**, 01258 (2013).
- [38] I. Gusachenko, M. Chen, and K. Dholakia, “Raman imaging through a single multimode fibre,” *Opt. Express* **25**, 13782–13798 (2017).
- [39] T. Čižmár and K. Dholakia, “Exploiting multimode waveguides for pure fibre-based imaging,” *Nat. Commun.* **3**, 1027 (2012).
- [40] S. Turtaev *et al.*, “High-fidelity multimode fibre-based endoscopy for deep brain in vivo imaging,” *Light Sci. Appl.* **7**, 92 (2018).
- [41] J. Trägårdh *et al.*, “Label-free CARS microscopy through a multimode fiber endoscope,” *Opt. Express* **27**, 30055 (2019).
- [42] H. Pahlevaninezhad *et al.*, “Nano-optic endoscope for high-resolution optical coherence tomography in vivo,” *Nat. Photonics* **12**, 540–547 (2018).
- [43] Y. Liu and M. Yu, “Investigation of inclined dual-fiber optical tweezers for 3D manipulation and force sensing,” *Opt. Express* **17**, 13624–13638 (2009).
- [44] I. T. Leite *et al.*, “Three-dimensional holographic optical manipulation through a high-numerical-aperture soft-glass multimode fibre,” *Nat. Photon.* **12**, 33–39 (2018).
- [45] M. Plidschun *et al.*, “Nanobore fiber focus trap with enhanced tuning capabilities,” *Opt. Express* **27**, 36221–36230 (2019).
- [46] M. Plidschun *et al.*, “Ultra-high numerical aperture meta-fiber for flexible optical trapping,” *Light Sci. Appl.* **10**, 57 (2021).
- [47] M. A. Schmidt, A. Argyros, and F. Sorin, “Hybrid Optical Fibers – An Innovative Platform for In-Fiber Photonic Devices,” *Adv. Opt. Mater.* **4**, 13–36 (2016).
- [48] A. F. Abouraddy *et al.*, “Towards multimaterial multifunctional fibres that see, hear, sense and communicate,” *Nat. Mater.* **6**, 336–347 (2007).
- [49] G. Tao, A. M. Stolyarov, and A. F. Abouraddy, “Multimaterial Fibers,” *Int. J. Appl. Glass Sci.* **3**, 349–368 (2012).
- [50] G. Kostovski, P. R. Stoddart, and A. Mitchell, “The optical fiber tip: an inherently light-coupled microscopic platform for micro- and nanotechnologies,” *Adv. Mater.* **26**, 3798–3820 (2014).
- [51] N. Wang *et al.*, “Nanotrimer enhanced optical fiber tips implemented by electron beam lithography,” *Opt. Mater. Express* **8**, 2246–2255 (2018).
- [52] C. Xiong *et al.*, “Optical Fiber Integrated Functional Micro-/Nanostructure Induced by Two-Photon Polymerization,” *Front. Mater.* **7**, 369 (2020).

- [53] S. Jiang *et al.*, “Fiber-Integrated Absorption Spectroscopy Using Liquid-Filled Nanobore Optical Fibers,” *J. Lightwave Technol.* **36**, 3970–3975 (2018).
- [54] M. Chemnitz *et al.*, “Octave-spanning supercontinuum generation in hybrid silver metaphosphate/silica step-index fibers,” *Opt. Lett.* **41**, 3519–3522 (2016).
- [55] A. Tuniz *et al.*, “Hybrid-Mode-Assisted Long-Distance Excitation of Short-Range Surface Plasmons in a Nanotip-Enhanced Step-Index Fiber,” *Nano Lett.* **17**, 631–637 (2017).
- [56] N. Wang *et al.*, “Boosting Light Collection Efficiency of Optical Fibers Using Metallic Nanostructures,” *ACS Photonics* **6**, 691–698 (2019).
- [57] H. Schneidewind *et al.*, “Photonic candle – focusing light using nano-bore optical fibers,” *Opt. Express* **26**, 31706–31716 (2018).
- [58] F. Lindenfesler *et al.*, “An ion trap built with photonic crystal fibre technology,” *Rev. Sci. Instrum.* **86**, 033107 (2015).
- [59] J. A. Kim *et al.*, “Fiber-Optic SERS Probes Fabricated Using Two-Photon Polymerization For Rapid Detection of Bacteria,” *Adv. Opt. Mater.* **8**, 1901934 (2020).
- [60] A. Constable *et al.*, “Demonstration of a-fiber-optical light-force trap,” *Opt. Lett.* **18**, 1867–1869 (1993).
- [61] X. Zhao *et al.*, “Optical Fiber Tweezers: A Versatile Tool for Optical Trapping and Manipulation,” *Micromachines* **11**, 114 (2020).
- [62] P. R. T. Jess *et al.*, “Dual beam fibre trap for raman micro-spectroscopy of single cells,” *Opt. Express* **14**, 5779–5791 (2006).
- [63] H. Xin, Q. Liu, and B. Li, “Non-contact fiber-optical trapping of motile bacteria: Dynamics observation and energy estimation,” *Sci. Rep.* **4**, 6576 (2014).
- [64] J. Guck *et al.*, “The optical stretcher: A novel laser tool to micromanipulate cells,” *Biophys. J.* **81**, 767–784 (2001).
- [65] M. E. Solmaz *et al.*, “Optical stretching of giant unilamellar vesicles with an integrated dual-beam optical trap,” *Biomed. Opt. Express* **3**, 2419–2427 (2012).
- [66] M. Kreysing *et al.*, “Dynamic operation of optical fibres beyond the single-mode regime facilitates the orientation of biological cells,” *Nat. Commun.* **5**, 5481 (2014).
- [67] B. Li, W. Piyawattanametha, and Z. Qui, “Metalens-Based Miniaturized Optical Systems,” *Micromachines* **10**, 301 (2019).
- [68] T. H. Kim *et al.*, “Surface-electrode point Paul trap,” *Phys. Rev. A* **82**, 043412 (2010).
- [69] A. W. Snyder and J. D. Love, *Optical Waveguide Theory* (Chapman and Hall, New York, 1983).
- [70] P. St. J. Russel, “Photonic Crystal Fibers,” *Science* **299**, 358–362 (2003).
- [71] P. St. J. Russel, “Photonic-Crystal Fibers,” *J. Lightwave Technol.* **24**, 4729–4749 (2006).

- [72] F. Benabid *et al.*, “Stimulated Raman Scattering in Hydrogen-Filled Hollow-Core Photonic Crystal Fiber,” *Science* **298**, 399–402 (2002).
- [73] A. Hartung *et al.*, “Low-loss single-mode guidance in large-core antiresonant hollow-core fibers,” *Opt. Lett.* **40**, 3432–3435 (2015).
- [74] T. M. Monro and H. Ebendorff-Heidepriem, “PROGRESS IN MICROSTRUCTURED OPTICAL FIBERS,” *Annu. Rev. Mater. Res.* **36**, 467–495 (2006).
- [75] H. W. Lee *et al.*, “Pressure-assisted melt-filling and optical characterization of Au nanowires in microstructured fibers,” *Opt. Express* **19**, 12180–12189 (2011).
- [76] C. Jain *et al.*, “Micron-sized gold-nickel alloy wire integrated silica optical fibers,” *Opt. Mater. Express* **6**, 1790–1799 (2016).
- [77] T. Lühder *et al.*, “All-Fiber Integrated In-Line Semiconductor Photoconductor,” *J. Lightwave Technol.* **37**, 3244–3251 (2019).
- [78] B. Doherty *et al.*, “Nanoparticle functionalised small-core suspended-core fibre – a novel platform for efficient sensing,” *Biomed. Opt. Express* **8**, 790–799 (2017).
- [79] M. Nissen *et al.*, “UV Absorption Spectroscopy in Water-Filled Antiresonant Hollow Core Fibers for Pharmaceutical Detection,” *Sensors* **18**, 478 (2018).
- [80] S. Jiang *et al.*, “Three dimensional spatiotemporal nano-scale position retrieval of the confined diffusion of nano-objects inside optofluidic microstructured fibers,” *Nanoscale* **12**, 3146–3156 (2020).
- [81] R. Förster *et al.*, “Tracking and Analyzing the Brownian Motion of Nano-objects Inside Hollow Core Fibers,” *ACS Sens.* **5**, 879–886 (2020).
- [82] R. S. Rodrigues Ribeiro *et al.*, “Fabrication of Fresnel plates on optical fibres by FIB milling for optical trapping, manipulation and detection of single cells,” *Sci. Rep.* **7**, 4485 (2017).
- [83] Y. Zhang *et al.*, “3-dimensional dark traps for low refractive index bio-cells using a single optical fiber Bessel beam,” *Opt. Lett.* **43**, 2784–2786 (2018).
- [84] M. Khorasaninejad *et al.*, “Metalenses at visible wavelengths: Diffraction-limited focusing and subwavelength resolution imaging,” *Science* **352**, 1190–1194 (2016).
- [85] K. Yamada *et al.*, “Multilevel phase-type diffractive lenses in silica glass induced by filamentation of femtosecond laser pulses,” *Opt. Lett.* **29**, 1846–1848 (2004).
- [86] A. Asadollahbaik *et al.*, “Highly Efficient Dual-Fiber Optical Trapping with 3D Printed Diffractive Fresnel Lenses,” *ACS Photonics* **7**, 88–97 (2020).
- [87] A. Siemion, “Terahertz Diffractive Optics—Smart Control over Radiation,” *J. Infrared Millim. Terahertz Waves* **40**, 477–499 (2019).
- [88] B. Amos, G. McConnell, and T. Wilson, in *Comprehensive Biophysics*, edited by E. Egelman (Elsevier, Amsterdam, 2012).

- [89] S. Joseph *et al.*, “A long DNA segment in a linear nanoscale Paul trap,” *Nanotechnology* **21**, 015103 (2010).
- [90] S. Fiedler *et al.*, “Dielectrophoretic Sorting of Particles and Cells in a Microsystem,” *Anal. Chem.* **70**, 1909–1915 (1998).
- [91] G.-H. Lee *et al.*, “Separation and sorting of cells in microsystems using physical principles,” *J. Micromech. Microeng.* **26**, 013003 (2016).
- [92] N. van Kampen, *Stochastic Processes in Physics and Chemistry*, Third Edition, North-Holland Personal Library (Elsevier, Amsterdam, 2007).
- [93] B. Lin, J. Yu, and S. A. Rice, “Direct measurements of constrained Brownian motion of an isolated sphere between two walls,” *Phys. Rev. E* **62**, 3909–3919 (2000).
- [94] P. Dechadilok and W. M. Deen, “Hindrance Factors for Diffusion and Convection in Pores,” *Ind. Eng. Chem. Res.* **45**, 6953–6959 (2006).
- [95] K. C. Neuman and S. M. Block, “Optical trapping,” *Rev. Sci. Instrum.* **75**, 2787–2809 (2004).
- [96] M. J. Saxton and K. Jacobson, “SINGLE-PARTICLE TRACKING: Applications to Membrane Dynamics,” *Annu. Rev. Biophys. Biomol. Struct.* **26**, 373–399 (1997).
- [97] N. Ruthardt, D. C. Lamb, and C. Bräuchle, “Single-particle tracking as a quantitative microscopy-based approach to unravel cell entry mechanisms of viruses and pharmaceutical nanoparticles,” *Mol. Ther.* **19**, 1199–1211 (2011).
- [98] A. Ashkin and J. P. Gordon, “Cooling and trapping of atoms by resonance radiation pressure,” *Opt. Lett.* **4**, 161–163 (1979).
- [99] K. C. Neuman and A. Nagy, “Single-molecule force spectroscopy: optical tweezers, magnetic tweezers and atomic force microscopy,” *Nat. Methods* **5**, 491–505 (2008).
- [100] Y. Pang and R. Gordon, “Optical Trapping of 12 nm Dielectric Spheres Using Double-Nanoholes in a Gold Film,” *Nano Lett.* **11**, 3763–3767 (2011).
- [101] O. Brzobohatý *et al.*, “Three-dimensional optical trapping of a plasmonic nanoparticle using low numerical aperture optical tweezers,” *Sci. Rep.* **5**, 8106 (2015).
- [102] W. Guan *et al.*, “Non-vanishing ponderomotive AC electrophoretic effect for particle trapping,” *Nanotechnology* **22**, 245103 (2011).
- [103] J. H. Park *et al.*, “Tunable aqueous virtual micropore,” *Small* **8**, 907–912 (2012).
- [104] S. Arnold, L. M. Folan, and A. Korn, “Optimal long term imaging of a charged microparticle at the center of a Paul trap in an atmosphere near standard temperature and pressure: Experiment and stochastic model,” *J. Appl. Phys.* **74**, 4291–4297 (1993).
- [105] W. Guan *et al.*, “Paul trapping of charged particles in aqueous solution,” *P. Natl. Acad. Sci. USA* **108**, 9326–9330 (2011).
- [106] LUMICKS, *Optical Tweezers*, <https://lumicks.com/optical-tweezers-working-principle> (visited on 10/18/2020).

- [107] J. A. Käs, *Optical Traps*, <https://home.uni-leipzig.de/pwm/web/?section=introduction&page=opticaltraps> (visited on 10/18/2020).
- [108] T. Čižmár *et al.*, “The holographic optical micro-manipulation system based on counter-propagating beams,” *Laser Phys. Lett.* **8**, 50–56 (2011).
- [109] D. B. Ruffner and D. G. Grier, “Optical Conveyors: A Class of Active Tractor Beams,” *Phys. Rev. Lett.* **109**, 163903 (2012).
- [110] O. Brzobohatý *et al.*, “Experimental demonstration of optical transport, sorting and self-arrangement using a ‘tractor beam’,” *Nat. Photon.* **7**, 123–127 (2013).
- [111] M. P. MacDonald, G. C. Spalding, and K. Dholakia, “Microfluidic sorting in an optical lattice,” *Nature* **426**, 421–424 (2003).
- [112] K. Ladavac, K. Kasza, and D. G. Grier, “Sorting mesoscopic objects with periodic potential landscapes: Optical fractionation,” *Phys. Rev. E* **70**, 010901 (2004).
- [113] J. P. Barton, D. R. Alexander, and S. A. Schaub, “Theoretical determination of net radiation force and torque for a spherical particle illuminated by a focused laser beam,” *J. Appl. Phys.* **66**, 4594–4602 (1989).
- [114] J.-B. Decombe, S. Huant, and J. Fick, “Single and dual fiber nano-tip optical tweezers: trapping and analysis,” *Opt. Express* **21**, 30521–30531 (2013).
- [115] M. M. Burns, J.-M. Fournier, and J. A. Golovchenko, “Optical binding,” *Phys. Rev. Lett.* **63**, 1233–1236 (1998).
- [116] T. Čižmár *et al.*, “Multiple optical trapping and binding: new routes to self-assembly,” *J. Phys. B: At. Mol. Opt. Phys.* **43**, 102001 (2010).
- [117] R. W. Bowman and M. J. Padgett, “Optical trapping and binding,” *Rep. Prog. Phys.* **76**, 026401 (2013).
- [118] N. Bellini *et al.*, “Femtosecond laser fabricated monolithic chip for optical trapping and stretching of single cells,” *Opt. Express* **18**, 4679–4688 (2010).
- [119] K. Taguchi and N. Watanabe, “Single-beam optical fiber trap,” *J. Phys. Conf. Ser.* **61**, 1137–1141 (2007).
- [120] R. Kasztelanec *et al.*, “Integrating Free-Form Nanostructured GRIN Microlenses with Single-Mode Fibers for Optofluidic Systems,” *Sci. Rep.* **8**, 5072 (2018).
- [121] M.-Y. Wu *et al.*, “Stable optical trapping and sensitive characterization of nanostructures using standing-wave Raman tweezers,” *Sci. Rep.* **7**, 42930 (2017).
- [122] T. Gissibl *et al.*, “Sub-micrometre accurate free-form optics by three-dimensional printing on single-mode fibre,” *Nat. Commun.* **7**, 11763 (2016).
- [123] O. Stern, “Zur Theorie der elektrolytischen Doppelschicht,” *Zeitschrift für Elektrochemie* **30**, 508–516 (1924).
- [124] B. M. Taff and J. Voldman, “A Scalable Addressable Positive-Dielectrophoretic Cell-Sorting Array,” *Anal. Chem.* **77**, 7976–7983 (2005).

- [125] M. Nasse and C. Foot, “Influence of background pressure on the stability region of a Paul trap,” *Eur. J. Phys.* **22**, 563–573 (2001).
- [126] J. H. Park and P. S. Krstić, “Stability of an aqueous quadrupole micro-trap,” *J. Phys. Condens. Mat.* **24**, 16420 (2012).
- [127] G. Littich, “Electrostatic Control and Transport of Ions on a Planar Trap for Quantum Information Processing,” MA thesis (ETH Zürich and University of California, Berkeley, 2011).
- [128] J. Chiaverini *et al.*, “Surface-Electrode Architecture for Ion-Trap Quantum Information Processing,” *Quantum Inf. Comput.* **5**, 419–439 (2005).
- [129] S. Seidelin *et al.*, “Microfabricated Surface-Electrode Ion Trap for Scalable Quantum Information Processing,” *Phys. Rev. Lett.* **96**, 253003(4) (2006).
- [130] J. H. Wesenberg, “Electrostatics of surface-electrode ion traps,” *Phys. Rev. A* **78**, 063410 (2008).
- [131] M. Balci and H. Foroosh, “Subpixel estimation of shifts directly in the Fourier domain,” *IEEE Trans. Imag. Process.* **15**, 1065–1972 (2006).
- [132] W. P. Wong and K. Halvorsen, “The effect of integration time on fluctuation measurements: calibrating an optical trap in the presence of motion blur,” *Opt. Express* **14**, 12517–12531 (2006).
- [133] A. van der Horst and N. R. Forde, “Power spectral analysis for optical trap stiffness calibration from high-speed camera position detection with limited bandwidth,” *Opt. Express* **18**, 7670–7677 (2010).
- [134] B. M. Lansdorp and O. A. Saleh, “Power spectrum and Allan variance methods for calibrating single-molecule video-tracking instruments,” *Rev. Sci. Instrum.* **83**, 025115 (2012).
- [135] S. F. Nørrelykke and H. Flyvbjerg, “Power spectrum analysis with least-squares fitting: Amplitude bias and its elimination, with application to optical tweezers and atomic force microscope cantilevers,” *Rev. Sci. Instrum.* **81**, 075103 (2010).
- [136] K. Berg-Sørensen and H. Flyvbjerg, “Power spectrum analysis for optical tweezers,” *Rev. Sci. Instrum.* **75**, 594–612 (2004).
- [137] P. Welch, “The Use of Fast Fourier Transform for the Estimation of Power Spectra: A Method Based on Time Averaging Over Short, Modified Periodograms,” *IEEE Trans. Audio & Electroacoust.* **15**, 70–73 (1967).
- [138] C. Ti, Q. Wen, and Y. Liu, “Objective-lens-free Fiber-based Position Detection with Nanometer Resolution in a Fiber Optical Trapping System,” *Sci. Rep.* **7**, 13168 (2017).
- [139] K. Schaarschmidt *et al.*, “Bending losses and modal properties of nano-bore optical fibers,” *Opt. Lett.* **43**, 4192–4195 (2018).

- [140] W. Singer *et al.*, “Self-organized array of regularly spaced microbeads in a fiber-optical trap,” *J. Opt. Soc. Am. B* **20**, 1568–1574 (2003).
- [141] D. S. Bykov *et al.*, “Long-range optical trapping and binding of microparticles in hollow-core photonic crystal fibre,” *Light. Sci. Appl.* **7**, 22 (2018).
- [142] Y. Han *et al.*, “Brownian Motion of an Ellipsoid,” *Science* **314**, 626–630 (2006).
- [143] J. Decombe *et al.*, “Single and Multiple Microparticle Trapping Using Non-Gaussian Beams From Optical Fiber Nanoantennas,” *IEEE J. Sel. Top. Quantum Electron.* **21**, 247–252 (2015).
- [144] A. Kuchmizhak *et al.*, “High-quality fiber microaxicons fabricated by a modified chemical etching method for laser focusing and generation of Bessel-like beams,” *Appl. Opt.* **53**, 937–943 (2014).
- [145] S. M. Rodrigues *et al.*, “Fabrication of multimode-single mode polymer fiber tweezers for single cell trapping and identification with improved performance,” *Sensors* **18**, 2746 (2018).
- [146] X. Tang *et al.*, “Super-low-power optical trapping of a single nanoparticle,” *Opt. Lett.* **44**, 5165–5168 (2019).
- [147] A. Koshelev *et al.*, “High refractive index Fresnel lens on a fiber fabricated by nanoimprint lithography for immersion applications,” *Opt. Lett.* **41**, 3423–3426 (2016).
- [148] J. Yang *et al.*, “Photonic crystal fiber metalens,” *Nanophotonics* **8**, 443–449 (2019).
- [149] Z. L. Wu *et al.*, “Polymer-based device fabrication and applications using direct laser writing technology,” *Polymers* **11**, 553 (2019).
- [150] K. Vanmol *et al.*, “3D direct laser writing of microstructured optical fiber tapers on single-mode fibers for mode-field conversion,” *Opt. Express* **28**, 36147–36158 (2020).
- [151] W. T. Chen *et al.*, “Immersion Meta-Lenses at Visible Wavelengths for Nanoscale Imaging,” *Nano Lett.* **17**, 3188–3194 (2017).
- [152] T. Gissibl *et al.*, “Refractive index measurements of photoresists for three-dimensional direct laser writing,” *Opt. Mater. Express* **7**, 2293–2298 (2017).
- [153] M. Schmid, D. Ludescher, and H. Giessen, “Optical properties of photoresists for femto-second 3D printing: refractive index, extinction, luminescence-dose dependence, aging, heat treatment and comparison between 1-photon and 2-photon exposure,” *Opt. Mater. Express* **9**, 4564–4577 (2019).
- [154] H. Ren *et al.*, “Complex-amplitude metasurface-based orbital angular momentum holography in momentum space,” *Nat. Nanotechnol.* **15**, 948–955 (2020).
- [155] M. Schade *et al.*, “Chemical functionalization of carbon/polymer bipolar plate materials via oxygen plasma activation and subsequent silanization,” *Surf. Coat. Technol.* **240**, 225–260 (2014).

- [156] X. Liu *et al.*, “3D Printing of Bioinspired Liquid Superrepellent Structures,” *Adv. Mater.* **30**, 1800103 (2018).
- [157] J. Fischer and M. Wegener, “Three-dimensional direct laser writing inspired by stimulated-emission-depletion microscopy [Invited],” *Opt. Mater. Express* **1**, 614–624 (2011).
- [158] Z. Gan *et al.*, “Three-dimensional deep sub-diffraction optical beam lithography with 9 nm feature size,” *Nat. Commun.* **4**, 2061 (2013).
- [159] J. Fischer *et al.*, “Exploring the Mechanisms in STED-Enhanced Direct Laser Writing,” *Adv. Opt. Mater.* **3**, 221–232 (2015).
- [160] C. E. Shannon, “Communication in the Presence of Noise,” *Proc. IRE* **37**, 10–21 (1949).
- [161] H. Ren *et al.*, “Three-dimensional vectorial holography based on machine learning inverse design,” *Sci. Adv.* **6**, eaaz4261 (2020).
- [162] G. Tkachenko *et al.*, “Optical trapping with planar silicon metalenses,” *Opt. Lett.* **43**, 3224–3327 (2018).
- [163] H. Liang *et al.*, “Ultrahigh Numerical Aperture Metalens at Visible Wavelengths,” *Nano Lett.* **18**, 4460–4466 (2018).
- [164] B. U. Brandstätter *et al.*, “Integrated Fiber-Mirror Ion Trap for Strong Ion-Cavity Coupling,” *Rev. Sci. Instrum.* **84**, 123104 (2013).
- [165] M. Zeisberger *et al.*, “Nanoboomerang-based inverse metasurfaces—A promising path towards ultrathin photonic devices for transmission operation,” *APL Photonics* **2**, 036102 (2017).
- [166] P. Lambracht, “Materialwissenschaftliche Aspekte bei der Entwicklung bleifreier Lotlegierungen,” PhD thesis (TU Darmstadt, 2002).
- [167] micromod Partikeltechnologie GmbH, *Technisches Datenblatt*, https://www.micromod.de/pdf/aktuell/01-02-503_tds_de.pdf (visited on 02/05/2021).
- [168] D. E. Austin *et al.*, “Halo ion trap mass spectrometer,” *Anal. Chem.* **79**, 2927–2932 (2007).
- [169] Wikimedia Commons, *Zeta Potential for a particle in dispersion medium*, https://commons.wikimedia.org/wiki/File:Zeta_Potential_for_a_particle_in_dispersion_medium.png (visited on 08/28/2020).

Acknowledgements

At the end, I wish to take the opportunity to express my greatest appreciation to the people involved in helping me accomplish this work.

- * First off, I gratefully acknowledge the scientific support from Prof. Markus Schmidt, his dedicated mentoring and patient guidance throughout the entire time of my PhD. Thank you!

- * I also appreciate the help from Dr. Karina Weber, Dr. Jens Kobelke and the fiber drawing team, Dr. Alessandro Tuniz, Dr. Uwe Hübner and the clean room team, Albrecht Graf, Prof. Tomáš Čížmár, Dr. Martin Šiler, Dr. Ondrej Stranik, Jisoo Kim, Dr. Jan Dellith, Dr. Ivo Leite, and Dr. Sergey Turtaev throughout various stages of the project.

- * I thank Dr. Haoran Ren, Dr. Ronny Förster, and Dr. Matthias Zeisberger for countless fruitful discussions and critical, yet constructive feedback on the scientific results.

- * I gratefully thank Dr. Brenda Doherty, Ramona Scheibinger, Tilman Lühder, and Bumjoon Jang for their invested time and effort in helping with proof reading the thesis.

- * I wish to acknowledge the kind support from Dr. Ning Wang, Dr. Mario Chemnitz, Torsten Wieduwilt, Shiqi Jiang, Mona Nissen, Kay Schaarschmidt, and other colleagues of the Hybrid Fibers Working Group at the Leibniz IPHT over many years.

- * Finally, I thank my friends and family for their long-term caring support, understanding, encouragement, and cheering up over the course of many years throughout my PhD time.

List of Publications

Journal publications

1. M. Zeisberger, H. Schneidewind, U. Hübner, T. Wieduwilt, M. Plidschun, and M. A. Schmidt, “Plasmonic Metalens-Enhanced Single-Mode Fibers: A Pathway Toward Remote Light Focusing,” *Adv. Photonics Res.* **2**, 2100100 (2021).
2. F. Gui, S. Jiang, R. Förster, M. Plidschun, S. Weidlich, J. Zhao, and M. A. Schmidt, “Ultralong Tracking of Fast diffusing Nano-Objects Inside Nano-Fluidic Channel Enhanced Microstructured Optical Fiber,” *Adv. Photonics Res.* **2**, 2100032 (2021).
3. M. Plidschun, H. Ren, J. Kim, R. Förster, S. A. Maier, and M. A. Schmidt, “Ultrahigh numerical aperture meta-fibre for flexible optical trapping,” *Light Sci. Appl.* **10**, 57 (2021).
4. S. Jiang, R. Förster, M. Plidschun, J. Kobelke, R. Fatobene Ando, and M. A. Schmidt, “Three-dimensional spatiotemporal tracking of nano-objects diffusing in water-filled optofluidic microstructured fiber,” *Nanophotonics* **9**, 4545–4554 (2020).
5. S. Jiang, J. Zhao, R. Förster, S. Weidlich, M. Plidschun, J. Kobelke, R. Fatobene Ando, and M. A. Schmidt, “Three dimensional spatiotemporal nano-scale position retrieval of the confined diffusion of nano-objects inside optofluidic microstructured fibers,” *Nanoscale* **12**, 3146–3156 (2020).
6. M. Plidschun, S. Weidlich, M. Šiler, K. Weber, T. Čížmár, and M. A. Schmidt, “Nanobore fiber focus trap with enhanced tuning capabilities,” *Opt. Express* **27**, 36221–36230 (2019).
7. H. Schneidewind, M. Zeisberger, M. Plidschun, S. Weidlich, and M. A. Schmidt, “Photonic candle – focusing light using nano-bore optical fibers,” *Opt. Express* **26**, 31706–31716 (2018).
8. M. Plidschun, M. Chemnitz, and M. A. Schmidt, “Low-loss deuterated organic solvents for visible and near-infrared photonics,” *Opt. Mater. Express* **7**, 1122–1130 (2017).

Conference proceedings

1. M. Plidschun, H. Ren, J. Kim, R. Förster, S. A. Maier, and M. A. Schmidt, “Ultra-high numerical aperture meta-fiber for flexible optical trapping,” in *2021 Conference on Lasers and Electro-Optics Europe & European Quantum Electronics Conference (CLEO/Europe-EQEC)* (IEEE, 2021), pp. 1–1.
2. M. A. Schmidt, T. Wieduwilt, M. Plidschun, M. Nissen, S. Jiang, and R. Förster, “Optofluidic fiber-based nanoparticle tracking analysis: tool to characterize diffusing nanoscale specimen such as SARS-CoV-2,” in *Proc. SPIE 11773, Micro-structured and Specialty Optical Fibres VII* (SPIE, 2021), 117309.
3. M. A. Schmidt, T. Wieduwilt, M. Plidschun, M. Nissen, S. Jiang, and R. Förster, “Optofluidic microstructured fibers: a base for measuring the Brownian motion of diffusing nano objects,” in *Proc. SPIE 11690, Smart Photonic and Optoelectronic Integrated Circuits XXIII* (SPIE, 2021), 116900C.
4. S. Jiang, J. Zhao, S. Weidlich, M. Plidschun, and M. A. Schmidt, “Three Dimensional Particle Tracking in Microstructured Graded Index Fiber,” in *2019 Conference on Lasers and Electro-Optics Europe & European Quantum Electronics Conference (CLEO/Europe-EQEC)* (IEEE, 2019), pp. 1–1.
5. M. Plidschun, S. Weidlich, K. Weber, M. Šiler, T. Čížmár, and M. A. Schmidt, “Nano-bore fiber focus trap with enhanced performance,” in *Conference on Lasers and Electro-Optics (CLEO)* (OSA, 2019), SM2L.1.

Ehrenwörtliche Erklärung

Ich erkläre hiermit ehrenwörtlich, dass ich die vorliegende Arbeit selbstständig, ohne unzulässige Hilfe Dritter und ohne Benutzung anderer als der angegebenen Hilfsmittel und Literatur angefertigt habe. Die aus anderen Quellen direkt oder indirekt übernommenen Daten und Konzepte sind unter Angabe der Quelle gekennzeichnet.

Bei der Auswahl und Auswertung folgenden Materials haben mir die nachstehend aufgeführten Personen in der jeweils beschriebenen Weise unentgeltlich geholfen:

1. Ziehen der Paul-Faser: Dr. Jens Kobelke (IPHT Jena)
2. Polieren der Paul-Faser: Albrecht Graf (IPHT Jena)
3. Mikrostrukturieren der Paul-Faser: Dr. Uwe Hübner (IPHT Jena)
4. Ziehen der Nanobore-Faser: Stefan Weidlich (Heraeus Glas Hanau)
5. FEM-Simulation der Doppelfaserfokusfalle (Fig. 5.6): Dr. Martin Šiler (Institute of Scientific Instruments of the CAS, Brno, CZ)
6. Bereitstellen der *E. coli* Bakterien: Dr. Karina Weber (IPHT Jena)
7. Anfertigen der REM-Bilder: Dr. Jan Dellith (IPHT Jena) und Dr. Haoran Ren (LMU München)
8. 3D-Druck des Polymerturms (Fig. 6.3A): Dr. Haoran Ren (LMU München)

Weitere Personen waren an der inhaltlich-materiellen Erstellung der vorliegenden Arbeit nicht beteiligt. Insbesondere habe ich hierfür nicht die entgeltliche Hilfe von Vermittlungs bzw. Beratungsdiensten (Promotionsberater oder andere Personen) in Anspruch genommen. Niemand hat von mir unmittelbar oder mittelbar geldwerte Leistungen für Arbeiten erhalten, die im Zusammenhang mit dem Inhalt der vorgelegten Dissertation stehen.

Die Arbeit wurde bisher weder im In- noch Ausland in gleicher oder ähnlicher Form einer anderen Prüfungsbehörde vorgelegt.

Die geltende Promotionsordnung der Physikalisch-Astronomischen Fakultät ist mir bekannt.

Ich versichere ehrenwörtlich, dass ich nach bestem Wissen die reine Wahrheit gesagt und nichts verschwiegen habe.

Jena, 26. Oktober 2021

Malte Plidschun